UNIVERSITAT DE BARCELONA

Development of high-resolution L4 ocean wind products

Ana Filipa Mestre Trindade

PhD Thesis

Development of high-resolution L4 ocean wind products

Ana Trindade

October 21, 2022

UNIVERSITAT DE BARCELONA

Development of high resolution L4 ocean wind products

Memoria presentada para optar al grado de doctor por la Universidad de Barcelona

Programa de doctorado en Física

Ana Trindade

Director - Dr. Marcos Portabella (ICM-CSIC)

Co-Director - Dr. Ad Stoffelen (KNMI)

Tutor - Dr. Joan Bech (UB)

Ana Trindade

UNIVERSITAT DE BARCELONA

Abstract

Heat, moisture, gas, and momentum exchanges at the oceanic and atmospheric interface modulate, inter alia, the Earth's heat and carbon budgets, global circulation, and dynamical modes. Sea surface winds are fundamental to these exchanges and, as such, play a major role in the evolution and dynamics of the Earth's climate. For ocean and atmospheric modeling purposes, and for their coupling, accurate sea-surface winds are therefore crucial to properly estimate these turbulent fluxes. Over the last decades, as numerical models became more sophisticated, the requirements for higher temporal and spatial resolution ocean forcing products grew. Sea surface winds from numerical weather prediction (NWP) models provide a convenient temporal and spatial coverage to force ocean models, and for that they are extensively used, e.g., the European Centre for Medium-range Weather Forecasts (ECMWF) latest reanalysis, ERA5, with ubiquitous hourly estimates of sea-surface wind available globally on a 30-km spatial grid. However, local systematic errors have been reported in global NWP fields using collocated scatterometer observations as reference. These rather persistent errors are associated with physical processes that are absent or misrepresented by the NWP models, e.g., strong current effects like the Western Boundary Current Systems (highly stationary), wind effects associated with the oceanic mesoscale (sea surface temperature gradients), coastal effects (land see breezes, katabatic winds), Planetary Boundary Layer parameterization errors, and large-scale circulation effects, such as those associated with moist convection areas. In contrast, the ocean surface vector wind or wind stress derived from scatterometers, although intrinsically limited by temporal and spatial sampling, exhibits considerable spatial detail and accuracy. The latter has an effective resolution of 25 km while that of NWP models is of 150 km. Consequently, the biases between the two mostly represent the physical processes unresolved by NWP models. In this thesis, a high-resolution ocean surface wind forcing, the so-called ERA*, that combines the strengths of both the scatterometer observations and of the atmospheric model wind fields is created using a scatterometer-based local NWP wind vector model bias correction. ERA* stress equivalent wind (U10S) is generated by means of a geolocated scatterometer-based correction applied separately to two different ECMWF reanalyses, the nowadays obsolete ERA-interim (ERAi) and the most recent ERA5. Several ERA* configurations using complementary scatterometer data accumulated over different temporal windows (TW) are generated and verified against independent wind sources (scatterometer and moored buoys), through statistical and spectral analysis of spatial structures. The newly developed method successfully corrects for local wind vector biases in the reanalysis output, particularly in open ocean regions, by introducing the oceanic mesoscales captured by the scatterometers into the ERAi/ERA5 NWP reanalyses. However, the effectiveness of the method is intrinsically dependent on regional scatterometer sampling, wind variability and local bias persistence. The optimal ERA* uses multiple complementary scatterometers and a 3-day TW. Bias patterns are the same for ERAi and ERA5 SC to the reanalyses, though the latter shows smaller bias amplitudes and hence smaller error variance reduction differences in verification (up to 8% globally). However, because of ERA5 being more accurate than ERAi, ERA* derived from ERA5 turns out to be the highest quality product. ERA* ocean forcing does not enhance the sensitivity in global circulation models to highly localized transient events, however it improves large-scale ocean simulations, where large-scale corrections are relevant. Besides ocean forcing studies, the developed methodology can be further applied to improve scatterometer wind data assimilation by accounting for the persistent model biases. In addition, since the biases can be associated with misrepresented processes and parmeterizations, empirical predictors of these biases can be developed for use in forecasting and to improve the dynamical closure and parameterizations in coupled ocean-atmosphere models.

Resumen

Los vientos de la superficie del mar son fundamentales para estimar los flujos de calor y momento en la interfaz oceánica-atmosfera, ocupando un papel importante en la evolución y la dinámica del clima del planeta. Por tanto, en modelación (oceánica y atmosférica), vientos de calidad son cruciales para estimar adecuadamente estos flujos turbulentos. Vientos de la superficie del mar de salidas de modelos de predicción numérica del tiempo (NWP) proporcionan una cobertura temporal y espacial conveniente para forzar los modelos oceánicos, y todavía se utilizan ampliamente. Sin embargo, se han documentado errores sistemáticos locales en campos de NWP globales utilizando observaciones de dispersómetros co-ubicados como referencia (asociados con procesos físicos que ausentes o mal representados por los modelos). Al contrario, el viento de la superficie del mar derivado de los dispersómetros, aunque intrínsecamente limitado por el muestreo temporal y espacial, presenta una precisión y un detalle espacial considerables. Consecuentemente, los sesgos entre los dos representan principalmente los procesos físicos no resueltos por los modelos NWP. En esta tesis, se crea un producto de forzamiento del viento en la superficie del océano de alta resolución, el ERA*. ERA* se genera con una corrección media basada en diferencias geolocalizadas entre dispersometro y modelo, aplicadas por separado a dos reanálisis diferentes, el ERA-interim (ERAi) y el ERA5. Varias configuraciones de ERA* utilizando datos de dispersómetros complementarios acumulados en diferentes ventanas temporales (TW) se generan y validan frente a datos de viento independientes, a través de análisis estadísticos y espectrales de estructuras espaciales. El método corrige con éxito los sesgos del vector de viento local de la reanálisis. Sin embargo, su eficacia depende del muestreo del dispersómetro regional, la variabilidad del viento y la persistencia del sesgo local. El ERA* óptimo utiliza múltiples dispersómetros complementarios y un TW de 3 días. Las dos reanálisis muestran los mismos patrones de sesgo en la SC, debido a que ERA5 es más preciso que ERAi, ERA* derivado de ERA5 es el producto de mayor calidad. El forzamiento oceánico ERA* mejora las simulaciones oceánicas a gran escala, donde las correcciones a gran escala son relevantes.

Contents

List of Tables

List of Figures

List of Equations

Acronyms List

4DVAR : Four Dimensional Variational

ACC : Antarctic Circumpolar Current

ADEOS : Advanced Earth Observation Satellite

AMM : Atlantic Meridional Mode

AMO : Atlantic Multidecadal Oscillation

AMSR : Advanced Microwave Scanning Radiometers

ASCAT-A : Advanced Scatterometer on board Metop-a

ASCAT-B : Advanced Scatterometer on board Metop-b

ASCAT-C : Advanced Scatterometer on board Metop-c

AV : Added Value

AWDP : ASCAT Wind Data Processor

BLUE : Best Linear Unbiased Estimation

BUFR : Binary Universal Form for the Representation of meteorological data

CCMP : Cross-Calibrated Multi-Platform

CDR : Climate Data Record

CEOS : Committee on Earth Observing Satellites

CFS : Climate Forecast System

CSIC : Consejo Superior de Investigaciones Científicas

CONAE : Comisión Nacional de Actividades Espaciales

EBCS : Eastern Boundary Current Systems

EBUS : Eastern Boundary Upwelling Systems

ECMWF : European Centre for Medium-Range Weather Forecasts

ENSO : El Niño–Southern Oscillation

ERA5 : Fifth ECMWF Reanalysis

ERS : European Remote Sensing Satellite

ESA : European Space Agency

ESM : Earth System Models

FC : Forecast

FFT : Fast Fourier Transform

FOV : Field of View

GCM : Global Circulation Models

GCOB :Global Climate Observing System

GMAO : Global Modeling and Assimilation Office

GMF : Geophysical Model Functions

GoF : Golf of Lyon

GRIB : Gridded Binary or General Regularly-distributed Information in Binary form

GS : Gulf Stream

GTS : Global Telecommunication System

HSCAT-A : HY-2A scatterometer

HSCAT-B : HY-2B scatterometer

ICM : Institut de Ciències del Mar

IFS : Integrated Forecast System

IPCC : Intergovernmental Panel on Climate Change

ISRO : Indian Space Research Organization

ISS : International Space Station

ISO : International Organization for Standardization

ITCZ : Intertropical Convergence Zone

JAMSTEC : Japan Agency for Marine-Earth Science and Technology

KNMI: Royal Netherlands Meteorological Institute

L2 : Level 2 Product: Directly retrieved (derived) geophysical variables in given locations

L3 : Level 3 Product: Composite of L2 Product for a period of time, mapped on uniform space-time grid scales, usually with some completeness and consistency method applied

L4 : Level 4 Product: Model output or results from analyses of combination of lower level data of at least two different variables

LTAN : Local Time of Ascending Node

MABL : Marine Atmospheric Boundary Layer

MEDS : Canadian Marine Environmental Data Service

MERRA : Modern-Era Retrospective Analysis for Research and Applications

MJO : Madden–Julian oscillation

MLE : Maximum Likelihood Estimator

MWRI : Micro-Wave Radiation Imager

NCEP : National Centers for Environmental Prediction

NDBC : National Data Buoy Center

NEMO : Nucleus for European Modelling of the Ocean

netCDF : Network Common Data Format

NOAA : National Oceanic and Atmospheric Administration

NRCS : Normalized Radar Cross Section

NSCAT : NASA Scatterometer

NTA: North Tropical Atlantic

NWP : Numerical Weather Prediction

NWPSAF : Numerical Weather Prediction Satellite Applica- tion Facility

ODAS : Ocean Data Acquisition System

OGCM : Ocean General Circulation Models

OI : Optimal Interpolation

OSCAR : Observing Systems Capability Analysis

OSCAT-1 : Oceansat-2 SCATterometer

OSCAT-2 : SCATSat-1 scatterometer

PDC : Pacific Decadal Oscillation

PenWP : Pencil-beam Wind Processor

PIRATA : Prediction and Research Moored Array in the Atlantic

PMEL : Pacific Marine Environmental Laboratory (NOAA)

QC : Quality Control

RAMA : Research Moored Array for African–Asian–Australian Monsoon Analysis

ROMS : Regional Oceanic Modeling System

SAR : Synthetic Aperture Radars

SC : Scatterometer Correction

SLA : Sea Surface Anomaly

SSH : Sea Surface Height

SSM/I : Special Sensor Microwave Imager

SST : Sea Surface Temperature

TAO : Tropical Atmosphere Ocean

TRITON : Triangle Trans-Ocean Buoy Network

U10S : Stress-equivalent wind

VAR : Variational Analysis

VRMS : Vector Root Mean Square

VRMSD : Vector Root Mean Square Difference

VRMSE : Vector Root Mean Square Error

WBCS : Western Boundary Current Systems

WMO : World Meteorological Organization

WVC : Wind Vector Cell

WWB : Westerly Wind Bursts

Chapter 1

Introduction

1.1 Energy transfers at the air-sea interface

Earth's Climate is dictated by the energy transfer occurring from the equatorial region to the poles. This large scale latitudinal transport occurs in order to balance an unevenly distributed heating on the planet's surface (Cronin et al., 2019), i.e., simply put, more heat is absorbed near the equator than lost by the upper atmosphere, while the reverse happens at high latitudes, creating flow patterns that transport heat from the equator to the poles. In a way, our climate is shaped by this motion, driven by the winds in the atmosphere and the currents in the ocean. Hence, global circulation is determined by the heat, moisture and momentum exchanges at the atmospheric and the oceanic boundary.

Ocean surface winds are crucial to estimate these exchanges. Fluxes of momentum, energy, and mass between the atmosphere and the ocean, include the surface stresses that drive ocean circulation and wave generation, the sensible heating that warms or cools the boundary layer, evaporation processes that moistens the atmosphere and increases ocean salinity, and gaseous exchanges that transfer CO_2 and other gases between the ocean and the atmosphere (Atlas et al., 2011). Furthermore, precipitation processes reduce ocean salinity and add surface wind variability.

Shifts in the patterns of surface fluxes turn into weather oscillations and affect surface wind patterns and local heat and moisture budgets, that in turn drive the ocean circulation, e.g., El Niño–Southern Oscillation (ENSO), Westerly Wind Bursts (WWBs), the Madden–Julian oscillation (MJO), the Pacific Decadal Oscillation (PDC), the Atlantic Multidecadal Oscillation (AMO), and the North Atlantic Oscillation (NAO).

Understanding the role and properly reproducing the dynamics of ocean surface winds in the Earth dynamical system, i.e., its imprint in the oceanic and atmospheric circulation, is crucial to address the uncertainties in climate change predictions. However, these circulations flow at a different pace, and physical processes at the air-sea interface occur on a wide range of spatio-temporal scales, e.g., diurnal cycle, extra-tropical cyclones and storms, boundary currents and oceanic fronts and eddies, with uncertainties growing with the natural variability of the weather at local and regional scales (Hurrell, 2008; Clarke et al., 2001). In short, the response of the coupled ocean-atmosphere system to continued climate change is complex, and to date not well known. Joint efforts between the experts of the multiple fields of the weather sciences, e.g., climatologists, physical oceanographers, modelers and meteorologists, as well as the use of models and long records of observations with the appropriate temporal and spatial resolution to resolve these interface dynamics, are both vital to improve our knowledge of past, current and future trends.

Therefore, regardless of the timescale, resolving long-term (climate), short-term (weather forecast), or even faster (nowcasting) dynamics requires the use of high resolution models with accurate initial forcing conditions, where ocean vector surface winds are imperatively included as a prime coupling agent between atmosphere and ocean.

1.2 Wind driven oceanic dynamics

At the air-sea interface many processes are dependent on the surface wind. Of utmost importance is the role played by surface winds in driving the global oceanic circulation and its variability, and regulating global and regional climate.

In the upper oceanic layers, the wind forcing largely governs the dynamical and thermal response of the system. In this manner, shear stress and atmospheric pressure generate waves and in extreme cases storm surges (Giesen et al., 2021; De Biasio et al., 2017), thereby affecting coastal currents and influencing sediment and nutrient transport (Desbiolles et al., 2014b,a). Moreover, local wind effects, such as wind funneling (gap winds), strengthen tidal currents and induce cooling of the SSTs under the gap flow (Hong et al., 2018). Additionally, surface winds play an important role in the momentum, heat and mass exchange with the atmosphere (turbulent fluxes), e.g., the sensible and latent heat fluxes are linear functions of the wind speed, the momentum fluxes have a square dependence (Subrahamanyam et al., 2009), while gas exchanges have a higher order dependence on wind speed. Whilst, beneath the ocean surface, the kinetic energy from this surface momentum and heat exchange propagates through the water column inducing vertical turbulent mixing and deep convective responses.

Wind stress and wind stress curl are fundamental in driving large-scale horizontal circulation in the upper layer of the ocean. This wind-induced large-scale circulation modulated by the amount of energy that goes into the ocean gyres, drives Ekman transport and Ekman pumping (Chelton, 1982). This way the subtropical gyres fed by the trades in the tropics and the westerly winds in the extra-tropics, induce poleward flow on the western side of the basins, through the Western Boundary Current Systems (WBCS), and equatorward flow on the eastern boundary, through the Eastern Boundary Currents Systems (EBCS). Nonetheless, the mean state of the ocean circulation is dominated by smaller scale (mesoscale) phenomena, where the surface momentum exchanges cause for an important part of the variability, e.g., ocean eddies present everywhere in the ocean, meandering currents or fronts, and upwelling filaments. In turn, these mesoscale structures influence key features of the large-scale ocean circulation like major oceanic currents such as the above mentioned WBCS, e.g., the Gulf Stream (GS), the Kuroshio, the Somali and the Agulhas currents, as well as the Southern Ocean overturning, and consequently the total poleward heat transport (Gruber et al., 2011; Gaube et al., 2015; Seo, 2017). Improved understanding of the processes modulating ocean circulation and its effect on climate, namely those driven by surface winds, is mostly achieved through ocean modelling.

1.3 Ocean modeling

For the most part, numerical ocean models, and specifically general circulation models (GCM), are optimal for diagnosis of interface dynamics and very useful to represent oceanic circulation. Effectively, ocean models are numerical models used to represent the physics governing the evolution of oceanic physical variables, such as temperature (T), salinity (S), horizontal (u, v) and vertical (w) velocities. The first ocean circulation model attempting to solve the primitive equations late in the 1960s was introduced by Bryan and Cox (1967). Nowadays the advances in computational capabilities have widened the scope of oceanic physical processes reproduced in numerical simulations, enabling a more meaningful understanding of the ocean. Accordingly, ocean simulation studies can now resolve scales that go from global (as the above mentioned GCM, e.g., Nucleus for European Modelling of the Ocean (NEMO) (Madec and the NEMO Team, 2014)) to regional and local, e.g., Regional Oceanic Modeling System (ROMS) (Shchepetkin and McWilliams, 2005). Some of those are integrated as part of Earth System Models (ESM), others in coupled systems, or simply used as stand-alone models.

On the one hand, stand-alone models allow for ocean simulations at higher resolution horizontal grids than can be integrated into data assimilation frameworks or perform hindcasts and produce ocean re-analysis or short-range ocean forecasts (Dombrowsky et al., 2009; Chassignet et al., 2019). On the other hand, as the number of interdependent systems grows, the horizontal grid resolution in which ocean simulations run decreases. Consequently, ocean models in coupled model systems, e.g., coupled ocean-wave or ocean-atmosphere models, can produce seasonal to decadal forecasts, whilst when part of fully coupled ocean-ice-atmosphere models, they are generally intended for climate applications. For many anthropogenic activities, these forecasts (Chassignet and Verron, 2006) and hindcasts are extremely important.

For accurate initialisation, the implementation of data assimilation schemes is vital to produce reliable forecasts, both for the atmosphere and the ocean.

Whatever the type, and despite the advances in high performing computing, running physical ocean models requires information on boundary fluxes. Assuming the ocean is a forced dissipative system (Griffies, 2008), the atmospheric forcing of the upper ocean occurs by exchange of heat and water and by wind stress acting on the sea surface. Depending on the type of ESM, i.e., coupled or stand-alone, these fluxes are prescribed differently. Generally, the ocean model integrated in an ESM relies on boundary fluxes computed from the atmospheric, cryospheric, and hydrological models, which are based on interactions with the evolving ocean. In coupled ocean-atmosphere simulations the boundary layer fluxes are computed by the atmospheric model and fed into the ocean model, while surface information from the latter may be fed into the former, i.e., there is a feedback mechanism at play, and a two-way interaction between models operating at different spatio-temporal scales, or simulating interdependent processes (Kantha and Clayson, 2000; Seo, 2017; Warner et al., 2008). Resorting to couple model runs has been demonstrated to improve the relationship between SST, wind and other atmospheric variables in several studies, such as those from Bryan et al. (2010) and Small et al. (2014), using coupled models with eddy resolving ocean resolution.

Nevertheless, stand-alone high-resolution global and regional ocean circulation models are still extensively used to understand the upper ocean variability (mostly on seasonal to decadal scales) with boundary fluxes usually initialized from data sets or parameterized (Griffies, 2008). In these studies, to reproduce oceanic phenomena happening on a wide spectrum of spatial and temporal scales, it is essential to keep a steady network of ocean observations in both space and time. Evidently, such boundary conditions must include high resolution ocean wind forcing able to capture both the temporal and spatial variability on the small scales, i.e., the prescribed forcing must capture the upper ocean structure and mesoscale features such as eddies and meandering fronts (Chassignet and Verron, 2006). Using remotely sensed sea surface wind observations from Earth observing satellites makes for accurate ocean wind forcing (Vogelzang and Stoffelen, 2021). In studies by Chelton et al. (2004); Blanke et al. (2005), the use of scatterometer estimates as wind forcing properly reproduces ocean circulation as well as other ocean mesoscale features. While Tokmakian (2005) shows that sea level anomalies (SLA) and wave mechanisms are better represented when using scatterometer observations as opposed to Numerical Weather Prediction (NWP) outputs. These wind and stress inputs to ocean models from observations and atmospheric models are described below.

1.4 Sea surface wind observations

Sea surface wind observations are important for many applications, while crucial to improve weather and marine forecasts and warnings. Knowledge about maritime conditions, wind and waves, is necessary for many human activities, and extremely relevant for hazard management and at times for search and rescue activities. Needed for ocean forcing, sea surface wind is a key parameter in studies of oceanic waves, ocean circulation, marine meteorology and the coupling of oceanic and atmospheric systems. As such, ocean surface wind stress is considered as one of the Essential Climate Variables (`https://gcos.wmo.int/en/essential-climate-variables`) by the World Meteorological Organization (WMO) Global Climate Observing System (GCOS).

Sustained ocean surface wind observations gathered from *in situ* networks and continued satellite missions, starting in 1987 with microwave radiometers and followed with a series of scatterometers since 1991, together with surface data on other ocean variables, e.g., SST, SSH, SSS, are crucial to document specific oceanic processes as well as truthfully represent them in models (Chassignet et al., 2019). High-quality observations are required to constrain ocean models through data assimilation and also to validate them, assessing their skills and limitations. As in operational meteorology (Stoffelen et al., 2019), the use of satellite Earth Observation (EO) measurements is fundamental for operational oceanography. In particular, surface wind fields derived from scatterometers have been routinely used in data assimilation for over 20 years, improving model estimates and forecasts (De Chiara, 2014) by NWP centers, like the European Centre for Medium-Range Weather Forecasts (ECMWF) or the Met Office.

Despite the value of satellite wind observations when used in data assimilation schemes, short-range meteorological forecasts have persistent biases in ocean surface wind and stress fields (Belmonte Rivas and Stoffelen, 2019), implying errors in the forcing of ocean models. Hence, in this thesis scatterometer measurements are addressed in further detail, with the objective of their use in the generation of a high-quality and high-resolution ocean surface wind forcing product. That said, scatterometers and passive radiometers have been systematically measuring near-surface ocean winds for more than 30 years (Wentz et al., 2017; Ricciardulli and Manaster, 2021), enabling the development of multi-satellite gridded products, with the subsequent advance in inter-calibration methods as well as the generation of diverse climate data records (CDR) to monitor global and local variability trends in climate (Wentz et al., 2017; Verhoef et al., 2017).

1.4.1 *in situ* measurements

in situ wind data such as those acquired from oceanic buoys installed on mooring platforms or measured by ships are often considered as ground truth (García-Reyes and Largier, 2010; Freeman et al., 2017). Despite their poor spatial sampling characteristics (point measurements), and overall scarcity globe wise (see Figure 1.1 for the moored buoy distribution in 2020), buoy wind information is of immense value, whether used to constrain ocean simulations, assimilated in NWP systems, or used as the only absolute reference for the monitoring and calibration of satellite wind data (Stoffelen, 1998). These buoys are managed by different institutions. Overall, open ocean buoys are distributed over the tropical band, while surface winds near the coast are mainly available alongshore USA and Canada. Of note, is the decrease in the number of monitored buoys, from 2014 onward.

Moreover, it is necessary to take into consideration the spatial and temporal characteristics of these measurements, and thereafter the representativeness errors between buoy data and other remote sources. Compared to the latter, buoy winds are not only acquired at a higher temporal frequency (usually every 10-min), but also contain more wind variability in low wind conditions, leading to big discrepancies between the distinct data measures (Lin et al., 2015a). For consistent inter-comparisons, the quality of the winds is evaluated w.r.t. the error characteristics and the scales resolved by the diferent wind sources, e.g., through triple collocation (Portabella and Stoffelen, 2009; Vogelzang et al., 2011b; Vogelzang and Stoffelen, 2021). Further note that satellite measurements, e.g., from scatterometers or radiometers, measure sea surface roughness, rather than the wind (De Kloe et al., 2017a; Wright et al., 2021).

Within the aims of this thesis, *in situ* surface wind continuously acquired from moored buoy, namely those displayed in Fig. 1.1, are used to validate and further improve the ocean wind forcing product being developed. These observations are obtained by the U.S. National Data Buoy Center (NDBC) and the Canadian Marine Environmental Data Service (MEDS), in the coastal and offshore waters of the continental United States and Canada and the Pacific Ocean around Hawaii and Alaska; the Ocean Data Acquisition System (ODAS) buoys in the northeast Atlantic and British Isles inshore waters; the Tropical Atmospheric Ocean (TAO/TRITON) array in the Pacific Ocean; the Japan Agency for Marine-Earth Science and Technology (JAMSTEC) Triangle Trans-Ocean Buoy Network (TRITON) buoys in the western Pacific; the Pilot Research Moored Array in the Tropical Atlantic (PIRATA) in the Atlantic; and the Research Moored Array for African–Asian–Australian Monsoon Analysis (RAMA) in the Indian Ocean.

1.4.2 Satellite measurements

In comparison with *insitu* observations, satellite wind data derived from active, e.g., Synthetic Aperture Radars (SAR), altimeters and scatterometers, or passive microwave radiome-

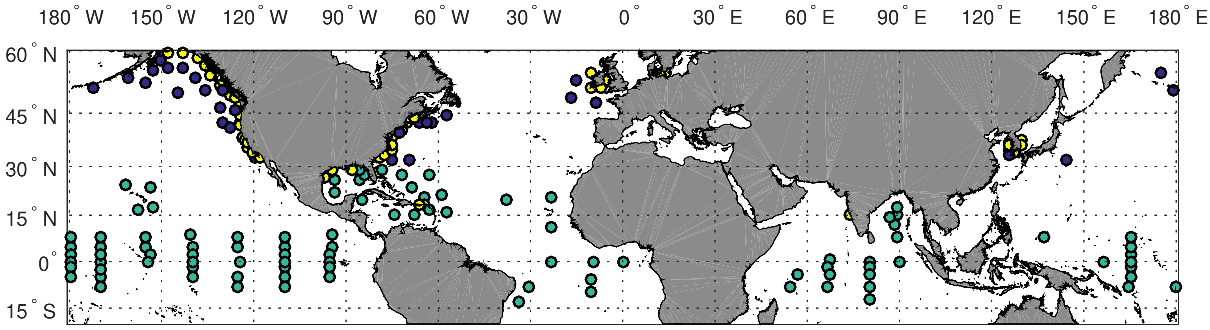

Figure 1.1: Global distribution of active oceanic moored buoys in 2020, obtained from the ECMWF Meteorological Archival and Retrieval System (ECMARS) buoy data set. Buoy locations are represented as colored dots and categorised according to region and proximity to the coast. Specifically, tropical data sets in green ([-30 30]° N), extra-tropical buoys are shown in blue and buoys within 100 km from the coast are colored yellow.

ters, continuously provide great spatial coverage of the global ocean (Gade and Stoffelen, 2019). Among these, the limited swath width (about 5 km) and spatial coverage poses some challenges for altimeters, as well as for SARs (not ideal for Climate studies), while radiometers and scatterometers sample over 90% of the earth's ocean every day. Nevertheless, satellite SARs allow the retrieval of wind fields with spatial resolutions on the few-kilometer scale (Portabella, 2002; Lin et al., 2008), i.e., an order of magnitude higher than that of scatterometers, which makes SAR data particularly well suited for studies of coastal processes, and the observation of short-scale wind features.

Passive co-polarized radiometers produce only wind speed from the analyses of the brightness temperature (electromagnetic radiation) emitted by the roughened sea surface, e.g., Special Sensor Microwave Imager (SSM/I), the Advanced Microwave Scanning Radiometers (AMSR-E and AMSR2) or Micro-Wave Radiation Imager (MWRI), (Wentz, 1997; Meissner et al., 2014). In addition, polarimetric radiometers, e.g., WindSat (Gaiser et al., 2004), were developed to measure the wind vector and have shown reasonable wind direction estimates above 8 $m.s^{-1}$ (Freilich and Vanhoff, 2006; Monaldo, 2006; Soisuvarn et al., 2007).

Whilst radiometers produce scalar winds, i.e., wind speed, with a spatial resolution better suited for global studies (Lenti et al., 2015; Meissner and Wentz, 2009; Bourassa et al., 2019), typically between 20-35 km, scatterometer estimates can effectively attain 20 km spatial scales on an operational basis (Chelton and Xie, 2010; Vogelzang et al., 2011a; Lin et al., 2015a; Vogelzang et al., 2015a; Vogelzang and Stoffelen, 2017). Additionally, the latter estimate ocean vector winds (OVW), i.e., the zonal and meridional wind vector components from measurements of radar backscatter over the ocean, thus providing information on the wind direction, and thereby a means to estimate dynamically important quantities such as divergence and wind stress curl (Kilpatrick and Xie, 2016; O'Neill et al., 2015; Belmonte Rivas and Stoffelen, 2019; King et al., 2022), imperative to properly reproduce Ekman dynamics like those driving the eastern boundary coastal upwelling systems in ocean simulations (Desbiolles et al., 2014b).

Scatterometers are active microwave radar sensors that provide high precision radiometric measures of the normalized radar cross section (NRCS, backscatter or σ_0) of the ocean surface, where the Bragg resonant mechanism (Bragg scattering) dominates the back-scattered signal

Table 1.1: Details of past, present and future OVW scatterometer missions, covering the period between 2010 and 2030, according to the instruments operating frequency (first column). The length of each mission is presented in table 1.2. This information is in accordance with the Committee on Earth Observing Satellites (CEOS) and the World Meteorological Organization (WMO) Observing Systems Capability Analysis (OSCAR).

	Instrument	Satellite	System	Orbit	Space Agency
C-band	AMI-SCAT	ERS-2[1]	fixed fan beam	10:30 desc	ESA/EUMETSAT
	ASCAT-A	Metop-A[2]		8:46 desc	
	ASCAT-B	Metop-B[3]		9:30 desc	
	ASCAT-C	Metop-C[4]		9:30 desc	
	SCA-1	Metop-SG-B1[5]		9:30 desc	
C-/Ku-band	WindRAD	FY-3E[6]	rotating fan beam	5:30	CMA
	WindRAD	FY-3I[7]		5:30	
Ku-band	CSCAT	CFOSAT[8]		7:00 desc	CNSA/CNES
	SCAT	CFOSAT[9]follow on		7:00 desc	
	HSCAT-A	HY-2A[10]	rotating pencil beam	6:00 desc	NSOAS/CAST
	HSCAT-2B	HY-2B[11]		6:00 desc	
	HSCAT-2C	HY-2C[12]		66°	
	HSCAT-2D	HY-2D[13]		66°	
	HSCAT-2E	HY-2E[14]		6:00 desc	
	HSCAT-2F	HY-2F[15]		66°	
	HSCAT-2G	HY-2G[16]		66°	
	OSCAT-1	OceanSat-2[17]		12:00 desc	ISRO
	OSCAT-3	OceanSat-3[18]		12:00 desc	
	OSCAT-2	ScatSat-1[19]		8:45 desc	
	SeaWinds	QuikSCAT[20]		6:00 asc	NASA
	RapidScat	ISS[21]		51.6°	NASA/CSA/ESA/ JAXA/Roscosmos

*Table 1.2: Length/expected length of the scatterometer missions. Note that the satellites presented in Table 1.1 directly correspond to the 1st column and are represented numerically. The state of a mission is displayed over a gray scale going from black to light gray, respectively for considered, planned and operational. The ** is used to inform that the expected life time of the mission is longer than displayed.*

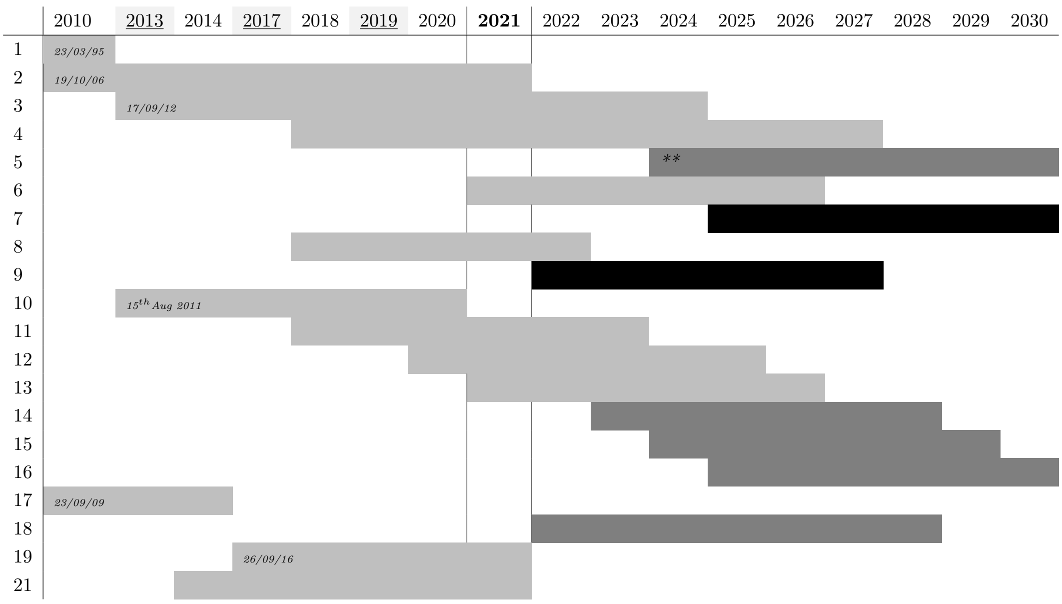

that reaches the satellite (De Chiara, 2014; Naderi et al., 1991; Figa-Saldaña et al., 2002; Chelton and Freilich, 2005). This mechanism is dominated by centimetre wavelength surface gravity-capillary waves formed either instantaneously by the blowing winds or, for winds above 5 $m.s^{-1}$, also by breaking waves. In both cases, the ocean short-wave spectrum is in equilibrium with the local winds (Mastenbroek, 1996). As physically-based models are relatively complex and inaccurate (Fois et al., 2015), empirical geophysical model functions (GMF) are used to relate NRCS to the wind vector (Stoffelen et al., 2017; Wang et al., 2019; Wentz and Smith, 1999). Using the GMF, the surface wind is inferred from the normalized radar backscatter as a function of wind speed, wind direction relative to the antenna azimuth, incidence angle, polarization, and radar frequency, at the reference height of 10 meter above the ocean surface. Scatterometer wind products are derived at 10-m height above the ocean for convenience only, to align them with the standard measurements available for calibration and validation (Stoffelen et al., 2019). To eliminate a dependency on air mass stability and air mass density, the so-called stress-equivalent 10-m winds are defined (De Kloe et al., 2017a).

These active sensors typically operate at C-band (5.255 GHz) or Ku-band (13.4 GHz) frequencies, providing quality wind vector observations in almost all weather conditions.

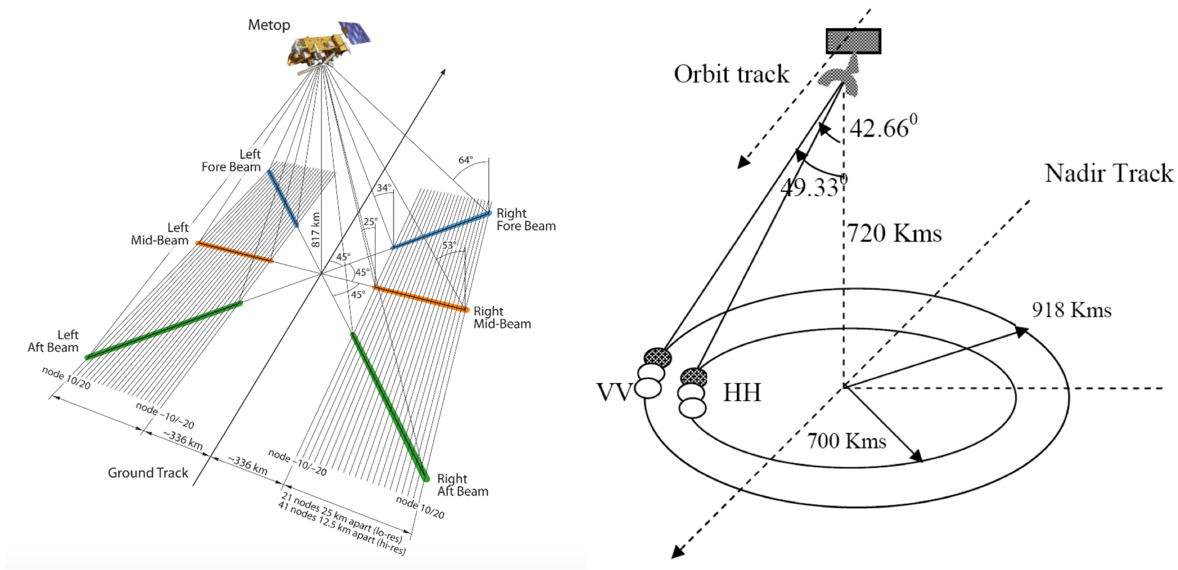

Figure 1.2: Fixed and varying viewing geometry for C and Ku-band systems. Left side diagram of ASCAT's measurement geometry (Figa-Saldaña et al., 2002) and right side diagram OSCAT's pencil beam geometry (Kirti Padia, 2010).

The scatterometers operating at C-band are hardly affected by the presence of rain (Lin et al., 2015a; Portabella et al., 2012; Stopa et al., 2017), whilst those operating in Ku-band are sensitive to both rain (Portabella and Stoffelen, 2001a; Milliff et al., 2004; Lin et al., 2016) and sea surface temperature (SST) (Polito et al., 2001; Wang et al., 2017; Wang et al., 2017). Rain contamination degrades the wind measurement accuracy, thus rain contaminated wind vectors need to be identified so that they can be treated properly during analysis, hence the need for the development of quality control (QC) algorithms in scatterometry (Xu and Stoffelen, 2020a; Figa and Stoffelen, 2000). As a result, using the inversion residual, or Maximum Likelihood Estimator (MLE), the singularity analysis, and the 2DVar QC, based on the methodologies in Portabella et al. (2012), Lin et al. (2015b) and Xu and Stoffelen (2020a), only about 0.5%–1% of the ASCAT-A/B retrieved winds are quality controlled (QCed), while 2%–5% of OSCAT/HSCAT winds are filtered out globally.

During high wind variability conditions, 2DVar QC indicators prove effective for filtering lower quality winds at both C and Ku-band frequencies (Xu and Stoffelen, 2020a). Nevertheless, cases with high variability in rainy areas depict physically plausible convergence and divergence associated with the hydrological processes (King et al., 2017). Moreover, for the Ku-band scatterometers, systematic errors emerge at high latitudes over very cold SST $< 5°C$ (Bentamy and Fillon, 2012) and SST-dependent GMFs are necessary to improve the retrieval, cf. Wang et al. (2017).

After passing QC procedures, scatterometers onboard satellites flying in sun-synchronous orbits provide an exceptional spatial coverage over the entire globe. HY-2C, HY-2D and the International Space Station (ISS) RapidScat in inclined non-sun-synchronous orbits, do not cover high latitudes. Figure 1.3, taken from Bourassa et al. (2019), represents the coverage provided throughout the day, with each screenshot displaying a quarter of the daily coverage for two sun-synchronous scatterometers (with partially overlapping swaths) and RapidScat.

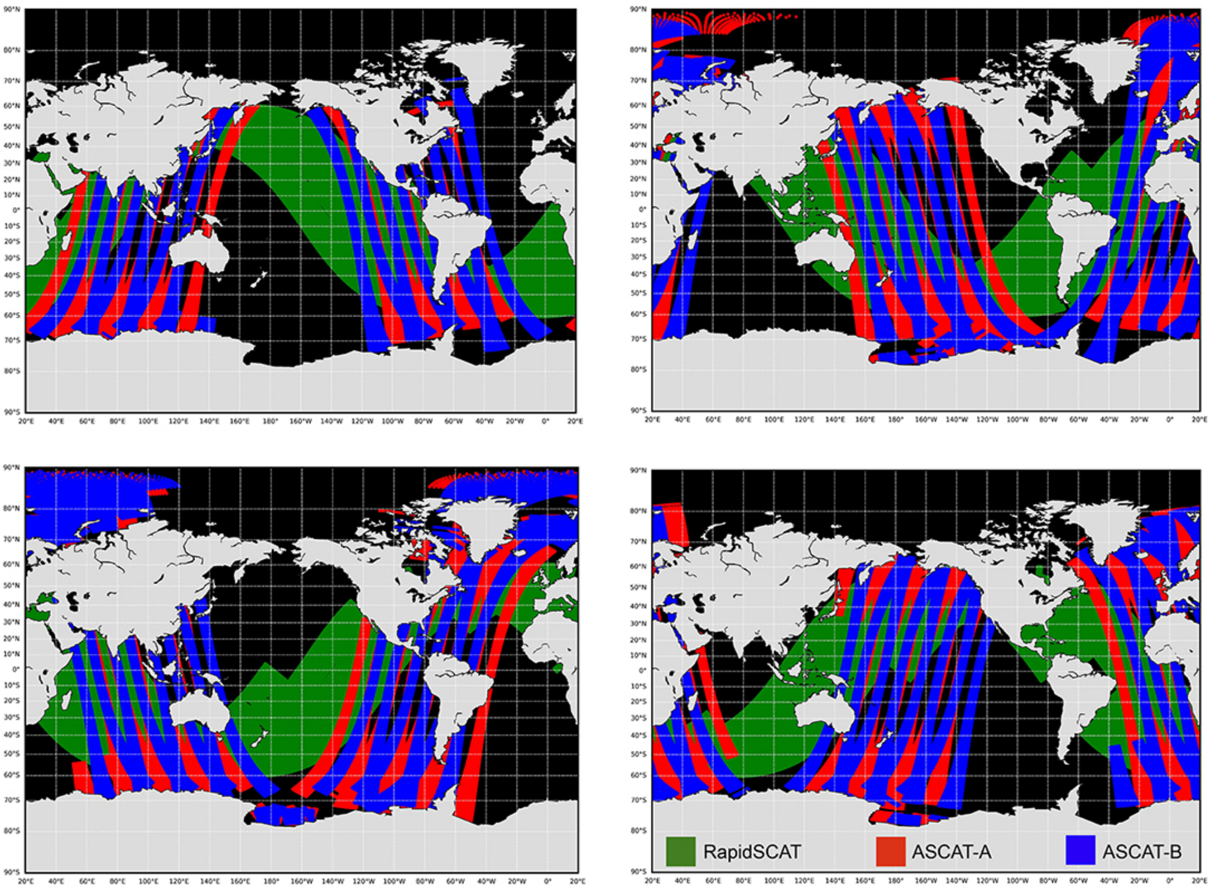

Figure 1.3: Examples of coverage: swaths from sun-synchronous scatterometers in red and blue, and from RapidScat in green. Four panels add up to daily coverage. From top to bottom, in the upper left from 0 to 6Z, upper right from 6 to 12Z, bottom left from 12 to 18Z, and 18 to 24Z at bottom right position (Fig. 3 from Bourassa et al. (2019)).

Even so, the fact that most scatterometers are flown in sun-synchronous orbits, represents passing each location approximately at the same solar local times every day.

In practical terms, it means that by themselves, each lack the appropriate temporal resolution to resolve some atmospheric dynamics, e.g., daily measurements cannot capture synoptic weather variability in the middle latitudes or the diurnal cycle in coastal areas. It is also important to take into account that most scatterometers launched by different Space Agencies observe the same location at different times of the day, and that because C-band and Ku-band radar signatures differ (see Figure 1.2) inter-calibration efforts become mandatory. Consequently, gathering the data from different scatterometers to produce consistent data records is challenging, specially for monitoring subtle changes in the wind field across satellite records and over long periods (Verhoef et al., 2017; Wentz et al., 2017).

Verhoef et al. (2017) also state that collocating other scatterometers to Rapidscat, thus providing simultaneous wind estimates at the same location, makes RapidScat ideal for cross-calibration between sensors. By itself, due to the orbit characteristics of the ISS and unlike a sun-synchronous scatterometers, RapidScat captures systematic changes in the diurnal cycle. HY-2C and HY-2D provide today similar capability (Wang et al., 2021).

Information on viewing geometry and operating frequency, plus additional mission details, are included in Table 1.1 for several ocean vector wind (OVW) scatterometer missions. Details are provided for past, current and scheduled OVW missions spanning back to 1995. The life time for each scatterometer is represented in scales of grey in Table 1.2 from 2010 onward. Note that before 2010, other earth observing missions were fully operational, amongst them: SeaSat (1978, only for 3 months), AMI-SCAT on ERS-1 (1991-2000) and ERS-2 (1995-2011, but only regional acquisitions since 2003 (Crapolicchio et al., 2007)), NASA Scatterometer (NSCAT) on the Advanced Earth Observation Satellite (ADEOS-1) (1996-1997), Seawinds on QuikSCAT (1999-2009), and Seawinds on ADEOS-2 (2002-2003)

From these two are listed in Table 1.1), because they provided a long-term time series of high-quality surface vector winds (Vogelzang and Stoffelen, 2021), e.g., the long lived C-band ERS-2 (1995-2011) and the Ku-band QuikSCAT (1999 to 2009) (Dunbar et al., 2006), both contributing to the first thematic and fundamental CDRs of scatterometer vector winds since 1991 (Ricciardulli and Manaster, 2021).

A limitation in using high-quality remotely-sensed vector winds from scatterometers is the spatial/temporal coverage of the retrievals. Scatterometers accurately capture spatial variability at high frequencies (Vogelzang et al., 2011a; Lin et al., 2015b; Patoux and Brown, 2001), but their uneven sampling patterns, mainly driven by orbital characteristics and swath widths, makes single instrument coverage unfit to force ocean models.

1.5 Atmospheric forcing for ocean modelling

As key drivers of the physical processes that take place at the air-sea interface, ocean winds are the primary forcing component for ocean numerical models. Wind forcing is necessary to reproduce oceanic circulation, wave and surge generation (Giesen et al., 2021), and to compute sea surface currents and air-sea fluxes. However, the available global sea surface wind observations are unevenly distributed and lack the required high spatial and temporal resolution, i.e., sampling, for the atmospheric model to capture the temporal and spatial scales of variability associated with the forcing of the ocean.

Traditionally and as a matter of convenience, ocean models rely on low resolution data assimilation approaches, such as from the NWP wind outputs (as briefly pointed in section 1.3) in order to achieve a gap free regularly spaced temporal/spatial grid. These approaches arise from the necessity to meet the sampling requirements in space and time for high resolution simulations, while trying to maintain the high quality information inherent in the observations (Stoffelen and Vogelzang, 2020). To improve on these NWP wind products, several hybrid products (Level 4 or L4) have been developed over the past years to try to bridge the gap between single satellite products, either swath-based (i.e., at Level 2 or L2) or fixed-gridded (i.e., at Level 3 or L3), and NWP models. These products may combine both observations and numerically simulated ocean surface winds, e.g., data assimilation, merging wind observations acquired from different instruments, or filling the gaps in observation coverage with specific interpolation techniques, e.g., Kriging method.

It is however problematic that merging techniques mix the spatial and temporal characteristics of the observed wind phenomena. For example, scatterometers are able to depict wind divergence associated with moist tropical convection (King et al., 2017), while such processes are very fast and can change the surface wind field within 30 minutes. Besides the scatterometer snapshots, no sufficient 4-dimensional dynamical information is available to deterministically initialize moist convection processes in global NWP models, hence resulting in lacking spatial and temporal description and a poor quality of local wind fields near convection (Lin et al., 2015a). In data assimilation techniques, both spatial and temporal averaging kernels are used to fill gaps in observations, while these act as so-called low pass filters, thereby ignoring the high spatial or temporal detail brought by the observations (Stoffelen and Vogelzang, 2020).

The deficits in global NWP model winds were well elaborated by Belmonte Rivas and Stoffelen (2019), depicting both small and large-scale errors and both spatially and temporally. The analysis moreover extends to spatial derivatives and Ekman pumping, which are both relevant for ocean forcing. Taking account of ocean currents does not reduce these deficits, but allows an improved physical representation of the modelling errors. The model errors found are very persistent in time and locally bound. This opens the way for observation-based bias correction procedures, as further elaborated in this thesis.

Satellite measurements from either radiometers or scatterometers are commonly used in the generation of L4 wind forcing products. In truth, because these sensors respond to the ocean state, primarily driven by stress rather then by wind, they are ideal for ocean simulations. Section 1.5.1 develops this concept and explains how the interpretation of the satellite winds as closer to stress imposes the need to represent the NWP and in-situ winds as 10-m height stress-equivalent winds for calibration and validation purposes. Validated stress-equivalent 10-m winds are also very suitable for ocean forcing.

1.5.1 U10S and wind stress

Satellite winds contain unique novel information with respect to both conventional observations and NWP outputs. Among these, ocean surface vector winds from scatterometers, recently redefined as 10-m stress-equivalent winds (U10S) by De Kloe et al. (2017a), are particularly interesting for forcing. Scatterometers retrieve the backscatter with respect to a moving ocean, therefore providing a wind measure from which ocean-atmosphere fluxes at the interface, governed by shear processes, can be accurately determined (Kelly et al., 2001; Chelton and Freilich, 2005), and both the large scale ocean circulation features like WBCS, and the associated mesoscale eddies around them are accounted for.

Moreover, sea surface winds acquired from these earth observing satellites respond to ocean characteristics that are driven by stress. True 10-m winds are in equilibrium with the ocean drag, but are moderated by air mass stability and are mass density, which dependencies are eliminated for U10S. As such, the notion that scatterometer retrievals are closer associated with stress than with real 10-m winds, makes them a good proxy for wind stress, i.e., wind forcing (Portabella and Stoffelen, 2004).

Note that in the past scatterometer retrievals were derived as 10-m equivalent neutral winds (U10N) to consider the influence of surface layer stability. Currently, scatterometer data are redefined as U10S to consider variations of air mass density, but not altered nor changed in any way after the use of the GMF for wind inversion. For NWP outputs or buoy observations, atmospheric stability and mass density variations must be accounted for to compute stress-equivalent winds, such that these winds are compatible with the scatterometer data. NWP U10S are calculated with Eq.1.1, where U10N is the 10-m equivalent neutral winds (obtained through a surface layer model to account for atmospheric stability effects), ρ_{air} the local air density and $< \rho_{air} >$ is the average global air density taken as 1.225 $[kg/m^3]$.

$$U10S = U10N\sqrt{\frac{\rho_{air}}{< \rho_{air} >}} \tag{1.1}$$

Consequently, the general bulk formulation to obtain wind stress for U10N is adapted so that wind stress can be computed from U10S. Thus Eq. 1.2 displays the bulk formulation for τ.

$$\tau = \rho_{air} CD \mid U_{10n} \mid U_{10n} \tag{1.2}$$

Then, because U10S accounts for variation of air mass density (Eq. 1.1), and according to De Kloe et al. (2017a), the bulk formulation for τ is given by Eq. 1.3.

$$\tau =< \rho_{air} > CD \mid U_{10s} \mid U_{10s} \tag{1.3}$$

1.5.2 Hybrid forcing products

With the growing demand of accurate high-resolution ocean wind forcing data sets (with global coverage at high temporal and spatial frequency), many attempts to improve the current ocean forcing products (generally provided by NWP outputs) were explored. As a result, gridded gap-free wind products were obtained by combining satellite data with NWP outputs using different blending techniques or data assimilation. Most of these L4 products re-sample or re-interpolate satellite data onto regular grids in regular time intervals, and/or make use of NWP outputs as background winds, in order to fill observational gaps. This allows for increased temporal sampling, but the spatial detail in the observations is often lost, and in the end blended products are affected by the spatial characteristics and caveats of the NWP models.

Amongst the proposed blended high resolution ocean wind forcing products, the available options are similar. The simplest approach, from Zhang et al. (2006), uses a spatial-temporally weighted interpolation to generate wind speed on a global 0.25° grid available for a few time resolutions, namely 12-hourly, daily, and monthly. The cross-calibrated multi-platform (CCMP) wind product (Atlas et al., 2011), developed with variational analysis (VAR), uses cross-calibrated microwave data from radiometers and scatterometers, *insitu* data, and, as background, wind reanalyses from NWP, to create a near-global Level 4 vector wind product on a 0.25° grid, available on 6-hourly intervals. Likewise, Yu and Jin (2014) and Bentamy et al. (2001, 2003) try to maximize global coverage by merging satellite wind fields into a single gridded L4 wind fields. The merging of data sets through objective analysis, respectively using a least variance linear statistical estimator and the Kriging method (Bentamy et al., 1996) results in a global daily vector wind product on a 25 km resolution grid, and a weekly product on a 1° grid.

Recently, newer versions of the CCMP product (Mears et al., 2019) and a new multiyear blended product (Desbiolles et al., 2017) were presented. In line with Atlas et al. (2011), newer CCMP versions use VAR to blend satellite data, but discontinued the use of buoy data in the generation of the product, included inter-calibrated wind observations and changed the NWP background source to either ERA-interim reanalysis (ERAi) or, aiming at a closer to near real time product, operational National Centers for Environmental Prediction (NCEP) model outputs. The multiyear blended product developed by Desbiolles et al. (2017), combines retrievals from four scatterometers, radiometers and ERAi reanalysis as background (using the Kriging method) to generate 6-hourly wind estimates globally on a 0.25° regular grid.

Despite the fact that the above mentioned products tend to outperform the NWP wind reanalysis, because they represent different spatial scales, different geophysical processes with systematic biases in geophysical variables and/or large-scale circulation errors, the result is a L4 product with rather artificial and mixed spatio-temporal characteristics, depending on where the satellite measures, where the gaps are and how the local transient weather evolves (Trindade et al., 2020; van Cranenburgh, 2022).

The four-dimensional variational (4DVAR) data assimilation is currently the most advanced method of blending wind observations and NWP estimates. Yet, NWP data assimilation follows the BLUE paradigm (Best Linear Unbiased Estimation), which requires unbiased data sets. This condition is clearly violated with the use of NWP wind fields (NWP biases discussed in subsection 1.5.3), but through local bias correction in NWP, the use of the BLUE paradigm should provide improved gridded products.

1.5.3 NWP outputs

Like ocean models, NWP models are mathematical representations of the physical and dynamical processes, in this case occurring in the atmosphere, on a wide variety of scales that go from a few kilometres and up to a couple of thousand kilometres (Jacobson, 2005).

Continuously improving since the mid-1990s, global atmospheric reanalyses simulated with these models have proven revolutionary for meteorological and marine weather forecasting by providing consistent gap free maps. These are obtained by reprocessing historical records of observations relying on the forecast model to coherently combine them through data assimilation, and produce fully gridded data sets of directly observed variables, as well as indirect ones (Carton and Giese, 2008; Gelaro et al., 2017). The latest global atmospheric reanalyses are available at higher grid resolution, use more sophisticated data assimilation schemes, e.g., BLUE and SODA (although none is free from the biases due to model/observations differences), and have benefited from the continuous development of forecast models.

As such, in the absence of high frequency spatial and temporal sampling of sea surface wind data observations, ubiquitous NWP forcing products are widely used in ocean simulations although the use of NWP and scatterometer wind products in simulations of ocean circulation yields significantly different ocean responses, as shown by Fu and Chao (1997) with NCEP reanalysis and ERA-1, respectively. Numerically simulated atmospheric winds are currently available either from reanalysis or from downscaled versions of these. Among the most commonly used in ocean forcing are the winds generated by Global Circulation Models (GCM), intended for climate predictions, with the latest generation used in the forthcoming 2022 IPCC Sixth Assessment Report. Also, winds from recent reanalyses like the Modern-Era Retrospective Analysis for Research and Applications, version 2 (MERRA-2), produced by NASA's Global Modeling and Assimilation Office (GMAO) (Gelaro et al., 2017), those from the National Oceanic and Atmospheric Administration (NOAA) NCEP produced by the Global Forecast System and Climate Forecast System (GFS and CFSR (version 2)(Saha et al., 2014)), or from the Integrated Forecast System (IFS) at ECMWF, e.g., ERAi (Dee et al., 2011) or ERA5 (Hersbach et al., 2020), the latter climate reanalysis available on an hourly base.

However, in addition to the initial condition errors present in the analysis that propagate and increase in time, the physics of the numerical models are not perfect. Physics related errors may be due to inaccurate parameterization of surface fluxes, frictional turbulence of surface winds, convection. Such errors lead to intrinsic model biases, e.g., local biases in specific climate zones dominated by specific weather regimes. Moreover, the systematic errors in the reanalysis winds project onto the circulation produced by the ocean general circulation models driven by these winds.

The use of sea surface wind observations from scatterometers to characterize NWP biases is a common practice to assess the quality of the simulated atmospheric winds, i.e., of the NWP ocean forcing products. A summary of the reported systematic biases in the NWP outputs, and further explanation on how this adds to the their limitations as wind forcing products can be found in the next subsection (1.5.4).

1.5.4 Current limitations

Currently, none of the proposed ocean wind forcing solutions fits the requirements to carry out high resolution simulations that study oceanic mesoscale processes.

As far as wind observations go, the use of satellite scatterometer U10S with all the adjacent benefits, i.e., accurate information on oceanic mesoscale features, an established effective resolution around 25 km, and the closest available proxy for wind stress, is mostly conditioned by sampling. Ocean forcing from individual sensors is strongly limited by their spatio-temporal coverage, which on a daily basis for a QuikSCAT-like satellite implies a global coverage of about 90% of the ocean (with two wind estimates available only for about 60% of it) (Lee et al., 2008). In addition to orbital constrains, gaps due to quality control, e.g., excluded rain contaminated winds from Ku-band sensors, add to an already poor sampling frequency.

As opposed to satellite measurements, simulated winds in NWP outputs are available everywhere but computed relative to an Earth-fixed location (each grid point), therefore requiring additional information on ocean currents, as well as atmospheric stratification and mass density prior to being used as ocean forcing (i.e., wind stress). For some blended products, e.g., newer CCMP versions, the influence of surface currents is implicitly included via satellite winds (Mears et al., 2019). This is particularly relevant in the tropical oceans, where surface currents can be of comparable magnitude with respect to ocean winds, as well as over the WBCSs, due to the magnitude and stationarity of these currents. Nevertheless, background winds in CCMP and other blended products have not been corrected for atmospheric stability.

On top of that, although data assimilation of wind data is general practice in NWP models, NWP wind outputs are of coarser resolution w.r.t. that of scatterometer estimates, i.e., the interpolation of winds between satellite overpasses may be performed on the larger scales (100-200 km), but the small-scale variability measured by scatterometers is generally lost in NWP fields, and by design global NWPs lack deterministic mesoscale structure (Belmonte Rivas and Stoffelen, 2019; Sandu et al., 2013a). Furthermore, 4DVAR does not work well with 25 km scale winds and observations only a few times a day (Bourassa et al., 2019). Consequently, persistent mesoscale features in scatterometer winds, such as those described by Chelton (2016) with 4-year averages of 25-km QuikSCAT winds, are missing in the model wind fields. These persistent features are the cause for systematic differences between model winds and scatterometer estimates.

These and several other issues on the quality of the NWP outputs have been described in studies comparing the simulated winds to scatterometer data. For ECMWF model winds, Belmonte Rivas and Stoffelen (2019) provide an empirical assessment of the NWP errors included in the ERAi and ERA5 reanalyses, and their timescales, using ASCAT-A ocean surface wind observations. The authors report large-scale circulation errors in both ECMWF reanalyses, from a systematic lack of meridional wind variability to poorly resolved small-scale dynamics, such as those associated with moist convection. Adding to those, local systematic errors, e.g., lack of cross-isobaric winds in ECMWF model winds, were monitored with ERS-2 data by Hersbach (2010b) and also by Gille et al. (2005), who had previously looked at the ERS-1,2. Brown et al. (2005b); Sandu et al. (2013a) describe these errors while assessing the quality of the NWP winds in comparison to other wind measurements.

The temporal frequency in which NWP L4 ocean forcing products are available is convenient for many ocean simulations. However, satellite ocean wind observations do not cover such temporal detail. As a consequence, because the multi-platform blended products incorporate all the available wind observations at one or more stages during the generation of the synthesized winds, assessing the skill and realism of the final product against independent wind sources poses a problem. The lack of an independent observational truth is aggravated by the fact that these products combine different spatial-temporal scales onto a single grid, which happens because different sources of wind represent different perspectives and stages of an evolving atmospheric disturbance, leading to somewhat artificial wind fields.

An alternative (to NWP background winds) for a L4 higher resolution ocean wind forcing with coherent wind fields containing mesoscale information obtained from scatterometer U10S is proposed in the next section (1.5.5).

1.5.5 New forcing: ERA^*

As established in previous sections, the regular sampling frequency of lower resolution NWP outputs, with respect to observations, makes them a widely used convenience for forcing in ocean models, as well as the background wind data for several hybrid products, despite the well documented errors present in these data sets. Many of the NWP errors are persistent in time and readily evident when collocating simulated model winds to scatterometer measurements. For the most part, the systematic differences between these two sources of wind data represent unresolved geophysical processes by the NWP models, within $\pm$ 2 $m.s^{-1}$. Such differences are hereafter referred to as local biases and can be seen in Fig. 1.4, for the zonal and meridional U10S wind components, from collocations of accumulated differences between ASCAT-A and ERAi, over a 30-day temporal window. Note that the darker blues and reds in Fig. 1.4 are located where these processes are missing, therefore some of these biases can persist over relatively long time periods, e.g., as in the presented 30 day in-time accumulation of ASCAT-A and ERAi U10S local differences.

In light of that, the development, validation and applicability in ocean simulations of a new ocean wind forcing product, ERA*, is explored throughout this manuscript. The ERA*, unlike common merging techniques, consists of scatterometer-based corrections (SC) of the mentioned local and persistent biases present in the NWP output. Note that an alternative bias mitigation approach has been previously explored on a regional scale by Biasio et al. (2017) and Bajo et al. (2017) to improve storm surge forecasting over the Golf of Lyon (GoL). However, their method aims to correct wind speed biases by scaling the model winds with weighted SCs averaged over a fixed time window (three days). Moreover, the wind conditions over three days during a storm are extremely variable. The methodology presented in this thesis is more generic and corrects the wind vector biases globally using multiple scatterometers and exploring several temporal windows.

The method is motivated by the persistence of the local model biases over time, allowing model wind corrections at each earth location based on a local time series. Therefore, gridded L4

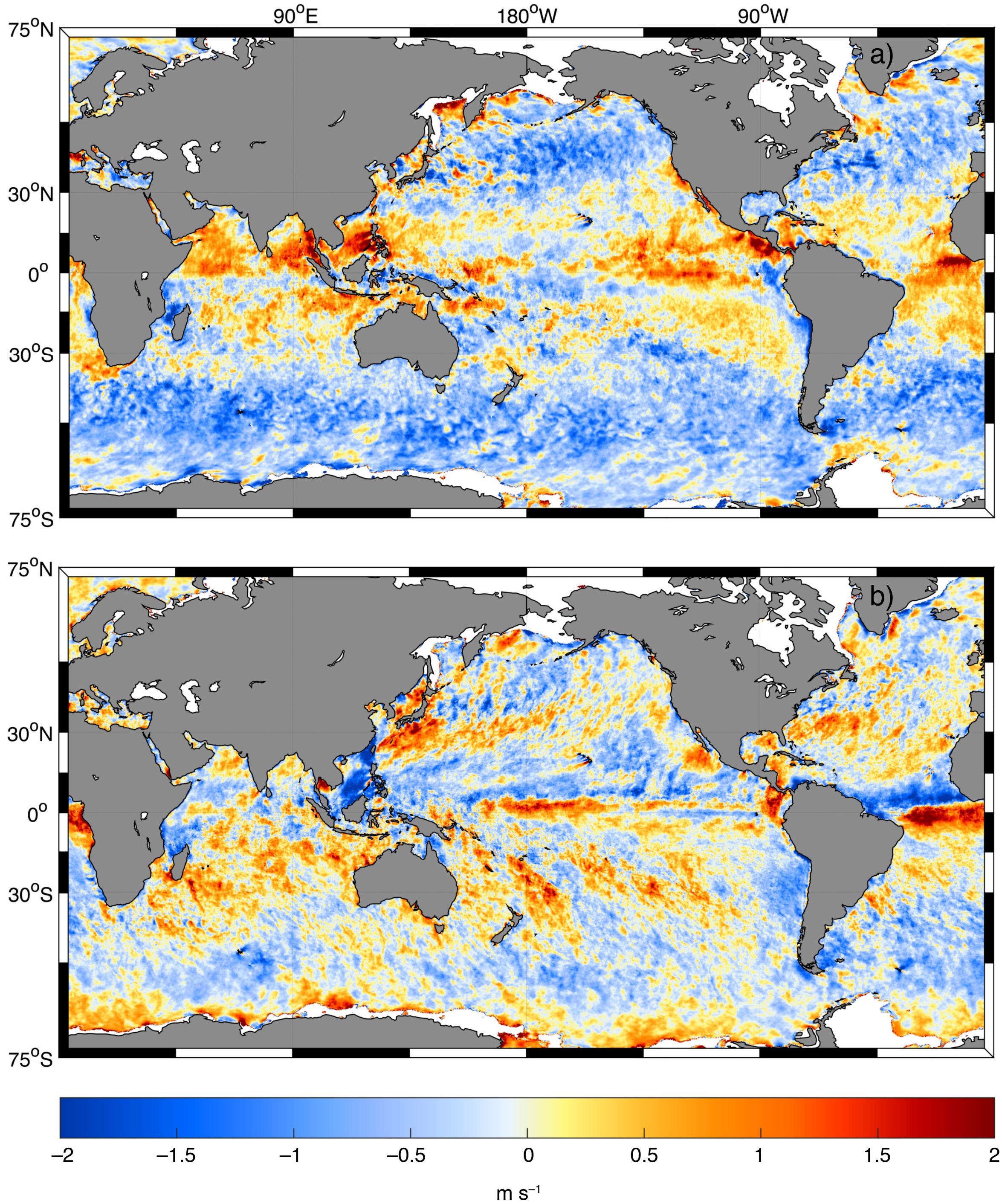

Figure 1.4: Collocated differences between ASCAT-A (12.5 km) and ERAi U10S for the zonal (a) and meridional (b) wind components, accumulated over a 30-day temporal window. The colors represent the differences in $m.s^{-1}$ (see color scale).

wind products may be produced by correcting the model winds at any time and any position. It exploits the repeated sampling of scatterometer observations by using one or more scatterometers for a temporal accumulation of the scatterometer wind data over the shortest possible period of time, and in this manner compute and correct model errors, while maintaining some of the most beneficial scatterometer features, i.e., accounting for highly stationary strong current effects, and other wind effects associated to ocean mesoscale processes, such as interface dynamics as wind-SST interaction, and meanwhile, correcting the large-scale NWP parameterization and dynamical errors.

With this approach, a scatterometer-based correction is applied to NWP U10S forecasts, using accurate, unbiased, high spatial resolution ocean vector winds from several scatterometers, in order to produce geophysically consistent L4 wind fields.

1.6 Research Questions

This thesis aims at addressing the following research questions:

1. Is it possible to improve the currently available surface wind forcing products by developing a more accurate, high resolution forcing with the information contained in the scatterometer data?

2. How does regional scatterometer sampling and weather affect the performance of static corrections, particularly in regions dominated by fast evolving atmospheric phenomena or increased wind variability?

3. Does ERA* wind forcing make for more realistic representations of oceanic circulation in numerical simulations than NWP forcing?

4. Can the ocean models response to high wind variability conditions, e.g., storm surges, be improved by static corrections of the NWP forecast winds?

1.7 Aim and overview of the thesis

The main aim of this thesis is to correct for local persistent model biases in NWP outputs by integrating mesoscale information contained in scatterometer measurements, and thereby generate a higher quality surface wind forcing product.

This thesis addresses the need for high-resolution ocean forcing. To do so, the research presented here explores a new approach for the development of L4 ocean wind products, based on applying scatterometer-based corrections (SC) to NWP forecasts. ERA* is the new L4 high resolution ocean wind product generated with this approach. In Chapter 2, the data methods used to produce and validate the ERA* data set are presented. It starts with a detailed description of the data (section 2.1), followed by an explanation of the hypothesis behind our rationale, which includes the layout of the methodology used to develop the algorithm (section 2.2) and its adaptation to a theoretical scenario through the simulation framework (section 2.3). Chapter 2 ends with the description of the most important wind validation techniques that are applied to the real ERA* data sets (section 2.4).

Chapter 3 is dedicated to evaluate the SC efficiency to correct for systematic biases in model output wind using synthetic wind data sets generated by means of Monte Carlo simulations. The analysis presented here follows the simulation framework described in section 2.3, and uses the parameterization in 2.3.1 to simulate realistic wind distributions with the Monte Carlo scheme.

Within this Chapter, two sections focus on weighing the key aspects/factors expected to affect the effectiveness of the proposed methodology, including a meticulous look at the regional effects of the scatterometer sampling (section 3.1) and wind variability (section 3.2) on simulated ERA* winds. A summary of the main findings of this Chapter can be found in section 3.3.

In Chapter 4, a detailed description is provided of the several configurations explored during the development of ERA*. A comparison between the quality of the generated product w.r.t. the model reanalysis (baseline reference) is included. Initial findings on the potential of ERA* for ocean wind forcing are obtained by correcting the ERAi reanalysis background winds in section 4.1. With the availability of the latest ECMWF reanalysis dataset, i.e., the fifth ECMWF reanalysis (ERA5), which contains similar error characteristics (although of smaller amplitude) as those found in its predecessor (ERAi), it became pertinent to assess the quality of a new ERA* generated from the ERA5 model output in section 4.2. In section 4.3, an optimized set of ERA* configurations, accounting for the varying scatterometer constellation, is achieved in order to produce an 11-year long (2010-2020) ocean forcing data set. Chapter 4 ends with a joint discussion on the comprehensive verification of the ERA* products described in the above mentioned sections.

Chapter 5 includes a couple of oceanographic applications of the new L4 ocean wind forcing products. The added value of ERA* w.r.t. other, commonly used forcing alternatives, i.e., ERAi and the ERA5 reanalyses, is addressed in this chapter by running the simulations separately for the different atmospheric forcing. Section 5.1 presents a climate variability study, in which the NEMO model is used for the ocean simulations, with either ERA* or ERAi wind stress as initial forcing predictions to study the impact of the 2017 North tropical Atlantic (NTA) warming on equatorial SST variability, and compared these results with those obtain with an EC-Earth control run. In section 5.2 a regional oceanographic application of ERA* winds under a high wind variability scenario is presented. The ERA* forecasts are used as the ocean forcing, with the aim of improving storm surge prediction capabilities over the Adriatic Sea. The storm surge response of The Shallow Water Hydrodynamic Model (SHYFEM) surge model, developed at the Institute of Marine Sciences (ISMAR), for a couple *aqua alta* events, is evaluated w.r.t the same run with NWP forecasts as atmospheric forcing, namely the ERA5. A comprehensive look at the ocean model responses to the enhanced forcing is included in section 5.3.

The last Chapter (Chapter 6) summarizes the main conclusions obtained while addressing the research questions proposed in this thesis. It includes a general outlook of the potential of this methodology in the development of high resolution ocean wind forcing products, alongside future perspectives and planned activities for future improvements of the present ERA* approach.

Chapter 2

Data & Methodologies

[1]

Local systematic differences observed when collocating NWP model outputs and scatterometer wind observations (Fig.1.4) stand out where physical processes are misrepresented or absent in the model. From the aforementioned zonal (Fig. 1.4a) and meridional (Fig. 1.4b) wind component differences, it is readily evident that they are more pronounced in certain regions of the global ocean, and that the phenomena to which they are associated dictate whether the model biases manifest stronger in the zonal or the meridional wind component, or whether these differences are positive or negative, with magnitudes of up to ± 2 $m.s^{-1}$, which in some locations represents a substantial part of the mean wind speed.

From the empirical point of view, with the methodology described in section 2.2 of this chapter, the biases behind those differences are computed and handled such that some of the missing information can be added to the new forcing product (ERA*), in the form of a SC. The data sets used to accomplish that, including the verification stages are previously described at processing detail in section 2.1. As just mentioned, the rationale behind the ERA* algorithm is introduced in section 2.2, alongside the advantages of exploiting combined scatterometer sampling in the creation of the SC, and the steps for product generation following the processing chain in Fig. 2.4. This general flow chart summarizes the necessary steps to generate the ERA* L4 product and the ERA* wind stress product using the ERA* processor. In addition, and to understand the sampling and noise effects of the ERA* procedure, simulation experiments are performed. Identical processing steps are adopted in real and simulated data experiments, with minor adaptations to the latter, and in line with the schematic diagram presented in Fig. 2.5. Those adaptations are described in section 2.3.

In what concerns verification methods (section 2.4), product validation starts with an empirical observation of the new U10S wind component forecast maps to look for additional true small scale wind variability w.r.t the reanalysis. In addition to this qualitative assessment of both reanalyses forecasts, i.e., from ERAi and ERA5, against the generated ERA* configurations, other empirical validation approaches, often applied in wind scatterometry, are used to quantify the ability of the SC to correct for the model biases illustrated in Fig. 1.4, and the skill of the new product. Those include a verification of the *ERA** U10S against independent, collocated scatterometer and *in situ* buoy U10S (2.4.1) and a spectral analysis of the different data sets (2.4.2).

[1]**Wind vector component (u, v) difference maps of collocated ASCAT-A and ERAi using the approaches summarized in this chapter were presented in the paper: *Trindade, A., Portabella, M., Stoffelen, A., Wenming, L., and Verhoef, A., 2020. ERAstar: A High-Resolution Ocean Wind Forcing Product***

2.1 Data sets

The ERA* product versions described in this manuscript use multiple remotely sensed surface wind observations from different scatterometers, alongside forecast data from a couple of NWP re-analyses and operational wind outputs. Wind observations from ocean moorings and scatterometers with either non-global (RapidScat) or non-continuous (HSCAT-A/B) coverage are used for verification purposes only.

High spatial resolution ocean vector U10S products derived from scatterometers are used to build different configurations of the ERA* product, or as independent validation sources, over different time periods. Table 2.1 summarises the scatterometers used in the development and/or validation of the different ERA* product versions evaluated/used in each section of the manuscript. Note also that different data periods have been used in the manuscript, as properly specified in each section.

Table 2.1: List of the scatterometer (SCAT U10S) products and ECMWF reanalysis (NWP U10s) used to generate and/or validate the ERA configurations in each section of the manuscript (marked in grey).*

SCAT U10S	section 4.1	section 4.2	section 4.3	section 5.1	section 5.2
ASCAT-A (Metop-a)					
ASCAT-B (Metop-b)					
ASCAT-C (Metop-c)					
OSCAT-1 (OceanSat-2)					
OSCAT-2 (ScatSat-1)					
HSCAT (HY-2A)					
HSCAT (HY-2B)					
NWP U10S	section 4.1	section 4.2	section 4.3	section 5.1	section 5.2
ERAi					
ERA5					

All the scatterometers listed in Table 2.1 fly in sun-synchronous orbits, i.e., with a specific local Equator passing time (note that the local Equator passing time of the ascending node is referred to as LTAN). In particular, the local Equator passing times of the ASCATs is 21:30 UTC and 9:30 UTC, for, respectively, the ascending and descending nodes; those of OSCAT are 12:00 UTC and 0:00 UTC; those of OSCAT-2 are 20:45 UTC and 8:45 UTC; while those of HSCAT-A/B are 18:00 UTC and 6:00 UTC (see Table 1.1). Note these LTAN are w.r.t. the years considered for product development, during which neither of the satellites significantly drifted from its orbit. Besides the LTAN, subsection 1.4.2 summarizes some of the most relevant characteristics of these systems. Amongst them, the instrument operating frequency, geometry, and footprint size, which affect spatial sampling, and therefore the daily coverage provided per instrument, a key aspect in product development.

In brief, the ASCATs provide accurate wind retrievals in nearly all weather conditions, i.e., hardly affected by rain because of their operating frequency (C-band), although for a relatively limited total swath width (1100 km) and a long repeat cycle (29 days or a quasi-repeat cycle of 5 days). Whilst the OSCAT and HSCAT instruments provide less (more quality controlled) and less accurate winds over rainy areas, they have a wider swath (1400-1700 km) and shorter revisit cycles that result in more homogeneous coverage over sets of several consecutive days. The latter is particularly true for OSCAT with a 1400 km swath and a 2-day repeat cycle. The

HSCAT data (1700 km with a 14-day) is only used for verification.

Another fundamental and relevant difference between ASCAT and pencil-beam scatterometer winds is related to the measurement geometry. The ASCAT measurement geometry with three fixed fan beam beams is optimized for wind scatterometry, while rotating pencil-beam scatterometers trade wind retrieval accuracy for swath width. This results in more noise and in particular wind vector ambiguity. Reduction of wind vector ambiguity in the wind retrieval is achieved by the so-called Multiple Solution Scheme, essentially compromising spatial resolution in order to achieve a unique wind vector solution at every WVC in the swath. Although, the empirical spatial properties of ASCAT have been successfully exploited to improve the Ku-band winds (Xu and Stoffelen, 2020b; Vogelzang and Stoffelen, 2018), the difference in spatial resolution remains relevant. Nevertheless, ASCAT and OSCAT winds are more similar than either of them with ECMWF winds (Vogelzang and Stoffelen, 2021), where after intercalibration (Wang et al., 2019) the ASCAT and OSCAT SC show great similarity.

Level-1B (L1B) data, i.e., swath-gridded geolocated radar backscatter information, was provided by the different space agencies. In particular, the Chinese National Ocean Satellite Application Center provided HSCAT-A/B L1B data, the Indian Space Research Organization (ISRO) provided the OSCAT-1 and OSCAT-2 L1B data, and EUMETSAT provided ASCAT L1B data. All L1B datasets were processed with the latest versions of EUMETSAT NWP Satellite Application Facility (NWP SAF) scatterometer data processors, i.e., the ASCAT Wind Data Processor (AWDP) for ASCATs and the pencil-beam wind processor (PenWP) (Verhoef et al., 2018) for OSCATs and HSCATs, to obtain L2 wind data. Further details on the reprocessing of the data, e.g., GMF version, background and QC flags, are provided within the corresponding section.

All the NWP data sets were originally downloaded from ECMARS in their native grids in GRIB format. Specifically, both the ERAi and the ERA5 surface winds were retrieved on a reduced Gaussian grid (N128), respectively with a spatial grid resolution of about 80 km on a 3-hourly basis and in a 30 km spatial resolution grid on an hourly basis, and converted to U10S to become more compatible with scatterometer wind retrievals (see eq. 1.1 in subsection 1.5.1). Whilst for the Monte Carlo simulations, a few months of operational ECMWF hourly surface winds from 2013 were downloaded to be used as wind truth (with no additional conversion). Though, it is important to clarify that these winds were used for their one hour temporal frequency, which at the time of the simulation experiments, was only available for the ECMWF operational forecasts.

in situ wind data from buoy moorings on 10 min intervals, hereafter referred to as continuous buoy data, was also downloaded from the ECMARS archive, alongside a list of buoy measurements blacklisted by ECMWF that are excluded from the data set. Note that buoy wind vectors are distributed by the Global Telecommunication System (GTS), which have been retrieved, quality controlled, and segregated into 1 $m.s^{-1}$ speed bins and 10-deg direction bins for storage purposes in the ECMWF MARS archive.

Although most of the available buoys have been maintained for decades, a slight decrease in the number of working buoys has been reported from 2014 onward. Fig. 2.1 displays the locations of the used buoys in 2013 and 2019, respectively in Fig. 2.1a and Fig. 2.1b. Note that

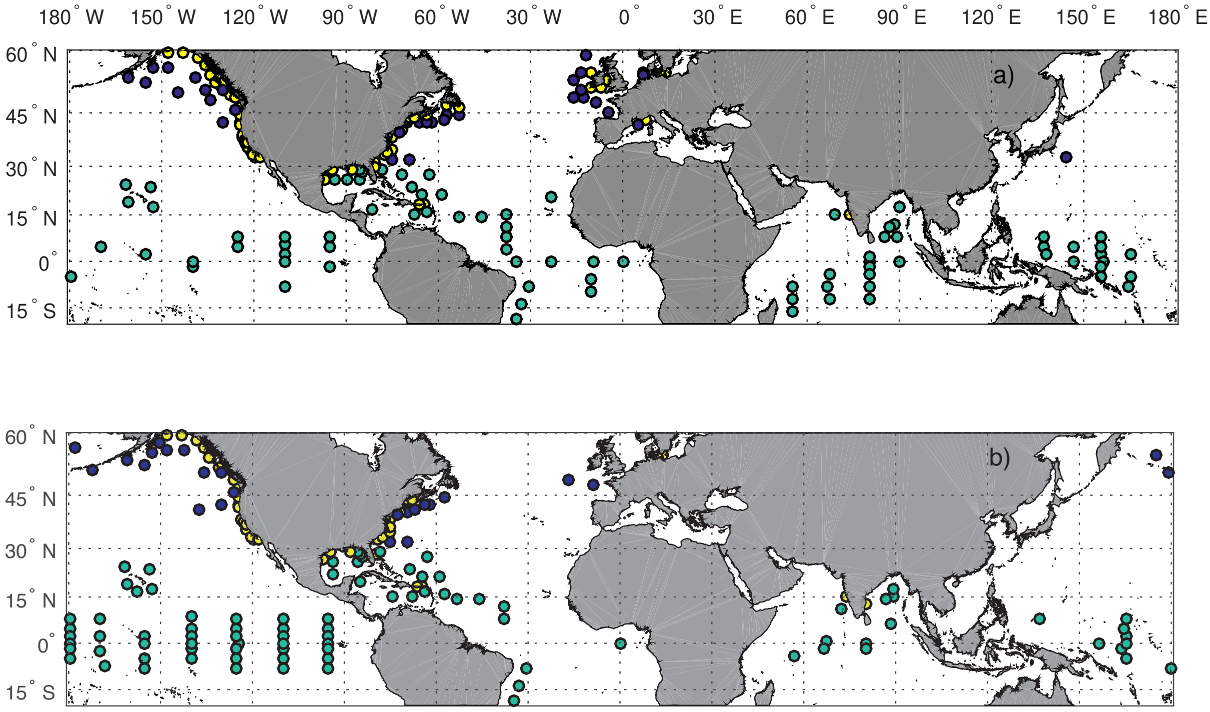

Figure 2.1: Global distribution of the moorings used to acquire wind measurements in 2013 (a) and 2019 (b). Same color scale is used to classify buoys according to location as in Fig. 1.1.

buoy observations are not used in the generation of the ERA^* product, but used in product verification and to estimate the error values used to parameterize the Monte Carlo simulations in subsection 2.3.1 using the triple collocation technique adopted in Lin et al. (2015b).

2.2 ERA^* approach

As mentioned in section 1.5.5, the ERA* approach attempts to correct for persistent local NWP model output wind vector biases using scatterometer data. These output errors are associated with physical processes that are absent or misrepresented by the model, e.g., strong current effects like the WBCS (highly stationary), wind effects associated with the oceanic mesoscale (SST), coastal effects (land see breezes, katabatic winds), Planetary Boundary Layer parameterization errors, and large-scale circulation effects, such as those at the ITCZ. Therefore, these are readily evident from the collocated U10S differences between scatterometer and model, respectively ASCAT-A and ERAi, in Figs. 1.4a and 1.4b (see dark blue and red regions). The zonal and meridional U10S differences in these figures show very pronounced biases over the WBCS, i.e., the Agulhas, the Gulf Stream or the Kuroshio current regions, the Antarctic Circumpolar Current (ACC), and in adjacent regions where the eddies generated by these currents detach. Likewise, in the tropics (see, e.g., the Inter Tropical Convergence Zone or ITCZ), U10S differences (particularly in the meridional component in Fig. 1.4b) are notable where the model U10S field is unable to capture both the detailed and large-scale wind circulation. Additionally, local wind effects like see breeze, katabatic flows, corner winds or wind funneling effects (gap winds) are also visible from these figures, with the latter most noticeable in the the meridional component in Fig. 1.4b, e.g., see the gap wind effect in the Gulf of Tehuantepec.

The proposed methodology takes information from these instruments to generate a scatterometer-based correction (SC) for each wind vector component ($u10s, v10s$) which is then applied to the reanalysis to produce the zonal and meridional ERA* U10S/wind stress fields. The SC consists of geo-located scatterometer-NWP averaged differences over a specific temporal window (TW) for every model time step (t), that may include sampling from one to several scatterometers, and in which each wind vector component is corrected in the same manner. For the zonal component, the formulation used is displayed in Eq. 2.1:

$$SC(i,j,t_f) = 1/M \sum_{t=1}^{M} (u_{10s}^{SCAT_k}(i,j,t) - (u_{10s}^{NWP}(i,j,t)) \tag{2.1}$$

Here $u_{10s}^{SCAT_k}$ and u_{10s}^{NWP} respectively refer to scatterometer and model U10S collocations, with the number of sensors discriminated as k. These are collocated for a TW of N days, centered at forecast time (t_f), i.e., $t_f \pm N/2$ days, where M is the number of scatterometer/model collocations (samples) at grid point (i,j) within the defined time window around the reanalysis t_f. Note that the meridional wind component ($v10s$) is discretized in the same way.

With further detail, for every forecast time of a fixed TW configuration (N days), the scatterometer/NWP collocated fields (collocation procedure explained later in this section) within t_f ± N/2 days are collected and the corresponding U10S differences averaged at each grid point cf. Eq. 2.1. As such, for every t_f time step, respectively 3-hourly and hourly for the ERAi and the ERA5 reanalysis forecasts, a SC U10S field is generated for the predefined TW (N) and based on the selected combination of scatterometers (k).

To effectively reduce local NWP biases, a trade-off between optimal scatterometer sampling length and the ability to keep the small spatial and temporal ocean induced scales is required. The scatterometer instruments used in the SC are flown on-board sun-synchronous satellites, which, as mentioned in section 1.4.2, results in a non-uniform temporal sampling across the globe, and potentially in sampling characteristics that produce a large impact over the method's ability to reduce local NWP biases. On a daily basis, incomplete spatial coverage by these instruments over the tropical band (from 30°S to 30°N), as compared to other latitudes, presents a relevant limitation to the effectiveness of the method. Persistent errors may be captured by accumulation over time and using data from several scatterometers allows for a significant reduction in revisit time (Tang et al., 2014). As illustrated in Fig. 2.2, the global scatterometer coverage obtained for a single day can be improved by the accumulation of data from several scatterometers, e.g., compare the daily coverage from ASCAT-A in Fig. 2.2a w.r.t. that obtained by the scatterometer constellation of ASCAT-A/B/C and ScatSat-1 represented in Fig. 2.2d).

In particular, k goes from one (single scatterometer) to the maximum number of instruments used to build the SC, i.e., it refers to different combinations of scatterometer sampling. Throughout this thesis several combinations of scatterometer sampling are investigated, amongst them those described in Trindade et al. (2020) with $k = 1$ (ASCAT-A), $k = 2$ (ASCAT-A/B and ASCAT with OSCAT), and $k = 3$ (ASCAT-A/B and OSCAT) . In some cases, the opti-

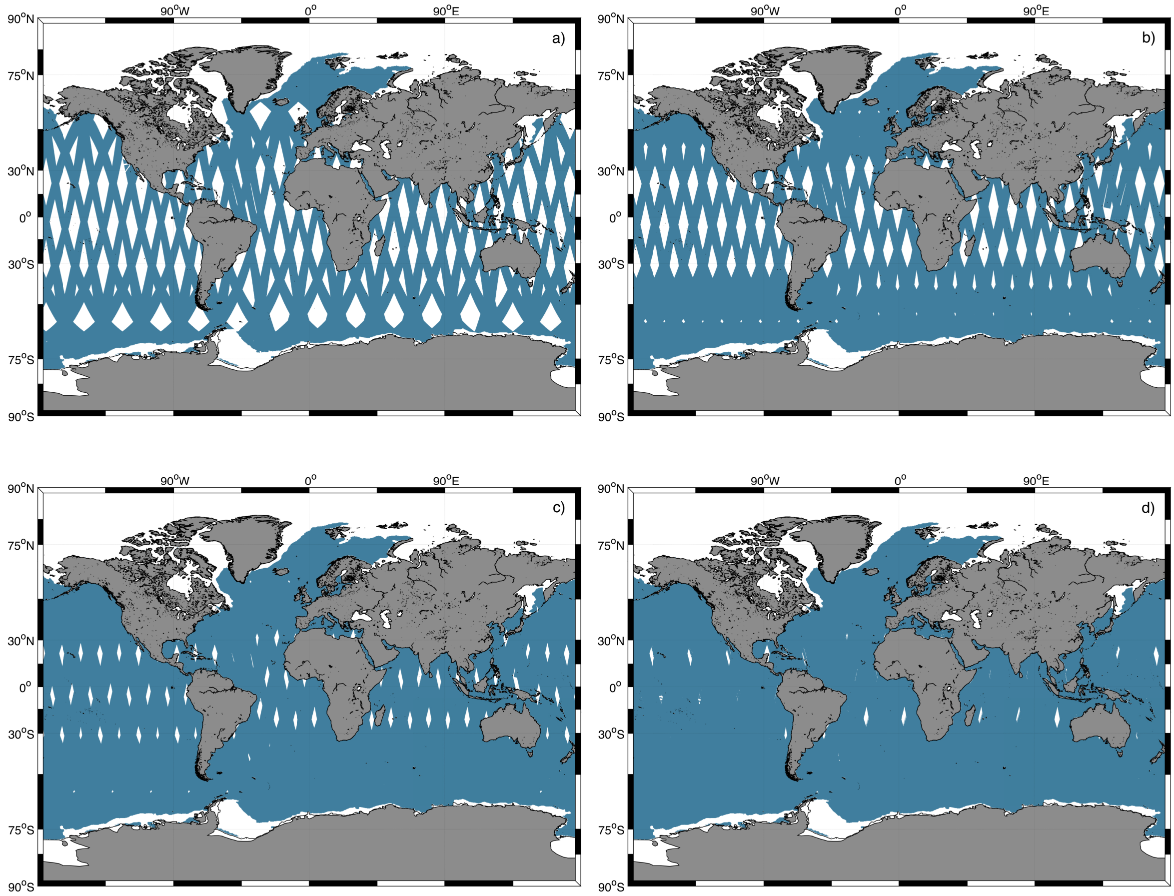

Figure 2.2: Global scatterometer coverage for a single day (15^{th} February 2019), with every point in blue representing a different time of the day. In (a) coverage from ASCAT-A ($k = 1$), in (b) from ASCAT-A/B ($k = 2$), in (c) from ASCAT-A/B/C ($k = 3$) and in (d) from ASCAT-A/B/C and OSCAT-2 ($k = 4$).

mal scatterometer sampling for the SC includes observations from scatterometers working at different frequencies, namely ASCAT and OSCAT sensors, respectively at 5.2 GHz (C-band) and 13.5 GHz (Ku-band). Although the fixed fan beam (ASCAT) and the rotating pencil-beam (OSCAT) systems have different sampling characteristics that result in higher accuracy and resolution winds for the former, wind retrievals from the Ku-band system provide good quality winds (Vogelzang and Stoffelen, 2021), which are largely consistent with ASCAT.

Besides scatterometer sampling, the performance of the corrected NWP field is determined by the persistence of the NWP local biases and the choice of the accumulation over time denoted by N. By trying different TW for the SC, i.e., using different accumulation lengths N, it is possible to check the temporal persistence of the local biases for several configurations. Initially, the efficacy of the method for shorter accumulations, i.e., $N <= 5$, was investigated in Trindade et al. (2020), but due to sampling limitations for subsequent testing periods, e.g., 2009, 2010, 2011, longer accumulations of $N = 10, 15, 30$ days were also investigated. That is, sampling from the available scatterometers was insufficient to reduce the error variance and outperform the original NWP U10S, requiring longer temporal accumulation for more optimal scatterometer sampling. Note that the performance of the NWP* U10S for different k's and N's is evaluated in detail in Chapter 4.

Furthermore, the choice of TW used in Eq. 2.1 takes into account that such biases are relatively persistent over time, but that persistence is also regionally dependent (recall Fig. 1.4), i.e., longer in the trades and higher latitudes (beyond 55°) as compared to the storm-track regions (middle-latitudes) or over the ITCZ. As such, the trade-off between sampling and local bias persistence is analysed in Chapter 3, also considering this regional dependence.

Finally, to generate the ERA* in Eq. 2.2, the SC ($SC(i, j, t_f)$ in Eq. 2.1) is added to the NWP U10S forecast ($u_{10s}^{NWP}(i, j, t_f)$), at time t_f as follows:

$$u_{10s}^{ERA^*}(i, j, t_f) = u_{10s}^{NWP}(i, j, t_f) + SC(i, j, t_f) \tag{2.2}$$

Note that throughout the thesis the ERA* will correspond to either corrected ERAi or corrected ERA5 U10S forecast fields on regularly spaced lat/lon grids, with latitudes (longitudes) in °N (°E), and available respectively at 3-hourly or hourly time steps. Note also that following the processing chain introduced next in the diagram of Fig. 2.4, the algorithm is applied such that the new ocean forcing product is generated on the SC grid , i.e., with the L3 grid resolution of the ASCAT coastal product (0.125 °), the exception being the case study in 5.1 with a coarser resolution of 0.25 °.

The SC was developed to optimise data coverage both in time and space, allowing the ERA* processor to be flexible and accommodate different TW or varying number of scatterometers, according to the intended application of the product. Still, due to limited scatterometer sampling some SC configurations will have gaps that by construction are filled with NWP winds only, i.e., ERA* winds will be the same as the original NWP winds. The alternative is resorting to longer temporal accumulations windows, at the cost of efficiency in error variance reduction and resulting U10S fields with less small scale variability (particularly, non-persistent or moving small-scale features are smoothed).

However, the methodology in use cannot correct for transient weather effects and additional filtering may be required to remove those effects from the SC (e.g., storm phase shifts in NWP, location errors in fronts, etc.). The latter appear as outliers when looking at the SC standard deviation distribution, as can be seen from the example in Fig. 2.3 that holds the distribution of SC values for a temporal window of 3 days and the combination of 4 sensors (i.e., N3 with $k = 4$), specifically from its tails, which exceed by far the expected local systematic effects, i.e., around $\pm$ 2 $m.s^{-1}$.

Consequently, later versions of the algorithm include a 3σ filter applied to the scatterometer-NWP differences, i.e., filtering SC values above 3σ to remove the aforementioned effects. These outliers are mostly found in moist convection regions (particularly when using Ku-band systems) and seasonally when doing sea ice screening. The 3σ filter is calculated separately for each wind vector components and for both ASCATs-NWP and OSCAT-NWP differences, using a test period in 2019 and an accumulation length of 72 hours (N3). Respectively, the fixed values $\sigma_C(u, v) = (1.67, 1.59)$ and $\sigma_{Ku}(u, v) = (1.27, 1.33)$ are taken from the test period to be used on the remaining periods, filtering about 1.4% and 1.1% of the wind observations. Moreover, the

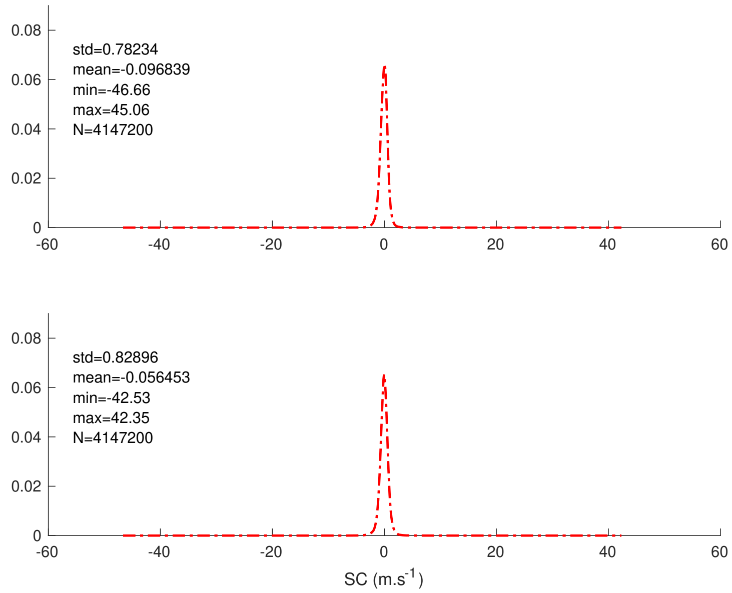

Figure 2.3: Normalized histogram of the zonal (top) and meridional (bottom) SC values obtained for a N3 and $K = 4$ (ABCO) configuration.

scatterometer observations undergo several quality control screenings, which are integrated in the winds software, before being used in the SC. The quality verification for the 3σ ERA* and the result of disregarding SCs with insufficient scatterometer samples, i.e., not correcting the NWP at these grid locations, is discussed in subsection 4.2.2, Chapter 4. The processing stages where filtering takes place are marked as $*$ in Fig. 2.4.

Finally, the ERA* algorithm includes the conversion of the higher resolution ERA* U10S ocean forcing product to wind stress (τ). Eq. 2.3 holds the formulation to convert from U10S to τ.

$$ERA^*_\tau(i,j,t_f) = C_{D10} < \rho_{air} >\mid U_{10s}(i,j,t_f) \mid U_{10s}(i,j,t_f) \tag{2.3}$$

Here, $< \rho_{air} >$ is the standard average air density taken as 1.225 kg/m3, and C_{D10} the drag coefficient determined from the parameters extracted from a linear fitting between the drag coefficient taken from the ECMWF ERAi wave model against the ERAi U10S (converted from the ECMWF ERAi atmospheric model winds) for a full year of data. The resulting linear fit is characterized by the following equation:

$$C_{D10}(U_{10s}) = aU_{10s} + b;\ with\ a = 7.94E10 - 5\ and\ b = 6.12E - 4; \tag{2.4}$$

Note, that the a and b are taken as the default values for the drag fitting equation and follows De Kloe et al. (2017b) with data from 2012. This generalization is commonly used to produce the wind stress data available from the EumetSat OSI-SAF L3 scatterometer products, and very close to the relation used by the COARE3.5 parameterization (Edson et al., 2013). Still, to generate the ERA^*_τ forcing for the data set in the case study in section 5.1 (oceanographic

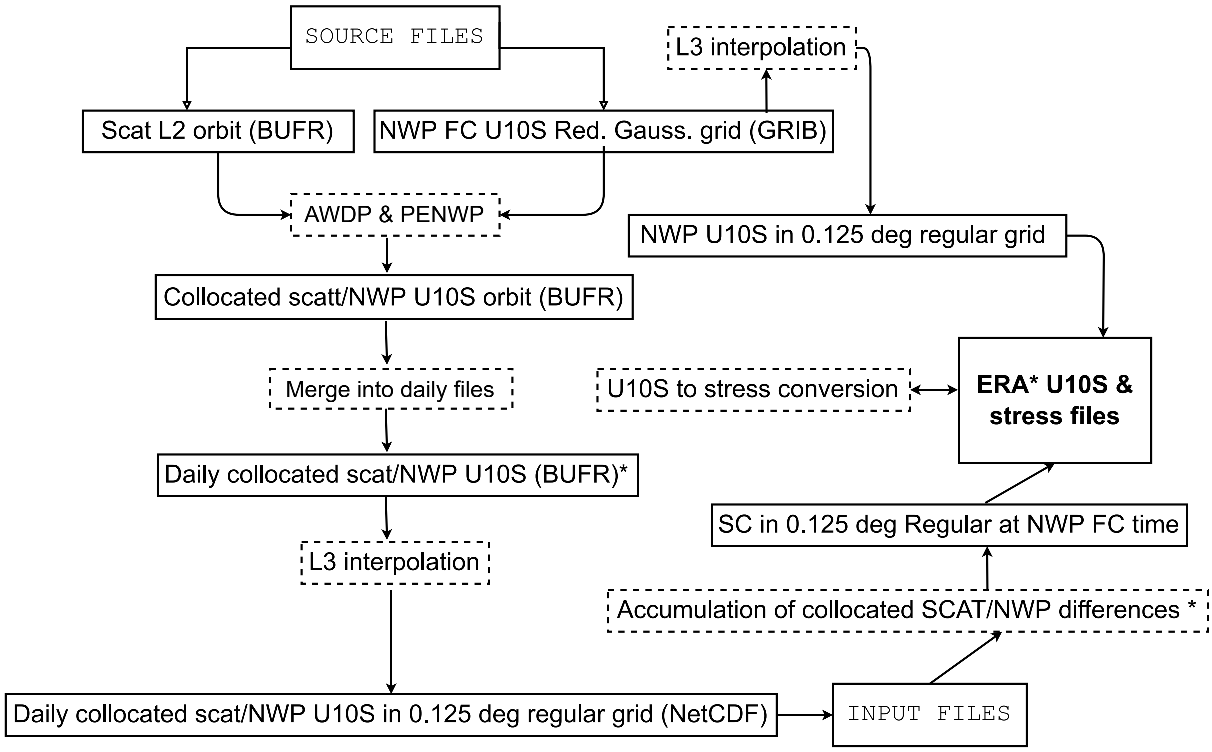

Figure 2.4: General flow chart of the adopted methodology to generate the L4 ERA and ERA* wind stress products.*

application), these parameters were recalculated for the year 2017. By taking constant values for the air density and drag coefficient parameters any dependence of the scatterometer stress on a particular model is avoided.

The implementation of the ERA* methodology is summarized with a diagram in Fig. 2.4. The entire processing chain can be divided in two main phases, with an additional/optional step that generates wind stress files using the above mentioned parameters. Phase one goes from the SOURCE FILES to the generation of the INPUT FILES. It comprehends the conversion of NWP U10N available from the ECMARS archive into NWP U10S using Eq. 1.1, therefore making the two wind sources more compatible before generating scatterometer/NWP collocations by means of the NWP SAF PenWP and AWDP (Verhoef et al., 2020) wind processors. At this stage the QC step is taken as marked by $*$, i.e., poor-quality retrievals are first flagged. Both the collocated NWP U10S and the scatterometer (ASCATs and OSCATs) L2 wind data are then spatially interpolated from swath to a regular 12.5 $\times$ 12.5 km grid Level 3 (L3) using the Royal Netherlands Meteorological Institute (KNMI) genscat tool packages (top left box to bottom right box in Fig. 2.4). Once the INPUT FILES are generated, the second phase (right side of the diagram) uses these files to produce the SC, with or without the 3σ filtering, and generate the ERA* U10S and the stress files (ERA$^*_\tau$), see larger box in Fig. 2.4.

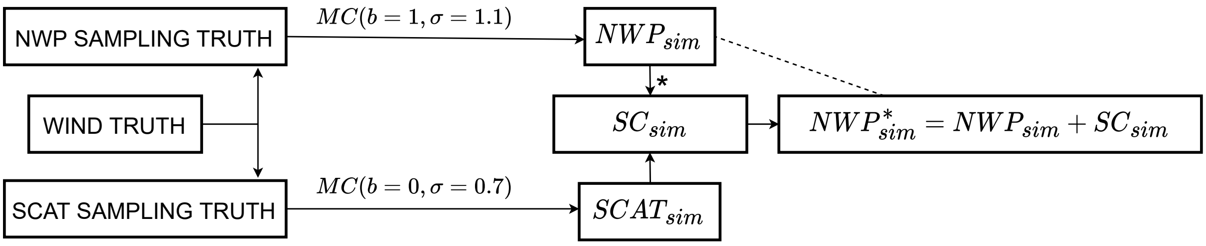

*Figure 2.5: Schematic diagram of the methodology used to generate the simulated NWP^*_{sim} (see Eq. 2.6) by means of MC simulations. ECMWF hourly forecast fields are used as WIND TRUTH, SC_{sim} corresponds to the simulated scatterometer-based correction obtained with Eq. 2.5. The arrow with * represents the NWP_{sim} collocated to the scatterometer sampling.*

2.3 Simulation framework

Under a theoretical scenario, Monte Carlo simulations are used to mimic the algorithm introduced in section 2.2, in which a scatterometer correction based on temporally-averaged differences between the scatterometer and the NWP winds corrects local NWP wind biases. The specifics of the simulation framework are detailed within this section, and follow the schematic diagram presented in Fig. 2.5. This diagram flows in two parallel branches that converge in the creation of the simulated NWP* (hereafter NWP$^*_{sim}$). Note that to simulate realistic wind distributions, the Monte Carlo scheme is applied to several sets of five consecutive days of ECMWF NWP hourly surface winds from March 2013. These hourly NWP winds are assumed as the reference, hereafter wind truth, and used to produce simulated data sets.

Hence, according to the diagram in Fig. 2.5, the NWP^*_{sim} is generated when the wind truth is perturbed with different random and systematic error values, thus creating the scatterometer and the NWP synthetic winds. Note that the scatterometer sampling truth is extracted from the ASCAT-A/B and the OSCAT-1 actual sampling. Further description on the error parameterization used to generate the synthetic winds can be found in subsection 2.3.1.

From left to right, in the upper branch of the diagram, after being spatially interpolated to a regular 12.5 x 12.5 km grid, the three-hourly truth (e.g., to simulate ERAi corrected winds) on a global sampling, at forecast time t_f , is perturbed to generate synthetic model winds (NWP_{sim}). Whereas, in the lower branch, the hourly truth is collocated to the scatterometer sampling and then perturbed to generate synthetic scatterometer ($SCAT_{sim}$) wind fields. The latter, together with the NWP_{sim} from the upper branch collocated to scatterometer sampling, are used to generate the simulated scatterometer-based correction (SC_{sim}), by means of the formulation in Eq. 2.5 (adapted from 2.1) , i.e., to produce the temporal averages of the collocated wind vector difference between the simulated scatterometer and model distributions, for M scatterometer/model collocations at grid point (i, j) and at time sample t. Finally, similar to 2.3, from the SC_{sim} and the NWP_{sim} the NWP^*_{sim} is generated using Eq. 2.6.

$$SC_{sim}(i, j, t_f) = 1/M \sum_{t=1}^{M} SCAT_{sim}(i, j, t) - NWP_{sim}(i, j, t) \tag{2.5}$$

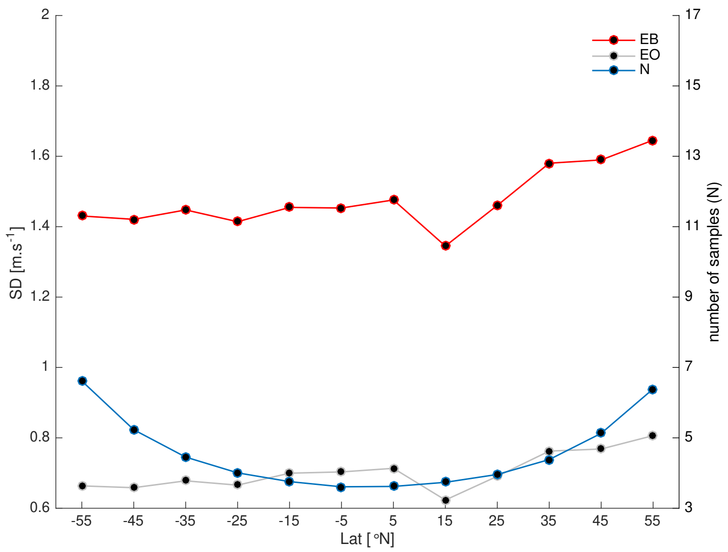

Figure 2.6: Estimated mean wind component error SDs, i.e., $SD = \sqrt{(SD_u^2 + SD_v^2)/2}$ for background ECMWF (EB) in red and ASCAT 12.5 km (EO) in grey, at scatterometer scales, for January 2013 per 10° bins. Average number of scatterometer samples per location per 10° bins (N) in blue.

$$NWP^*_{sim}(i,j,t_f) = NWP_{sim}(i,j,t_f) + SC_{sim}(i,j,t_f) \tag{2.6}$$

2.3.1 Error parameterization

The wind truth is perturbed by Gaussian random noise distributions to generate synthetic wind fields for NWP and scatterometer (i.e., ASCATs and OSCAT) winds, and the choice of error parameters to simulate these data sets is taken according to estimated error values from literature (Vogelzang et al., 2011a) as well as from triple collocation results.

To this end, for each wind component, the total error standard deviation (ϵ) (obtained from triple collocation of buoy, scatterometer and ECMWF winds at global scale) was adopted from Vogelzang et al. (2011a), respectively these values are of 1.5 $m.s^{-1}$ and 0.7 $m.s^{-1}$ for the NWP and the ASCAT coastal products (at scatterometer scales).

To verify whether such errors are highly dependent on latitude, the triple collocation methodology used in Lin et al. (2015b) is taken to assess the buoy, ASCAT, and ECMWF errors. As seen in Fig. 2.6, although different wind variability conditions as well as NWP model limitations (e.g., lack of moist convection in the tropics and misplacement of storm tracks in the extra-tropics) are expected as a function of latitude, both ASCAT and ECMWF winds show nearly constant wind errors, except for latitudes above 40° N, where there is a significant degradation of the wind quality.

Note that, although OSCAT errors are larger than those of ASCAT and furthermore regionally affected by rain (Portabella and Stoffelen, 2001b; Stiles and Dunbar, 2010; Lin and Portabella, 2017; Xu and Stoffelen, 2020b) and SST biases (Wang et al., 2017), the same error value is used for both the C-band and Ku-band sensors. An alternative would be to attribute an average error value for the Ku-band system.

$$\epsilon = \sqrt{\sigma^2 + b^2} \tag{2.7}$$

Hence, to estimate the contribution of the NWP local biases to the total NWP error, the latter is assumed to be the square root of the sum of random and systematic error variances globally (see Eq. 2.7). By assuming a fixed local bias (b_{NWP}) of 1 $m.s^{-1}$ and a total NWP wind component error (ϵ_{NWP}) of 1.5 $m.s^{-1}$ (see Fig. 2.6), the estimated NWP random error (σ_{NWP}) for each (zonal and meridional) wind component is 1.1 $m.s^{-1}$, as deduced from Eq. 2.7.

Considering the aforementioned error values, the wind truth is therefore perturbed component wise by the following Gaussian distributions, $\mathrm{N}_{NWP}(1, 1.1)$ for the NWP (NWP_{sim}) and, assuming that the scatterometers are unbiased, $\mathrm{N}_{SCAT}(0, 0.7)$ for the scatterometers (SCAT_{sim}). Note that both transient and persistent model errors are spatially correlated as, e.g., in resp. Vogelzang and Stoffelen (2018) and Belmonte Rivas and Stoffelen (2019), while for the sake of simplicity we here assume globally constant biases.

2.4 Validation approach

Once the ERA* U10S/wind stress forcing fields are generated a comprehensive characterization of theses fields is required to verify the quality of the L4 forcing product. Thus, in line with the most common techniques used in scatterometry for wind verification, several validation steps are applied to the ERA* wind vector components. Those are described in the next subsections and explained within the context of the ERA* product validation.

To start with, an empirical assessment as to the presence of added variance in the new forcing fields will be performed, via visual check of the global and regional U10S maps, i.e., by comparing the ERA* with the ERA reanalysis (sometimes ERAi, others ERA5). Furthermore, by comparing the latter with the SC, it is possible to qualitatively establish a link between the additional variance and the location of the systematic biases.

Then, the U10S quality will be assessed against reference observations, namely from independent scatterometers (i.e., those not used in the generation of the ERA* product) and buoys. As mentioned in section 1.4, *insitu* and remotely sensed wind observations yield different representations of the same wind, i.e., while buoy verification is local, HSCAT-A and -B verification is global. Indeed, the scatterometer measurements are spatially a more coherent wind source for the validation of the ERA*, as they resolve the spatial oceanic variability aimed for by the new L4 products, and are therefore the main source of validation used in the thesis. In addition, buoy U10S resolve all temporal variance which is used for the quality assessments of the products. As such, statistical analysis by comparison against buoy U10S is also included in the validation approach of the product. Section 2.4.1 includes the discretization of the metrics used in the statistical analysis as well as the spatio/temporal interpolations involved.

The next step is meant to check whether the signal present in the U10S maps and metrics indeed correspond to true variance. To this end, the derived ERA* U10S fields were assessed in terms of their geophysical consistency and effective resolution, using the spectral analysis procedure in section 2.4.2. An additional way to validate the new product aside from those described in this section, e.g., spectral and statistical analysis using independent scatterometer and buoy data, is to evaluate ocean model responses to ERA* forcing by assessing model outputs. Hence, the added value of the ERA* in what concerns its implementation as atmospheric forcing to ocean model simulations is evaluated using a couple of case studies. Further description of the prescribed wind forcing for these applications and the subsequent model output verification are detailed according to each case study in Chapter 5.

2.4.1 Statistical analyses

Throughout the thesis, independent scatterometer, either from HSCAT-A, HSCAT-B or Rapidscat, have been used as wind reference in the statistical analysis. For such purpose, both L4 U10S products, e.g., the NWP (ERAi or ERA5) and the ERA* forecasts, are collocated to the independent scatterometer U10S on the swath grid (L2). The Vector Root Mean Square (VRMS) can then be computed for both L4 *model* products (NWP and ERA*) w.r.t. the *reference* (scatterometers) using Eq. 2.8, where N corresponds to the number of NWP/scatterometer (*model*/*reference*) collocations within the region of interest.

$$VRMS = \sqrt{1/N \sum_{i=1}^{N} (u_{model_i} - u_{ref_i})^2 + (v_{model_i} - v_{ref_i})^2} \tag{2.8}$$

Note that Eq. 2.9 links Eq. 2.7 to Eq. 2.8, where the u and v notations are respectively used in reference to the zonal and meridional U10S components.

$$VRMS = \sqrt{\epsilon_u^2 + \epsilon_v^2} \tag{2.9}$$

Then, Eq. 2.10 can be used to quantify the percentage of error variance (VRMS^2) reduction of ERA* (*model**) w.r.t. NWP (*model*).

$$ERROR_{reduction}(\%) = [1 - \frac{{VRMS_{model^*}}^2}{{VRMS_{model}}^2}] * 100 \tag{2.10}$$

In fact, VRMS simply refers to the variance of a particular wind vector source, while the VRMS formulation shown in Eq. 2.8 refers to the VRMS difference (VRMSD) between two noisy sources, i.e., between *model* (NWP or ERA*) and a *reference* (scatterometer). Moreover, Eq. 2.8 can also be used to compute the VRMS error (VRMSE), which is defined as the error of a (noisy) data source, i.e., *model* (simulated NWP or NWP$_{sim}$) or model* (NWP$^*_{sim}$), w.r.t. the *reference* (simulated) truth. Likewise, the VRMSE variance reduction can be calculated with Eq. 2.10

In summary, VRMSE is the error with respect to the truth, and is mostly used in the simulation experiments of Chapter 3, while VRMSD is the difference between the vector components of two noisy sources, and is mostly used in the real data analysis of Chapter 4.

Table 2.2: Domain coordinates and regional characteristics of the geographical areas used for product verification.

Region	**Domain (°)**	**Characteristics**
Global (G)	[-55 55] N	Open ocean
Tropics (T)	[-30 30] N	Trades/ITCZ (steady winds vs. moist convection induced wind variability)
Middle-latitudes (X)	[-55 -30] [30 55] N	Storm track region (fast evolving weather)
High-latitudes (HL)	beyond 55	Abundant sampling vs. sea-ice seasonality/transient weather
Mediterranean Sea (MS)	green polygon in Fig. 2.7 *	Semi closed Sea (high wind variability/coastal)
Adriatic Sea (AD)	yellow polygon in Fig. 2.7 *	highly coastal (Sirocco winds/storm surges)

As baseline, the statistical analysis is initially performed globally, and then extended to other regions to assess the performance of the product over different weather regimes and scatterometer sampling. The details for each region are listed in Table 2.2. This table contains the domains over which metrics are calculated, and their most important characteristics in what concerns wind variability and sampling. Furthermore, Fig. 2.7 shows the polygon masks applied to select the data used for verification in the Mediterranean (MS) and Adriatic basins (AS). Also, the * denotes that, in these two cases, map limits are in reference to the full U10S domain of the forcing fields delivered for the storm surge model simulations (addressed in Chapter 5).

Although statistical analysis was initially performed on the L3 regular grid, both L4 U10S products (NWP reanalysis and ERA*) are first spatially (bilinear interpolation) and temporally (linear interpolation) collocated to the L2 grid with the NWP SAF PenWP wind software. From here, an additional spatial interpolation using the nearest neighbour technique is required to go from the L2 swath grid to the L3 regular grid, using the same genscat tool package as in the generation of the input files necessary to produce the ERA* (Driesenaar et al., 2022). Such is the case for the U10S verification described in Trindade et al. (2020).

Alternatively, the use of buoy U10S as reference to assess the VRMSD (see Eq. 2.8) or the error variance reduction (see Eq. 2.10) of the ERA* product, alike the verification against scatterometers, requires the collocation of the L4 U10S to the reference wind source, which now corresponds to single point measurements from the buoy moorings displayed in the global map of Fig. 2.1b. For this, the nearest L3 grid point in space and time to the buoy observation is taken. Specifically, the buoy arrays displayed in Fig 2.1b, and used in the verification correspond to: the NDBC coastal data set of the US, the ODAS buoys in the north-east Atlantic and British Isles inshore waters, NOAA TAO arrays in the tropical Pacific, JAMSTEC TRITON buoys in the western Pacific, the PIRATA array in the tropical Atlantic, and the RAMA tropical array in the Indian Ocean.

The ERA* is then evaluated as to the variance differences, i.e., the VRMSD between the L4 products and the wind reference (U10S buoys). Note though, buoys are not ideal for spatial analysis because of their sparsity, and indeed scatterometers are more adequate for this analysis.

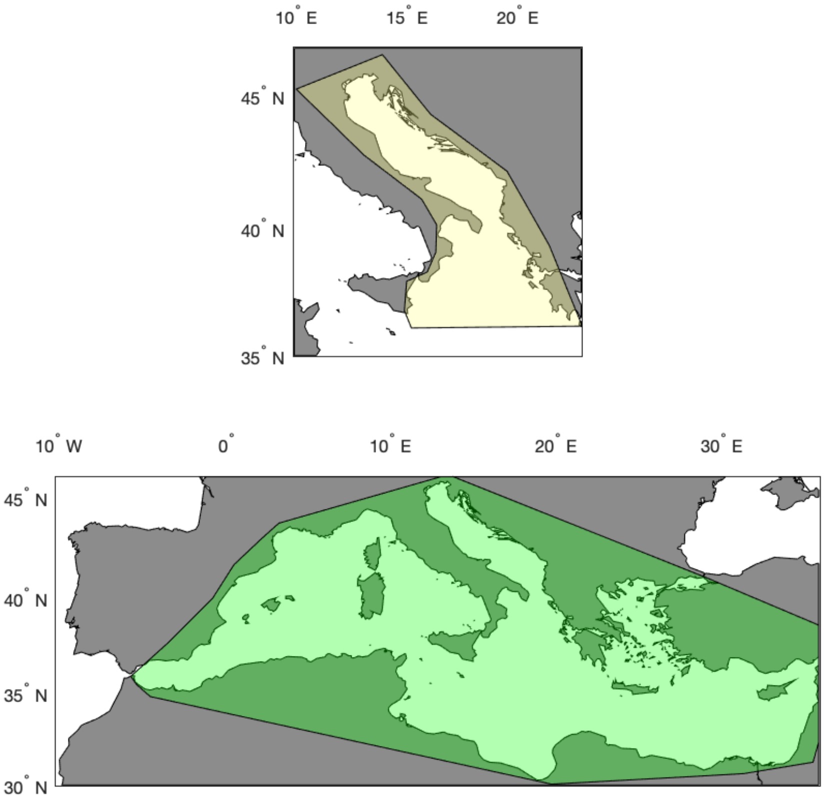

Figure 2.7: Selected areas for verification in the Mediterranean (green mask) and the Adriatic (yellow mask) Seas, delimited by polygon coordinates. Note the latter also includes a part of the Ionian Sea.

2.4.2 Spectra

The use of spectral analysis to evaluate the effective resolution of wind data sets has for long been a common practice within the winds community. In line with that, the spatial power density spectra of the generated ERA* U10S components are computed to assess the geophysical consistency of theses fields with collocated scatterometer observations, which are used as an independent source of validation.

In accordance with Vogelzang et al. (2011b), the U10S spectra are obtained from valid samples of the U10S components collected over a month in the scatterometer along-track direction for each across-track wind vector cell (WVC). To comply with the assumption of periodicity imposed when using Fast Fourier Transform (FFT), a linear transformation detrending method is applied to the samples. The final power density spectrum is the result of the individual spectra averaged over all WVC numbers across the swath and over the mentioned time period.

Overall, depending on the version of the ERA* product and the year for which the product is generated, the power density spectra are obtained from the individual spectra of the HSCAT-A/B and ASCAT-A, and averaged in the region of interest (globally, in the tropics or the middle latitudes). A substantially larger number of individual spectra is used for ASCAT-A with respect to the HSCATs, this is linked to the much lower QC rejection rate of C-band systems (0.5%) with respect to that of Ku-band systems (5%) (Lin et al., 2015a; Lin and Portabella, 2017). As FFTs need long series of input areas with QC, where gaps occur in the data series, these will not be sampled by the spectra. This implies that ASCAT spectra ,with low QC rejection rates, are more global in nature than HSCAT spectra, the latter tend to "fair weather" samples, in which the QC is rather inactive. Instead of using spectra, Vogelzang et al. (2015b) therefore reverted to spatial covariances, which do not suffer much from sampling gaps. Here we note this effect and still use spectra, where specifics as to the number of individual spectra used in the analysis are mentioned in the corresponding results section of this manuscript, as well as in Trindade et al. (2020) analysis, and in the ESA WOC project report (Portabella et al., 2022). Note furthermore that the SC field contains both ascending and descending passes and hence many swath edges implied in ERA* cross the HSCAT samples, potentially causing a white noise (flat) spectrum tail contribution when insufficiently sampled.

Chapter 3

Monte Carlo

[1]

The findings reported in this Chapter concern the analysis of the L4 algorithm performance in a theoretical experiment set-up, using simulated realistic wind distributions generated with the Monte Carlo scheme described in subsection 2.3. In this framework, to first verify the viability of the proposed methodology under theoretical conditions, an attempt is made to assess the different performances of the methodology with the heterogeneous scatterometer sampling over the globe (data coverage) and the natural weather variability (transient local weather dynamics) using statistical analysis. For the former, the characterization of the scatterometer sampling for different configurations of the simulated NWP* (NWP$^*_{sim}$), i.e., varying the number of combined scatterometer sampling over different temporal windows of accumulation in the simulated SC, is carried out by analysing the performance obtained from the simulated winds, and presented in section 3.1. As for the natural variability effects, considering how the ERA* approach makes use of a static bias correction to improve NWP winds, section 3.2 focuses on how the lack of persistence should affect the successful removal of the aforementioned systematic biases, as simulated weather phase-shifts are used to represent the prevailing weather conditions in the middle latitudes and the tropics. Note though that the high latitudes are excluded from this analysis.

It is assumed that due to the large wind variability conditions over the middle latitudes (e.g., high frequency of fast evolving phenomena, like extra-tropical cyclones, in the storm track regions), the persistence of the observed biases is likely reduced, thus limiting the effectiveness of the SC, despite the increased sampling at such latitudes. Whilst in the tropics, the quasi-stationary regime of the trades is dominant, hence a SC based on the persistence of local biases is expected to be more effective, except in regions of tropical moist convection, where despite the presence of NWP persistent biases, increased wind variability that is missed by the model may be the dominant effect (e.g., in the ITCZ).

Persistent biases and random errors are furthermore associated with errors in air-sea interaction, in particular associated with SST gradients. These are acknowledged, but not specifically accounted for in the simulations. Finally, a discussion on the combined effect of sampling and persistence along with concluding remarks can be found in section 3.3.

[1] **Part of the results presented in this chapter are included in the following proceedings:** ***Trindade, A., Portabella, M., Lin, W., and Stoffelen, A. (2017). On the development of a scatterometer-based correction for NWP wind forcing systematic errors: Impact of satellite sampling. In International Geoscience and Remote Sensing Symposium (IGARSS), volume 2017.***

3.1 Scatterometer sampling

In this section, the effectiveness of the simulated SC is evaluated through statistical analysis, using as metrics the bias, the standard deviation and the VRMS between the simulated wind fields and the wind truth, i.e., a few sets of 5 days of actual ECMWF wind forecasts which are taken to be the wind truth (see section 2.3). However, before presenting the metrics obtained with the simulated wind distributions, the error parameterization adopted for the Monte Carlo simulations (see subsection 2.3.1) is used to estimate the theoretical skill of this methodology as a function of the number of scatterometer samples used to generate the SC$_{sim}$, and speculate on the effectiveness of the simulated products.

In brief, assuming that the goal of SC is to remove the NWP local biases (in this case, a fixed local bias of 1 $m.s^{-1}$ in each wind component), with a single scatterometer sample ($M = 1$) per ocean grid point, the total wind component error of the synthetic SC (SC$_{sim}$) defined in Eq. 2.5, i.e., $\sigma_{SC_{sim_{M=1}}}$, can be computed as the square root of the sum of two error variances, i.e., the NWP random (unbiased) error ($\sigma^2_{NWP_{sim}}$) and the scatterometer error ($\sigma^2_{SCAT_{sim}}$) variances, as shown in Eq. 3.1.

$$\sigma_{SC_{sim_{M=1}}} = \sqrt{\sigma^2_{NWP_{sim}} + \sigma^2_{SCAT_{sim}}} \tag{3.1}$$

In a more general framework, $\sigma_{SC_{sim}}$ depends on the number of samples (M) as follows:

$$\sigma_{SC_sim} = \sigma_{SC_{sim_{M=1}}} / \sqrt{M} \tag{3.2}$$

That is, the accuracy of SC$_{sim}$ to correct for the local bias improves with the number of samples.

Recall that according to the error parameterization in subsection 2.3.1, respectively, $\sigma_{NWP_{sim}}$ and $\sigma_{SCAT_{sim}}$ correspond to 1.1 $m.s^{-1}$ and 0.7 $m.s^{-1}$. As such, using Eq. 3.1, $\sigma_{SC_{sim_{M=1}}}$ is estimated as 1.3 $m.s^{-1}$, i.e., $\sigma_{SC_{sim}}$ for $M = 1$ (see Eq. 3.2).

Then, the accumulated error in NWP$^*_{sim}$ can be estimated as the square root of the sum of σ^2_{NWP} and σ^2_{SCsim},

$$\sigma_{NWP^*_{sim}} = \sqrt{\sigma^2_{NWP_{sim}} + \sigma^2_{SC_{sim}}} \tag{3.3}$$

rising to a total error of 1.7 $m.s^{-1}$ for $M = 1$, clearly surpassing the total error (which includes random and systematic errors, as shown in Eq. 2.7) assumed for the NWP (1.5 $m.s^{-1}$, as estimated in subsection 2.3.1). The deduction suggests that with this parameterization, correcting the NWP$_{sim}$ with a single scatterometer sample proves detrimental. Such result is the consequence of using a noisy source to correct for the local biases.

A more realistic determination for multiple scatterometer configurations, as well as, in longer temporal windows of accumulation, would account for a SC$_{sim}$ generated with more than one sample. We quantify the impact of additional samples in Eq. 3.2). Such that by using $M = 2$,

Table 3.1: Simulated forecast corrections (NWP^{*}_{sim}), according to the simulated scatterometer sampling and temporal window used to correct the NWP_{sim} forecasts.

	Temporal Window		
Scatterometer Sampling	1-d (N1)	3-d (N3)	5-d (N5)
ASCAT-A	NWP*$_A$N1	NWP*$_A$N3	NWP*$_A$N5
ASCAT-A,ASCAT-B	NWP*$_{AB}$N1	NWP*$_{AB}$N3	NWP*$_{AB}$N5
ASCAT-A, OSCAT	NWP*$_{AO}$N1	NWP*$_{AO}$N3	NWP*$_{AO}$N5
ASCAT-A, ASCAT-B, OSCAT	NWP*$_{ABO}$N1	NWP*$_{ABO}$N3	NWP*$_{ABO}$N5

the new error σ_{SCsim} becomes 0.92 $m.s^{-1}$, and the total error in the new NWP$^{*}_{sim}$ becomes 1.43 $m.s^{-1}$. Thus, theoretically, with only two scatterometer samples in each ocean grid point, the resulting NWP$^{*}_{sim}$ outperforms the original NWP$_{sim}$. Also note that, for an infinite number of samples ($M \rightarrow \infty$), σ_{SCsim} would go to zero (see Eq. 3.2), and the error of the resulting NWP$^{*}_{sim}$ would equal the NWP$_{sim}$ random error, i.e., 1.1 $m.s^{-1}$.

Because in every configuration the NWP$^{*}_{sim}$ is intrinsically restricted by the number of samples used to compute the SC$_{sim}$, all configurations are expected to eventually converge if allowed by the number of scatterometers and the length of the temporal window of accumulation. This assumption is true for the oversimplified conditions of our theoretical set up, in which local biases are constant and do not change over time, i.e., assuming infinite persistence of the local biases. Note that the theoretical error characterization is performed component wise, i.e., the values derived above are shown for one wind component only, and the same conclusions are valid for the other, whilst the error analysis of the simulated configurations presented next, is performed using the vector RMS error, i.e., with the VRMSE, which accounts for the errors in both wind components. Note though that some systematic biases are associated to fast processes, e.g., moist convection, which are not well resolved by ECMWF, and associated with enhanced wind speeds (King et al., 2022).

Thus, considering the total vector error (Eq. 2.9), and that the error for each wind component is the same, one can compute the error variance reduction of the NWP^{*}_{sim} error with respect to that of the benchmark NWP_{sim} (i.e., a $VRMSE_{NWP}$ of $1.5\sqrt{2} = 2.1$ $m.s^{-1}$ using Eq. 2.9), with the maximum reduction corresponding to the removal of the systematic biases using infinite number of samples (i.e., a $VRMSE_{NWP^{*}}$ of $1.1\sqrt{2} = 1.56$ $m.s^{-1}$). In this case, the maximum vector error variance reduction that can be achieved under the current parameterization setting amounts to about 46.2%, as deduced from Eq. 2.10.

Non-infinite (scatterometer) sampling and/or non-infinite persistence of local biases, i.e., the real case, will make the computed SC less effective. Consequently, if one extrapolates the effects of poor sampling to real cases, e.g. due to relatively long periods (over a few days) of instrument failure or other issues that lead to missing data, the orbit cycle of each scatterometer is particularly relevant, especially if only of a few days length and resulting in non-uniform sampling patterns, probably further aggravated by interference with short TWs of accumulation in the SC. As a result, the new L4 will only take the NWP data in swath gaps (no SC), notably for the OSCATs (with a 2-day repeat cycle), whereas for scatterometers with longer revisit times, such as the ASCATs (29 days), insufficient data availability may generate areas that have

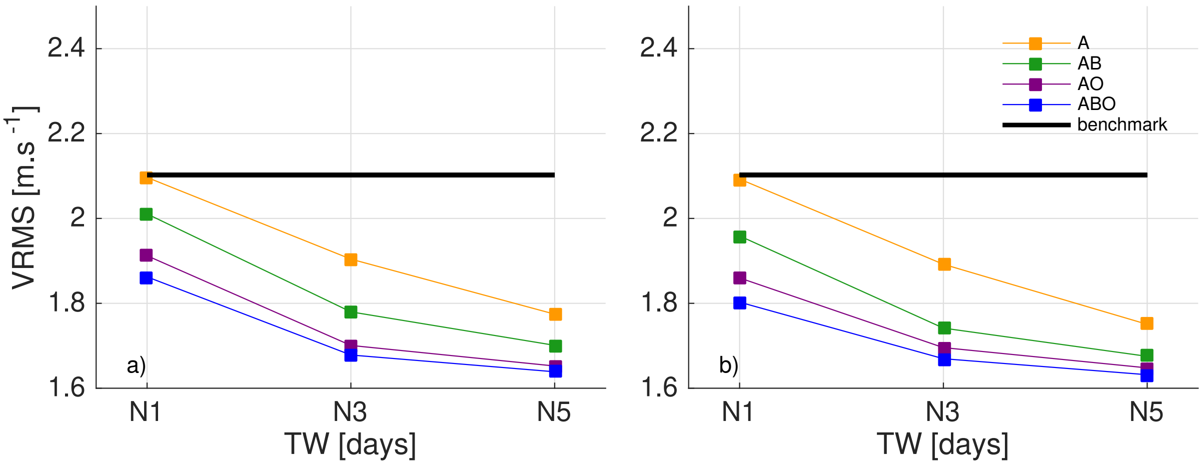

Figure 3.1: Estimated vector root mean square error (VRMSE in $m.s^{-1}$, see Eq. 2.9) for NWP_{sim} (i.e., the benchmark in solid black line) and the different NWP^{*}_{sim} configurations, the latter being a function of the SC temporal window (TW) size, in the tropics (a) and at the middle latitudes (b). The different colour lines show the VRMSE scores for the following NWP^{*}_{sim} configurations using: only ASCAT-A (orange line), ASCAT-A and B (green line), ASCAT-A and OSCAT (purple), and ASCAT-A, ASCAT-B and OSCAT (blue).

temporally mixed data with reduced sampling.

Outside the theoretical set up, because the method assumes persistence of local biases, and the characteristics of theses biases vary regionally (recall Fig. 1.4), it is safe to assume that local weather patterns must influence the effectiveness of this method, with higher instantaneous VRMS differences in the middle latitudes. With the current simulation set up, it should be possible to dissociate between the expected effect caused by local weather and the varying regional sampling characteristics.

Next, the vector error, i.e., the VRMSE scores obtained from the NWP$^{*}_{sim}$ flavours listed in Table 3.1 are analysed. Note that each configuration addresses different combinations of scatterometer sampling for several temporal windows of accumulation with a fixed global error set.

Fig. 3.1 shows these VRMSE scores at a given forecast time, and calculated for the aforementioned NWP$^{*}_{sim}$ configurations (colored lines in orange, green, purple and blue) and the common benchmark NWP$_{sim}$ (solid black). The latter, as previously mentioned, is obtained from Eq. 2.9, where the total vector error for the benchmark is 2.1 $m.s^{-1}$. The error reduction is verified regionally with respect to the truth, for the tropics in Fig. 3.1a and for the middle latitudes in Fig.3.1b.

In here, no distinction (besides sampling) is made between the tropics and middle-latitudes, i.e., the same error is used to produce the NWP$_{sim}$, therefore, the same benchmark of 2.1 $m.s^{-1}$ can be seen in the right and left panels of Fig. 3.1. Consequently, the metrics displayed for both regions are very similar, and apart from the single-scatterometer SC configuration (ASCAT-A sampling), all NWP$^{*}_{sim}$ configurations lay below the benchmark. Overall, better results are expected with larger sampling (i.e., in the middle latitudes), instead both regions show very similar scores, thus suggesting a compensation effect must play a role to balance the metrics scores.

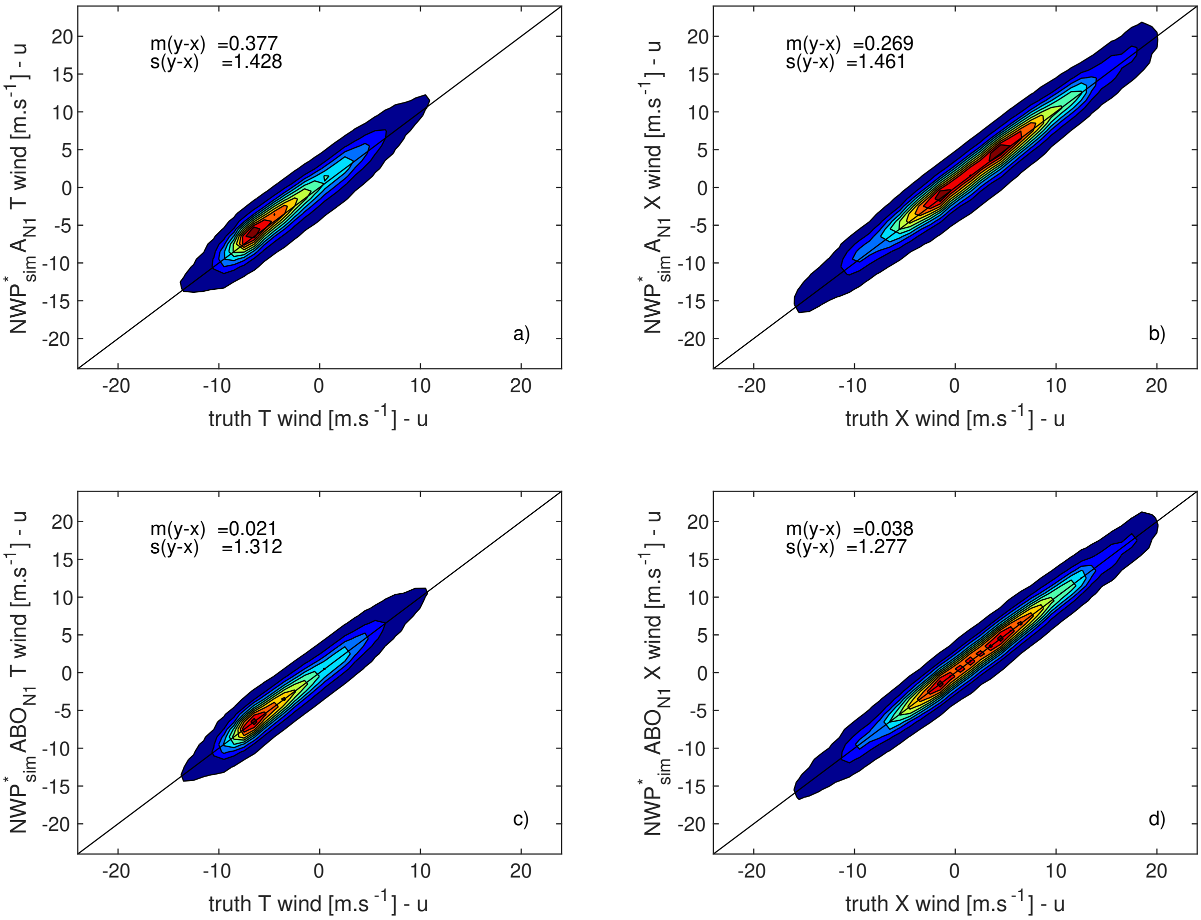

Figure 3.2: Two-dimensional histogram of two synthetic NWP^*_{sim} forcing configurations versus the wind truth (truth) for the zonal wind component, in the tropics (left) and at the mid-latitudes (right), with a TW of ± 12 h (N1): m(y-x) and s(y-x) are the mean (bias) and the standard deviation of the wind differences. NWP^*_{sim} for a single scatterometer ((a)(b)) is shown in the top panels, while NWP^*_{sim} using ASCAT-A/B and OSCAT ((c)(d)) is shown in the lower panels.

A very clear dependence on the TW length is observed for single-scatterometer SC simulation ($NWP^*_{sim}A$ in orange), in which a neutral effect with respect to the benchmark is observed for the smallest TW (N1). Followed by an abrupt drop of the error going from N1 to N3. The reduction of the errors with TW size (i.e., as the spatial sampling increases) is more pronounced for $NWP^*_{sim}A$ (orange) and $NWP^*_{sim}AB$ (green). These fixed fan beam scatterometers have a reduced daily coverage with respect to that of OSCAT (rotating pencil beam), a consequence of their narrower swaths combined with the non-optimal (for this purpose) overlap (the ASCATs are on the same orbit but with different phase, leading to substantial swath overlaps). As such, although the gain in coverage afforded by a larger accumulation in time reduces the error for all configurations (as expected), the reduction is sharper for the ASCATs only configurations, as seen in Fig. 3.1b from N1-N3.

These results are coherent with the implications of the prescribed systematic and random error parameterizations, from which it is estimated that at least two measurements per grid point are required for NWP^*_{sim} to outperform NWP_{sim} (recall Eq. 3.1). Moreover, the current parameterization establishes that with infinite scatterometer sampling the minimum vector error possible would be of 1.56 $m.s^{-1}$. The results in Fig.3.1 clearly show which NWP$^{*}_{sim}$ configurations have close to optimal scatterometer sampling, in particular those using ASCAT-A/B, and OSCAT for a TW of 5 days (N5).

Fig. 3.2 illustrates the ability of the simulated SC to correct for persistent NWP$_{sim}$ local biases, as well as the noise reduction achieved in the tropics (left) and the middle latitudes (right) for two configurations within a ± 12h temporal window (N1) (i.e., those specified in the first and fifth rows of Table 3.2, where the percentage of surface ocean corrected with the SC$_{sim}$ is also provided). While similar scores were obtained for the meridional wind component, metrics are only presented for the zonal wind component.

In spite of the observed error reduction, the simulated bias is still present in the NWP$^{*}_{sim}$ configuration from Fig. 3.2ab (top panels). Other configurations corrected with a 1-day temporal window (N1), such as the one displayed in Fig. 3.2cd (bottom panels), no longer exhibit this bias suggesting that the simulated scatterometer sampling (coverage) affects the ability to correct for the biases.

In the same way, though in NWP$*_{sim}A_{N1}$ (Fig. 3.2ab top panels) about the same noise reduction was obtained for the tropics and the middle latitudes, in NWP$*_{sim}ABO_{N1}$(Fig. 3.2cd bottom panels) the noise is further reduced for the latter. As coverage is always larger at middle latitudes, where for the configurations corrected with SC of N1, the enhanced coverage provided by additional scatterometers allows not only for more ocean points to be corrected, but also ensures that the percentage of ocean points corrected with more than 3 overpasses also increases. This is exposed in Table 3.2, in which the SC$_{sim}$ coverage in the NWP$^{*}_{sim}$ is decomposed by categories, in accordance with the number of scatterometer samples used per SC, i.e., the effective scatterometer sampling.

Note that even if not all the NWP$^{*}_{sim}$ configurations in Table 3.1 appear in Table 3.2, an evaluation of the sampling characteristics for these configurations was also performed. Table 3.2 shows the percentage of ocean coverage obtained in the tropics and the middle latitudes, for a few selected cases.

As expected, Table 3.2 shows that more ocean surface is covered by the sensors in the middle latitudes than in the tropics, albeit, in the former 8% more ocean points are covered with only one scatterometer sample for NWP$^{*}_{sim}A_{N1}$. The compensation effect between the overall coverage and the ratio of ocean points corrected by a single sample may explain the metrics in Fig. 3.1.

On the one hand, this table shows that in NWP$^{*}_{sim}A_{N1}$, the SC$_{sim}$ corrects the NWP$_{sim}$ for 60.4% of the grid points in the tropics, and 76.3% in the middle-latitudes, thus indicating higher (and in principle more beneficial) coverage in the latter. However, while only 46.5% of the grid points belong to the category PSCsim=1 in the tropics, 54.4% belong to this category in the middle latitudes. As already discussed, SC based on one scatterometer sample proves detrimental for NWP$_{sim}$ quality. As such, for the NWP$^{*}_{sim}A_{N1}$ configuration, there is a compensation effect between ocean coverage and number of scatterometer samples that lead to similar NWP$_{sim}$ scores in the tropics and the middle latitudes. On the other hand, Fig. 3.1b and Fig. 3.2d, indicate a better performance of the SC$_{sim}$ with a N1 temporal window for both NWP$^{*}_{sim}AO_{N1}$

Table 3.2: Percentage of the ocean surface corrected with the SC_{sim} in categories according to the number of scatterometer samples used, both in the tropics and in the middle latitudes, for several NWP^*_{sim} configurations. PSC_{sim} is the percentage of corrected ocean grid points in the product; PSC_{sim} = 1 is percentage of corrected grid points with only one scatterometer sample; $PCS_{sim} \geq 3$ gives the percentage of grid points corrected with at least three samples. PCS_{sim} =1 and $PCS_{sim} \geq 3$ are with respect to the PSC_{sim}. A dash is shown when these percentages are not significant.

Coverage %	tropics			middle-latitudes		
	PSC_{sim}	$PSC_{sim} = 1$	$PSC_{sim} \geq 3$	PSC_{sim}	$PSC_{sim} = 1$	$PSC_{sim} \geq 3$
$NWP^*_{sim}A_{N1}$	60.4	46.5	-	76.3	54.4	2
$NWP^*_{sim}A_{N5}$	98.8	2.2	90.4	99	1.3	96.1
$NWP^*_{sim}AB_{N1}$	70.5	18.3	18.9	90.9	19.5	30.2
$NWP^*_{sim}AO_{N1}$	97.2	23	26.2	99.1	8.3	56
$NWP^*_{sim}ABO_{N1}$	98	13.8	55.5	99.4	2.5	84
$NWP^*_{sim}ABO_{N3}$	99.7	0.7	98.1	99.4	0.2	98.8

and $NWP^*_{sim}ABO_{N1}$ in the middle latitudes, with about 5% error reduction in both when compared to the benchmark. In these configurations, the SC_{sim} is applied to more than 97% of the ocean surface, yet, in the middle latitudes slightly more than half of the ocean is always corrected with more than two samples, whilst in the tropics despite the high percentage of ocean points covered more than twice, a significant percentage of points is still corrected with less than three samples.

These results are coherent with the theoretical effectiveness of the method as derived at the beginning of the section, in which at least two samples are needed to reduce the total error in the simulated products (for the assumed parameterization errors), while the larger the number of scatterometer samples, the further the error reduction. Evidence for further error reduction with increased scatterometer sampling is clear from category $PSC_{sim} \geq 3$ in Table 3.3. In this table, the total vector error of $NWP^*_{sim}A_{N1}$ and $NWP^*_{sim}ABO_{N1}$ is displayed according to the aforementioned categories. The configuration with the largest percentage of $PSC_{sim} \geq 3$, i.e., $NWP^*_{sim}ABO_{N1}$, has the lowest overall errors (see PSC_{sim} column scores). By construction, all configurations should lead to the same VRMSE for the same PSC_{sim} and region. This is the case, except for PSC_{sim}=1 in the tropics, where $NWP^*_{sim}A_{N1}$ shows larger scores than $NWP^*_{sim}ABO_{N1}$. The reason must be statistical (not enough number of occurrences for the former).

For the ASCAT-only configurations, similar scores are obtained for the single-scatterometer SC configuration accumulated for its quasi-repeat cycle ($NWP^*_{sim}A_{N5}$) and for the 2-ASCAT configuration over 3 days ($NWP^*_{sim}AB_{N3}$), i.e., see Fig. 3.1 orange square over N5 and green square over N3, showing that increased sampling can be achieved either with larger temporal

Table 3.3: Total vector error for NWP^*_{sim} with respect to the wind truth and sampling category, for the tropics and middle latitudes.

VRMS $[m.s^{-1}]$	tropics			middle-latitudes		
	PSC_{sim}	$PSC_{sim} = 1$	$PSC_{sim} \geq 3$	PSC_{sim}	$PSC_{sim} = 1$	$PSC_{sim} \geq 3$
$NWP^*_{sim}A_{N1}$	2.10	2.15	0.00	2.09	2.17	1.76
$NWP^*_{sim}ABO_{N1}$	1.86	2.08	1.78	1.80	2.16	1.77

windows or more scatterometers.

On other configurations built with more than one scatterometer (NWP$^{*}_{sim}AO$ and NWP$^{*}_{sim}ABO$), the VRMSE reduction almost reaches a plateau by N3, with a substantial error variance reduction in the NWP$^{*}_{sim}$ with respect to NWP$_{sim}$, i.e., about 36% reduction). Taking into account the theoretical implications imposed by the parameter settings, the sampling obtained with these combinations proves optimal to reduce the local persistent errors with respect to the wind truth. Furthermore, for temporal windows of $\pm$ 1.5 days (N3) and three scatterometers, the simulated scatterometer correction mostly falls into the category PSC$_{sim} \leq 3$, thus, every ocean point is corrected with at least three measurements (Table 3.2).

Up until now, the analysis of the scatterometer sampling impact on the performance of the method has been focused either on the tropics or the middle latitudes. Over these regions the majority of points used to compute the simulated scatterometer correction are indeed open ocean points, therefore it is argued that these points strongly modulate the scores of the simulated data sets previously analysed.

In comparison with open ocean regions, closer to the coast, the scatterometer sampling is always poorer and more irregular (see Fig. 3.3). This is mostly due to land contamination over the scatterometer footprint as the distance to the coast decreases, i.e., the WVCs may be contaminated by a small fraction of land and consequently flagged. Moreover, the position of WVCs with respect to the SC fixed grid is variable, resulting in a gradual reduction of the number of samples as a function of the distance to the coast.

Fig. 3.3 illustrates the irregular sampling produced in the Mediterranean basin by combining three scatterometers over a 3-day temporal window (one of the configurations previously evaluated for open ocean areas). In this semi-enclosed basin, although over certain areas, the combined sampling surpasses the theoretical threshold for an effective SC$_{sim}$, closer to the coast

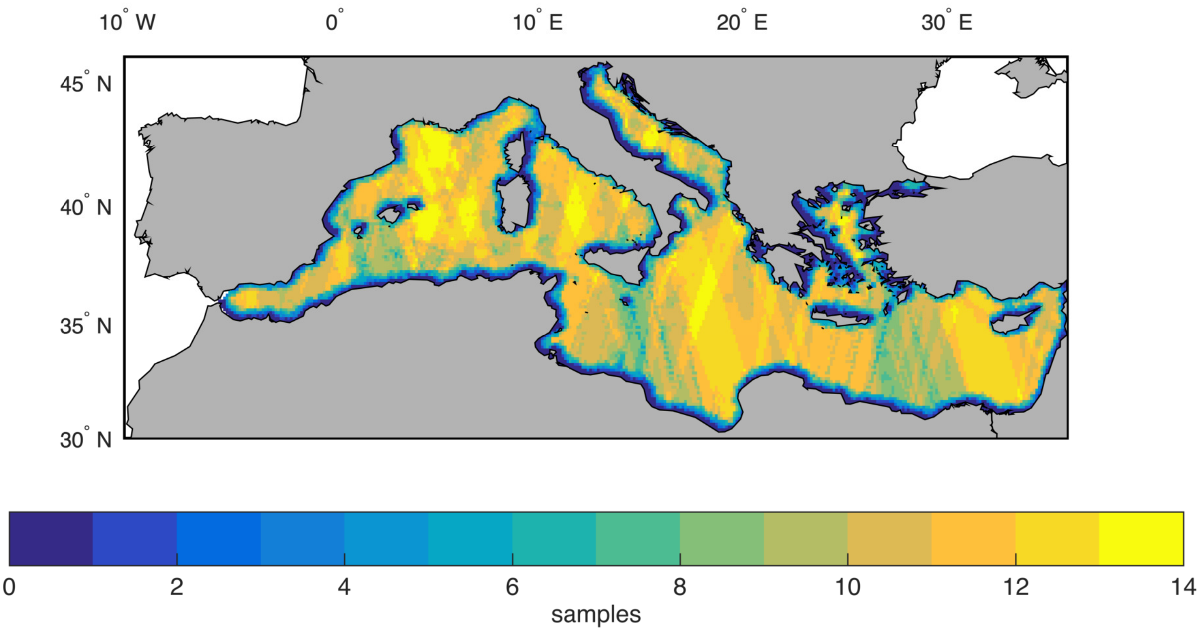

Figure 3.3: Combined ASCAT-A/B and OSCAT sampling pattern for a 3-day temporal window in the Mediterranean Sea.

and around small islands the sampling is compromised. Additionally, despite some heavy (very localised) sampling, the basin is characterized by irregular scatterometer sampling leading to several swath-edge induced artefacts that are readily evident throughout the entire basin. Hence, it appears advisable to avoid SC in undersampled coastal grid points.

Finally, assuming overall persistence and constant magnitude of the biases, in the simulation set up, the irregular scatterometer sampling and proximity to the coast negatively affects the method performance over the Mediterranean basin. The VRMSE values for this region are represented in Fig. 3.4, for all the configurations. It is clear how a single-scatterometer SC generated with a 1-day accumulation (N1) is detrimental in this area (see orange curve), and altogether every configuration analysed in here performs worse than its corresponding configuration over open ocean areas (see Fig. 3.1).

Considering the results from this oversimplified experimental set-up, improving the NWP winds over coastal regions in real case scenario is expected to be more challenging, not only due to sampling issues, but also because in these high wind variability regions, biases may not persist long enough to be captured by this SC. It is particularly noted that the model winds near the coast are generally biased due to artificial diffusion, interpolation and variable land-sea interaction effects that are often diurnal. It is clear that model errors will unlikely persist over a day and will therefore not be well corrected by a SC based on only a few daily scatterometer overpass times.

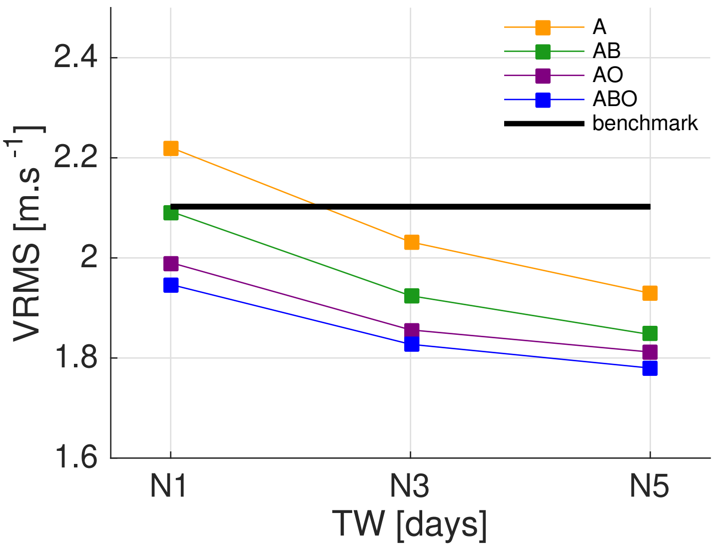

Figure 3.4: Same as Fig. 3.1 but over the Mediterranean Sea.

3.2 Wind variability

The statistical analysis presented in section 3.1 reveals that when comparing the simulated winds to the wind truth, although the scatterometer coverage is larger in the middle latitudes than in the tropics, similar metrics are obtained for both regions.

Here, constant and persistent biases are assumed and these are much in line with Bel-

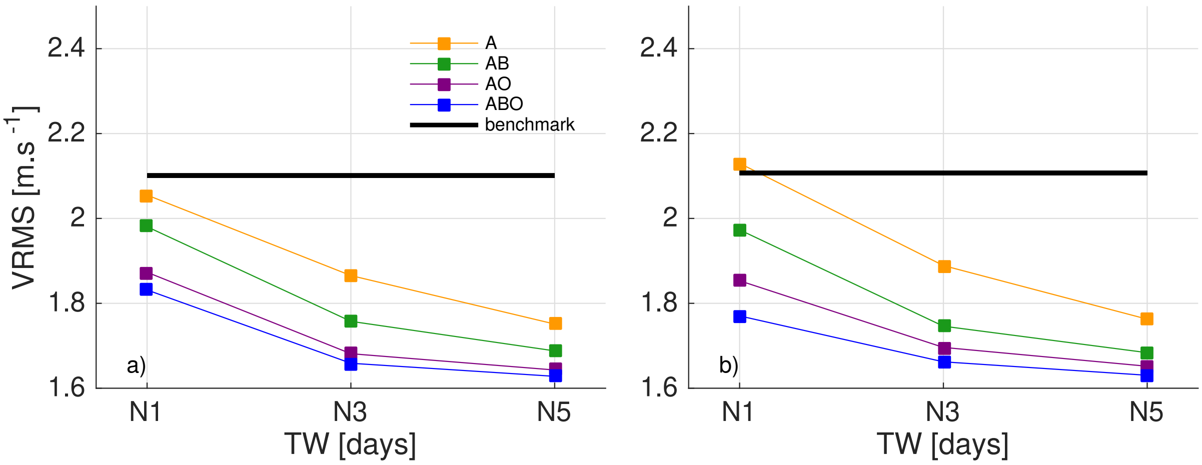

Figure 3.5: Same as Fig. 3.1, but using a 1-h time lag in the wind truth to generate the different NWP^*_{sim} ($NWP^*_{simlag1}$) configurations.

monte Rivas and Stoffelen (2019) who used monthly and annual periods. It is thought that these errors are related to air-sea interaction and Marine Atmospheric Boundary Layer (MABL) parameterization errors, hence a function of both oceanic and atmospheric conditions. Certainly, a more realistic simulation set up would take into consideration the local biases observed in different regions have different error values and varying temporal behaviour, raising the premise that in real scenarios the SC should be weather modulated, and expected to perform better in regions where these local biases are more persistent. With that premise, and taking into account that by our definition, to correct for local systematic NWP biases, these must persist for pre-defined temporal windows of at least 1 day, we examined whether in areas of transient weather, as is the case for the middle latitudes, the presence of fast evolving systems would blur the SC effectiveness (note transient weather is also present in the tropics, but less so than in the middle latitudes).

Thus, with the purpose of simulating a more realistic wind regime over the globe, a lagged version of NWP^*_{sim} is generated to replicate the effect of transient weather errors. More precisely, a phase shift of one or three hours is applied to the wind truth (i.e., the true wind distribution of either one or three hours later is used instead of the actual one) to generate NWP^*_{sim}, using the same error parameterization previously used to assess the scatterometer sampling effects (see section 2.3.1). The resulting NWP^*_{sim} wind distributions are hereafter referred to as $NWP^*_{simlag1}$ and $NWP^*_{simlag3}$, respectively, for the one and the three hour lagged distributions. Note that ideally, to characterize the transient effect of the weather over these latitudes, shorter phase shifts should be applied in the simulations, albeit, the shortest time interval available between NWP (ECMWF) forecasts is one hour.

Fig. 3.5 shows the instantaneous VRMSE scores for NWP_{sim} (solid black line) and the different $NWP^*_{simlag1}$ configurations (colored lines) for the tropics and the middle latitudes. As expected, the errors are higher in the middle latitudes than in the tropics. The same benchmark (NWP_{sim}) as in the sampling analysis in section 3.1 is used. Regional results for the simulated wind regimes, taken stationary in the tropics and more transient in the middle latitudes, are

Table 3.4: Error standard deviation (σ) and biases (b) in the tropics and middle latitudes for $NWP^*_{sim}ABO_{N3}$ (first row), $NWP^*_{simlag1}ABO_{N3}$ (second row) and $NWP^*_{simlag3}ABO_{N3}$ (third row), for the zonal and meridional wind component in ms^{-1}.

	tropics		mid-latitudes	
	$b_u(b_v)$	$\sigma_u(\sigma_v)$	$b_u(b_v)$	$\sigma_u(\sigma_v)$
NWP$^*_{sim}ABO_{N3}$	0.004 (0.004)	1.19 (1.19)	0.05 (0.03)	1.19 (1.18)
NWP$^*_{simlag1}ABO_{N3}$	0.01 (0.003)	1.25 (1.28)	0.04 (0.07)	1.41 (1.58)
NWP$^*_{simlag3}ABO_{N3}$	0.30 (0.38)	1.56 (1.66)	0.28 (0.22)	2.18 (2.73)

displayed in Fig. 3.5a for the tropics and Fig. 3.5b for the middle latitudes. Note that moist convection in the tropics evolves fast too, but since global NWP models (like ECMWF) do not well resolve rain-induced dynamics (Lin et al., 2015a), the time lags (phase shifts) in this experiment cannot reproduce such transient weather effects, leading to rather stationary simulated wind regimes in the tropics.

Even with a one hour phase shift these simulations are able to realistically reproduce the effect that weather patterns would have over this type of correction, which is meant to correct persistent model biases within a predefined temporal window. The sampled natural variability of these regions is readily evident in Fig. 3.5. Notice that in the tropics (Fig. 3.5a), the VRMSE scores are below the established benchmark and similar to those shown in Fig. 3.1a, whereas in the middle latitudes (Fig. 3.5b) the imposed increment in wind variability results in a worse performance of the method, as compared to the performance in Fig. 3.1b.

The simulated phase shifts are applied under the hypothesis that the model biases are not persistent locally, even for one day temporal windows. The results shown for a 1-hour lag of the wind truth are indicative that in increased wind variability areas a worse performance of the method may occur for real wind data sets.

To further understand the role of local bias persistence in the method ability to reduce model errors, and thus obtain a high quality product, the results from section 3.1 are considered in this section. Section 3.1 establishes (with the assumption of longer bias persistence) that, in the simulation environment with multiple scatterometer sampling over N3, the spatial coverage provided by the scatterometer is optimal. Therefore, by analysing the product configurations listed in Table 3.4, it should be possible to isolate the effect of transient weather. In this Table, the ability to correct for wind biases, as well as to reduce the total error is presented according to the simulation conditions in section 3.1 (first row), and the current section for NWP$^*_{simlag1}$ (second row) and NWP$^*_{simlag3}$ (third row).

Table 3.4 shows how a phase shift of only one hour induces additional error in both regions. On top of that, while in the tropics the error variance is reduced by about 27% when compared with that of the benchmark, in the middle latitudes the variance increases beyond this reference level. As expected, by increasing the phase shift from one to three hours, the added noise goes well beyond the benchmark (1.5 $m.s^{-1}$) for both wind components, destroying the ability to correct for local biases. Without the phase shifts, there is no noticeable difference in either region. The analysis suggests that, by using lagged winds to simulate transient storm phase shifts, lack of local bias persistence is successfully simulated where and when transient weather occurs. As such, the static correction of local biases should work on the persistent biases found at these (middle) latitudes (Belmonte Rivas and Stoffelen, 2019), but may prove less effective correcting more transient ones.

3.3 Discussion

The purpose of the simulations described in this Chapter is to evaluate the viability of the ERA* methodology using a theoretical framework, prior to its application to real data. The method (proposed in section 2.2) is intrinsically dependent on both local bias persistence and scatterometer sampling (recall Eq. 2.1). In the previous sections, an attempt is made to characterize the impact of increased scatterometer sampling (section 3.1) and transient weather phenomena (section 3.2) in the development of the new forcing product, by means of Monte Carlo simulations.

As such, following the simulation framework, several configurations of synthetic L4 products were tested by varying the number of scatterometers and the size of the accumulation time window used to construct a scatterometer based-correction, arguably able to correct for systematic local biases over the tropics and the middle latitudes.

From the theoretical scenarios evaluated in section 3.1, because of sampling, and compensation effects, longer averaging periods are required in both regions for a single-scatterometer SC. For the ASCATs configurations, those required correspond to at least five days of accumulation (N5), to achieve a minimum of three samples per ocean point corrected, as well as full ocean coverage. Additionally, in a real case scenario, it is advisable to apply the SC to every ocean grid point (i.e., a gap-free SC), so that the end product is not a construction of two data sets that represent different scales, i.e., NWP and ERA*, and therefore have mixed spatio-temporal characteristics. An alternative to achieve increased sampling over short time windows is to use multiple scatterometer combinations, while if this is not possible, larger temporal accumulation windows are advised.

It is found that where the SC_{sim} is constructed with less than three samples, the impact on the quality of the generated product may vary from neutral to, in the worst case, detrimental, when the majority of ocean points is corrected by a single scatterometer measurement (sample). This is in line with the estimated theoretical skill of the methodology under this parameterization. For those grid points, the recommendation is to avoid applying the SC. From the experiments in section 3.1, optimal sampling is achieved when all the ocean points for a particular region are corrected with at least three scatterometer measurements, within the shortest temporal window.

On a separate note, caution is advised if applying the methodology to coastal regions, e.g., the Mediterranean Sea, where the very irregular sampling over these regions is expected to create artifacts in the corrected winds and degrade the effectiveness of the method.

Nevertheless, although long persistence of the simulated local biases is assumed in the set up of the simulations, such condition is more unrealistic and unlikely the case in regions of high wind variability. Thus the use of a persistence-based correction would prove less effective, and could generate additional random noise. This was supported by the findings from section 3.2.

Although the simulated phase shifts applied to the reference (truth) wind distribution proved not to be realistic enough, it is fair to infer that by destroying the persistence of the biases over time, the effectiveness of the static mean correction behind this methodology strongly decays. Moreover, the results from this section reveal how the temporal characteristics of the NWP biases may affect the ability to correct for them with real data, i.e., the quality of the generated L4 U10S is expected to be degraded under high wind variability scenarios w.r.t. regions of predominant stationary signals. As the sampling characteristics of NWP^*_{sim} are evened regionally, i.e., either by enlarging the temporal window or with the use of complementary scatterometers in the SC, the metrics shown for the middle latitudes in section 3.2 bring forward the intrinsic dependence of the SC on the persistence of the local NWP bias. Thus, the ability to outperform the NWP_{sim} in the presence of fast evolving systems compared with that of steadier weather is reduced (but still possible) although further alternatives to correct for NWP biases may be pursued.

In summary, the limitations of these simulated phase-shift experiments in trying to simulate variable errors are taken into account in the analysis. Extrapolating these findings to real case scenarios, and anticipating a degradation of the ERA* product over regions of high wind variability seem quite reasonable. It is also reasonable to assume that for real wind data the natural weather variability of a particular region will modulate the effectiveness of the methodology assessed in here. Belmonte Rivas and Stoffelen (2019) provides maps of both real mean errors and variability errors over monthly periods from which local variability, errors and biases can all be assessed. In the next chapter, real effects will be further assessed and over periods of up to a month.

Chapter 4

The ERA* product

[1] [2]

Considering the overall positive outcome of the theoretical assessment of the ERA* methodology (discussed in Chapter 3), several configurations of the high resolution ERA* ocean surface wind forcing are evaluated with real data in this Chapter. Every configuration addressed here follows the main processing chain explained in the methodology (see diagram in Fig. 2.4), yet additional QC testing of the input data and 3σ filtering of the collocated NWP/scatterometer differences, which were not implemented in the early stages of the product generation, are carried out now.

Furthermore, improvements to the algorithm take into consideration the results from the theoretical simulations (Chapter 3) together with the ERA* beta configurations using real data from 2013, which are thoroughly analysed in section 4.1. In the latter, a comprehensive characterization of the new ERA* U10S product, i.e., the corrected ERAi reanalysis, is presented. At first the ERA and ERA* products are compared in a qualitative way, then the U10S quality is assessed against independent scatterometer observations, namely from HSCAT-A, and the geophysical consistency of the derived maps is assessed through spectral analysis by comparison to HSCAT-A and ASCAT-A observations.

As the ERAi reanalysis became obsolete, an effort was made to adapt the ERA* processor to produce a new ERA*, i.e., by correcting the ERA5 reanalysis. Such effort was supported by the interest of the oceanographic modelling community in the product, in the frame of ESA's World Ocean Circulation project (WOC).

Yet, in the generation of the ERA*, to properly transition from one NWP reanalysis (ERAi) to the next (ERA5), i.e., from an ERAi corrected to an ERA5 corrected product, both products must be compared. To fulfill this requirement the year 2013 is selected as testbed, and the results that arise from the analysis are presented in section 4.2. As proven by the latter, the ERA* algorithm can also successfully reduce local biases in the ERA5 reanalysis. Moreover, since the same theoretical conclusion apply, considering the increased number of available scatterometers in orbit providing high quality winds throughout the past decade, the year 2019, with five sun-synchronous scatterometers in orbit providing global (near) continuous coverage, is used to further improve the algorithm. Thus, additional QC testing, filtering of transient weather effects

---

[1] **Part of the results presented in this chapter are included in the following paper, proceedings and report: *Trindade, A., Portabella, M., Stoffelen, A., Lin, W., and Verhoef, A. (2020). ERAstar: A High-Resolution Ocean Forcing Product. IEEE Transactions on Geoscience and Remote Sensing,58(2)***

[2] ***Portabella, M., Trindade, A., Grieco, ,G., Makarova, E. (2022). A NEW HIGH-RESOLUTION OCEAN FORCING BASED ON ERA5 AND SCATTEROMETER DATA. International Geoscience and Remote Sensing Symposium (IGARSS))***

from the SC and a closer look at coastal effects on the quality of the ERA* are addressed at this point. Finally, this methodology is used in the development of a 11-year record of ERA*, from 2010 to 2020, which is discussed in section 4.3.

4.1 ERA* configurations

The ERA* ocean forcing product was first developed using wind retrievals from the available scatterometer constellation in 2013. To generate and validate the L4 forcing, four U10S products were derived from different scatterometer systems with global (near) continuous coverage during the selected year, i.e., two C-band (ASCAT-A/B), and two Ku-band instruments (OSCAT-1 and HSCAT-A). To recap, these scatterometers fly in sun-synchronous orbits with the following LTAN: 21:30 UTC for ASCAT-A/B, 12:00 UTC for OSCAT-1, and 18:00 UTC for HSCAT-A (further details on these instruments can be found in section 2.1). The former three are used in the generation of the ERA*, whilst the latter only for validation purposes. Note that although, the named instruments do not capture the diurnal cycle due to lack of temporal coverage (ASCAT and OSCAT retrievals are only 2.5 h apart in the tropics, since OSCAT descending node is at 00:00 UTC), it is assumed that the time gap between HSCAT LTAN and the remaining instruments is still a good validation reference. Essentially, it is assumed that the SC has no diurnal component and that the ECMWF diurnal cycle is perfect. Both conditions will particularly fail in coastal areas, as the open ocean diurnal cycle is rather weak. Also note that the configurations generated for 2013 coincide with those explored in the theoretical scenario presented in the previous Chapter by means of Monte Carlo simulations.

Four configurations of the ocean forcing product are generated for 2013, same as in the previous Chapter, that result from combining scatterometer measurements from the ASCATs and the OSCAT. The use of different sensors as the input data (see the right side of the flow chart diagram in Fig. 2.4), allows the analysis of the effects of the instrument sampling errors on the quality of the generated real wind data sets. Thus, recalling $u_{10s}^{SCAT_k}$ in Eq. 2.1, in 2013 up to 4 different sensor combinations are analysed, $k = 1, 2, 3, 4$, these include measurements going from a single scatterometer to multiple sensor combinations. A summary of the analyzed configurations, i.e., different sensor combination with respect to TW, is provided in Table 4.1. In here, $k = 1$ contains ASCAT-A data, $k = 2$, combines both C-band radars (ASCAT-A and ASCAT-B), $k = 3$ combines ASCAT-A and OSCAT, and finally $k = 4$ uses all three sensors. All four k configurations are analysed for the same TW. The TWs are noted as N in Table 4.1, and

Table 4.1: ERA generated products according to the number of sensors and temporal window used in the SC to correct the ERAi forecasts in 2013.*

	Temporal Window				
Scatterometer Sampling	1-d (N1)	2-d (N2)	3-d (N3)	4-d (N4)	5-d (N5)
ASCAT-A	ERA$*_{A}$N1	ERA$*_{A}$N2	ERA$*_{A}$N3	ERA$*_{A}$N4	ERA$*_{A}$N5
ASCAT-A,ASCAT-B	ERA$*_{AB}$N1	ERA$*_{AB}$N2	ERA$*_{AB}$N3	ERA$*_{AB}$N4	ERA$*_{AB}$N5
ASCAT-A, OSCAT	ERA$*_{AO}$N1	ERA$*_{AO}$N2	ERA$*_{AO}$N3	ERA$*_{AO}$N4	ERA$*_{AO}$N5
ASCAT-A, ASCAT-B, OSCAT	ERA$*_{ABO}$N1	ERA$*_{ABO}$N2	ERA$*_{ABO}$N3	ERA$*_{ABO}$N4	ERA$*_{ABO}$N5

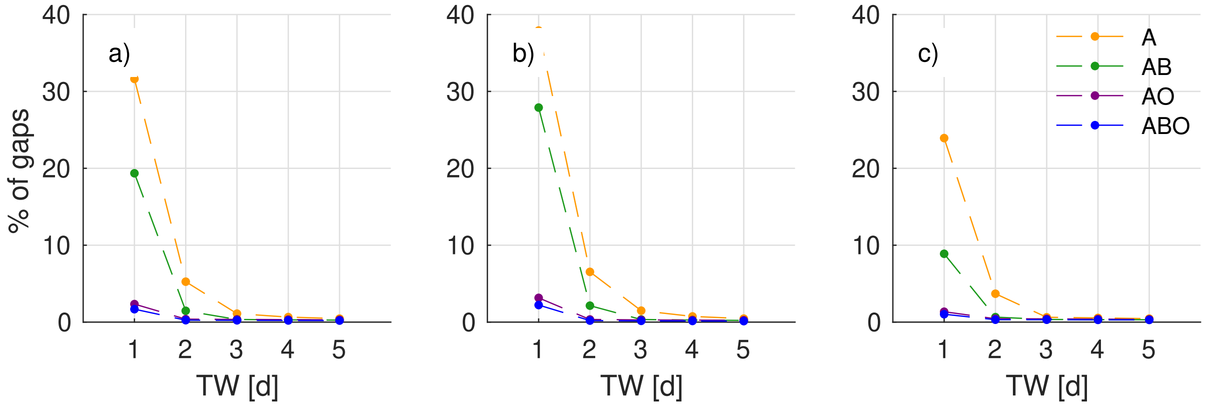

Figure 4.1: Percentage of gaps in the SC as a function of the TW (in days) and combination of sensors used to correct the original ERAi U10S, i.e., percentage of original ERAi data in the ERA configurations listed in Table 4.1. From left to right, the panels display the percentage of gaps for the entire global ocean (a), the tropics (b), and the middle latitudes (c).*

respectively N= 1, 2, 3, 4 and 5 corresponds to 1, 2, 3, 4 and 5 days of temporal accumulation centered at forecast time for every 3-h time step. The final ERA* U10S was produced globally on a grid resolution of 12.5 km $\times$ 12.5 km on a 3 h time step, following the highest scatterometer sampling used. Recall that for this each SC is applied to an ERAi U10S field that is previously interpolated from its native (much coarser) reduced gausian grid (about 80 km) to the higher L3 grid resolution of the scatterometer (see section 2.1).

Moreover, prior to the product assessment a couple of notes are required on the ERA* configurations listed in Table 4.1. Firstly, considering Eq. 2.1 and the simulation experiments, some SC configurations, specifically those with smaller k and N values, will have gaps due to poor scatterometer sampling (see Fig. 2.2a). Although it is not ideal, by construction, these gaps are filled with the ERAi winds only, i.e., ERA* winds will be the same as ERAi winds. In particular, for a 1-day and ASCAT-A-based correction in the tropics, there is about 37.9% of gaps. In contrast, for a 2-day (or longer) TW and two complementary scatterometers (e.g., ASCAT-A and OSCAT), there is less than 0.3% of gaps, as shown in Fig. 4.1. This figure provides information about the regional percentage of gaps, i.e., where poor scatterometer sampling is expected, according to the combination of sensors and the TW used in the SC.

Secondly, note that the last two k values combine observations from scatterometers working at different frequencies, i.e., ASCAT- A/B and OSCAT, respectively, at 5.2 GHz (C-band) and 13.5 GHz (Ku-band). As mentioned at the beginning of the Chapter, it is important to take into consideration that in the study of the configurations first generated with 2013 data, as those addressed in this section, the input data available came from reprocessed scatterometer data sets and good inter-calibration between sensors was assumed, despite that, these data sets did not account for latitude-dependent biases due to SST and wind speed dependent PDF differences (Wang et al., 2017; Wang et al., 2017). Furthermore, the effects of Ku-band SST errors are only about 0.02 $m.s^{-1}$ per Kelvin and relevant on a global scale, where SST varies by 30 K, culminating in a bias range of about 0.6 $m.s^{-1}$.

An extended characterization of the ERA* configurations listed in Table 4.1, is presented next. Please note that although the ERA* is generated for the entire global ocean, in the following evaluation of the product the global domain is considered to be between [-55 55]°, i.e., the higher latitudes (beyond 55°N and 55°S) are excluded in this section (see Table 2.2).

At high latitudes, the abundant (sun-synchronous) satellite sampling is expected to be optimal for model local bias reduction. However, in the ERA* configuration addressed withing this section the additional analysis on the effects of SST and the seasonality of the sea ice extent and its impact on the scatterometer wind-retrieval errors, quality control, and sampling, which becomes more relevant at these latitudes, was not performed. Moreover, the trade off between sampling and the more transient nature of the dynamical weather errors here, may result in a different optimum averaging period as compared to the rest of the globe (discussed in section 4.2).

4.1.1 Systematic local differences

As mentioned earlier in the document, local systematic differences of the scatterometer/ERAi U10S component fields are readily evident where the physical processes are misrepresented or absent in the model (Belmonte Rivas and Stoffelen, 2019), and generally fall within ± 2 $m.s^{-1}$ (see Fig.1.4 and Fig.4.2). As such, to do a qualitative comparison between the ERAi and ERA* products, a first assessment as to the location and magnitude of these differences was performed for the ERA* flavours addressed in 2013. Fig. 4.2 shows the collocated differences between ASCAT-A and ERAi U10S for the zonal 4.2a and the meridional 4.2b wind components, accumulated over a 5-day temporal window, i.e., the SC for the ERA*$_A$N5 configuration. In fact, the five-day period agrees with the longest quasi repeat cycle of the scatterometers addressed in this chapter, thus providing a near global coverage using single scatterometer collocations to the ERAi U10S.

Due to their stationary character, differences are very pronounced over the western boundary ocean current systems (WBCS, i.e., the Agulhas current, the Gulf Stream or the Kuroshio current), the Antarctic Circumpolar Current (ACC), and in adjacent regions where the eddies generated by these currents detach. Likewise, in the tropics (see, e.g., the Inter Tropical Convergence Zone or ITCZ), U10S differences (particularly in the meridional component in Fig.4.3b) are notable where the model U10S field is unable to capture both the detailed and large-scale wind circulation.

Local wind effects like see breeze, katabatic flows, corner winds or wind funneling effects (gap winds) are also visible in Fig. 4.2. The latter are readily evident from the meridional component in Fig. 4.2b, e.g., see the gap wind effect in the Gulf of Tehuantepec (Central America, south of Mexico). Apart from the increase in wind speed, gap winds also strengthen tidal currents, furthermore affecting ocean circulation.

Indeed, as expected these differences coincide with those already shown in Fig 1.4 for a 30-d temporal accumulation correction.

Fig. 4.3 shows an ERAi U10S global map (4.3a) and its corresponding ERA* (4.3b) generated with a four-scatterometer based correction (i.e., ASCAT-A/B, and OSCAT) over a one-day TW (ERA*$_{ABO}$N1). By simply comparing ERAi and ERA*$_{ABO}$N1 U10S global maps, it is

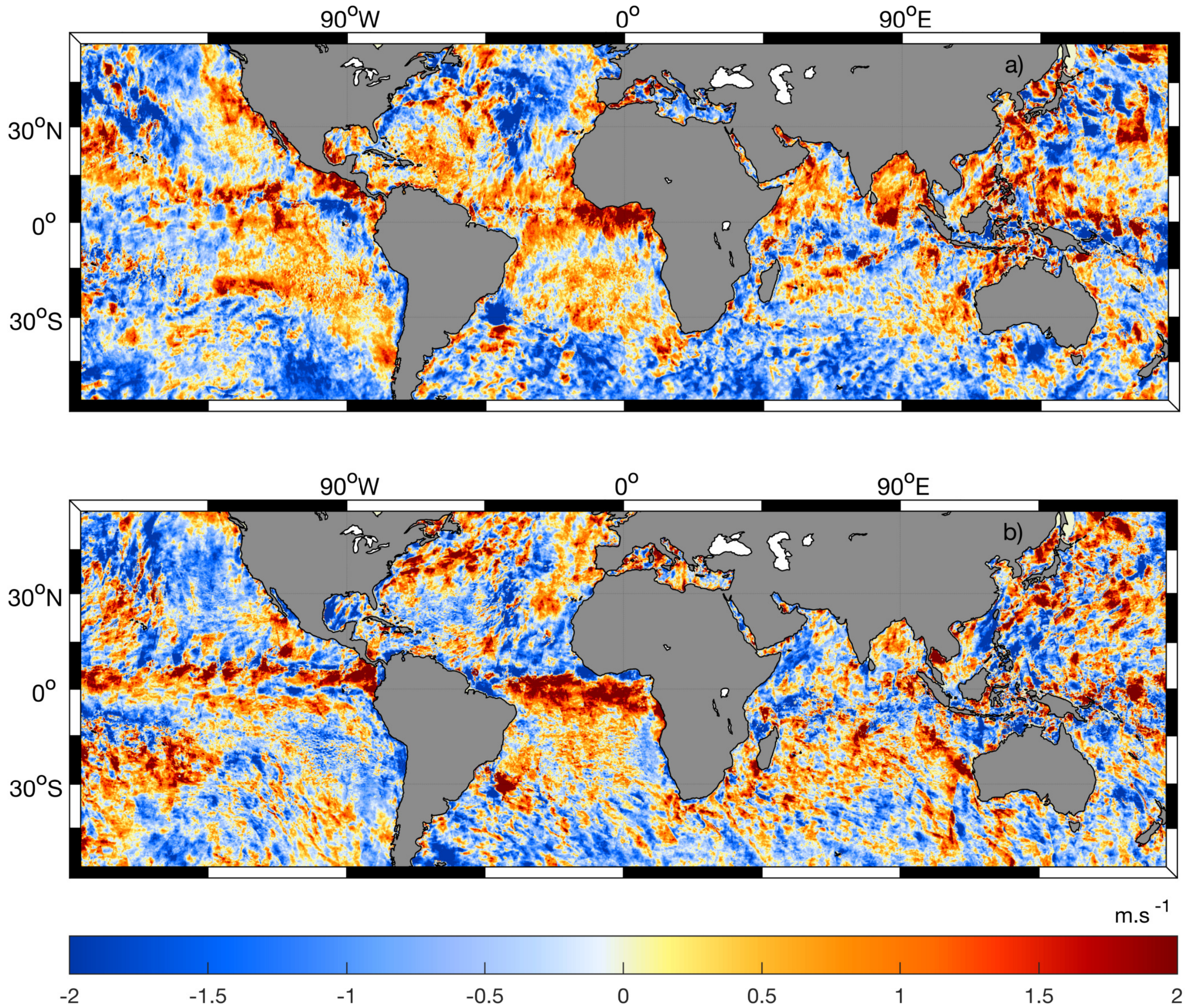

Figure 4.2: Scatterometer Correction (SC) for a given day, i.e., 15th January 2013. Collocated differences between ASCAT-A (12.5 km) and ERAi U10S for the zonal (a) and the meridional (b) components, accumulated over a 5-day TW centered around 06 UTC. The colors represent the differences in m.s^{-1} (see color scale). Figure included in Trindade et al. (2020).

clear that both contain very similar structures, as expected, since the ERA* does not aim at correcting transient weather effects but local systematic effects. ERA*$_{ABO}$N1 (Fig. 4.3b) contains additional small-scale variance as compared to ERAi (Fig. 4.3a), the latter being smoother than the former, notably at the same locations where larger local biases emerge in Fig. 4.3b, although this is difficult to appreciate in a global map. In this line, Fig. 4.3a differs from Fig. 4.3b in that the increased variability seen in the latter should better capture the stationary signal from WBCS, the wind shadowing effects in the vicinity of islands, and the coastal effects associated to coastal orography, as well as atmospheric model dynamics and MABL parameterization errors.

To discern the difference in small scale variance between the two maps in Fig. 4.3, a zoom over the tropical Atlantic region is shown in Fig. 4.4 (which corresponds to the red box in Fig. 4.3).

Additionally, Fig. 4.4c shows the same map for another ERA* product generated with a longer temporal window of three days (ERA*$_{ABO}$N3). Fig. 4.4b arguably shows moist convection induced variability south of the West African coast, clearly visible in the ERA*$_{ABO}$N1, but not in the ERAi (Fig. 4.4a). The ERA*$_{ABO}$N3 map (Fig. 4.4c) shows somewhat lower variability than the ERA*$_{ABO}$N1 map (Fig. 4.4b). The use of a longer temporal window in ERA*$_{ABO}$N3 than in ERA*$_{ABO}$N1 is responsible for the additional smoothing of the wind fields of the former, but also for the reduction of scatterometer weather sampling errors. This probably indicates that the ERA*$_{ABO}$N1 map (Fig. 4.4c) captures small-scale variability associated with relatively fast evolving atmospheric phenomena, while the ERA*$_{ABO}$N3 (Fig. 4.4b) does less so.

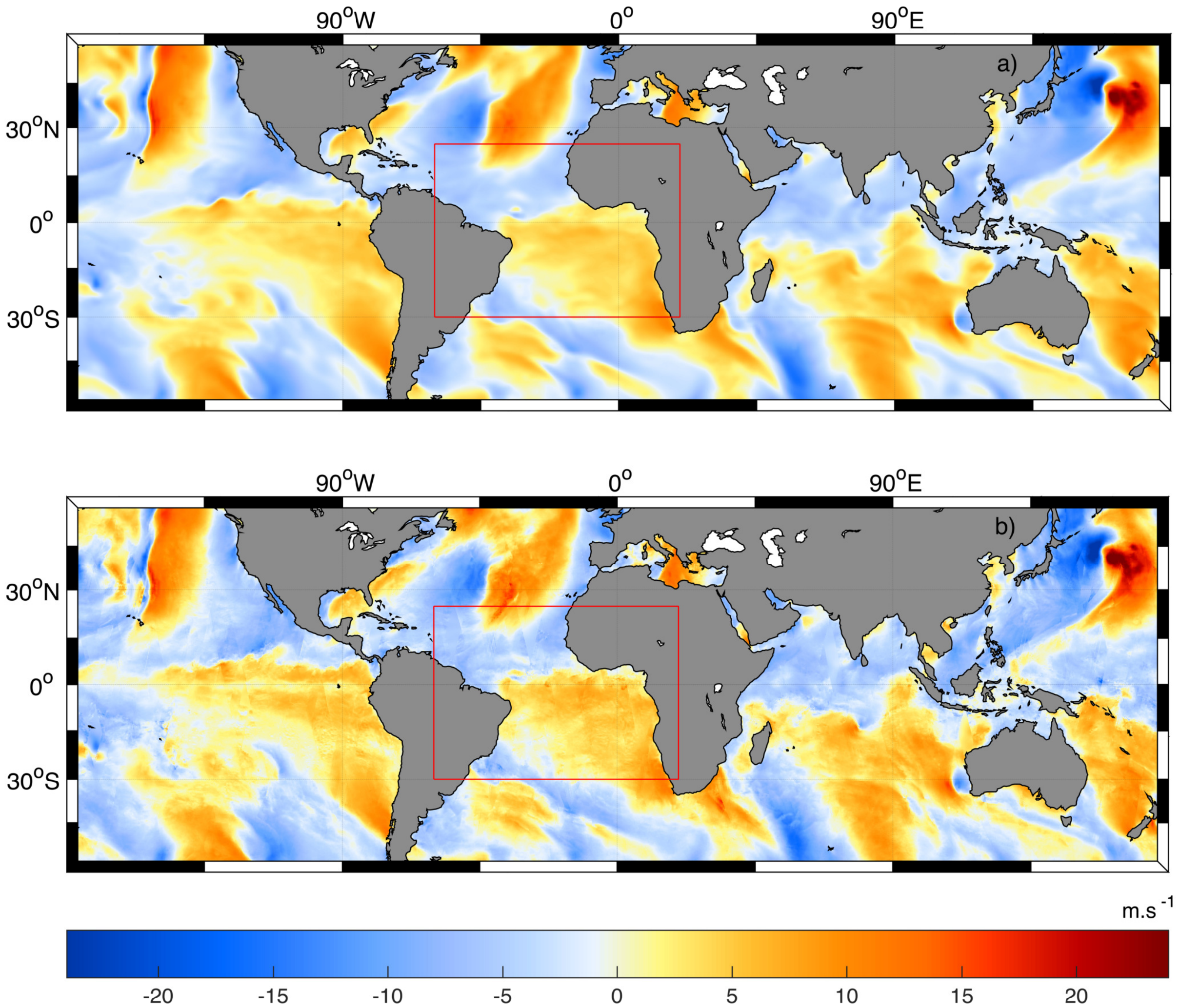

Figure 4.3: U10S meridional component for ERAi in (a) and ERA in (b) on the 15th January 2013 at 06 UTC. The ERA* map is based on ASCAT-A, ASCAT-B, and OSCAT-1 corrections over a one-day TW. The red box indicates the area shown in Fig. 4.4. Figure included in Trindade et al. (2020).*

Note also that this increased variability is attributed to moist convection, because it can be depicted by the scatterometers (due to updrafts and downdraft), in agreement with the findings of Lin et al. (2015b,a); King et al. (2022) over the tropical band. Although moist convection impacts the ocean exchange processes of momentum, heat and moisture and is fundamental to ocean model forcing, it will only be partly resolved using a static mean correction, since the SC likely misses the highly variable component in moist convection (wind changes up to 15 $m.s^{-1}$ over a 30-minute window). Due to the fast weather evolution during a satellite orbit, ERA*$_{ABO}$N1 clearly shows some small-amplitude "jumps" or artifacts (see, e.g., several straight lines in the top-left quadrant of 4.4b), which are not visible in the ERA*$_{ABO}$N3 (Fig. 4.4c), which smooths weather effects over 3 days. Such artifacts are associated with the edges of the different scatterometer swaths used, indicating that the 1-day corrections (N1) are based on relatively poor scatterometer weather sampling at these latitudes. Moreover, although such jumps may be small, they certainly become more evident in wind derivative products, such as divergence or curl (not shown). Additional spatial variance, as seen in these regional maps of the ERA* meridional U10S component, manifests alike in all the ERA* configurations in Table 4.1 and in the U10S zonal component (not shown), indicative of persistent mesoscale (ocean) variability. A more quantitative validation is presented in the next sections in order to verify and complete the preliminary conclusions drawn from the qualitative comparison presented in this section.

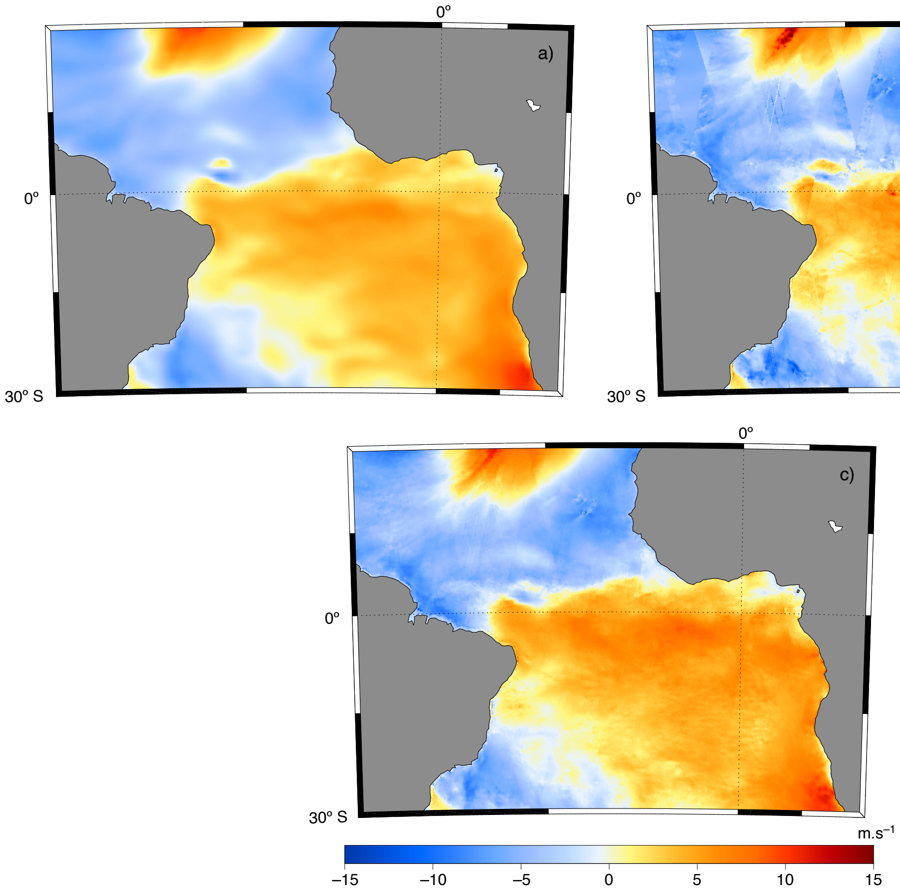

Figure 4.4: U10S meridional component over the West African coast for the ERAi in (a) and ERA in (b) products shown in Fig. 4.3 (see red box). The ERA* shown in (c) is the same as that of (b) but for a SC over a three-day temporal window (N3). The winds are truncated beyond [-15 15] $m.s^{-1}$ to better highlight the differences between the three maps. This Figure is included in Trindade et al. (2020).*

4.1.2 U10S verification

In subsection 4.1.1, a qualitative assessment of ERA* wind maps reveals enhanced variability with respect to the original ERAi wind. In this section, we check whether this additional variance is dominated by true wind signal rather than noise, by assessing the quality of the different ERA* gridded ocean forcing products (i.e., using different SCs and temporal window combinations as shown in Table 4.1) against independent U10S data. The ERA* products are validated against independent scatterometer data, i.e., the 25-km HSCAT U10S product. HSCAT-A is a good wind reference since the orbit pass (6 am/6 pm) is very different from that of the instruments used to correct the ERA fields, i.e., ASCAT-A/B at 9:30 am/9:30 pm and OSCAT-1 at 12:00 am/12:00 pm. The use of ASCAT-A/B and OSCAT-1 together substantially increases the local sampling but is insufficient to capture the diurnal cycle as these sensors sample the same location of the ocean with only a 2:30 h difference. However, if the model diurnal cycle is reasonable and local biases are persistent over longer periods (one to several days), then the scatterometer-based corrections would lead to a reduction of model errors at HSCAT-A verification times, which are 3:30 h and 6:00 h apart from ASCAT-A/B and OSCAT, respectively. Furthermore, if these local biases are persistent over several days, then the ERA* product generated with a larger temporal window (of several days) would be of higher quality than that generated with a 1-day temporal window, since the former has a better downsampling of the mesoscale weather variability than the latter.

Fig. 4.5 shows the vector root-mean-square difference (VRMSD) between different ERA* configurations (see legend) and HSCAT-A U10S as a function of the TW size (in days), for the tropics (left), the middle latitudes (middle), and both the tropics and the middle latitudes (right). Fig. 4.5abc (Fig. 4.5def) corresponds to collocations with HSCAT-A ascending (descending) passes, thus collocations at 6 pm (6 am) local time. For reference, the VRMSD between ERA and HSCAT-A is plotted with a thick black solid horizontal line. The latter is used as benchmark, i.e., only those ERA* configurations below the black line are of higher quality (with respect to HSCAT-A) than ERAi. At first glance, because the local bias distribution is not the same everywhere (already discussed in the previous subsection), and biases have different persistence times, which in regions of high wind variability may not be sufficiently long to be corrected by this method, different VRMSD reduction rates are found for the regions analysed here as opposed to those previously analysed in Chapter 3. For a single-scatterometer SC, ERA* (orange curves) is very much dependent on the temporal window size, indicating that the weather downsampling of a single scatterometer over 1 day is rather poor, and therefore, a larger temporal window is required to reduce the model weather errors. Note the abrupt drop in VRMSD that occurs if the ERA* is generated with a correction based on up to 3 days of accumulated scatterometer information. In particular, a 4–5 day window (N4 or N5) is needed to outperform ERAi. Interestingly, although the scatterometer sampling is larger in the middle latitudes than in the tropics, the ERA* quality for N1 and N2 is more degraded in the former. This is because of the transient weather in the middle latitudes (see e.g., Portabella and Stoffelen (2009)). As a result, a larger number of observations per grid point is required here to reduce model weather errors. When only one scatterometer is available, enhanced sampling is

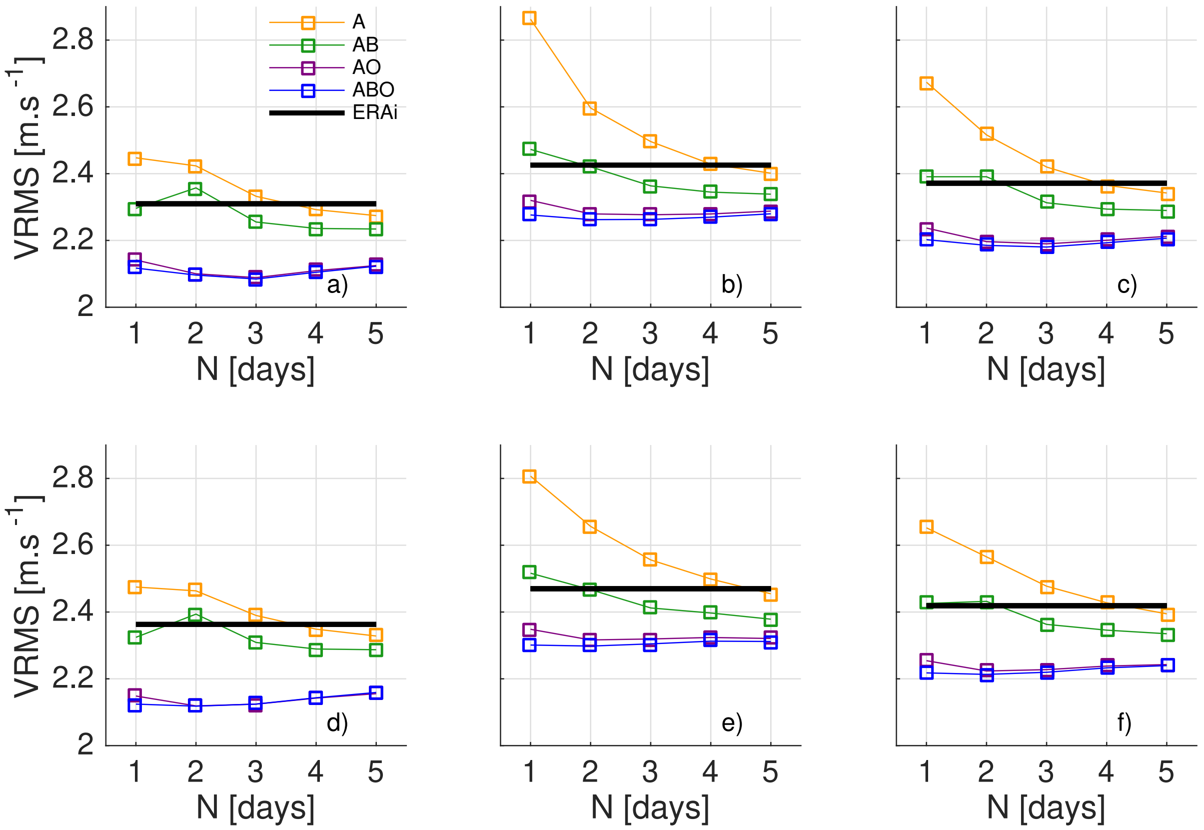

Figure 4.5: Vector root mean square difference (VRMSD in ms^{-1}) between different ERAi/ERA U10S products and HSCAT-A U10S ascending (top) and descending (bottom) passes as a function of the SC temporal window size, over an eight day period, for the tropics (a) and (d), the middle latitudes (b) and (e), and both the tropics and the middle latitudes [-55°, 55°] (c)and (f). The different colour lines show the VRMSD scores for ERA (black line in bold), ERA* configuration using only ASCAT-A (orange line), ERA* using ASCAT-A and B (green line), ERA* using ASCAT-A and OSCAT (purple), and ERA* using ASCAT-A, ASCAT-B and OSCAT (blue).*

Table 4.2: Mean (b) and standard deviation (ϵ) of the differences between different ERAi/ERA products and HSCAT-A, in the tropics and the middle latitudes for both the zonal (u) and the meridional (v) U10S components. The number of valid winds over which the statistics are computed is shown in parenthesis. Table included in Trindade et al. (2020)*

	mid-lat. (2331603)				tropics (2131292)			
ASC & DSC	$b_u(ms^{-1})$	$\epsilon_u(ms^{-1})$	$b_v(ms^{-1})$	$\epsilon_v(ms^{-1})$	$b_u(ms^{-1})$	$\epsilon_u(ms^{-1})$	$b_v(ms^{-1})$	$\epsilon_v(ms^{-1})$
$ERA*_{ABO}N1$	0.086	1.589	0.014	1.645	0.031	1.471	-0.041	1.527
$ERA*_{ABO}N3$	0.084	1.611	0.012	1.616	0.023	1.450	-0.051	1.513
ERAi	0.546	1.703	0.161	1.663	-0.035	1.596	-0.032	1.705

achieved by using larger temporal windows. Note that for a single ASCAT scatterometer or for its predecessor, the ERS scatterometer, with about half the coverage, a sampling period longer than 5-days would be profitable to further improve the bias estimates.

As expected, when adding more scatterometers, the model weather errors are considerably reduced at N1. In particular, when complementary scatterometer orbits are used in the corrections, the derived ERA* products (see purple and blue curves in Fig. 4.5a as well as the bias and standard deviation scores in Table 4.2) outperform ERAi at N1. In this table we decompose the VRMSD in the bias and standard deviation of each wind component and present the scores for HSCAT-A ascending and descending orbits together. In fact, for such ERA* products, the quality of the data does not significantly depend on the temporal window size, except in the tropics where a slightly higher quality U10S is achieved at N2 or N3. This is probably due to a compensation effect: on the one hand, the larger the temporal window, the larger is the sampling; on the other hand, the larger the temporal window, the more sensitive the system is to local bias changes. Specifically, the mid-latitude local biases seem to be less persistent than those in the tropics, since no further ERA* quality improvements are discernible at temporal windows larger than N1. This may be caused by the impact of fast evolving weather not well captured by ERAi, e.g., mislocation of mid-latitude synoptic variability. Note however that the improvements brought by ERA* over ERAi remain substantial and significant over the entire domain.

Most of the features discussed so far imply that this method is regionally dependent, i.e., its effectiveness is mainly modulated by weather sampling and on the longer term by local bias persistence. Since the biases persist quite well over time, large sampling is essential to improve these bias estimates both in the tropics and in the middle latitudes. Overall this is reflected by the VRMSD between the ERA* configurations and HSCAT-A when compared with the VRMSD between ERAi and HSCAT-A, displayed in Fig. 4.5.

4.1.3 U10S spectra

The verification against independent scatterometer data presented in the previous section shows a significant reduction of model errors, in particular when complementary scatterometer data are used to correct the U10S in the tropics. These findings support that overall most of the high frequency signal observed in the qualitative assessment of the derived ERA* maps (discussed in section 4.1.1) is dominated by true ocean-related wind signal rather than by noise.

In this section, the derived ERA* U10S fields are assessed in terms of their geophysical consistency and effective resolution, using spectral analysis. Note that only the results for the zonal U10S component are shown, but the same conclusions can be drawn for the meridional component.

In line with Vogelzang et al. (2011a), to obtain the U10S spectra, valid samples of the U10S components are collected over a month (January 2013) in the HSCAT-A along-track direction for each across-track wind vector cell (WVC). To comply with the assumption of periodicity imposed when using FFT, a linear transformation detrending method is applied to the samples. Figure 4.6 shows the final spectra, i.e., the individual spectra averaged over all WVC numbers across the swath and over the mentioned time period. Overall, for HSCAT-A, 1374 (7455) individual spectra were averaged in the tropics (extra-tropics). Likewise, for ASCAT-B we average 23812 (72807) individual spectra. The substantially larger number of individual spectra used for ASCAT-B with respect to HSCAT-A is due to the much lower QC rejection rate in rainy areas of ASCAT-B (see section 2.1). Note that the SC field contains both ascending and descending passes and hence many swath edges implied in ERA* cross the HSCAT-A samples, potentially causing a white noise (flat) spectrum tail when insufficiently sampled.

In particular, this Figure shows the spectra for the zonal U10S component (u) in the tropics (Fig. 4.6a) and the middle latitude (Fig. 4.6b) for a fixed combination of scatterometers (i.e., ASCAT-A, ASCAT-B, and OSCAT-1) and for various temporal window sizes (see the last row of Table 4.1).

The solid lines show the model U10S spectra for the same sample length (128) as those collected for the HSCAT-A data (dashed blue), while for the ASCAT-B 12.5 km (dashed purple) a sample size of length 256 is used. The red solid line shows the ERAi spectrum, while the different ERA* configurations (sorted as in the last row of Table 4.1) are shown in green, magenta, orange, cyan and brown. The black dashed line shows the spectral slope of $k^{-5/3}$ for comparison. Note that wave number spectra need periodicity and sufficient samples, which implies artificial numerical closure (Volgenzang, 2013). As such, data detrending and sampling can lead to vertical offsets in the spectra. In Fig. 4.6, the noticeable vertical offset between ASCAT-B and the other spectral curves is mainly due to sampling. That is, while HSCAT-A winds are collocated with both ERAi and ERA* winds, ASCAT-B winds are not (i.e., ASCAT-B and HSCAT-A orbits are rather complementary). Note that the swath width and QC differences between HSCAT-A and ASCAT-B lead to very different sampling patterns.

Globally, a spectral slope close to $k^{-5/3}$ is reported by Nastrom and Gage (1985) for aircraft wind measurements, and by Vogelzang et al. (2011a) for the ASCAT coastal U10S product at scales below 500 km, as they follow Kolmogorov 3D turbulent theory of the atmosphere. While a k^{-2} slope is referenced by several authors, among others, Patoux and Brown (2001) and Chelton et al. (2006), using QuikSCAT winds, i.e., a previously released instrument with a similar design to that of HSCAT.

The SC will at any instant amend the ERA spectrum to the projected scatterometer U10S turbulence spectrum. If this spectral correction would be the same and phase independent at every instant, then the SC would also have this spectrum, but at lower amplitude. In fact, after an infinite number of instances, the amplitude would converge to zero. However, random atmospheric 3D turbulence has a life cycle of only a few hours and therefore it's not likely captured by the SC and part of the unwanted instantaneous random weather contribution, and consequently not targeted by ERA*. However, wind features coupled to the ocean mesoscales will largely remain, as well as systematic ERAi flow errors, e.g., tied to the slower synoptic weather patterns and large-scale circulation errors (Belmonte Rivas and Stoffelen, 2019). As shown by Reynolds and Chelton (2010); Hoareau et al. (2018) the spectral slopes for oceanic turbulence tracers such as Sea Surface Temperature (SST) and Sea Surface Salinity (SSS) are typically between -1 and -3. Since oceanic turbulence is rather slowly evolving on scatterometer scales, it is assumed that the oceanic turbulence is well captured by the SC (i.e., oceanic features persist over a few days) and one expects gentler slopes in ERA* (i.e., more comparable to those of HSCAT-A or ASCAT-B winds) than in ERAi. This is in line with the spectral slopes shown in Fig. 4.6 for ASCAT-B (dashed purple) and HSCAT-A (dashed blue). Also, in line with the ECMWF spectra shown in Vogelzang et al. (2011a), the ERAi spectra present a steep slope at high frequencies, indicating a lack of spatial scales below 150 km in the model U10S.

The spectral slopes observed for the ERA* in Fig. 4.6 lay between those of ERAi and

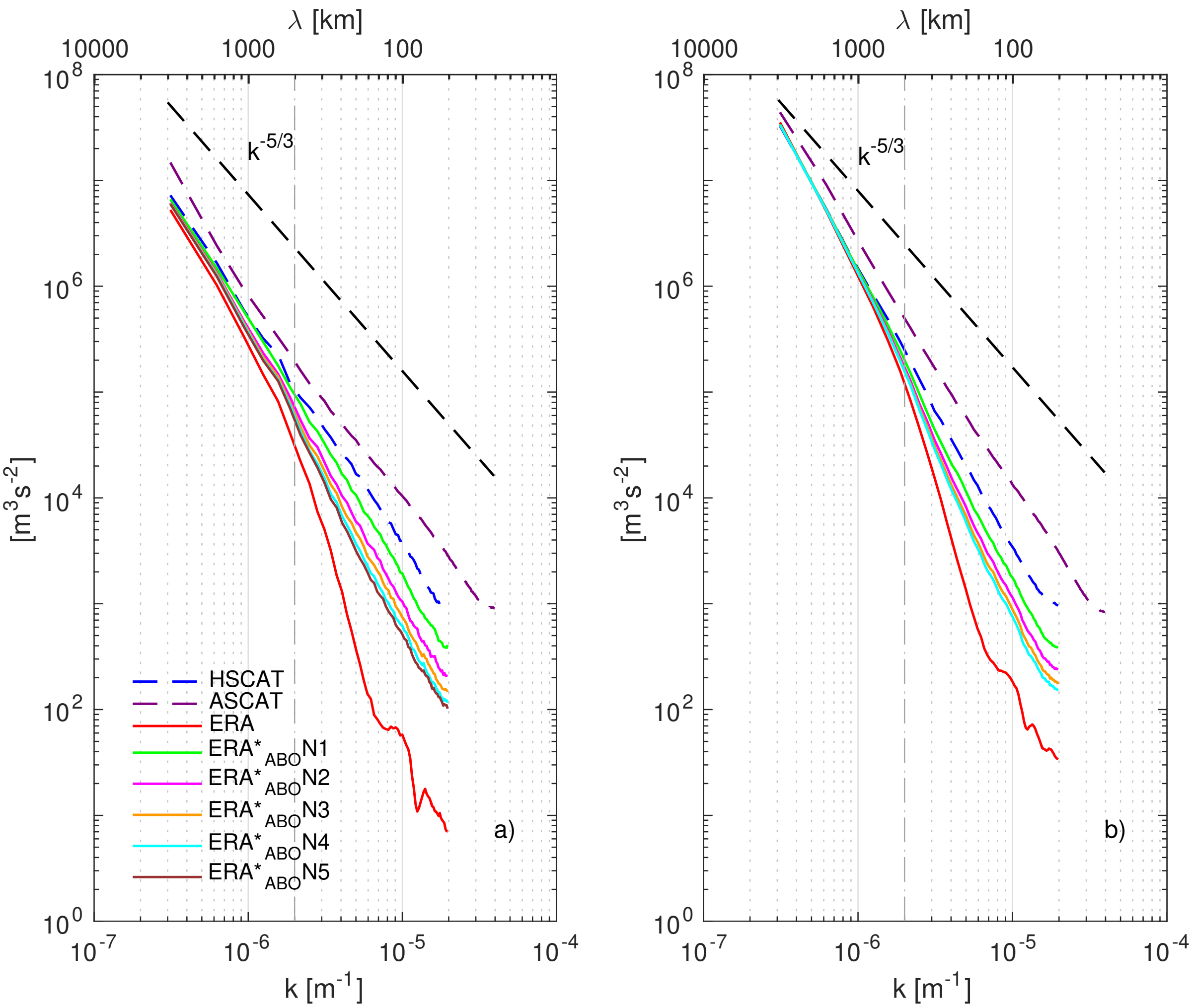

Figure 4.6: Power density spectra for the zonal U10S component (u) of HSCAT-A (dashed blue), ASCAT-B (dashed purple), and collocated ERAi (red) and ERA (see colour legend) products, in the tropics (a) and the middle latitudes (b). The ERA* products based on combined ASCAT-A, ASCAT-B and OSCAT (ABO notation) SC for different temporal windows are shown. The ERA$*_{ABO}$N notation from N1 to N5 corresponds respectively to SC temporal windows from 1 to 5 days (see Table 4.1). Figure included in Trindade et al. (2020).*

the scatterometers, in particular close to that of HSCAT-A, indicating that ERA* is able to resolve smaller scales than ERAi although the U10S fields are somewhat smoother than those of HSCAT-A and notably ASCAT-B. Note also that the shorter the temporal window used in ERA*, the closer the ERA* spectral slope is to that of HSCAT, i.e., a finer scale ERA* product is obtained showing more sampled 3D turbulence or weather, which is undesirable as noted above. However, following the verification carried out in section 4.1.2, we note that all SC substantially reduce the ERA*/HSCAT-A differences and hence are associated with persistent biases and not with random 3D atmospheric turbulence. Moreover, only a slight indication of a flat spectrum tail is noticeable at N1 (see green curve in Fig. 4.6b), which relates to the swath edge signatures. Following Fig. 4.5a, we note that part of the N1 SC variance is not justified, and better ERA* verification is obtained after 2 or 3 days. Seemingly, a small part of the fast and random $k^{-5/3}$ 3D turbulence and convection is present as sampling noise.

Furthermore, the smoothness observed in the derived map of Fig. 4.4c with respect to that of Fig. 4.4b is in agreement with their corresponding spectral slopes in Fig. 4.6a (i.e., the steeper orange curve with respect to the green solid curve).

The dependence of the spectral slope on spatial sampling is analysed in Fig. 4.7. The spectra for the zonal wind component (u) are displayed for a fixed time window with different combinations of scatterometers, as listed in the first column of Table 4.1, alongside HSCAT-A (dashed blue) and ERAi (solid red) spectra. As the number of scatterometers used in the corrections increases, the corresponding ERA* spectral slope becomes steeper, i.e., the derived U10S fields become smoother. Seemingly, the scatterometer wind aggregation procedure improves the bias estimate, while the shorter scales may also be less persistent than the larger scales. Furthermore, when OSCAT-1 U10S are aggregated to the ASCAT-based corrections, there is a marked decrease of the spectral slope (see change from the pink to the light-blue curve on Fig. 4.7b), i.e., the ERA* field becomes significantly smoother. This is due to the fact that the ASCAT-A and -B winds overlap in space and time on the weather scale and since OSCAT-1 winds are of lower resolution than ASCAT winds (Vogelzang et al., 2011a). In any case, by comparing Figs. 4.5a, 4.6 and 4.7, it is clear that both the size of the temporal window and the number and type of scatterometers used can have a pronounced effect on the spectral slope and quality of the ERA* product.

Note also that whether we fix the number of scatterometers (Fig. 4.6) or the time window (Fig. 4.7), the spectra in the middle latitudes are more energetic at small wave numbers than those in the tropics. Despite the presence of transient large-scale systems, still the same conclusions can be drawn in terms of spectral slopes. The exception is found for the ERA*$_A$N1 product spectra, which at mid-latitudes are slightly less steep than that of HSCAT-A. This is a very energetic region characterized by the presence of fast evolving systems, in which a product configuration using a single scatterometer for a one day mean correction is likely to also be affected by the previously mentioned weather sampling artifacts.

In order to correct for persistent model biases at the oceanic mesoscale, the accumulation time window is strictly dependent on the longevity of such biases. In that sense, from the geophysical perspective, taking into consideration the spectral analysis presented here, the relatively high VRMSD values for ERA*$_A$N1 or ERA*$_A$N2 shown in Fig. 4.5a indicate that the high-frequency variance depicted by spectral analysis is dominated by weather sampling artifacts rather than by ocean-related small-scale wind signal, particularly for the middle latitudes. Additionally, the same statistics suggest that for ERA*$_{ABO}$N1 the significant reduction of the local biases is at odds with the observed shallow spectral slopes (comparable to those of HSCAT-A, measuring 3D turbulence due to weather), and where a visual inspection of the derived maps indeed reveals the presence of swath-generated artifacts likely due to relatively poor scatterometer weather averaging. A reasonable trade-off between the spatial/temporal sampling and the accuracy/consistency of the derived maps is the ERA* based on a 2-3 days (N2 or N3) time window for ERA*$_{ABO}$, while longer windows are necessary for fewer scatterometers.

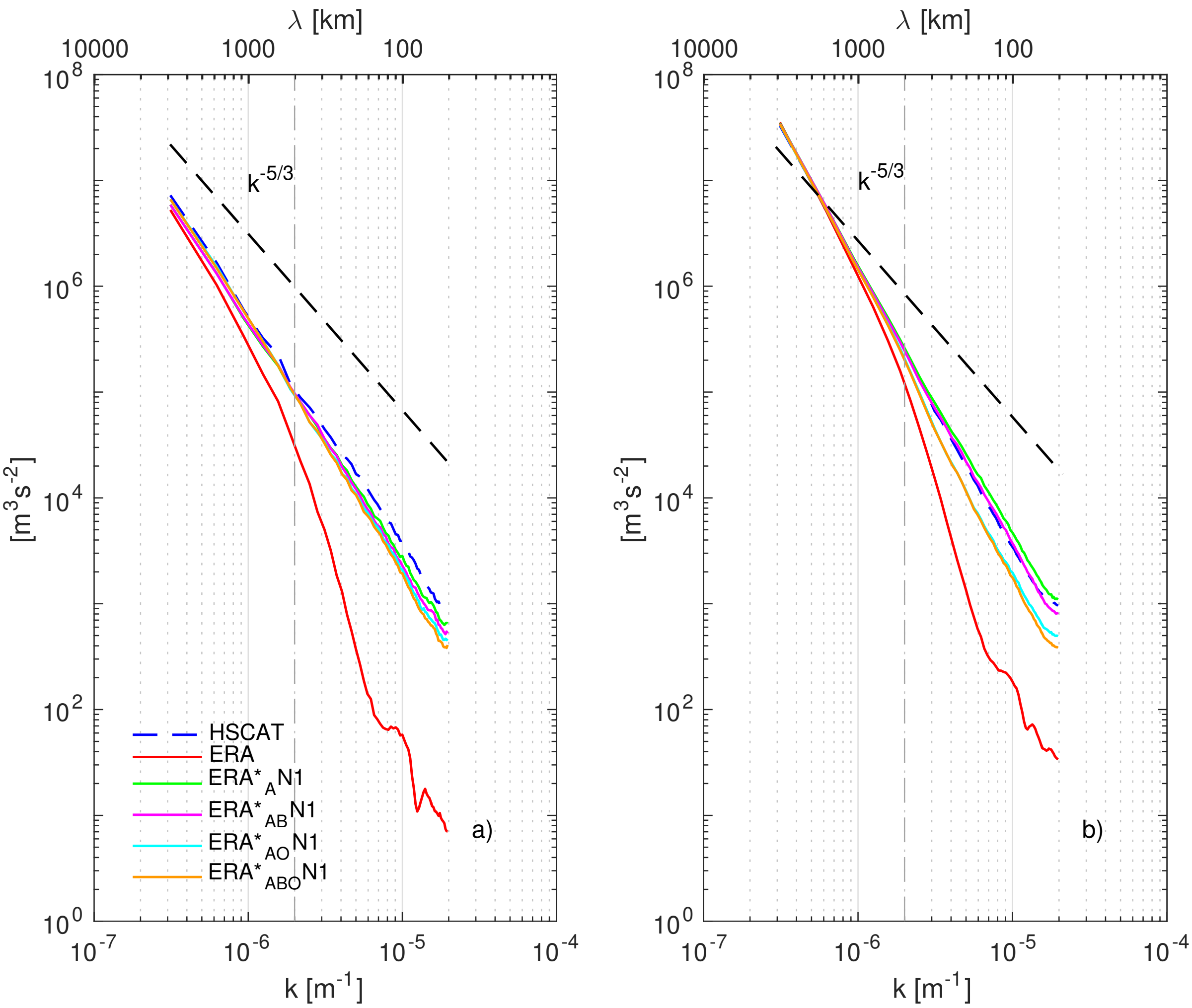

Figure 4.7: Power density spectra for the zonal U10S component (u) of HSCAT-A (dashed blue) and collocated ERAi (red) and ERA (see colour legend) products, in the tropics (a) and the middle latitudes (b). The different ERA* configurations shown here use a one-day SC temporal window (see notation in Table 4.1). Figure included in Trindade et al. (2020).*

4.2 Transition to ERA5

Considering the ERA* potential for improving ocean forcing established in the previous section, with the availability of ECMWF ERA5 reanalysis, which according to Belmonte Rivas and Stoffelen (2019) contains similar error characteristics as those found in ERAi, it is pertinent to assess the quality of a new ERA*, generated with the ERA5 reanalysis. Still the authors make note that those errors show smaller amplitudes for ERA5 than previously seen in ERAi. The latter is clear from observing Fig. 4.8 that shows the 30-d U10S differences for the meridional component between these reanalyses and the ASCAT-A scatterometer, respectively for ERAi/ASCAT-A in Fig. 4.8a and ERA5/ASCAT-A in Fig. 4.8b.

To this end, the next subsection (4.2.1) compares the two versions of the ERA* product using the year 2013 as reference, i.e., the quality of the ERAi-corrected and ERA5-corrected U10S is evaluated with respect to each other, such that it's possible to understand how smaller bias amplitudes may affect the effectiveness of this method. A thorough validation of the ERA5-

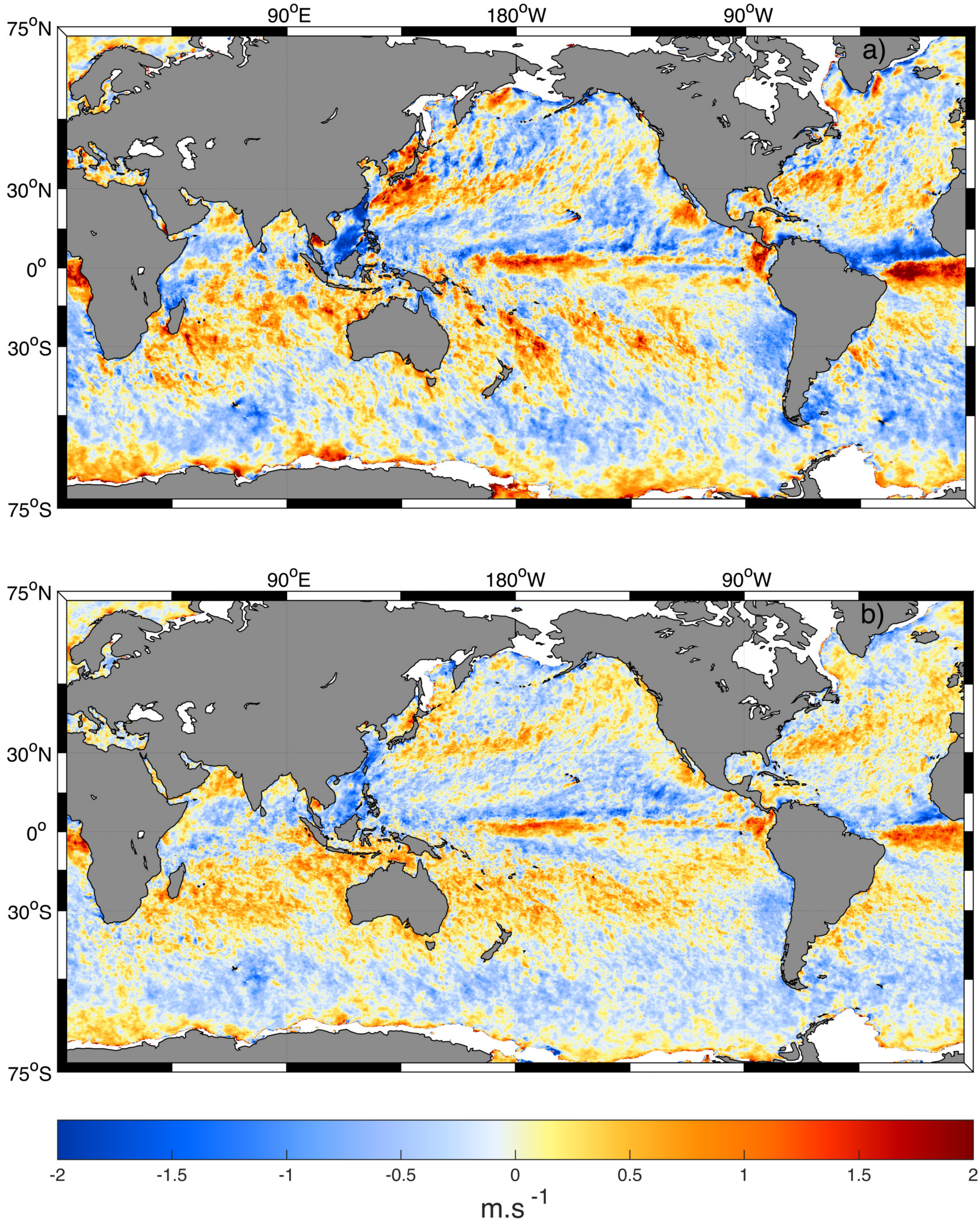

Figure 4.8: Scatterometer Correction (SC) for a given day, i.e., 15^{th} Fenbruary 2013. Collocated differences between ASCAT-A (12.5 km) and ERAi U10S (a) and ERA5 U10S (b) for the meridional wind component, accumulated over a 30-day temporal window centered around 06 UTC. The colors represent the differences in $m.s^{-1}$ (see color scale).

corrected ERA* using the same verification methodology as in Trindade et al. (2020) (see Chapter 2) is applied to the new ERA* configurations generated for 2013.

Subsection 4.2.2 evaluates configurations of the ERA5-corrected ERA* for 2019. In 2019, five complementary sun-synchronous scatterometers were in orbit allowing for the assessment of the effects of a dense global coverage in the ERA* approach, and making this year the ideal test bed to further improve the algorithm. Moreover, to add to the configurations explored in earlier sections of this manuscript, during 2019 temporal windows longer than 5 days are also analysed. This is done to check the temporal persistence of the local biases assumed in ERA5 U10S fields. While for longer time windows, a better scatterometer sampling is achieved, the performance of ERA* will rely on the persistence of such systematic errors. As such, the trade-off between sampling and local bias persistence is further analyzed with longer temporal windows.

4.2.1 ERA5-corrected ERA* for 2013

Although ERAi presents larger local biases than ERA5 (about 25% larger), as already mentioned, those have similar spatial and temporal characteristics. Thus, comparing the optimal ERA* configuration obtained from correcting the ERAi reanalysis, in 2013, to the new ERA5-corrected version of the product, helps evaluate the performance of the algorithm with the change (upgrade) of NWP reanalysis.

Fig. 4.9 shows an ERA5 U10S global map (4.9a) and its corresponding ERA* (4.9b) generated with a three-scatterometer based correction (i.e., ASCAT-A/B, and OSCAT-1) over a three-day temporal window (ERA$^*_{ABO}$N3). By simply comparing ERA5 and ERA$*_{ABO}$N3 U10S global maps, it is clear that both fields present similar weather features, not surprising since the ERA* does not aim at correcting transient weather effects but local systematic effects. Moreover, the U10S fields presented here correspond to the same snapshots as in Fig. 4.3 (15*th* January 2013 at 06 UTC). A quick look at the ERA5 and the ERAi (in 4.3a) already shows the higher effective spatial resolution of the former, the latter showing a smoother U10S. Also, as for the 1-day product in 4.3b, the ERA5-corrected ERA$*_{ABC}$N3 contains additional small-scale variance when compared with ERA5, i.e., Fig. 4.9a is smoother than Fig. 4.9b, notably at the same locations where larger local biases emerge in Fig. 4.8b, although such biases are not as evident (strong) for the ERA5-corrected U10s as for the ERAi-corrected ERA* (see Fig 4.8). Indeed, similar to the ERAi case, the ERA5 in Fig. 4.9a differs from the ERA5-corrected in Fig. 4.9b in that the increased variability seen in the latter should, inter alia, better capture the stationary signal from WBCS, the wind shadowing effects in the vicinity of islands, and the coastal effects associated to coastal orography.

Because it is difficult to appreciate the small scale added variance for a global map, focus is put on the tropical Atlantic region delimited by the red boxes in 4.9, and the zoomed area is shown in Fig. 4.10. In accordance with the ERAi corrected results from the previous chapter, for the three scatterometer and three-day TW configuration (Fig. 4.10b), the same increased wind variability (w.r.t. the NWP) is found south of the West African coast, yet not present in the ERA5 (Fig. 4.10a). The difference between the ERA5 and the corrected-ERA5 (ERA$*_{ABO}$N3) is shown in Fig. 4.10c, where the larger variability is clearly located at the equatorial band. As

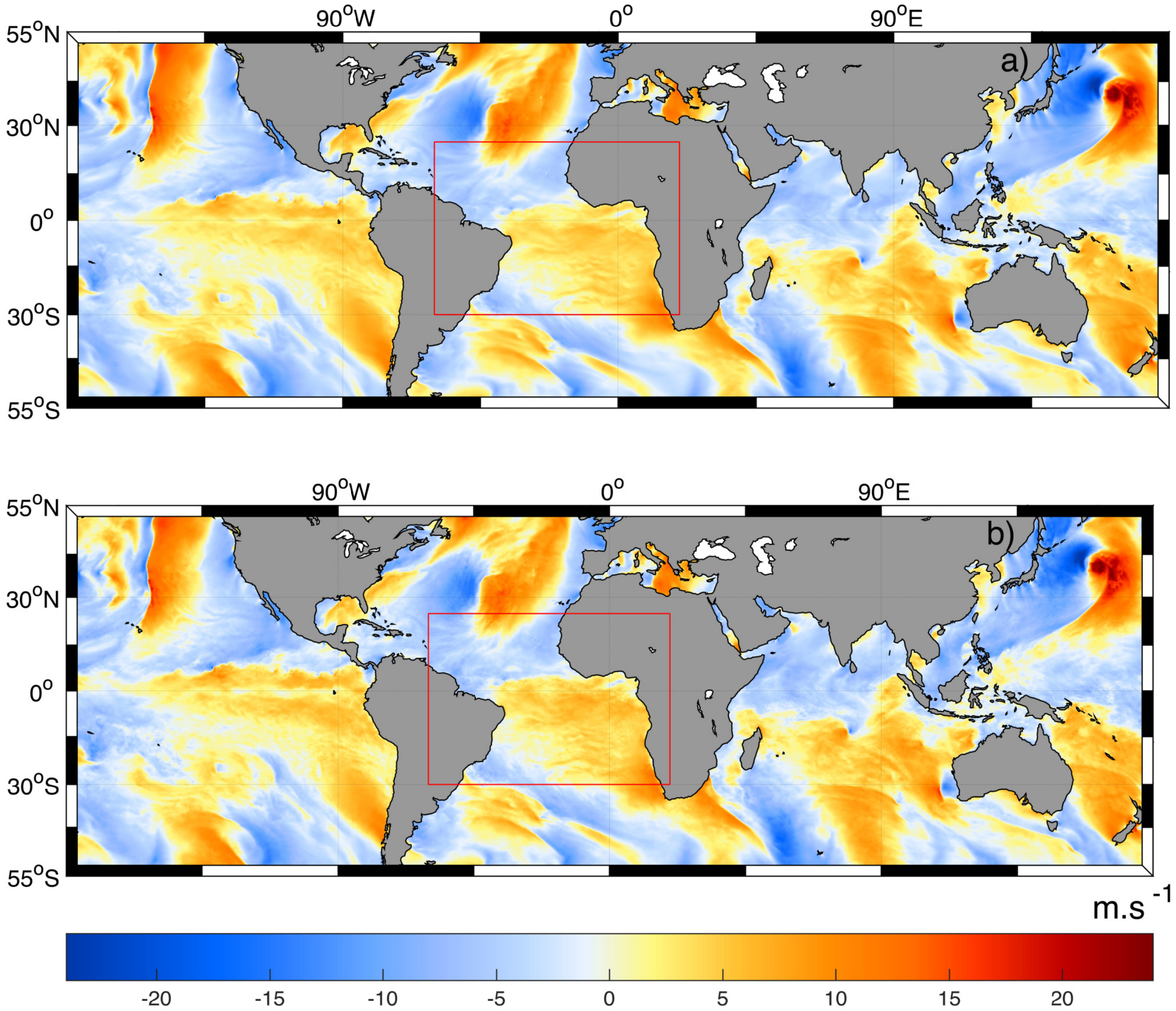

Figure 4.9: U10S meridional component for ERA5 in (a) and its corresponding ERA$_{ABO}$N3 in (b) on the 15th January 2013 at 06 UTC. The red box indicates the area shown in Fig. 4.10.*

previously mentioned, over this region, the increase in variability may arguably be caused by moist convection, sensed by the scatterometers that well resolve updrafts and downdrafts, despite that, the ERA*$_{ABO}$N3 is not expected to properly capture the small-scale variability associated with relatively fast evolving atmospheric phenomena, given the scales of these phenomena (with local wind changes up to 15 $m.s^{-1}$ over a 30 minute window) and the three-day TW used in the SC (thus aliasing the weather effects). Although not shown, when using smaller TWs of 1 day in the SC to correct the ERA5 U10S, swath-based artifacts as those present in Fig. 4.4b are also present in the new version of ERA*. Overall, the qualitative assessment of the new ERA5 corrected U10s maps, and alike the previously generated L4 product, i.e., the ERAi corrected product, suggests that additional small scale variance w.r.t. ERA5 is found in the corrected U10S fields, which correspond to persistent mesoscale (ocean) variability.

Evidence in Trindade et al. (2020), alongside the increased variance seen in the meridional U10S maps just discussed, suggests smaller error reduction in ERA5-corrected U10S w.r.t. ERA5

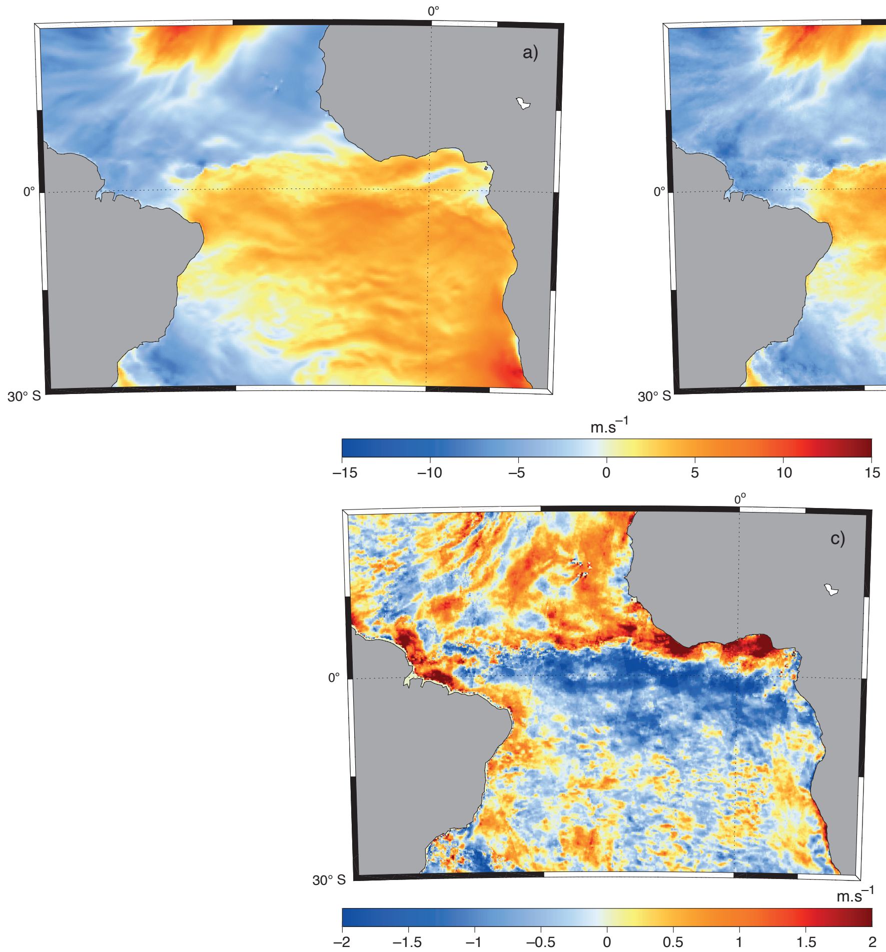

Figure 4.10: U10S meridional component over the West African coast for the ERA5 in (a) and ERA in(b) products shown in Fig. 4.9 (see red box). The ERA* shown in (c) is the difference between that in (a) and that on (b). The winds in (a) and (b) are truncated beyond [-15 15] m.s^{-1} to better highlight the differences, whilst (c) saturates those differences between ± 2 m.s^{-1}.*

than previously observed in ERAi-corrected ERA* U10S w.r.t. ERAi, due to the smaller amplitude of the observed biases for the ERA5 reanalysis. This assumption is further investigated by quantifying this reduction using an independent verification source, namely HSCAT-A, in a likewise manner as for ERAi-corrected ERA* products.

Because the effective change in the product is related to the ERA wind source only, the premise that the HSCAT-A is a good wind reference is also valid now. However, the aim of this section is to assess the most relevant changes in the performance of the ERA* with the transition to the new ERA5 reanalysis. As such, only the ERA5-corrected results for what is considered the optimal ERAi-corrected *ERA** configuration in 2013, i.e., three scatterometers and a three-day TW, are shown here.

Fig. 4.11 shows the time series of the daily vector root-mean-square difference (VRMSD) between the ERA5/ERA5-corrected (ERA$*_{ABO}$N3) and HSCAT-A U10S, for the global ocean (Fig. 4.11a), the middle latitudes (Fig. 4.11b), and the tropics (Fig. 4.11c). The VRMSD between ERA5 and HSCAT-A is represented with the black line, and represents the benchmark,

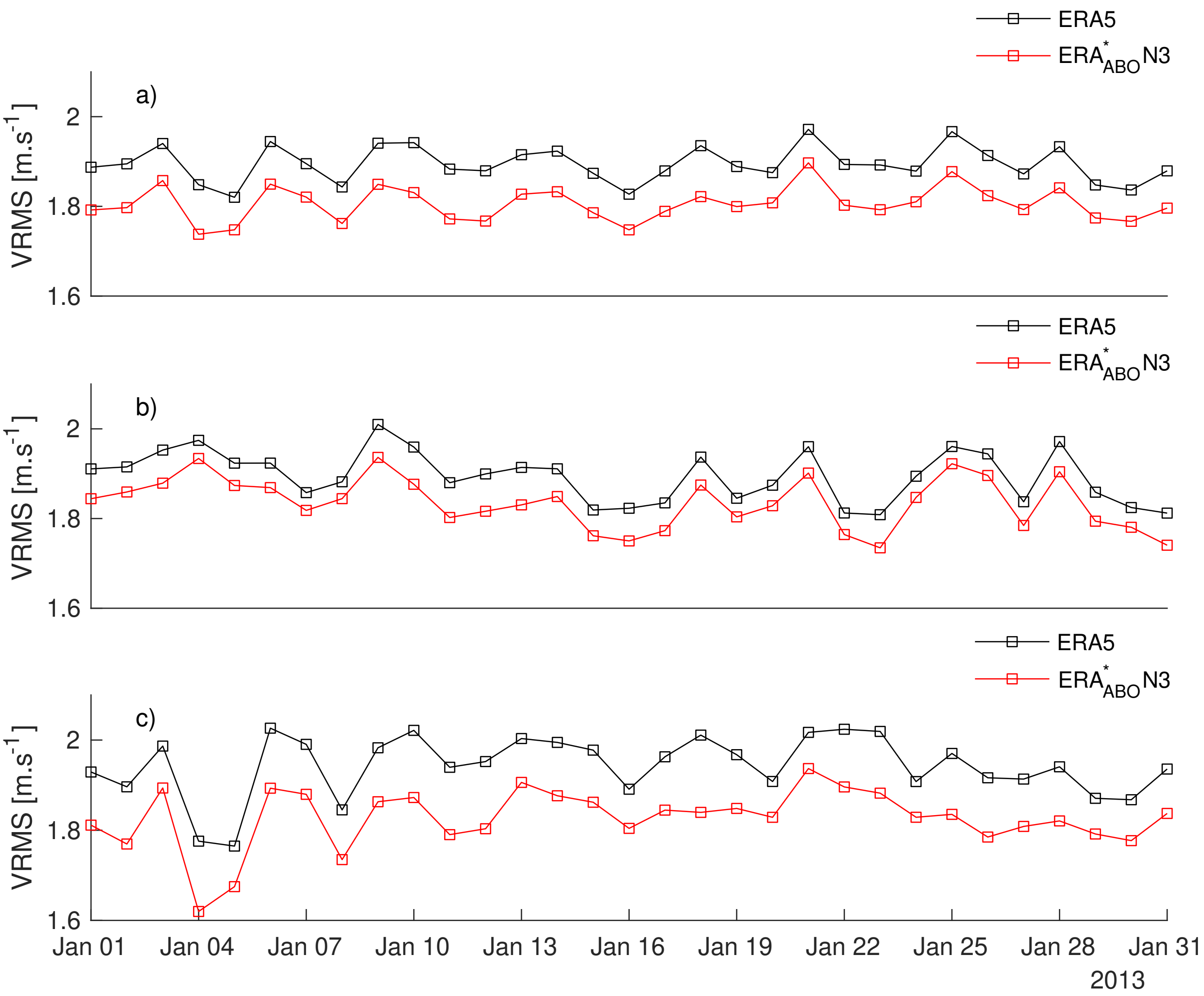

Figure 4.11: Daily vector root mean square difference (VRMSD in m.s^{-1}) between different ERA5/ERA$^*{}_{ABO}$N3 U10S product and HSCAT-A U10S over a month period (January 2013), for the global ocean (a), the middle latitudes (b), and the tropics (c). Values are plotted in black for ERA5 and in red for ERA.*

whilst the ERA* is plotted with a red line. For the analysed ERA* configuration, the generated product outperforms the ERA5 throughout the selected month, i.e., the red line is always below the black line thus of higher quality than ERA5 (with respect to HSCAT-A). Recall the limits of these geographical regions were defined in Table 2.2 as between [-55 55]° for the middle latitudes and [-30 30]° for the tropics. Note that, for all regions, the ERA5 reanalysis always shows a smaller vector error than ERAi (Fig. 4.5) w.r.t to HSCAT-A, indicating the overall higher quality of the ERA5 w.r.t. ERAi U10S. Note though that there are a few differences between both error assessments, specifically in what concerns the analysed period, and in the separation of the estimated errors in ascending and descending orbits of the scatterometer reference. Despite that, the benchmark value in Fig. 4.11 is always smaller than in Fig. 4.5, and the ascending and descending orbits follow the same trend, thus making the comparison hold.

Although the error reduction of ERA5-corrected w.r.t. ERA5 U10S is not as substantial as it is for the ERAi-corrected U10S, ERA5 errors are still significantly reduced with the proposed methodology. Furthermore, larger error variance reduction w.r.t. the benchmark is still observed for the tropical band (13%) than for the middle latitudes (about 7%). As shown in Trindade et al. (2020), the mid-latitude local biases seem to be less persistent than those in the tropics. Arguably due to the impact of evolving weather patterns, mid-latitude U10S biases evolve too.

In brief, the ERA$*_{ABO}$N3 configuration (i.e., three complementary scatterometers accumulated over a three-day TW) shows promising results whether generated by correcting the ERAi or ERA5 U10S, i.e., it always outperforms the original NWP U10S. This ERA* configuration after the transition to the ERA5 still proves optimal for the year addressed in this section, given that it seems to avoid fast weather corrections, while it still captures the oceanic related mesoscales (further analysed next). Nevertheless, as reported by Belmonte Rivas and Stoffelen (2019), and verified by comparison to HSCAT-A, the amplitude of the model biases in ERA5 is smaller than that in ERAi (see benchmark values in Fig. 4.5 and Fig. 4.11), and the ERA5 U10S maps contain more variance (recall Fig. 4.9a) than that observed in the ERAi U10s. Overall, since the ERA5 local biases are smaller than those in ERAi, the proposed corrections lead to smaller error reduction rates for the ERA5-corrected ERA* (w.r.t. ERA5) than for the ERAi-corrected ERA* (w.r.t. ERAi).

So far, the results from this section align with those obtained with the ERAi-corrected version of the ERA*, suggesting the added variance observed in the qualitative assessment of the ERA5-corrected ERA* maps is also dominated by true ocean-related wind signal rather than by random noise. As with the ERAi-corrected ERA*, spectral analysis is again used to evaluate the geophysical consistency of the new ERA* derived U10S, as well as the effective resolution of the generated U10S in the ERA$*_{ABO}$N3 configuration.

The spectral analysis is performed as explained in 2.4.2, and separately for the tropics and the middle latitudes, respectively averaging over 1374 and 7455 individual spectra (using ERA5/ERA*/HSCAT-A collocations), as in subsection 4.1.3. Fig. 4.12 shows the final spectra, obtained by averaging the individual spectra over all WVC numbers across the swath for January 2013. For the sake of comparison, the total power density spectra are computed for both the ERA5 corrected ERA$*_{ABO}$N3 configuration and the ERA5. Notice only spectra for the zonal U10S component in the tropics (Fig. 4.12a) and the middle latitudes (Fig. 4.12b)) are shown, although the same conclusions apply to the meridional component. The solid lines show the ERA5 (red) and the ERA$*_{ABO}$N3 (blue) U10S spectra for the same sample length (128) as those collected for the HSCAT-A data (dashed pink). The black dashed line shows the spectral slope of $k^{-5/3}$ as energetic scale reference.

The spectral slope observed for the ERA$*_{ABO}$N3 in Fig. 4.12 lies between that of the ERA5 and HSCAT-A, but closer to that of the latter, confirming the analysed ERA* configuration is able to resolve smaller scales than ERA5, yet the new U10S fields are still smoother than those of the scatterometer. In comparison to the findings for the ERAi-corrected ERA* assessed in subsection 4.1.3, it is found that the ERA$*_{ABO}$N3 generated from the ERA5 reanalysis is able to resolve smaller scales than the same configuration for the former product version. This is in agreement with the gentler slopes found for the ERA5 w.r.t. those of ERAi (subsection 4.1.3, which supports that the former contains somewhat more small-scale variance than the latter. Also, as described in subsection 4.1.3, the spectra in the middle latitudes (Fig. 4.12b) are more

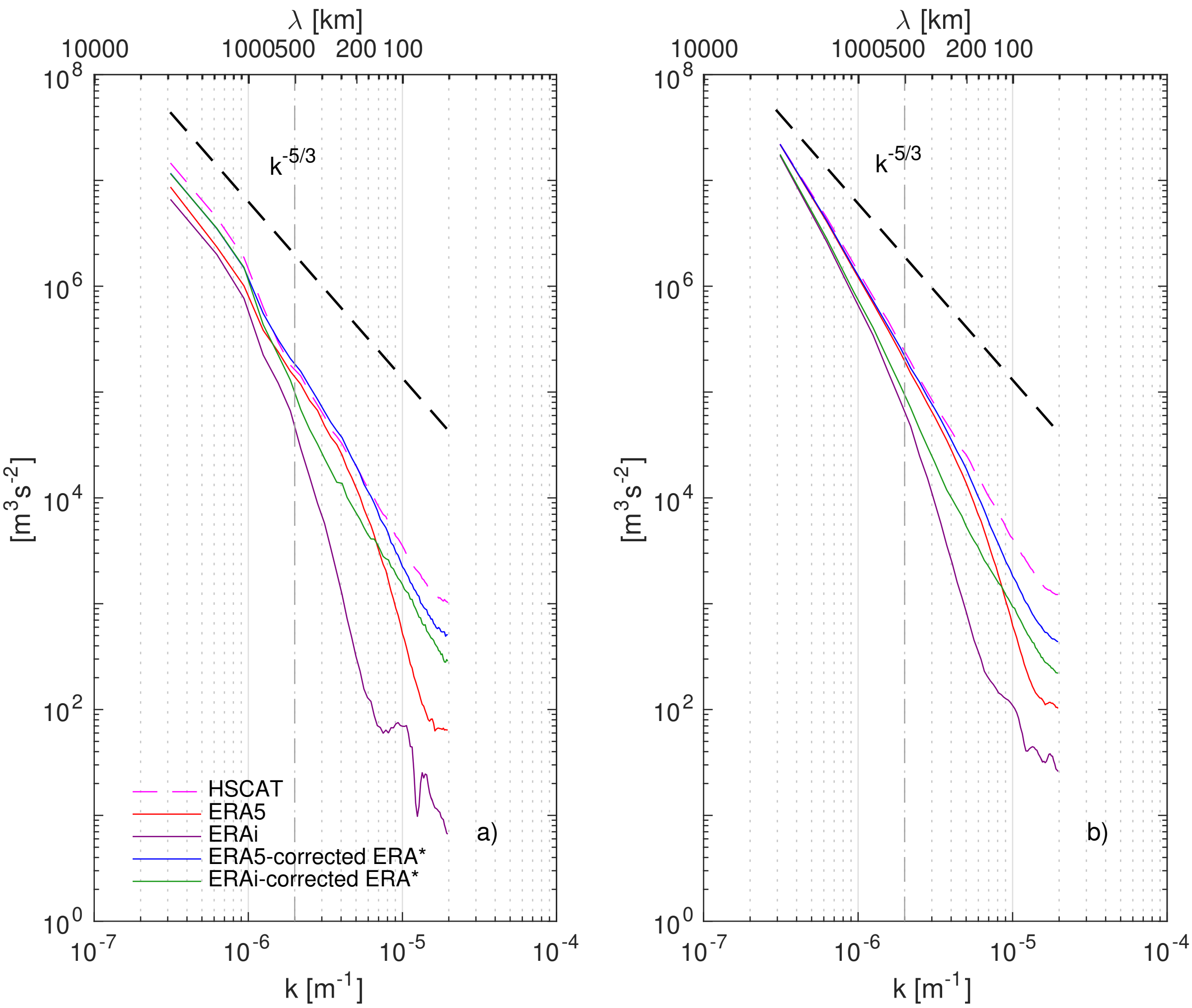

Figure 4.12: Power density spectra for the zonal U10S component (u) of HSCAT-A (dashed pink) and collocated ERA5 (red), ERAi (purple), ERA5-corrected (blue) and ERAi-corrected (green) for a SC generated with three scatterometers over a three-day TW (ERA$*_{ABO}$N3), in the tropics (a) and the middle latitudes (b).

energetic at higher wavelengths (i.e., lower frequencies) than those in the tropics, due to the presence of large-scale systems in the former. The same conclusions can be drawn in terms of spectral slopes.

In light of the validation results presented in here, using the recommended configuration for 2013 (section 4.1), it is found that the new ERA* (ERA5-corrected) is still able to reduce the model errors in this reanalysis in a similar manner it does for ERAi, although to a smaller extent, due to the smaller amplitude of the local biases. The spectra for ERA5 also reflects the evolution of the ECMWF model in time (ERA5 is an upgraded version of the ECMWF deterministic model, w.r.t. that of ERAi), proven to resolve much smaller scale variance than before. This is clear when comparing the slopes from both reanalyses, where the ERAi slope is much steeper than that of ERA5.

However, despite the evolution of theses biases (mostly in amplitude) and the change in variance, both reanalyses are still missing mesoscale variability. Consequently, as long as a complementary scatterometer constellation and a small enough TW size is used for the SC, the

Table 4.3: Notation for the different ERA configurations, according to the combination of sensors and temporal window (TW) used in the SC.*

	Temporal Window					
Data Source	1-d (N1)	3-d (N3)	5-d (N5)	10-d (N10)	15-d (N15)	30-d (N30)
ASCAT-A	$ERA*_{A}N1$	$ERA*_{A}N3$	$ERA*_{A}N5$	$ERA*_{A}N10$	$ERA*_{A}N15$	$ERA*_{A}N30$
ASCAT-A/B	$ERA*_{AB}N1$	$ERA*_{AB}N3$	$ERA*_{AB}N5$	$ERA*_{AB}N10$	$ERA*_{AB}N15$	$ERA*_{AB}N30$
ASCAT-A/B/C	$ERA*_{ABC}N1$	$ERA*_{ABC}N3$	$ERA*_{ABC}N5$	$ERA*_{ABC}N10$	$ERA*_{ABC}N15$	$ERA*_{ABC}N30$
ASCAT-A, OSCAT	$ERA*_{AO}N1$	$ERA*_{AO}N3$	$ERA*_{AO}N5$	$ERA*_{AO}N10$	$ERA*_{AO}N15$	$ERA*_{AO}N30$
ASCAT-A/B, OSCAT	$ERA*_{ABO}N1$	$ERA*_{ABO}N3$	$ERA*_{ABO}N5$	$ERA*_{ABO}N10$	$ERA*_{ABO}N15$	$ERA*_{ABO}N30$
ASCAT-A/B/C, OSCAT	$ERA*_{ABCO}N1$	$ERA*_{ABCO}N3$	$ERA*_{ABCO}N5$	$ERA*_{ABCO}N10$	$ERA*_{ABCO}N15$	$ERA*_{ABCO}N30$

ERA* is expected to indeed outperform the reanalysis.

4.2.2 Further improvements to the algorithm

In light of the results from the previous subsection (subsection 4.2.1), for simplicity, the ERA* notation is hereafter used for ERA5-corrected U10S, for the remaining of Chapter 4, with the exception of section 4.4 that considers the overall findings for generated ERAi-corrected and ERA5-corrected ERA* configurations.

In this section, several configurations of the ERA* are assessed for the year 2019. As already mentioned this period contains the largest scatterometer constellation of the decade, therefore the performance of these scatterometer combinations that result in enhanced spatial sampling can be checked. The notation for the latter is listed in Table 4.3. Specifically, four complementary scatterometers are combined in order to evaluate the effects of the denser sampling. These are the ASCAT's (A/B/C) and OSCAT-2, here briefly noted as OSCAT, given that it does not overlap in time with the OSCAT-1 (recall Table 1.2).

Next, the performance of these different configurations is analysed in the same way as before, although the verification against independent U10S sources is carried out using the HSCAT-B scatterometer, and an additional validation against buoy U10S is also conducted afterwards.

A first qualitative assessment of the local biases for 2019 is illustrated in Fig. 4.13, which shows the snapshot of a thirty-day accumulation for a few combinations of scatterometer/ERA5 U10S differences for a specific forecast time. Contrary to previous analyses, the global domain under evaluation is extended to [-75 75]$°N$, such that high latitudes are included in the product performance assessment. In this figure, and as previously reported for 2013, the magnitude of these biases is between ± 2 $m.s^{-1}$. Overall, because these model biases are still present in the ERA5 reanalysis (although of smaller amplitudes), they pop up in the same geographic locations as previously described in this manuscript, e.g., more noticeable over the major WBCS (high stationarity) and their surrounding eddies or where the model lacks mesoscale variability (like in the extra-tropics). Indeed, over longer TWs, looking at snapshots of the collocated differences between some of the scatterometer combinations in Table 4.3 and ERA5 (differences shown for the 06 UTC in Fig. 4.13), these local biases are spotted over the same areas, with similar amplitude. However, because the C-band retrievals (12.5 km) are of higher spatial resolution than those from the Ku-band OSCAT-2 (25 km), the SC displayed in Fig. 4.13b and 4.13d

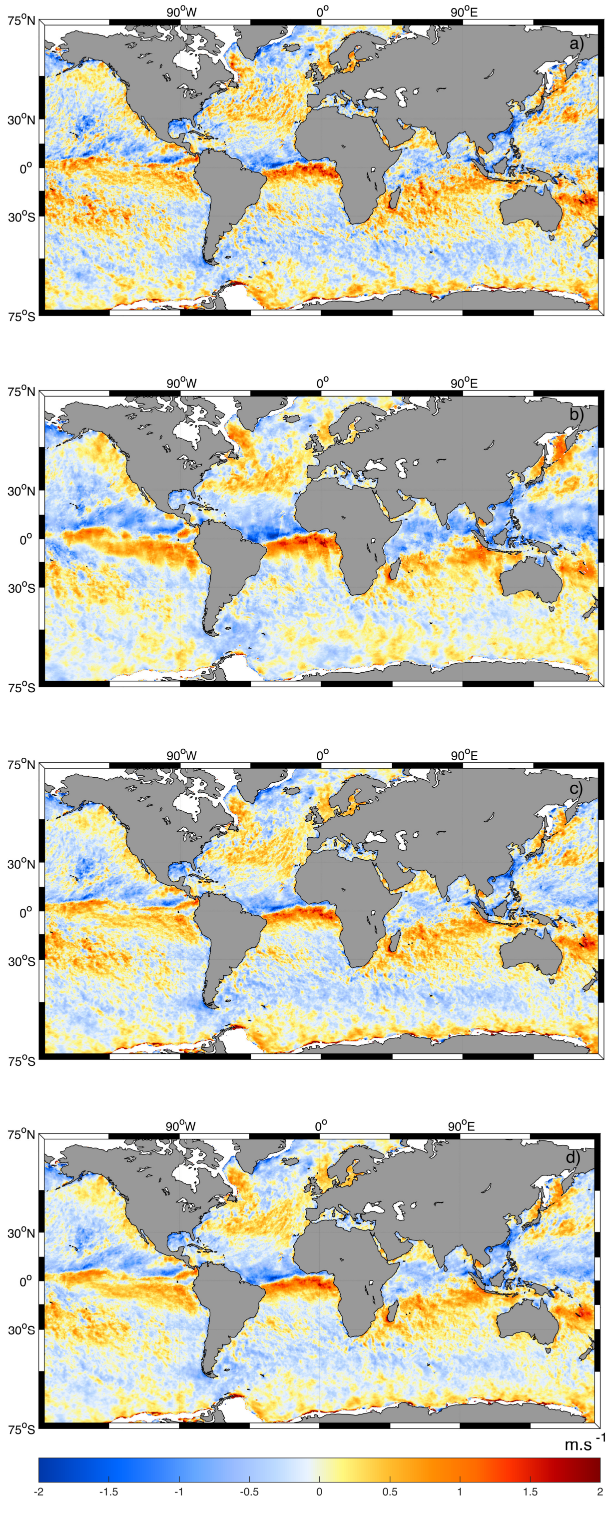

Figure 4.13: Scatterometer Correction (SC) for the meridional wind component on the 15th February 2019. Collocated differences of various scatterometer combinations and ERA5 U10S are accumulated over a thirty-day TW centered around 06 UTC. The colors represent the differences in m.s^{-1} (see color scale). The accumulated differences for the following scatterometer combinations are shown: ASCAT-A only (a), OSCAT-2 only (b), all ASCATs (c) and all ASCATs and OSCAT-2 (d).

appear to be slightly more smothered w.r.t the other two.

Since Fig. 4.13 shows that the differences between the scatterometers and the ERA5 are still present after thirty days, the derived U10S maps for ERA5 and the ERA$*_{ABCO}$N3 configuration are plotted in Fig. 4.14. The additional variance observed in the previous subsection is also evident for this configuration, as in all the configurations listed in Table 4.3 (not shown), indicative of persistent mesoscale (ocean) variability. Yet, because a three-day TW was previously found to best capture small oceanic-induced scales, the derived U10S map for ERA$*_{ABCO}$N3 is chosen to display the added variability under the improved coverage provided by the four scatterometers.

Considering that a three-day accumulation with sufficient scatterometer sampling has been proven to add small-scale variance to the corrected U10S, as expected, the meridional U10S component in Fig. 4.14a is smoother when compared to that of ERA$*_{ABCO}$N3 in Fig. 4.14b and more so at locations where larger local biases emerge. Recall from the previous analysis that this increased variability in the ERA* U10S reflects the stationary signal from WBCS, the wind shadowing effects in the vicinity of islands, and the coastal effects associated with coastal orography. Still, a closer look inside the area delimited by the red box for other TWs, helps to further examine the amount of variance introduced as a function of the accumulation.

Fig. 4.15 shows a zoom of the region inside the red box from Fig. 4.14. The U10S meridional component for the tropical Atlantic is shown for the ERA5 (Fig. 4.15a) and the SC used in ERA$*_{ABCO}$N3 (Fig. 4.15c). Additionally the same map is shown for a SC generated with a shorter temporal window of one day (Fig. 4.15b) and a longer one of fifteen days (Fig. 4.15d). Even though smoother ERA* U10S wind fields are observed as longer time windows are used to generate the SC (also seen in section 4.1), such smoothing is accompanied by the reduction of scatterometer weather sampling error. Furthermore,the SC for ERA$*_{ABCO}$N1 is largely affected by swath edge artifacts which, considering the shorter temporal windows, are a consequence of poorer sampling. This is in line with previous results, and likely indicates that the SC of ERA$*_{ABCO}$N1 (Fig. 4.15b) captures small-scale variability associated with relatively fast evolving atmospheric phenomena, while the others in Fig. 4.15cd do not.

Consequently, these small-amplitude “jumps” or artifacts (see, e.g., several straight lines in the top-left quadrant of Fig. 4.15b), are hardly visible in the other SC configurations (see Fig. 4.15cd). Again, these artifacts are associated with the edges of the different scatterometer swaths used, and show up due to the poorer scatterometer weather sampling at these latitudes, thus more noticeable for one-day corrections than for longer TW sizes.

Granted that the qualitative assessment of the derived U10S fields continues to show additional variance with respect to ERA5 which, although smoothed, is also observed in the longer TWs (N15 and N30) and with more scatterometer coverage (ABCO), the statistical analysis presented next is meant to check whether the additional variability is dominated by true wind signal rather than noise. The analysis uses the VRMSD with respect to the HSCAT-B scatterometer to evaluate model error reduction.

Alike HSCAT-A, HSCAT-B also passes at (6 am/6 pm), a very different equator crossing time from that of the instruments used to correct the ERA5 fields, thus making it a good independent verification source. Recall that, for the instruments used for the configurations in

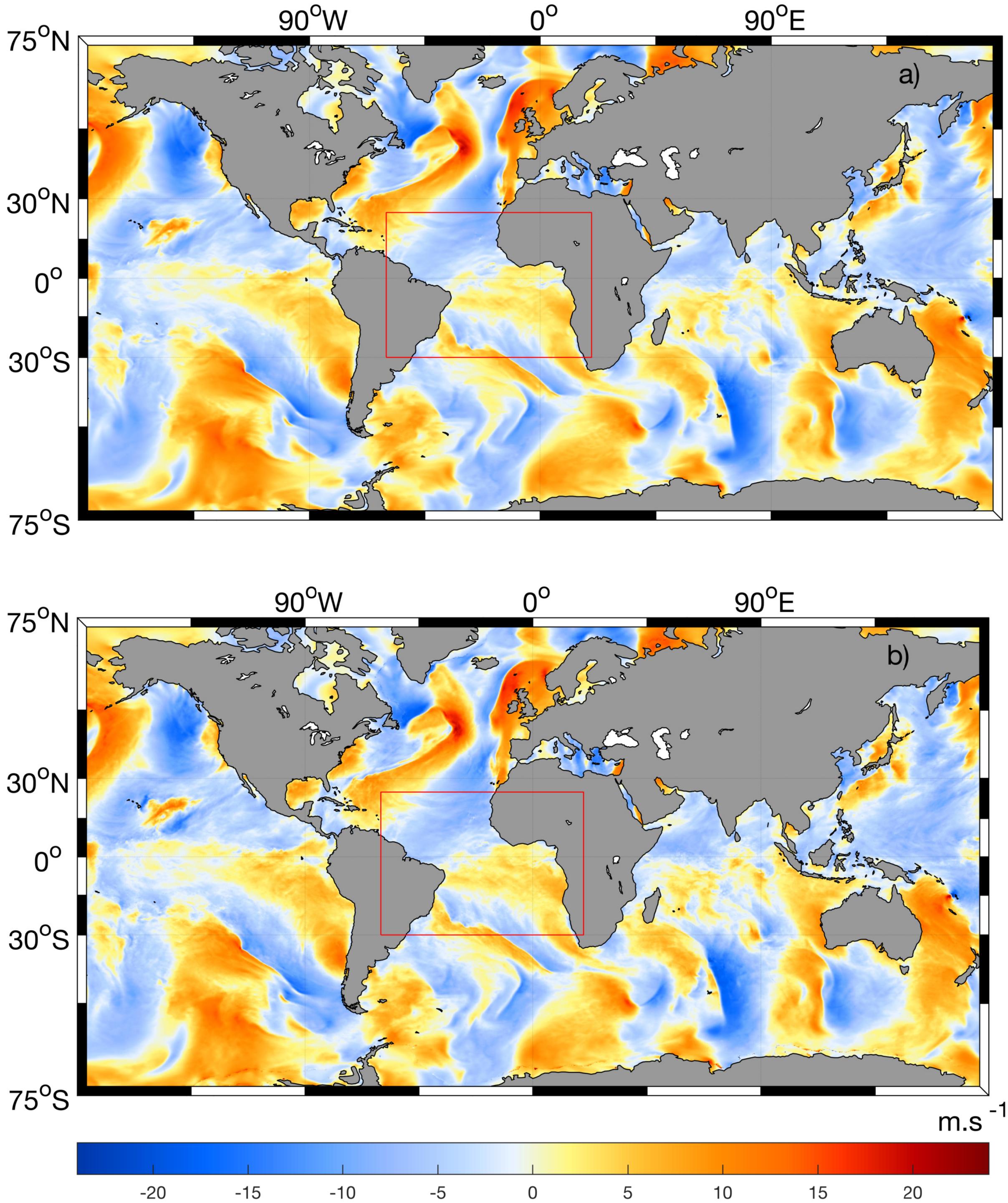

Figure 4.14: U10S meridional component for ERA5 (a) and ERA$_{ABCO}$N3 (b) on the 15th February 2019 at 09 UTC. The red box indicates the area shown in Fig. 4.15.*

Table 4.3, the respective LTAN is at 9:30 pm for the ASCATs while OSCAT-2 passes are at 8:45 am/8:45 pm. Like wit OSCAT-1, the scatterometer passes for the ASCAT-A/B/C and OSCAT-2 are too close in time (only 45 min difference in this case) to capture the diurnal cycle,

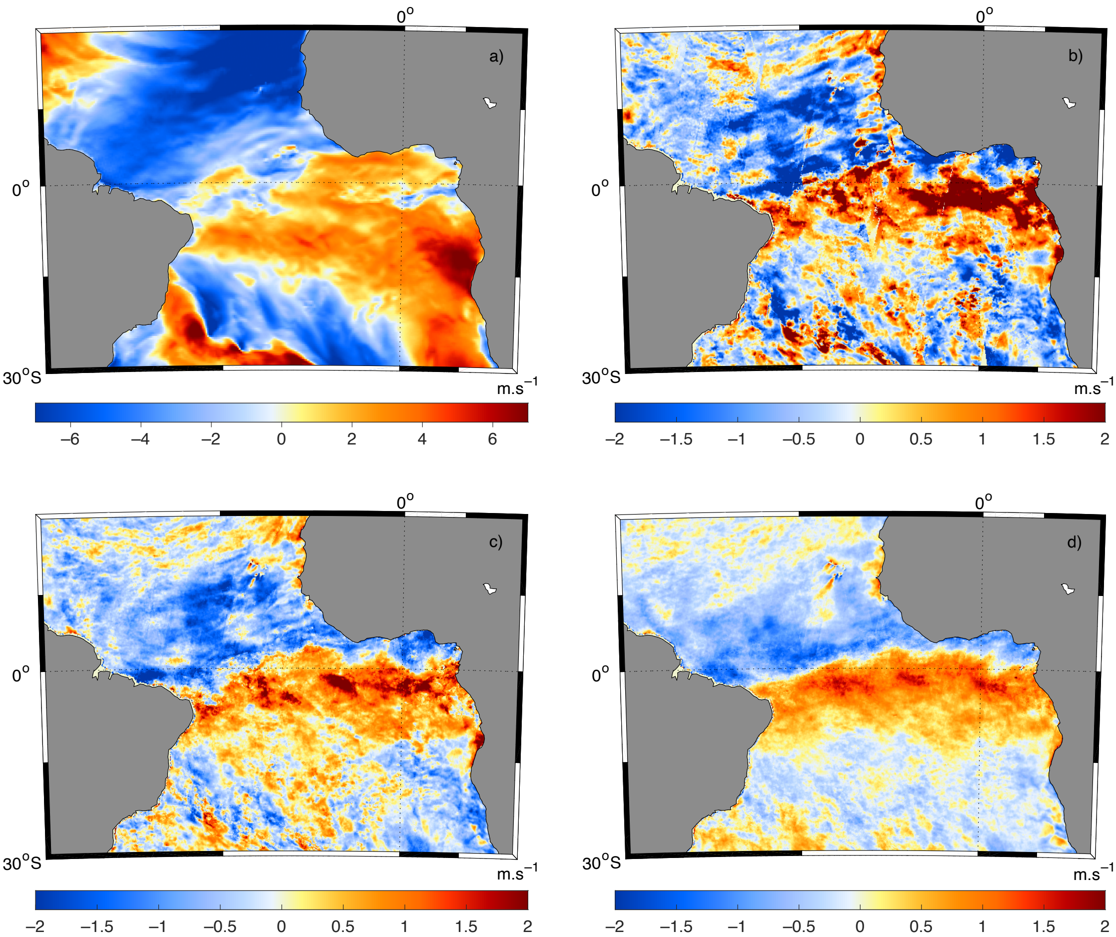

Figure 4.15: U10S meridional component over the West African coast for the ERA5 U10S (a) and different SC TW sizes combining all four scatterometers (ABCO): a one-day TW (N1) (b), a three-day TW (N3) (c), and a fifteen-day TW (N15) in (d). The winds are truncated beyond [-7, 7] m.s^{-1} for the ERA5 and between [-2, 2] m.s^{-1} for the SC. The zoomed region corresponds to the red box in Fig. 4.14.

in spite of the substantial increase in local sampling when used together. Despite that, assuming that local biases are persistent over longer periods, at HSCAT-B verification times (3:30 and 2:45 hours apart from, respectively, ASCAT-A/B/C and OSCAT-2), the SC should lead to a reduction of model errors. Moreover, for local biases that persist for longer periods (a couple of days), resorting to SC with longer TWs assures better downsampling of the mesoscale weather variability (as opposed to using a one-day TW).

Fig. 4.16 shows the VRMSD for the ERA5 and several ERA* configurations with enhanced sampling (see legend) w.r.t. HSCAT-B U10S as a function of the TW size (in days), for the tropics (4.16a), the middle latitudes (4.16b), the high latitudes (4.16c and the global ocean (4.16d). Considering the ERA5 as the benchmark, only those ERA* configurations below the black line are of higher quality (with respect to HSCAT-B) than ERA5. The different geographical regions are defined in Table 2.2 which, as opposed to previous analyses, include the high latitudes.

Except for the high latitudes, all the ERA* configurations show improved performance with TW sizes larger than one day, with best performance achieved around 3-10 days. The worst

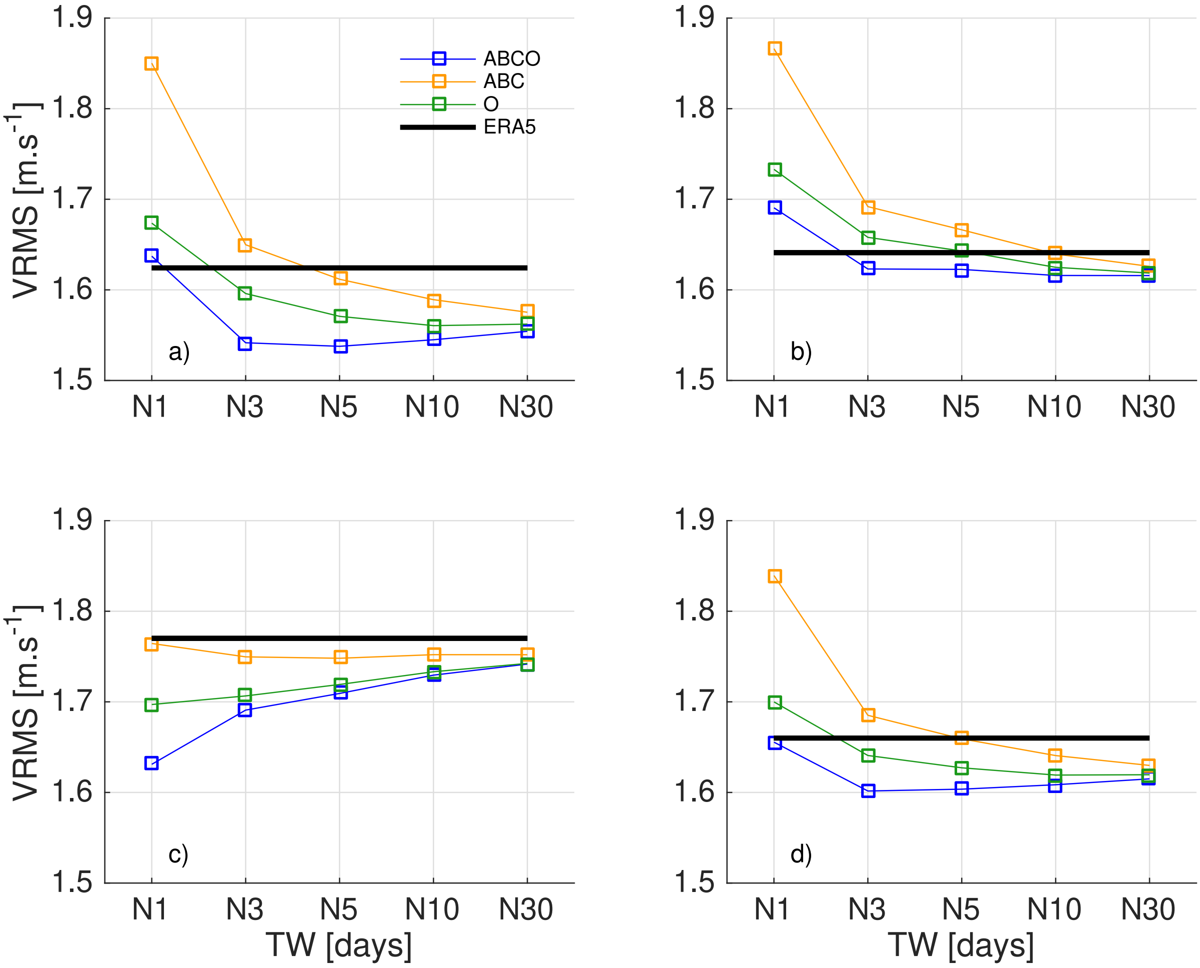

Figure 4.16: VRMSD (in m.s^{-1}) between different ERA5/ERA U10S products and HSCAT-B U10S as a function of the SC temporal window size, over a month period (February 2019), for the tropics (a), middle latitudes (b), high latitudes (c), and the global ocean (d). VRMSD scores for ERA5 are shown with black line in bold, and ERA* configuration for ASCAT-A/B/C, only OSCAT-2, and combining both ASCAT-A/B/C and OSCAT-2, are respectively shown in orange, green and blue. Figure included in Portabella et al. (2022).*

VRMSD values for N1 are in line with the already assumed poor weather downsampling of scatterometer data over short periods of time, such that larger temporal windows are required to reduce the model (transient) weather errors. Note the abrupt drop in VRMSD that occurs between the ERA* configuration of N1 and that of N3. In fact, to outperform ERA5 a 3-5 days TW (N3 or N5) is required, assuming enhanced scatterometer coverage is achieved over this period.

As expected, with the enhanced sampling that comes from combining all four scatterometers (ABCO), the model weather errors are considerably reduced at short temporal windows. The use of complementary scatterometer orbits in the corrections (see blue curves in Fig. 4.16) outperform ERA5 at N3 in all the regions. In fact, for ERA$*_{ABCO}$N3 configurations, the quality of the data does not significantly depend on the temporal window size when longer than N3, and only slightly degrades for N5-N30 (see e.g., blue curve on Fig 4.16d). This is probably due to a compensation effect: on the one hand, the larger the TW, the larger is the sampling; on the other hand, the larger the TW, the more sensitive the system is to local bias persistence.

Moreover, comparing the ERA5 quality (black solid line) against that of ERA*$_{ABCO}$ (blue curve) for the tropics (Fig. 4.16a) and the middle latitudes (Fig. 4.16b), the ability of the latter to outperform the former is much larger in the tropics. In particular, about 10% lower error variance (VRMSD^2 analogous to vector RMS error variance in Eq. 2.9) than ERA5 is found for ERA* in the tropics, while in the middle latitudes this reduction is only 2.5%. As shown in section 4.1 and 4.2.1, local biases in the middle latitudes seem to be less persistent than those in the tropics. This may be due to the slowly evolving (synoptic) weather in the middle latitudes by the ERA5, which might also evolve the MABL parameterization biases that are different in relatively warm and cold air masses.

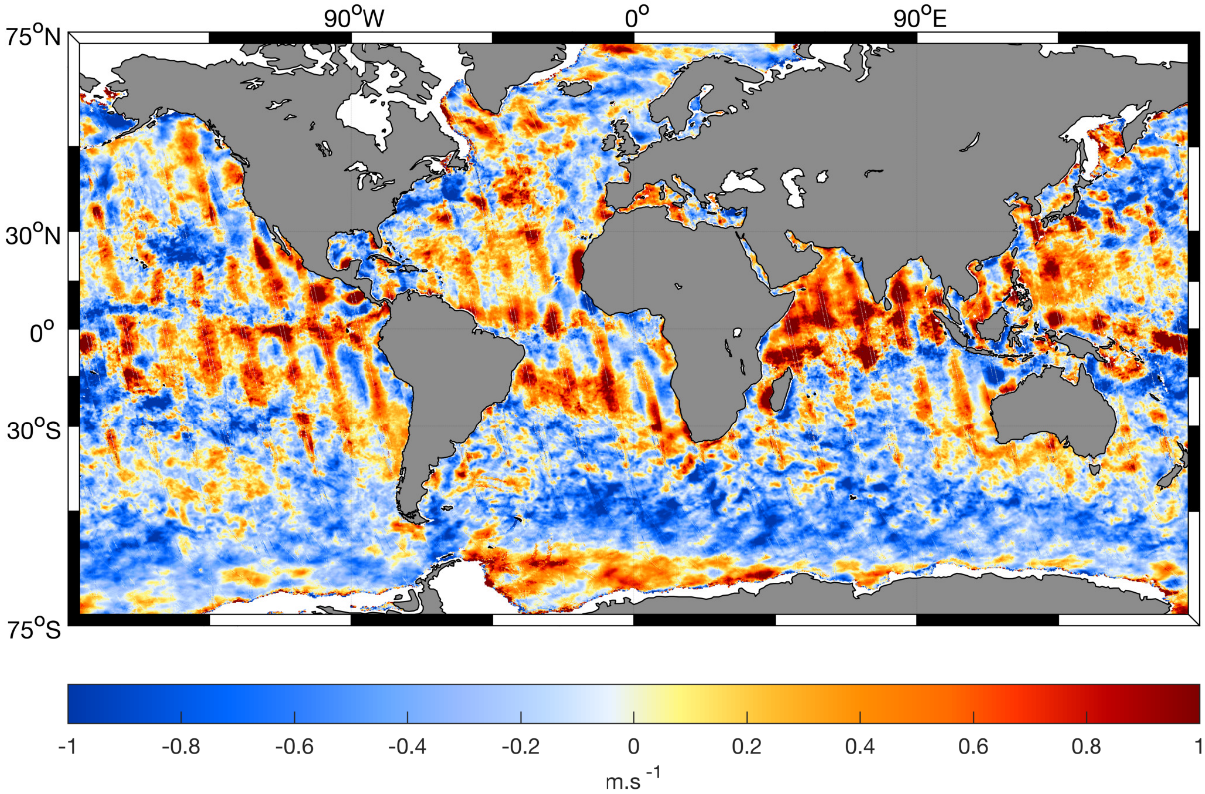

Figure 4.17: Collocations of the OSCAT-2/ERA5 U10S zonal component differences for the ascending orbits only during a 30-day TW.

Additionally, the relatively lower ERA* performance in the middle latitudes can also be due to the presence of residual biases in the OSCAT-2 U10S as a function of the across-track location (Wang et al., 2021). Since the OSCAT-2 orbit has a repeat cycle of 2 days (29 orbits), the mentioned biases have a geographical pattern (see Fig. 4.17), which could directly impact the effectiveness of the proposed ERA* method, which relies on the assumption of well inter-calibrated scatterometer data sets, i.e., the better the C-band and Ku-band systems are inter-calibrated, the better the ERA* performance is.

Also relevant, note the lower VRMSD scores for ERA*$_O$ than for ERA*$_{ABC}$, considering the latter contains substantially larger scatterometer sampling than the former, i.e., ERA*$_{ABC}$

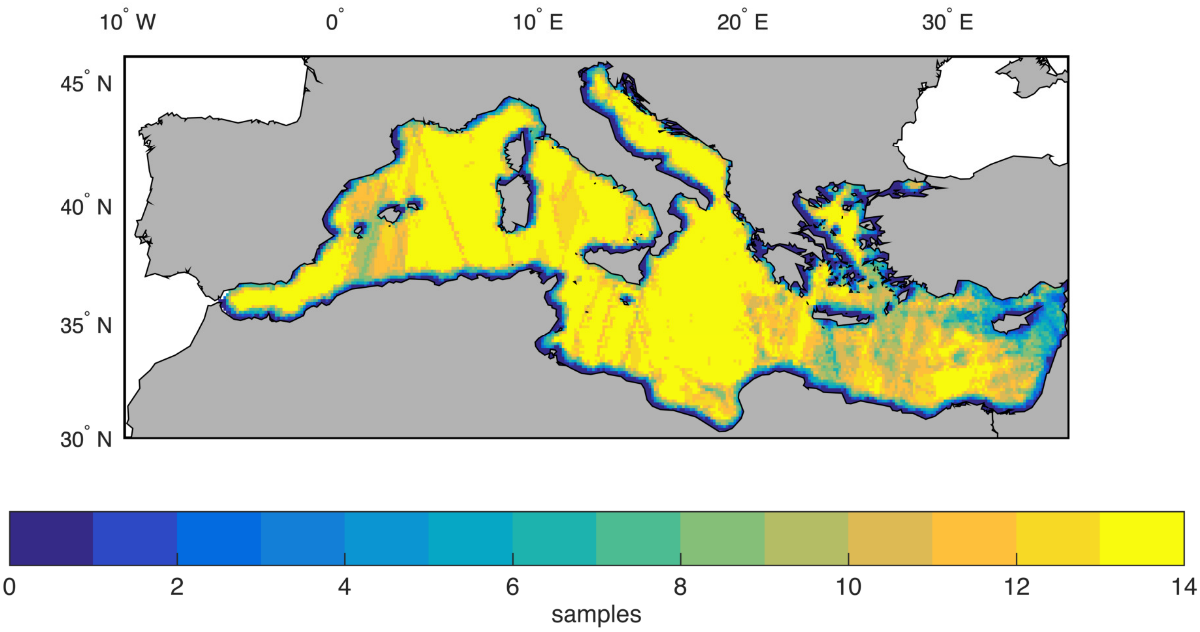

Figure 4.18: Combined ASCAT-A/B/C and OSCAT-2 sampling pattern for a 3-day TW in the Mediterranean Sea.

has the coverage of the three ASCAT instruments. This may be due to the fact that both the OSCAT-2 U10S and the independent HSCAT-B U10S source used for verification are Ku-band systems. As shown in Vogelzang et al. (2011b), rotating pencil-beam Ku-band systems are noisier than the fixed fan beam C-band ASCATs. A variational approach is used to reduce such additional noise, which in turn filters small-scale signal (Portabella and Stoffelen, 2004). Hence, Ku-band U10S fields are of lower resolution than C-band U10S, thus smoother (see SC maps in Fig. 4.13b and 4.13c). This may indeed lead to the lower VRMSD scores for ERA$*_O$, as compared to those for ERA$*_{ABC}$, since the spatial variability of OSCAT-2 and HSCAT-B better matches than that of ASCAT and HSCAT-B. Interestingly, the addition of ASCAT-A/B/C and OSCAT-2 sampling (ERA$*_{ABCO}$) leads to the lowest scores, which is consistent with the expected effect of the scatterometer sampling on ERA* performance.

While the higher spatial spectral content of ASCAT may imply improved SC, we will not be able to verify this with HSCAT-B, as it is also a Ku-band scatterometer. Vogelzang and Stoffelen (2018) shows that employing spatial NWP model error covariance structure functions, learned from the ASCAT missions, lead to better Ku-band scatterometer winds, as verified with buoys. However, the wind errors in Ku-band systems remain larger than those in ASCAT (Vogelzang and Stoffelen, 2021). In fact, Ku-band winds remain smoother than ASCAT winds and the additional mesoscale variance observed by ASCAT will add to the VRMSD with HSCAT-B. This is not the case for OSCAT-2 and hence it will seemingly perform better against HSCAT-B by also not resolving the smaller scales. ERA5 is also not resolving these smaller scales as well as ASCAT and hence it is difficult to conclude from the HSCAT-B VRMSD verification, how good the SCs based on ASCAT really are. Buoy verification would be needed to conclude on the ASCAT versus OSCAT SC quality. Fig. 4.16 indeed shows the better VRMSD performance for OSCAT-2 against HSCAT-B.

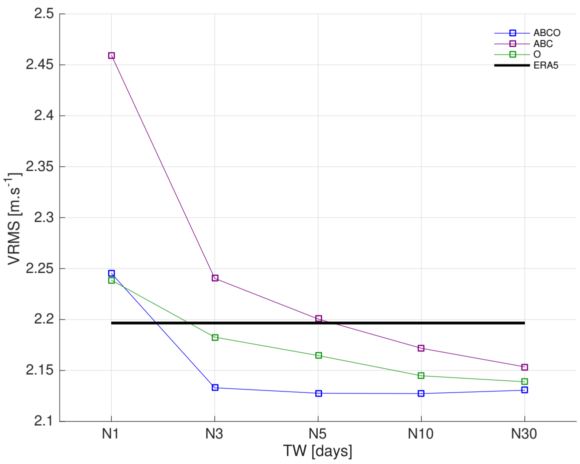

Figure 4.19: Same as Fig. 4.16, but for coastal regions only.

Nevertheless, the increased sampling by adding the ASCATs to the SC, everywhere improves the VRMSD scores against HSCAT-B. Seemingly, averaging out the local and variable weather effects is more relevant than the variability due to the better ASCAT resolution everywhere on the globe, in particular during the first few days. Three days of averaging appears generally sufficient to suppress the random weather noise for the ABCO scenario, where after the VRMSD (very) slowly increases up to accumulation over thirty days in the tropics and high latitudes. This suggests that the model biases slowly evolve, probably due to variable air-sea interaction effects (in insolation, mixing, etc.). This could be further tested by analyzing the SC variability over time. e.g., over one or more years.

The region of most abundant (sun-synchronous) satellite sampling, which is expected to be optimal for model local bias reduction, the high-latitude region, show indeed the strongest VRMSD reductions for a 1-day TW (N1). It implies a different behaviour than anywhere else on the globe. Sampling variations due to the changing sea ice, a high longitudinal spatial density of grid points and a variable temporal mix of scatterometer swaths, suggest that a dedicated study on how these different conditions (than observed for the rest of the globe) affects sampling, should be performed to further understand the results for this region. The dynamical weather errors are sampled temporally more irregularly here, which may affect the optimum averaging length for the SC. Fig. 4.16c) indeed shows the best performance at N1 rather than N3, indicating the relatively larger scatterometer sampling in this ocean region as compared to lower latitude regions. However, other seasons/years showed the lowest scores at N3 (not shown), which points to the sea ice seasonality effects. Note also that for N1, the time difference between the HSCAT-B overpasses (verification) and the scatterometer overpasses used in the generation of the ERA* product (ASCATs and OSCAT-2) is reduced at high latitudes, meaning that the verification at such latitudes is not as independent as the one in the tropics and middle latitudes, which generally leads to lower VRMSD values (i.e., the SCs for high latitudes are generated with similar sampled winds than the HSCAT-B used for the verification), thus underestimating the true ERA* errors.

A similar analysis is performed over coastal regions by verifying ERA* against HSCAT land-flagged, collocated WVCs (i.e., over the entire coastal regions of the oceans). Increased wind variability conditions, including relatively steep wind gradients, are expected near the coast, which are generally poorly resolved by ERA5. Moreover, as already seen in the theoretical simulation in Chapter 3, the scatterometer sampling is rather irregular and poor along the coastline as compared with open ocean grid points (more so in the theoretical scenario which only accounts for three scatterometers to simulate sampling). Fig. 4.18 shows a snapshot of the three-day scatterometer sampling pattern in the Mediterranean (taken as a reference for irregular sampling patterns closer to the coastline), for the combined ASCAT-A/B/C and OSCAT-2 scatterometers. Note how the sampling drastically drops along closest grid points to the continent or in the vicinity of islands. For HSCAT-B land-flagged points a worse yet similar trend in the ERA* performance is found at the coast (Fig. 4.19), as compared to other ocean regions, in particular the middle latitudes (Fig. 4.16). Once again, the extra sampling provided by the complementary scatterometer combination over a three-day TW (ERA*$_{ABCO}$N3 in blue) shows the lowest VRMSD scores and significantly outperforms ERA5 U10S.

An mentioned throughout the manuscript, the quality of the ERA* is achieved by the trade-off between scatterometer sampling and the persistence of local biases. Considering this methodology is based on a static correction, outperforming the ERA5 becomes more challenging in high wind variability conditions. Thus, the effect of transient weather and the diurnal cycle near the coast on the ERA* product quality is further examined through the distribution of the SC. Granted that local systematic biases are generally of the order of $\pm$ 2 $m.s^{-1}$ (previously shown for different SC derived maps), the outliers in the SC distribution (recall long tails in Fig. 2.3), are assumed to be caused by wind variability not properly captured by the ERA5. These are, as expected, more prominent in shorter temporal windows than in longer windows (the lower the sampling, the larger the impact of transient weather and diurnal cycle in the SC).

Using the distribution of SC values for a temporal window of three days and the combination of all ASCATs and OSCAT-2 (i.e., ABCO), these outliers are filtered out with a fixed value that corresponds to 3σ, i.e., three times the standard deviation of the SC distribution. This value is found separately for the SC produced with the C-band and the Ku-band sensors, the latter more affected by rain effects (Xu and Stoffelen, 2020b), and applied to the individual scatterometer-ERA5 differences before computing the corresponding SC (2.1). Further details on the SC distributions used to determine cut-off values for this filter can be found in section 2.2.

Fig. 4.20 shows the VRMSD scores (w.r.t. HSCAT-B U10S) for the ERA5 benchmark (in black), the ERA* configuration after 3σ filtering (ERA*$_{ABCO3\sigma}$ in orange), and the same configuration without the filter (ERA*$_{ABCO}$ in blue). These scores are plotted as a function of the TW size for the same four regions defined in Fig. 4.16, namely for the tropics (a), middle latitudes (b), high latitudes (c) and globally (d). Indeed, the outlier removal seems quite effective. Notice how ERA*$_{ABCO3\sigma}$ outperforms ERA*$_{ABCO}$ for short TWs. In particular, ERA*$_{ABCO3\sigma}N3$ has the lowest VRMSD scores, showing an error variance ($VRMSD^2$) reduction w.r.t. ERA5 of about 12.5% in the tropics (4.20a), while the reduction is of about 5% in the middle latitudes (4.20b) and 9% in the global ocean. Note that large differences tend to occur near moist convection in ASCAT (King et al., 2022), while HY-2B data are mostly rejected near moist convection.

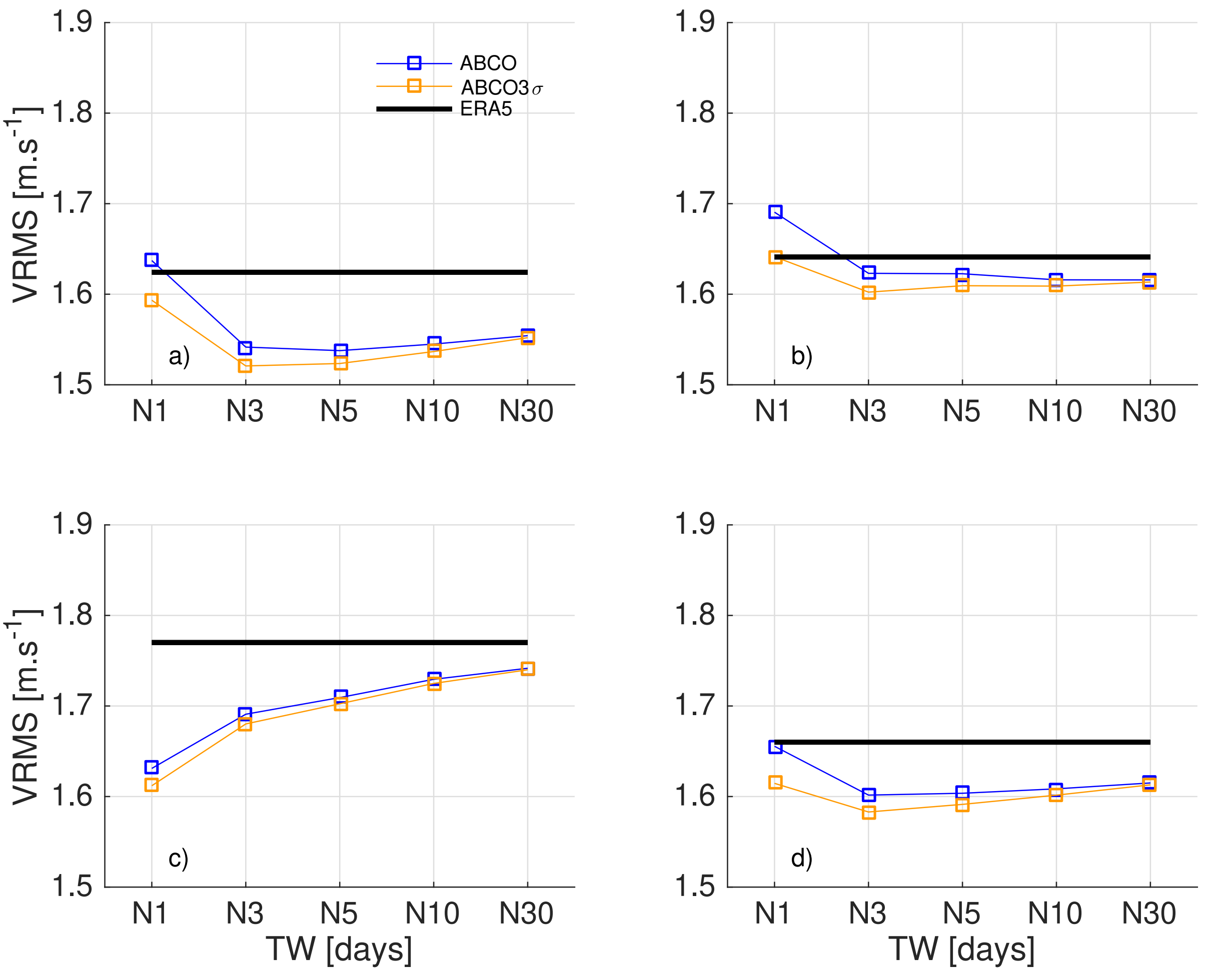

Figure 4.20: Same as Fig. 4.16, but for ERA$_{ABCO3}$N3 (blue) and ERA*$_{ABCO3\sigma}$N3 (orange).*

It implies that the relatively large (Lin et al. (2015a)) wind errors in moist convection are ignored in this verification, obviously resulting in better scores. However, given that the N10 and N30 verifications are largely unaffected, one may conclude that the mean effect of the exclusion of the outliers is negligible after a few days and the computed corrections are representative. (4.20c).

Furthermore, in line with the findings from the scatterometer sampling analysis in this Chapter, and also in Chapter 3, the quality of the ERA* generated without correcting (no SC applied) at those grid point locations considered to have insufficient sampling is analysed. The test is performed both in the Mediterranean and globally. The former provides a good test case because of the substantial drop of scatterometer samples closer to the coastline (i.e., the Mediterranean has a much higher percentage of coastal points than the global ocean).

Fig. 4.21 shows the VRMSD scores for November 2019 globally, for the ERA5 benchmark, and the ERA*$_{ABCO}$ configuration for a one-day (N1) and a three-day (N3) TW, as a function of the filtering. Specifically, the check done for just the 3σ filtering, the 3σ filtering but not correcting for less than 2 scatterometer samples (M2), and the 3σ filtering but not correcting for less than 4 samples (M4). Note that, for the former two, the non-corrected grid points will

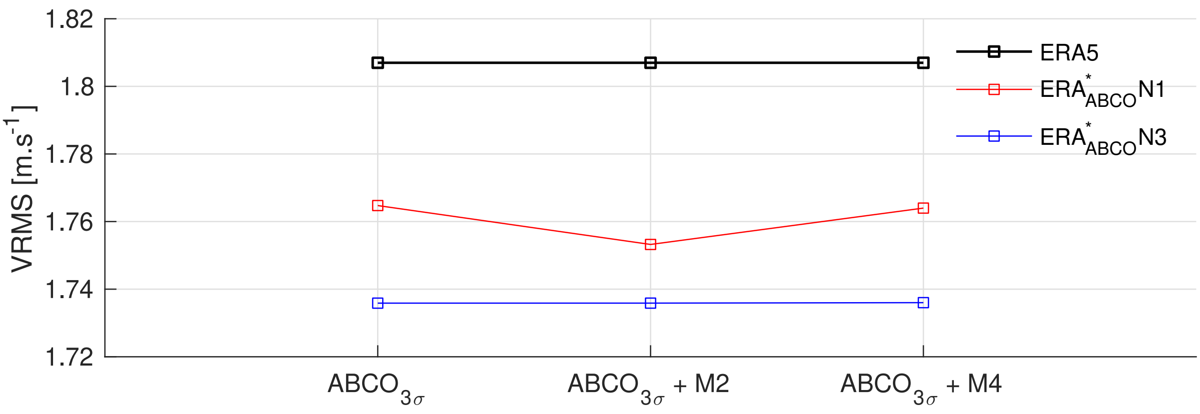

Figure 4.21: Global scores of VRMSD (in m.s^{-1}) between different ERA5/ERA$_{ABCO}$N3 U10S products and HSCAT-B U10S over a month period (November 2019), as a function of the applied filtering: a 3σ threshold, a 3σ threshold but discarding corrections in grid points with less than 2 (M2) or 4 (M4) scatterometer samples. The ERA* SC combines all ASCATs (A/B/C) and OSCAT-2 (ABCO notation) for one-day (N1) and three-day (N3) TWs.*

simply contain ERA5 U10S values.

No significant improvement for the ERA*$_{ABCO}$N3 quality is seen in the global verification by avoiding SC in grid points with less than two or four scatterometer samples, likely because of the enhanced sampling characteristics of this configuration. On the contrary, if a one day temporal window is used (ERA*$_{ABCO}$N1), the ERA* is somewhat improved by excluding M2 and M4 (in line with the expected larger abundance of M2 or M4). Still, the lower VRMSD scores are obtained for ERA*$_{ABCO}$N3, where the impact of this added filtering is null, although, as already mentioned, a one-day TW is discarded for the generation of ERA* (e.g., ERA*$_{ABCO}$N1) because of the already mentioned artifacts visible in the derived maps (see Figs. 4.4b and 4.15b).

The U10S verification shows further reduction of model errors after applying the 3σ filter, in particular when complementary scatterometer data are used to correct the U10S in the tropics, middle latitudes, high latitudes, and coastal regions. As such, it is assumed that most of the high frequency signal observed comes from ocean-related wind signal rather than from (transient weather) noise. Thus, the ERA* U10S configurations (after applying the 3σ filter) are also verified as to their geophysical consistency and effective resolution by means of spectral analysis. Note that only the results for the zonal U10S component are shown, but similar conclusions can be drawn for the meridional component.

The spectral analysis focuses on the tropics and the middle latitudes. For the verification of the ERA* close to coastal zones, such as the Mediterranean Sea, spectral analysis is not used to validate the consistency of the generated fields. To compute the U10S spectra using the HSCAT-B scatterometer as the independent source, this technique requires that at least a 3200-km long row covered by scatterometer ocean-only (no land gaps) tracks is present in order to properly compute the spectra, a requirement which is not met in the Mediterranean basin.

To obtain the U10S spectra for the tropics and the middle latitudes, valid samples of the U10S components are collected over a month (February 2019) in the HSCAT-B along-track direction for each across-track WVC. The final spectrum is obtained by averaging the individual spectra over all WVC numbers across the swath and over the mentioned time period. Overall,

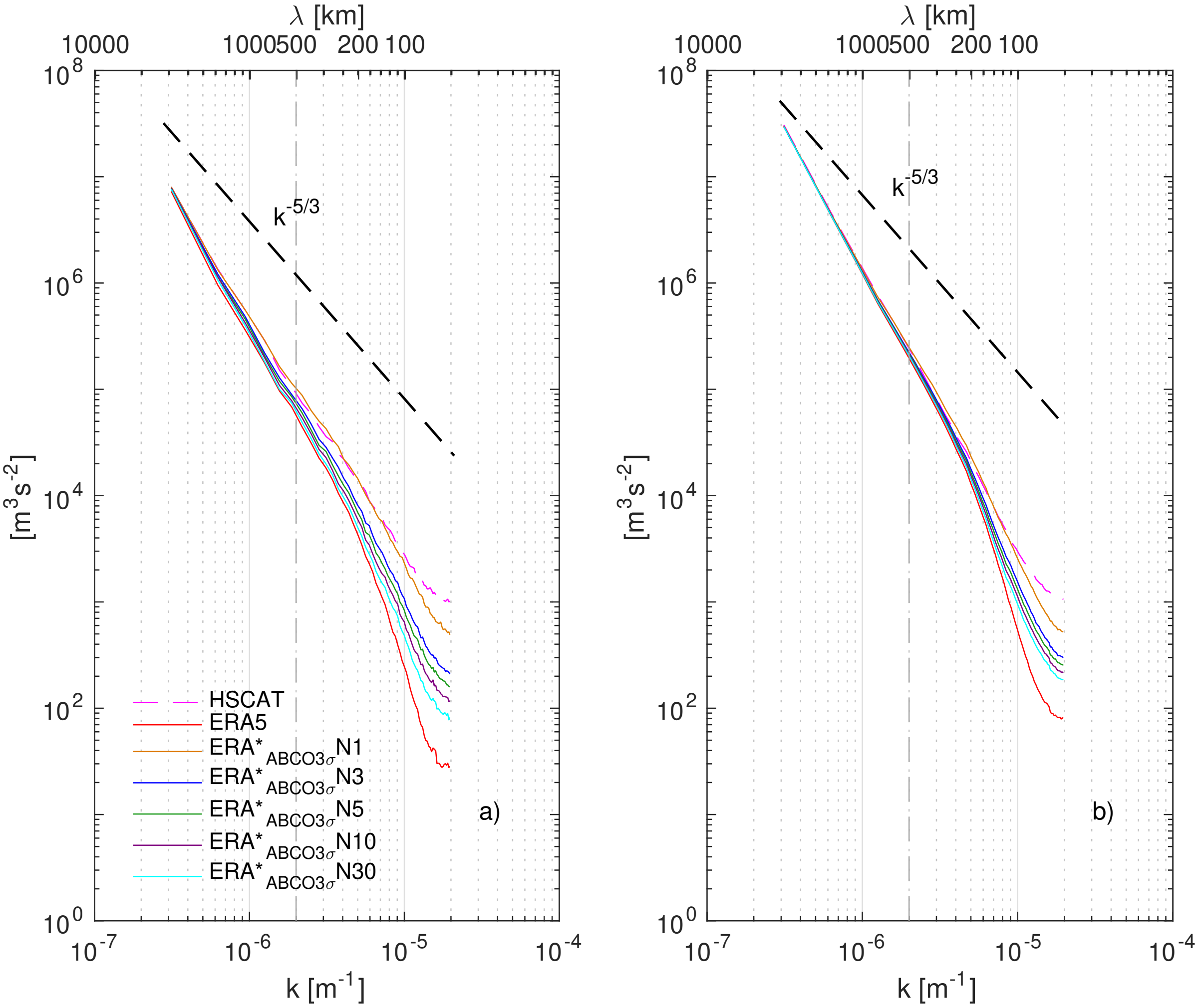

Figure 4.22: Power density spectra for the zonal U10S component (u) of HSCAT-B (dashed pink), and collocated ERA5 (red) and ERA (see colour legend) products, in the tropics (a) and the middle latitudes (b). The ERA* products based on all ASCATs (A/B/C) and OSCAT-2 (ABCO notation) for different TW are shown. The ERA*$_{ABCO}$N notation from N1 to N30 corresponds respectively to TWs from one to thirty days (see Table 4.3).*

for HSCAT-B, 1578 (8458) individual spectra are averaged in the tropics (middle latitudes).

The geophysical consistency of the ERA* is first inspected by varying the TW size used in the SC, for a fixed combination of scatterometers that has previously shown best performance over other scatterometer combinations, i.e., ASCAT-A/B/C, and OSCAT-2).

Fig. 4.22 shows the zonal U10S component in the tropics (Fig. 4.22a) and the middle latitudes (Fig. 4.22b). The solid lines show the model U10S spectra for the same sample length (128) as those collected for the HSCAT-B data (dashed pink). The red solid line shows the ERA5 spectrum, while the different ERA* configurations are shown in orange, blue, green, purple, and cyan (sorted as in the last row of Table 4.3). The black dashed line shows the spectral slope of $k^{-5/3}$ for comparison.

Indeed, the spectra in Fig. 4.22 resemble those of Fig. 4.6, as the spectral slopes observed for the ERA* mostly lay between those of ERA5 and HSCAT-B (except for the one-day TW plotted in orange). Hence, according to this Figure, the ERA* is able to resolve smaller scales than ERA5

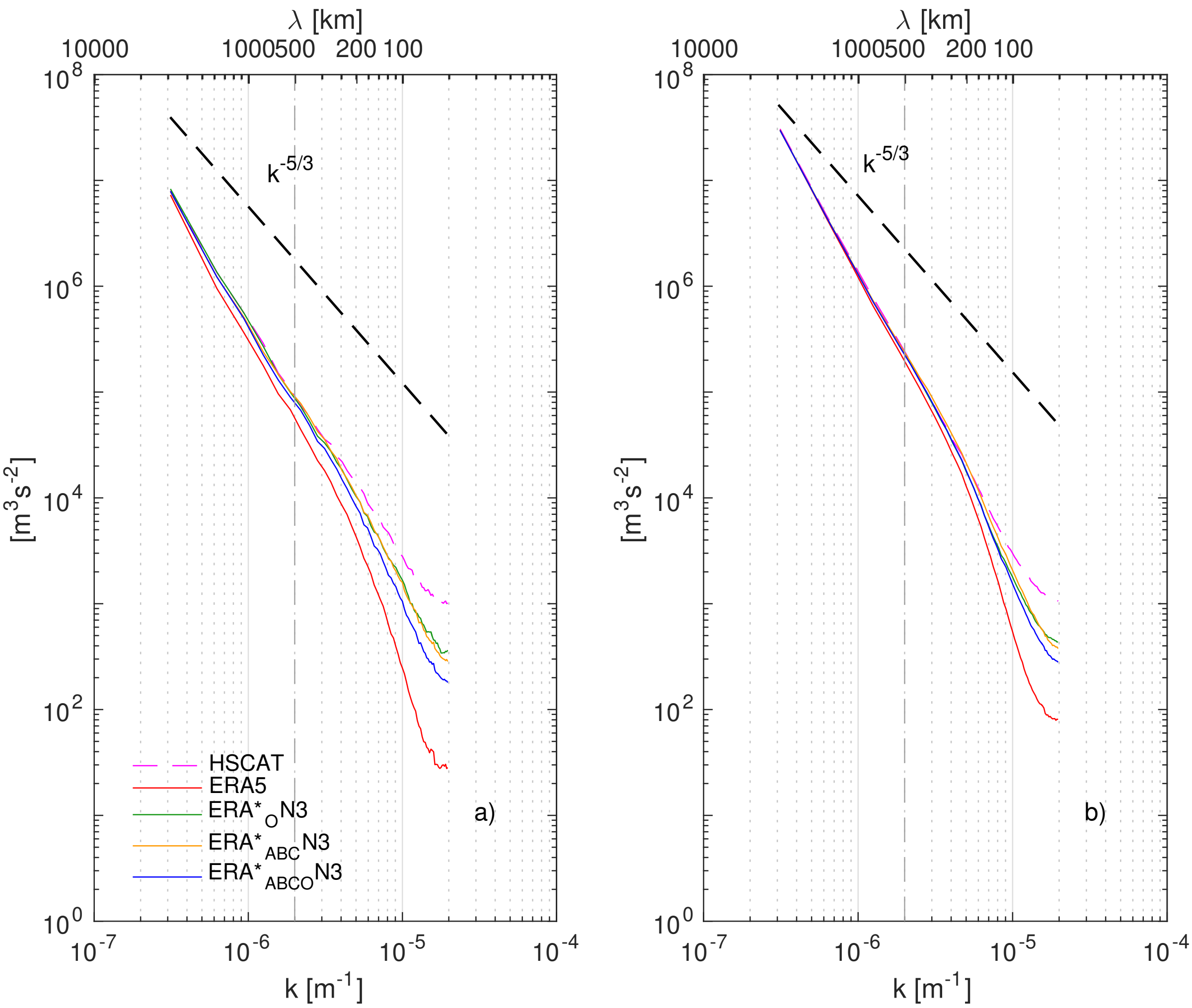

Figure 4.23: Power density spectra for the zonal U10S component (u) of HSCAT-B (dashed pink), and collocated ERA5 (red) and ERA (see colour legend) products, in the tropics (a) and the middle latitudes (b). The different ERA* configurations shown here use a three-day SC TW (see notation in Table 4.3).*

although the U10S fields are somewhat smoother than those of HSCAT-B, due to the implied averaging in SC. HSCAT-B contains structures related to random 3D turbulence and convection, while ERA5 is only amended by those structures that are correlated over time. Note that for the N1 configuration the apparently finest scale ERA* product (spectrally closest to HSCAT-B) is obtained, showing more sampled 3D turbulence or weather, which is undesirable as noted earlier. With the exception of N1, the SCs substantially reduce the ERA*/HSCAT-B VRMSD and are hence associated with persistent model biases and not with random 3D atmospheric turbulence. Note though that a slight indication of a flat spectrum tail is noticeable at high frequencies, also noticeable in HSCAT-B (see dashed pink curve), which indicates a small part of the fast and random 3D turbulence and convection may be present as noise.

The dependence of the spectral slope on spatial sampling is analysed in Fig. 4.23. The spectra for the zonal wind component are displayed for a fixed TW (N3) with different combinations of scatterometers, as listed in the second column of Table 4.3. The HSCAT-B and ERA5 spectral curves are respectively plotted with a dashed-pink line and a solid red line.

Note that, in the middle latitudes, while ERA*$_O$N3 and ERA*$_{ABCO}$N3 have similar spectral slopes, ERA*$_{ABC}$N3 has a somewhat less steep curve, similar to that of HSCAT- B. Moreover, ERA*$_{ABC}$N3 contains somewhat larger variance at intermediate scales than HSCAT-B. This is expected since the ASCATs are of higher resolution than the Ku-band systems like OSCAT-2. This can in turn have an impact on the verification of the ERA* products. That is, since ERA*$_{ABC}$N3 contains more variance than the other two ERA* configurations (ERA*$_{ABCO}$N3 and ERA*$_O$N3), the verification with the relatively low variance HSCAT-B winds may result in larger VRMSD values for the former than the latter ERA* configurations. Further verification with higher-resolution buoy U10S is therefore required to confirm that ERA*$_{ABCO}$N3 is indeed the optimal configuration. Furthermore, the spectral slopes observed in Fig. 4.22 and 4.23 are not significantly altered after applying the 3σ filter to the scatterometer-ERA5 difference.

It is clear from Figs. 4.22 and 4.23, that the size of the temporal window has a more pronounced effect on the spectral slope than the number of scatterometers used. As noted in the spectral analysis performed in this manuscript, the spectra for the middle latitudes, here displayed in Fig. 4.22b and 4.23b, are more energetic at small wave numbers than those of the tropics, as expected due to the synoptic scale weather systems. Apart from that, the spectra for all the configurations behave alike for these two regions.

4.3 11-year ERA*

Starting at the end of the previous decade (2017 onward), the golden Era of scatterometry (with several scatterometers currently operating in orbit and a few others to be launched in the near future) provides extended scatterometer sampling that, as previously demonstrated, further improves the quality of the ERA* L4 wind product. As such, the generation of a longer ERA* data record that benefits from this enhanced coverage is also explored, and included as part of the ESA World Ocean Circulation project (WOC). This data record is produced for an eleven-year period that starts in 2010. Granted that the exceptional coverage is not uniformly present within this period, a careful assessment of yearly scatterometer constellations is first performed and explained in subsection 4.3.1. Moreover, this decade contains a few long periods of unavailable scatterometer retrievals that are expected to affect the quality of the ERA*. This is inspected in subsection 4.3.2. Thorough verification of error variance reduction w.r.t independent validation sources (both HSCAT and buoy U10S) for the ERA* configurations that are included in the 11-year data set, as well as the periods of enhanced ERA* configurations, are discussed in subsection 4.3.3.

4.3.1 Assessment of the varying scatterometer constellation

Throughout this Chapter, the ERA* configuration based on a three-day (N3) SC with maximized scatterometer sampling, e.g., ABO in 2013 and ABCO in 2019, provided the best quality product. However, the optimal scatterometer sampling from 2019/2020 is exceptional, and unfortunately periods of three or more scatterometers are only available for a few years over the period of interest (2010-2020). This section is used to assess the performance of the different scatterometer combinations present over this period, using as validation reference both collocated buoy and independent scatterometer (HSCAT-B) U10S data sets for the year 2019. Note that 2019 is chosen as testbed since the scatterometer constellation in 2019 covers all the different scatterometer combinations present in the period 2010-2020.

Table 4.4: Scatterometer constellation, and corresponding notation, from 2010 to 2020.

Period (years)	Sun-synchronous Scatterometer constellation	Notation
2010-2012	ASCAT-A, OSCAT-1	AB
2013	ASCAT-A/B, OSCAT-1	ABO
2014-2016	ASCAT-A/B	AB
2017-2018	ASCAT-A/B, OSCAT-2	ABO
2019-2020	ASCAT-A/B/C, OSCAT-2	ABCO

Table 4.4 lists the sun-synchronous scatterometers (C- and Ku-band) included in the SC for the period of interest (2010-2020). In summary, these scatterometer combinations give the maximum coverage for their corresponding years. In particular, the optimal configuration ABCO (in terms of complementary sampling) is only available in 2019-2020, while AO is available in 2010-2012, ABO in 2013 and 2017-2018, and AB (i.e., a combination of C-band scatterometers only) in 2014-2016. Although other scatterometers were available within this period only those with global and (near) continuous coverage are listed in Table 4.4.

Given the wide range of possible configurations, the performance of the different configurations needs to be verified before a nominal ERA* configuration is set for the entire period 2010-2020. In particular, the non-polar RapidSCAT or the discontinuous HSCAT-A/B are used as independent scatterometer U10S sources for validation purposes only. On that note, buoy validation is performed using the moored arrays in Fig. 2.1b which, as specified earlier in the manuscript, include: the National Data Buoy Center (NDBC) moored buoys off the coasts of USA, the Ocean Data Acquisition System (ODAS) buoys in the north-east Atlantic and British Isles inshore waters, the National Oceanic Atmospheric Administration (NOAA) Tropical Ocean Atmosphere (TAO) buoy arrays in the tropical Pacific, the Japan Agency for Marine-Earth Science and Technology (JAMSTEC) Triangle Trans-Ocean Buoy Network (TRITON) buoys in the western Pacific, the Prediction and Research Moored Array in the Atlantic (PIRATA), and the Research Moored Array for African–Asian–Australian Monsoon Analysis and Prediction (RAMA) at the tropical Indian Ocean.

Fig. 4.24 shows the monthly VRMSD for ERA5 (in black) and ERA* against HSCAT-B (4.24a) and buoy (4.24b) U10S data for 2019. The ERA* configurations for a fixed TW of three days (N3) are assessed according to different scatterometer constellations: ERA*$_{ABC}$N3 (green), ERA*$_{AO}$N3 (blue) and ERA*$_{ABCO}$N3 (red). From the HSCAT-B verification (Fig. 4.24a), only configurations that combine both the ASCAT and OSCAT scatterometers (ERA*$_{AO}$N3 and ERA*$_{ABCO}$N3), outperform the ERA5 product. Note a degradation of the quality for the latter configurations from May to June 2019. This is due to an OSCAT-2 data interruption of about 30 days, which will be further analyzed in subsection 4.3.2. The ASCATs-only configuration (ERA*$_{ABC}$N3) generally shows a similar VRMSD than that of ERA5, when estimated against the smoother HSCAT-B winds.

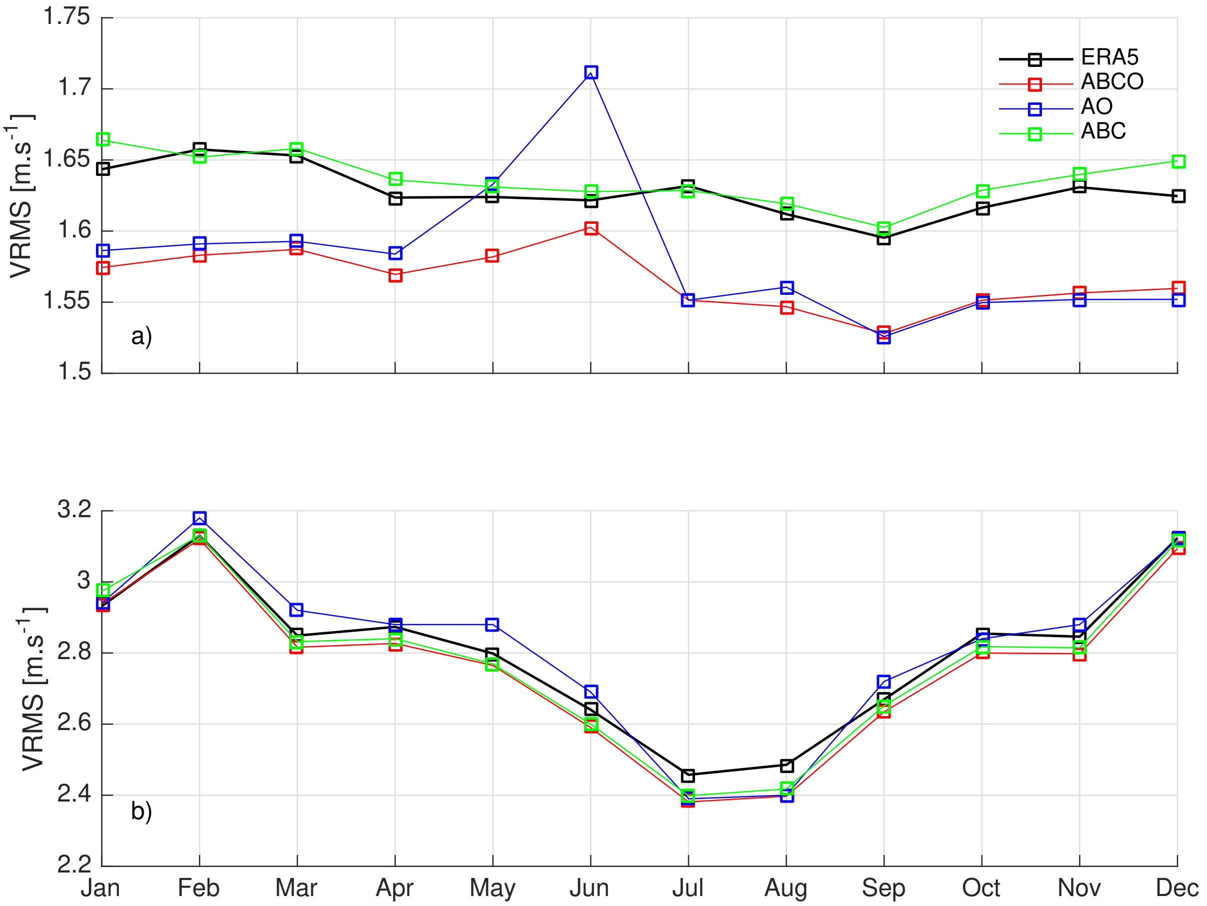

Figure 4.24: Estimated monthly VRMSD (in $m.s^{-1}$) between a few ERA5/ERA U10S products listed in Table 4.4, for 2019. The verification is shown w.r.t. HSCAT-B U10S (a) and w.r.t. buoy U10S in (b). The following ERA* 3-day TW configurations are shown: all ASCATs (A/B/C) and OSCAT-2 (ABCO notation in red), all ASCATs (ABC in green), and ASCAT-A and OSCAT-2 (AO in blue). The ERA5 is plotted in black.*

According to the buoy verification (see Fig. 4.24b), ERA$*_{ABCO}$N3 generally outperforms ERA5. However, the ERA* quality improvement with respect to ERA5 is smaller than that observed in Fig 4.24a. Moreover, in contrast to the HSCAT-B verification results, ERA$*_{AO}$N3 (ERA$*_{ABC}$N3) generally shows a small quality degradation (improvement) with respect to ERA5.

From the HSCAT-B VRMSD one may infer that ERA$*_{ABCO}$N3 contains the most small-scale variability, but which is not observed by HSCAT-B. A longer TW would be profitable to suppress this small-scale variability and improve the HSCAT-B VRMSD, as shown earlier. Also in line with earlier results, the small-scale suppression appears more effective for ERA$*_{AO}$N3 and ERA$*_{ABCO}$N3 generally. ERA5 does not resolve these small scales, but is hampered by model biases, which enhance the HSCAT-B VRMSD. coincidentally, the amplitude of the biases in ERA5 and that of the small-scale weather noise in ERA$*_{ABC}$N3 is similar with respect to HSCAT-B. Subsequently, the buoy verification shows that the small-scale ocean signal in ERA$*_{ABC}$N3 appears generally sufficient to improve ERA5, very similar to ERA$*_{ABCO}$N3, but unsimilar to ERA$*_{AO}$N3 that is generally worse than ERA5. Sampling noise due to the random

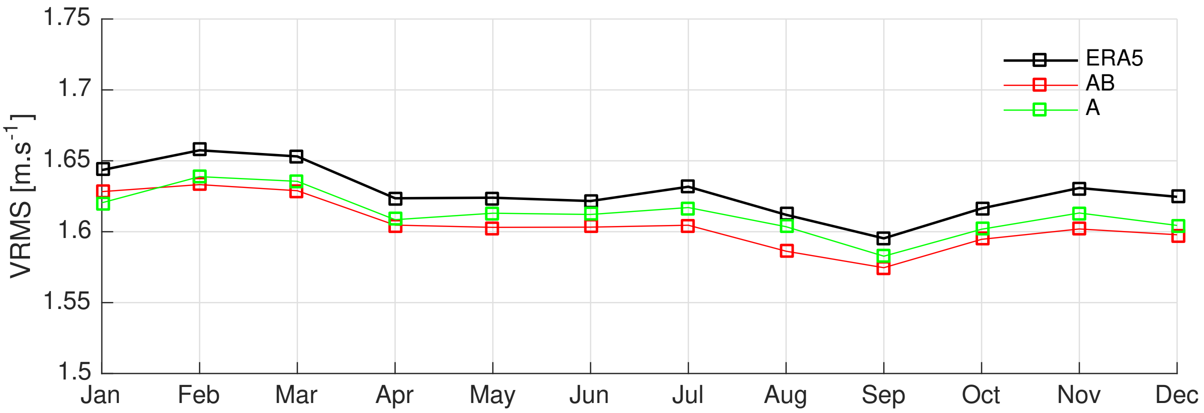

Figure 4.25: Monthly VRMSD (in m.s^{-1}) between ERA5 (black)/ERA$_{AB}$N15 (red)/ERA*$_{A}$N30 (green) U10S and HSCAT-B U10S, for 2019.*

weather at the overpass time of the scatterometers may contribute to the VRMSD and may be larger than the targeted local model bias signal, hence in total deteriorating the buoy verification of ERA* with respect to ERA5, which latter is lacking small-scale variability.

Note also that while buoy verification is local, i.e., for a few locations in the tropics and coastal areas (see Fig. 2.1b), HSCAT-B verification is global. As such, local sampling patterns of the different ERA* configurations (e.g., higher resolution 12.5-km ASCATs have improved coastal sampling in comparison to the 25-km OSCATs) likely play a more dominant role in the buoy than in the HSCAT-B verification. Additionally, as mentioned in 1.4, buoys and scatterometers measure the surface winds differently: while the buoys and ERA5 measure winds relative to earth-fixed coordinates, scatterometer winds are accurate relative to ocean surface motion, which better represent the oceanic variability scales that ERA* intends to capture (Belmonte Rivas and Stoffelen, 2019).

Fig. 4.25 shows the same metrics as Fig. 4.24 but for ERA* with ASCAT-only combinations, and using longer accumulation windows, namely ERA*$_{AB}$N15 and ERA*$_{A}$N30, respectively for a 15-day and a 30-day TW. Overall, for ASCAT only configurations, longer TWs are better suited to outperform ERA5. Furthermore, if only one ASCAT (ASCAT-A) is available, the 15-day TW leads to an ERA* quality similar to that of ERA5 (not shown), while the 30-day TW provides better quality U10S than ERA5 (see green curve below the benchmark). Note also that although the scatterometer sampling for a TW of 15 days and 2 ASCATs is very similar to that of a TW of 30 days and 1 ASCAT, the former leads to lower VRMSD scores as shown in Fig. 4.25, thus confirming that the persistence of local biases is in general shorter than 30 days. The same verification against buoys U10S as in Fig. 4.24b is performed for the ERA*$_{A}$N30 and ERA*$_{AB}$N15 (not shown), with very similar results as those from the ERA*$_{ABC}$N3 configuration shown in Fig. 4.24b.

4.3.2 Effects of lasting data gaps

In this section, a more detailed analysis of the impact of the OSCAT-2 data gap in May-June 2019 is carried out. In particular, the main data gap is from May 20th to June 19th, 2019.

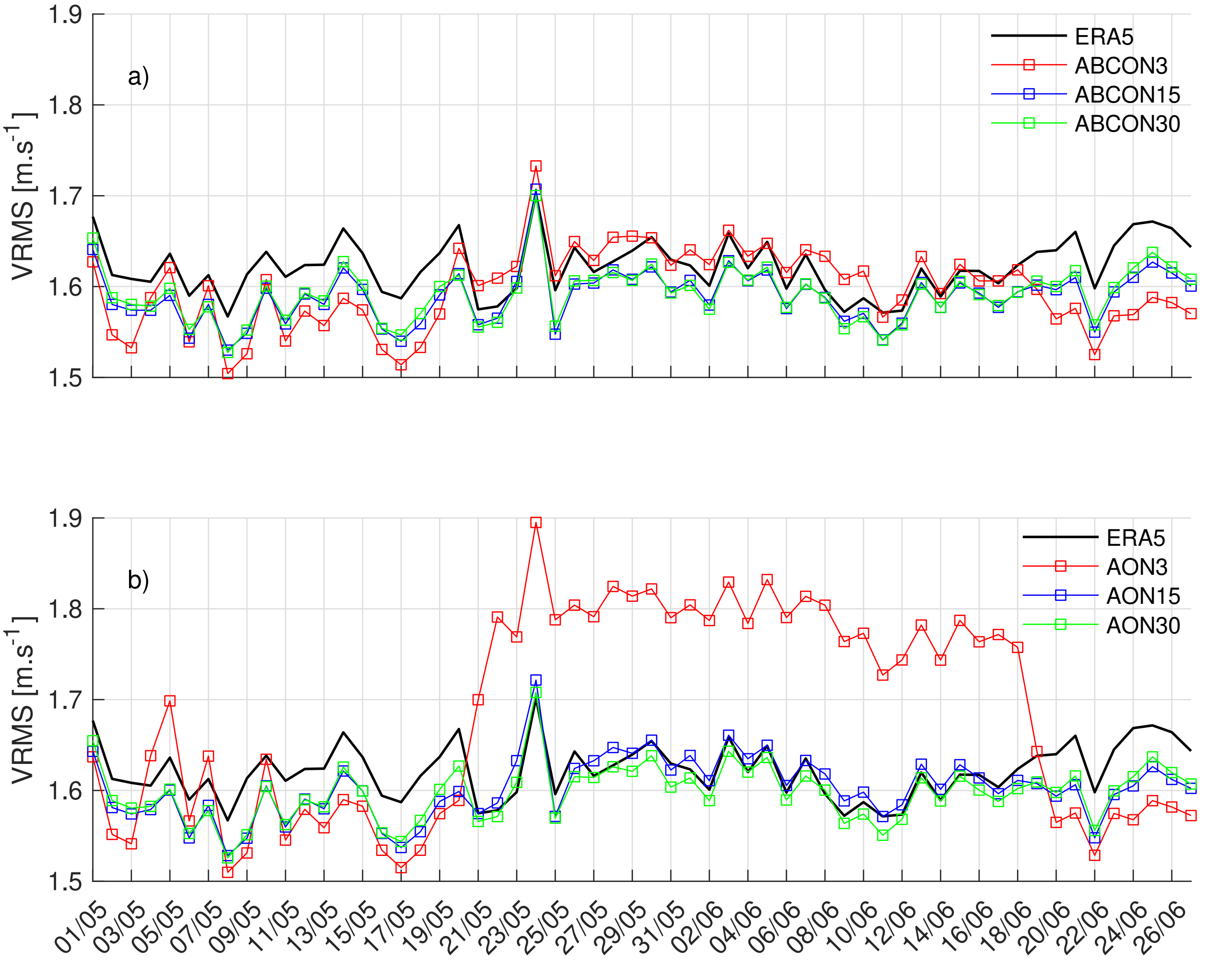

Figure 4.26: Daily VRMSD (in m.s^{-1}) for ERA5/ERA$^*_{ABCO}$ (a) and ERA5/ERA$^*_{AO}$ (b) U10S products w.r.t. HSCAT-B U10S, for N3 (red), N15 (blue) and N30 (green) TWs, from May 1st to June 27th 2019. The ERA5 is plotted in a solid black line.

Fig. 4.26a shows daily VRMSD estimates of ERA5/ERA$^*_{ABCO}$ versus HSCAT-B from May 1st to June 27th 2019, and the following TWs: 3-day (N3 red), 15-day (N15 blue), and 30-day (N30 green) days. As expected, the shortest TW (N3) provides the lowest VRMSD scores, except during the OSCAT-2 gap period. In this period, the 3-day configuration generally has a lower performance (higher VRMSD values) than the ERA5 product. That is, for OSCAT-2 long data gaps (longer than 1-2 days), i.e., the 3-day TW does not provide sufficient sampling to outperform ERA5 U10S. As such, a longer TW of at least 15 days is needed. Moreover, in the absence of OSCAT-2 data gaps, a 15-day time window leads to better ERA* performance than a 30-day time window.

Fig. 4.26b shows the same as Fig. 4.26a but for the ERA$^*_{AO}$ configuration. Likewise, the N3 TW is optimal for the data availability period. However, during the gap period, the ERA$^*_{AO}$N3 quality substantially drops. Although the N15 configuration is of much higher quality than the N3 configuration during the gap period, i.e., for an ASCAT-A only configuration (ERA$^*_{A}$, resulting from the OSCAT-2 gap), a 30-day TW is required for ERA* to outperform ERA5. In other words, a 30-day TW is required for the ASCAT-A only configuration (ERA$^*_{A}$N30) to

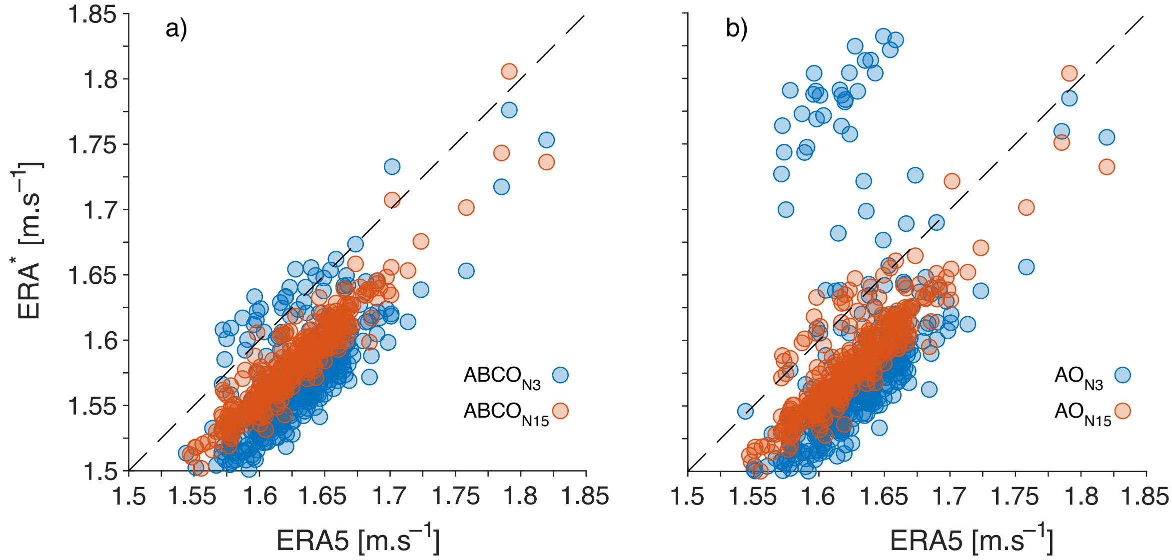

Figure 4.27: Scatterplot of daily VRMSD (in m.s^{-1}), w.r.t. HSCAT-B U10S, of ERA$_{ABCO}$ versus ERA5 (a) and ERA*$_{AO}$ versus ERA5 (b), for N3 (blue circle) and N15 (orange circle) TWs, over 2019.*

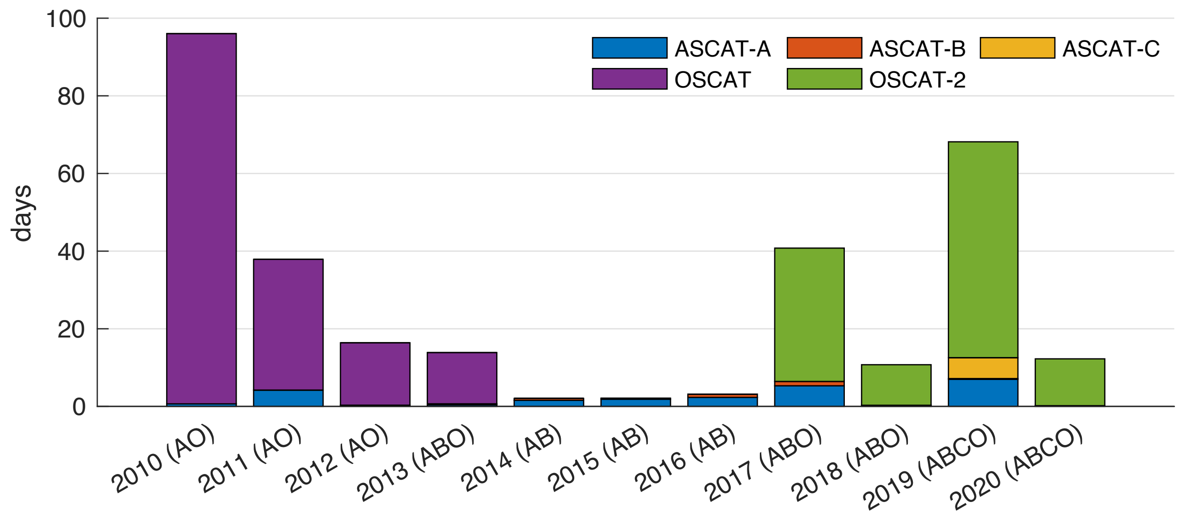

Figure 4.28: Number of accumulated data gaps (in days) per year, for the different scatterometers (see legend) in the period 2010-2020. The specific scatterometer sampling combination is specified for every year on the x-axis.

obtain better U10S performance than that of ERA5.

Fig. 4.27 shows the daily VRMSD scores of ERA* versus ERA5, both w.r.t. HSCAT-B U10S, for two TWs (N3 and N15) over the year 2019.

(4.26a) shows the ERA*$_{ABCO}$ configurations, while (4.26b) shows the same for ERA*$_{AO}$. Intuitively, the colored bullets lying above the diagonal represent the days in which ERA5 outperforms ERA*, and vice versa. As expected, these days mostly correspond to the OSCAT-2 data gap period (between May and June 2019). Although it is clear that N3 shows the best performance most of the time (see blue bullets lower position w.r.t. the diagonal), to minimize

Table 4.5: ERA baseline configurations for the 10 year period. Three years of Enhanced ERA* configurations listed in bold.*

Periods (years)	ERA* configurations
2010	ERA$^*_{AO}$N30
2011-2012	ERA$^*_{AO}$N15
2013	ERA$^*_{ABO}$N15
2014-2016	ERA$^*_{AB}$N15
2017-2018	ERA$^*_{ABO}$N15
2019-2020	ERA$^*_{ABCO}$N15
2013	**ERA$^*_{ABO}$N3**
2018	**ERA$^*_{ABO}$N3**
2020	**ERA$^*_{ABCO}$N3**

the amount of days in which the bullets lie above the diagonal and effectively neutralize the effect of theses gaps, a longer TW of 15 days (N15) is required (see orange bullets almost always below the diagonal). Also, in line with the results in Fig. 4.26b, the 15-day temporal window proves ineffective for the ASCAT-A & OSCAT (AO) configuration during the gap period (see the excess of orange bullets above the diagonal in 4.26b). As such, the longest TW (N30) is necessary in these cases, i.e., cases of effectively ASCAT-A only sampling.

The gap distribution throughout the data record (shown in Fig. 4.28) combined with the U10S verification for the scatterometer combinations specified in Table 4.3, leads to a baseline ERA* configuration in which a TW of 15 days (N15) makes the final data record more consistent in terms of performance, i,e., ERA* quality. In 2010 though, since the OSCAT data is missing for over 3 months, a 30-day temporal window (N30) is proposed instead. A summary of the ERA* baseline configurations is provided in Table 4.5, from 2010 to 2020.

However, the overall U10S verification shows that for selected years without long-lasting OSCAT data gaps an enhanced-quality ERA* configuration using a 3-day temporal window (N3) provides a better quality product. This is true for 2013, 2018, and 2020. These configurations are listed below the baseline configurations in Table 4.5 (bold).

4.3.3 2010-2020 U10S Verification

The percentage of the mean error variance reduction w.r.t. that of ERA5 (see Eq. 2.10), for most of the ERA*N15 configurations is shown in Fig. 4.29. Due to the lack of independent scatterometer validation source in 2010, the verification of ERA$^*_{AO}$N30 in 2019 is used instead. During 2019, the latter is shown to outperform ERA5 (see Fig. 4.26b), even when long OSCAT-2 data gaps exist.

Overall, the nominal ERA* 15-day product outperforms ERA5 with an VRMSD reduction of about 3-9%, showing that the performance is clearly regionally dependent. Those ERA* configurations using complementary scatterometers, i.e., a combination of C- (ASCATs) and Ku- (OSCATs) band scatterometers lead to the best performances. Note also that the largest

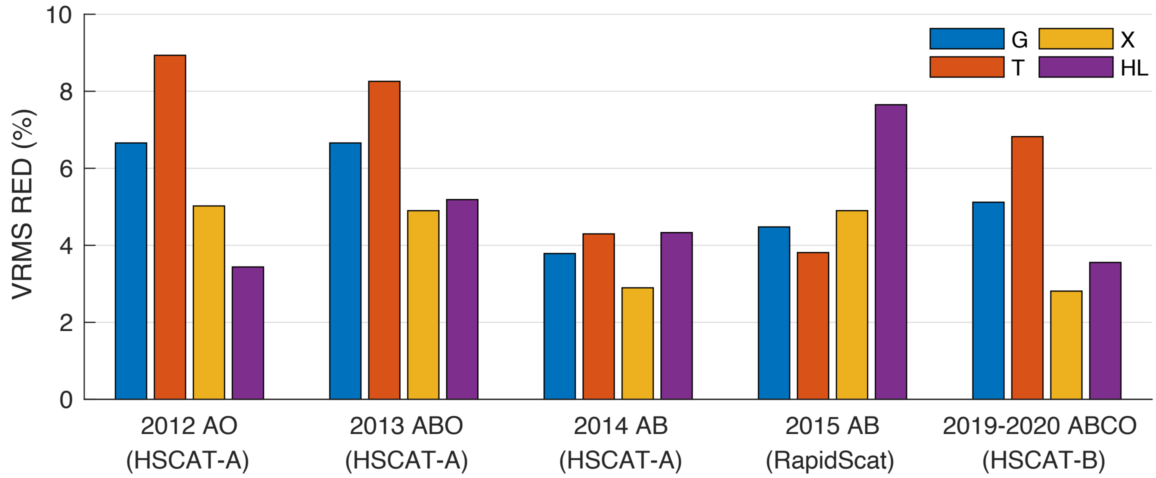

Figure 4.29: Mean VRMSD reduction of the ERA N15 configurations against independent scatterometers globally (G, blue bar), in the tropics (T, red bar), in the middle latitudes (X, yellow bar), and at high latitudes (H,L purple bar) (see legend). The corresponding ERA* configuration per year is referenced in the x-axis, alongside the independent scatterometer used for validation (in parenthesis).*

sampling configuration (ERA*$_{ABCO}$N15) shows slightly lower error variance reductions. This may be due to the fact that different periods of time and independent scatterometers are used in the verification of the different configurations. [Note also that the OSCAT data gaps shown in Fig. 4.28 also impact the ERA*N15 configurations, although the impact on the yearly/2-yearly scores of Fig. 4.29 is actually small (not shown)]. Such finding reinforces that a trade-off between sampling and temporal window size occurs, i.e., for sufficient sampling, a smaller temporal window is preferred since some ERA5 local biases may not persist over 2 weeks, but over shorter temporal scales. Despite that, for the period of interest, because there are long OSCAT data gaps, a rather conservative approach (to ensure sufficient sampling over the gap periods) is followed for the baseline product.

Furthermore, detailed characteristics may be noted from Fig. 4.29. First, the high-latitude impact of RapidScat is relatively large. This is interesting since all RapidScat winds occur below 60 degrees latitude. Seemingly, the corrections in the storm track region around 50 degrees latitude are particularly beneficial.

Second, the relative improvement in the tropics is much enhanced when OSCAT is included in ERA*N15. This may be attributed to the dominance of moist convection processes in the tropics, which are well depicted by ASCAT (King et al., 2022), but generally QC-ed by Ku-band winds (Xu and Stoffelen, 2020c). This implies that the Ku-band scatterometer verification excludes rainy areas, while the ASCAT-based SC include rainy areas. Hence, in fact, the ASCAT-based SC may in reality be more representative of the temporally mean biases averaged over all conditions. This may be further tested with buoy verification.

The same verification is done for two of the enhanced 3-day ERA* configurations in Table 4.5 (in bold), namely ERA$^*_{ABO}$N3 (in 2013) and ERA$^*_{ABCO}$N3 (in 2020). The same regional dependence is observed, with ERA* proving to be a better quality product than ERA5, with

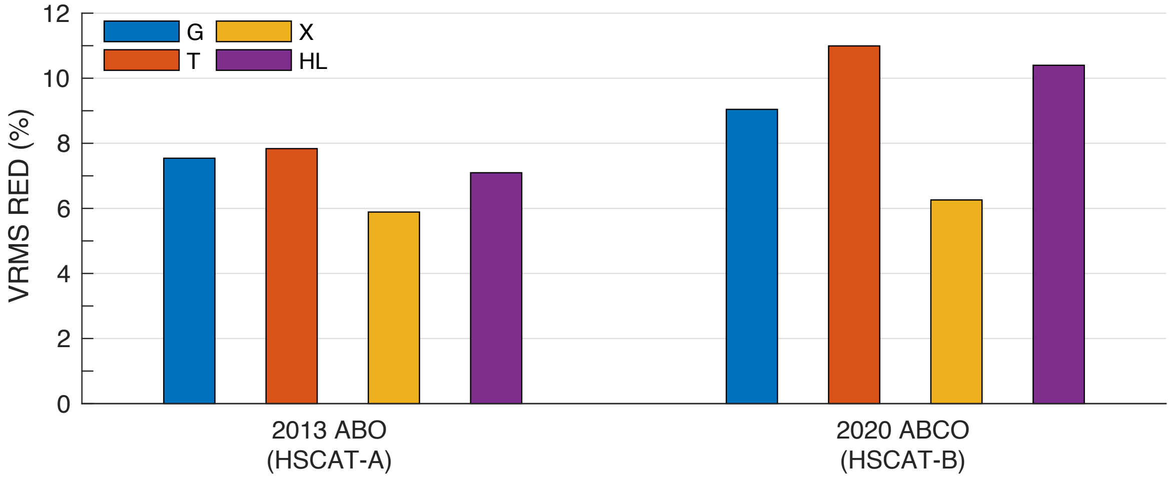

Figure 4.30: Percentage of mean VRMSD reduction for two of the ERA N3 enhanced configurations in Table 4.5(bold), i.e., ERA^*_{ABO}N3 and ERA^*_{ABCO}N3. Same layout as in Fig. 4.29.*

variance reductions of about 6-11%. As expected for short TWs, the ERA* configuration with the largest sampling (ERA^*_{ABCO}N3) gives the highest quality U10S. Regionally, the latter outperforms ERA5 with a VRMSD variance reduction larger than 10% in the tropics and high latitudes, while in the middle latitudes the reduction is only 6%. Thus, globally the VRMSD variance are about 9% lower than that of ERA5 as verified against Ku-band scatterometers.

4.4 Discussion

The new approach, which uses scatterometer U10S data to correct for persistent local NWP wind vector biases, is thoroughly analysed in this Chapter. For the configurations that keep adequate balance between temporal and spatial accumulation of scatterometer data in the SC, the ERA* product is of higher resolution and accuracy than the original ECMWF ERA5, particularly so in open ocean regions.

With the novel methodology it is possible to introduce true smaller-scale signal in the corrected reanalysis or ERA* (compared to the original reanalysis, i.e., ERAi or ERA5), that ultimately represents some of the physical processes absent or misrepresented in the original reanalysis, such as strong current effects (such as WBCS, highly stationary), wind effects associated with the ocean mesoscales (SST), coastal effects (land see breezes, katabatic winds), parameterization errors, and large-scale circulation effects, e.g., at the ITCZ.

Several ERA* configurations using different scatterometer combinations and temporal window sizes (over which the SCs are performed) are explored in this Chapter. The performance and geophysical consistency of such configurations are verified for U10S against an independent scatterometer, e.g., HSCAT-A/B U10S data. Moreover, the qualitative assessment of these ERA* configurations revealed enhanced mesoscale variability with respect to the original ERA reanalysis. For the ERA* versions with complementary scatterometers, and in the absence of long scatterometer gaps, a significant reduction in their VRMSD values (against either HSCAT-A or

HSCAT-B) is shown when compared to those of the original reanalysis. However, the magnitude of this reduction is always higher for the ERAi-corrected ERA* than for the ERA5-corrected ERA*. This due to the improvements in the ECMWF model over time, which in turn result in better quality reanalysis for ERA5, which includes the latest model and data assimilation scheme update (not included for ERAi). Therefore, the reduction in the magnitude of the local biases and the increment of intermediate to small scale variance in ERA5, also somewhat reduces the magnitude of the correction.

Moreover, the ERA* method is regionally dependent, i.e., its effectiveness is mainly modulated by scatterometer sampling of the locally variable weather-modulated model wind biases and on the longer term by local bias persistence. As such, both the ERAi-corrected and ERA5-corrected ERA* have the same performance trends. Evidence that improvement can be achieved by increasing the number of scatterometers, while reducing the temporal window of the SC is consistently shown for different years and scatterometer combinations. Note though that too short temporal windows (N1) are generally of worst quality even if enough scatterometers are used, i.e., with over 3 samples per grid point. Using a shorter TW adds small-scale transient weather noise to the SC, which can be qualitatively identified by the swath-edge artifacts in the derived U10S maps.

Furthermore, depending on the NWP-corrected ERA*, the ERA* configuration with the largest scatterometer sampling are ERA^*_{ABO} for 2013 (for the ERAi-corrected) and ERA^*_{ABCO} for 2019/2020 (ERA5-corrected) with the best performance approximately over a 3-day temporal window (N3). Additionally, for the latter removing transient weather effects by applying 3σ filtering of the scatterometer-ERA5 differences results in further improvement of the ERA* quality. The ERA*N3 has relatively low VRMSD scores and relatively shallow spectral slopes (in between those of the independent scatterometer and the reanalysis), thus indicating that indeed smaller scales are introduced in the new product, i.a., because the signature of oceanic mesoscale features is imprinted on the atmosphere, as previously shown in Tang et al. (2014) with SeaWinds data.

Regionally, the ERA* quality in the middle latitudes is in between that in the tropics and high latitudes. This is likely due to the transient character of weather phenomena at higher latitudes, i.e., Belmonte Rivas and Stoffelen (2019) point out that ERA reanalysis (both the ERAi and the ERA5) show deficient zonal and meridional wind variability, over the storm tracks, where wind variations generate westward baroclinic Rossby flow, which confine upper ocean response establishing the WBCS.

Furthermore, the performance of these configurations drops in coastal regions. Coastal effects are expected to negatively impact the ERA*, due to diurnal effects and sampling issue. An example of this is seen in the VRMSD verification within the Mediterranean basin. In the latter, a relevant limitation is the reduced scatterometer sampling near the coast or in the vicinity of islands that causes irregular (insufficient) sampling within the basin. Moreover, increased wind variability conditions are observed in the Mediterranean, more so in the Adriatic region, where the coastal effects are most prominent. The above negatively impacts the methodology proposed here, due to both insufficient nonuniform sampling and reduction of local bias persistence.

Another source of verification is required to understand the behavior of the methodology in the high-latitude region. The extensive sampling provided by the increase in scatterometer passes near the poles should indeed lead to improved quality ERA*. However, for short TW sizes, the near coincidence (in time) between the scatterometers used to generate ERA* and the one used for verification (HSCAT) may lead to ERA* product quality overestimation. Additionally, other relevant effects, such as the seasonality of the sea ice extent, the SST-dependent biases in Ku-band systems and their impact on the scatterometer wind-retrieval errors, quality control, and sampling should also be accounted for in this analysis.

Overall, spectral analysis shows that the new product (for the configurations addressed so far) contains more small scale variability than the original ERA reanalysis. The observed spectral slopes consistently lay between those of the scatterometers and the original reanalysis, in most cases closer to the former, indicating that the ERA* gridded fields keep some of the spatial scales resolved by scatterometers. However, only the persistent small scales are kept in the SC, which are due to oceanic features such as wind changes over SST gradients and ocean currents. A persistence correction cannot bring lacking 3-D atmospheric turbulence and moist convection as these processes are fast, hence the use of the 3σ filter to exclude this variance from the SC.

Both qualitative assessment and the spectral analysis show smoothing in the derived ERA* U10s fields with the use of longer temporal windows, which may also lead to a small decrease in the quality of the product when verified against HSCAT. This is verified for ERA$^*_{ABCO}$ on temporal windows larger than five days (N5), arguably because longer time windows will slowly blur the ocean-related processes captured in the scatterometer winds. This is particularly noticeable in the tropics. In general, a temporal window larger than N1 is necessary to avoid the reported sampling artifacts and average out the fast and transient weather effects.

Smoothing is also observed when increasing the number of scatterometers in the SC. However, this effect, which does not significantly depend on the temporal window size, is very small, both in the tropics and the middle latitudes. Moreover, the use of complementary scatterometers in the configurations show a clear benefit in terms of VRMSD scores, indicating that these are the most suitable configurations (when available).

Overall, this method shows more potential over regions of persistent local conditions, e.g., in the tropics over the trade winds region, and performs worse in areas characterized by transient weather or diurnal variations (middle latitudes and coastal regions). More so, it is demonstrated that, to effectively correct for persistent biases, the optimal trade-off between sampling and local bias persistence combines complementary scatterometers over relatively short TWs. In this manner, transient phenomena and sampling artifacts are minimized with only limited smoothing of the signature of oceanic mesoscale features and other persistent biases. These considerations are then used to generate both a consistent ERA* data set over a long (11-year) data period which contains long-lasting data gaps and an enhanced ERA* over a shorter period (for 3 years) with reduced data gaps. A large TW size (N15 and N30) is used for the former, while a short TW (N3) is used for the latter.

The next Chapter investigates the potential of the ERA* methodology in real oceanographic applications, specifically by comparing the ocean model response to the ERA* with respect to other wind forcing prescriptions. Note that the findings for two very distinct case-studies are presented, thus allowing for a more robust evaluation of the applicability of the novel forcing.

Chapter 5

Oceanographic applications

[1] Atmospheric forcing applied as ocean model boundary conditions can have a critical impact on the quality of ocean forecasts (Lewis et al., 2019). In addition to the inter-comparison between the performance of ECMWF ERA reanalysis and the novel ERA-corrected higher resolution U10S product, two separate case-studies were analyzed to verify the usefulness of the latter for ocean prediction purposes, i.e., to investigate the added value of the new ERA* ocean forcing products used as wind forcing, by evaluating the dynamical ocean model response. The General Circulation Model (GCM) used for numerical ocean modeling is a NEMO v3.6 model for both case-studies. In particular, the results for an open ocean and a coastal application are presented, respectively in sections 5.1 and 5.2 of this Chapter. Note these studies were conducted in collaboration with other research groups, and took place at different stages of the thesis. Consequently, the first case study (open ocean) over the Tropical Atlantic (TA) uses as ocean forcing conditions the EC-EARTH, the ERAi and the ERAi-corrected ERA*, whilst the second case study (coastal), within the Adriatic basin, uses the ERA5 and ERA5-corrected ERA*. Because the main focus is on the ocean response to the given atmospheric forcing, the following subsections include a description of the ERA* configurations used to force the model, a brief explanation of the case study, and the outcome from the simulations. A final section is dedicated to discuss whether the ERA* improves the model response w.r.t. other forcing solutions, for both regions.

5.1 Open ocean case-study: connection between North tropical and equatorial Atlantic variability

In 2017, the north Tropical Atlantic (NTA) experienced a profound warming, resembling the Atlantic Meridional Mode (AMM) pattern, that is associated with a destructive hurricane season with catastrophic social and economic losses (Nobre and Srukla, 1996; Xie and Carton, 2014; Klotzbach et al., 2018). While the impact of the 2017 NTA warming on equatorial SST variability has not been explored so far, recent findings put forward the key role of the AMM-associated cross-equatorial wind to trigger oceanic waves that impact on equatorial SSTs (Martín-Rey and Lazar, 2019; Foltz and McPhaden, 2010). As such, an 11-month ERAi-corrected wind stress (ERA*τ), from February 2017 to December 2017, was provided as one of the forcing data sets in the climate sensitivity experiments, together with ERAi wind stress, to evaluate the improvement of using realistic forcing to activate the ocean wave mechanisms connecting the NTA and equatorial Atlantic variability. Version 3.6 of NEMO ocean model was forced with the

[1] **Part of the results presented in this chapter is included in the following paper: *Martín-Rey, M., Trindade, A., Exarchou, E., Ortega, P., Portabella, M., Gómara, I.(2022). Dominant role of North tropical Atlantic 2017 warm event on equatorial variability. in preparation***

above-mentioned ERAi and ERAi-corrected wind stresses, and also with the EC-EARTH wind stress products. Notice that the air-sea fluxes in the three experiments are the same, provided by EC-EARTH. So, only the dynamical ocean mechanisms will be modified as response to the wind stress forcing. Further information on the experimental set-up is provided in this section after the characterization of the supplied ERA*.

5.1.1 ERA* adaptations

Unlike the other versions of ERA*, in here the ERA* is generated on a regular 25-km spatial grid, and computed for the period comprehended between the 1st of February and 31st of December 2017. In this 11-month period, three sun-synchronous scatterometers, namely the ASCAT-A/B and OSCAT-2 are used for the ERA* product generation.

At the time of the experiments, and considering the findings in section 4.1 (which assess ERAi-corrected ERA* performance in 2013, when only ASCAT-A/B, and OSCAT-1 were available), a three-day TW was chosen as the optimal choice to balance both scatterometer sampling and capturing oceanic induced mesoscale variability. Note that OSCAT-1 and OSCAT-2 have different LTAN, which are, respectively, 2:30 h and 1:15 h apart from the ASCAT overpasses, although the swath width and the revisit period are the same for both instruments. Evidence that for this ERA$^*_{ABO}$N3 configuration the derived U10S fields contain the above-mentioned signal is shown in Fig. 5.1.

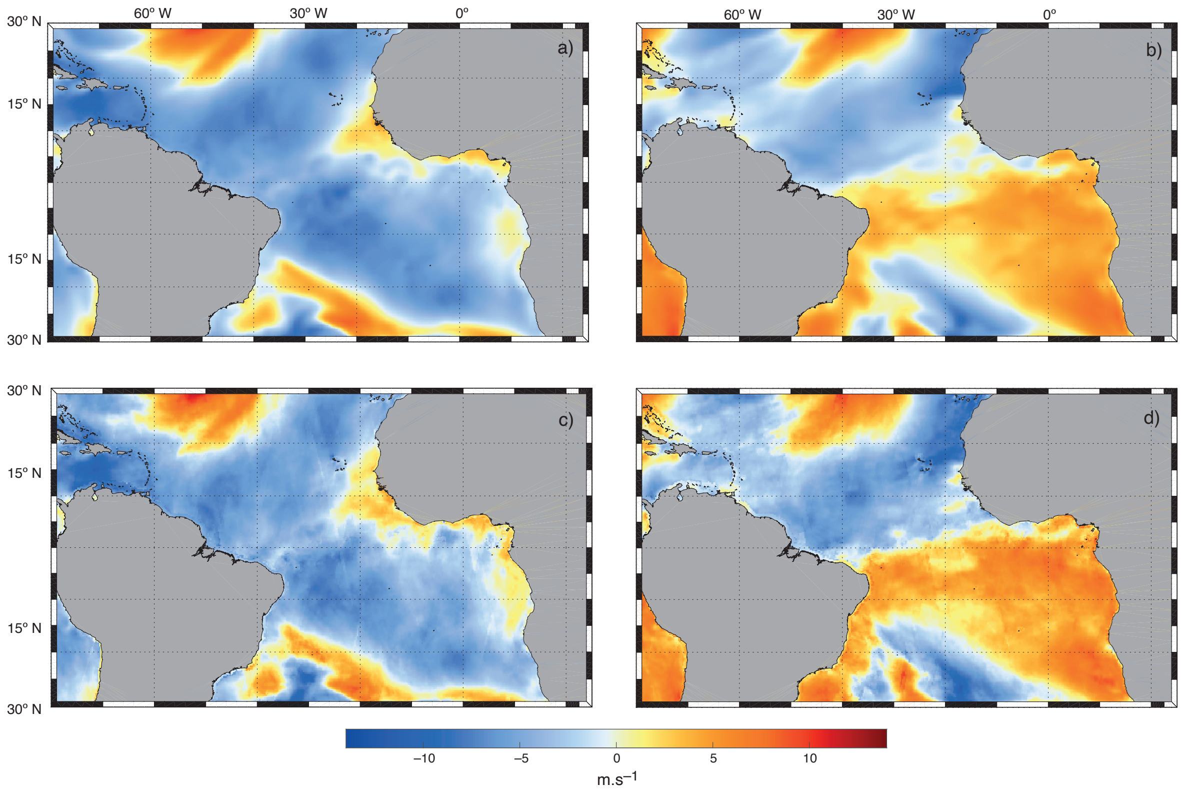

Figure 5.1: U10S derived maps for the zonal and meridional components of ERAi and ERA in the NTA, on March 31st at 03 UTC. The zonal (meridional) component of the ERA5 in (a) ((b)) and ERA* in (c) ((d)).*

Figure 5.1 shows a snapshot of ERAi and ERA^*_{ABO}N3 U10S within the region of interest (NTA) for a given day in 2017. It is readily clear that much more variance is present in Figs. 5.1c and 5.1d than in the corresponding ERAi maps, where this added variability is most noticeable over the areas where ERAi is unable to solve the physical processes known to occur in this region (like moist convection induced wind variability).

In the absence of independent scatterometer data to verify whether the signal present in the ERA* maps of Fig. 5.1 indeed corresponds to true variance and not noise, it was reasonably assumed that the findings from the statistical analysis in 2013 (in section 4.1) could be extrapolated to 2017. However, from the later analysis on the impact of long lasting scatterometer gaps (subsection 4.3.2), a decrease in the quality of the data set is expected for ERA* configurations based on complementary scatterometer data, e.g., ABO, specially when OSCAT-2 data (larger swath, shorter revisit time) is missing. With hindsight, it turns out that in 2017 all together about 30 days of OSCAT-2 data are missing during the 11-month period processed. However, in contrast with the 30-consecutive-day gap period in 2019 for OSCAT-2 (see subsection 4.3.2), the gaps of 2017 are rather short and well distributed all over the year (not shown). In fact, for the 11-months there are a few gap periods longer than one day, i.e., the largest corresponding to two close 3-day gap periods and one 6-day gap period. As such, only a slightly decreased performance of the ERA^*_{ABO}N3 configuration is expected during these few relatively long-lasting gap periods. In fact, additional variance is still present in ERA*, w.r.t. ERAi, as seen in Fig.5.1.

Apart from the visual confirmation in the derived U10S maps (Figs. 5.1c and 5.1d), evidence of additional variance at smaller scales is clear from the spectral slopes displayed in Fig. 5.2, i.e., ERA* contains more U10S variance than ERAi in the high-frequency part of the spectrum. Note that for spatial analysis purposes, buoys are sparse and thus not considered adequate for this type of verification. For comparison purposes, the spectra derived from collocated ASCAT-B U10S are also included in this analysis. Fig. 5.2 shows the spectra of ASCAT-B (dashed blue) and collocated ERAi (red) and two ERA*_{ABO}N3 configurations (see colour legend) in the tropics, for the zonal U10S component (u) in 5.2(a) and the meridional U10S component (v) 5.2(b). Very similar spectral curves are obtained for both wind components. Note that both ERA* spectral curves lay between those of ASCAT-B (much more energetic at small scales following Kolmogorov 3-D turbulent theory of the atmosphere) and ERAi. Despite that, $\text{ERA*}_{ABO}N3_{interp}$ (pink curve) shows a steeper slope, that unlike the original ERA* is closer to that of ERAi in this part of the spectrum.

As already mentioned, in this study ERA* (U10S and τ) are originally generated on a regular 25 km grid for each forecast time (every 3 hours), in spite of that, for forcing purposes a spatial interpolation to the NEMO circular 1° horizontal grid is required. The abrupt drop in the spectra seen for $\text{ERA*}_{ABO}N3_{interp}$ is a direct result from interpolation of the original ERA* on to this coarser grid.

The joint analysis of the qualitative visual assessment and the spectral analysis suggests that although the ERA* loses some of the the small scale variance introduced by the SC after the spatial interpolation, the interpolated product contains significantly more small scale variance than ERAi. Note also that, as common practice by climate modelers, the CDO remap tool

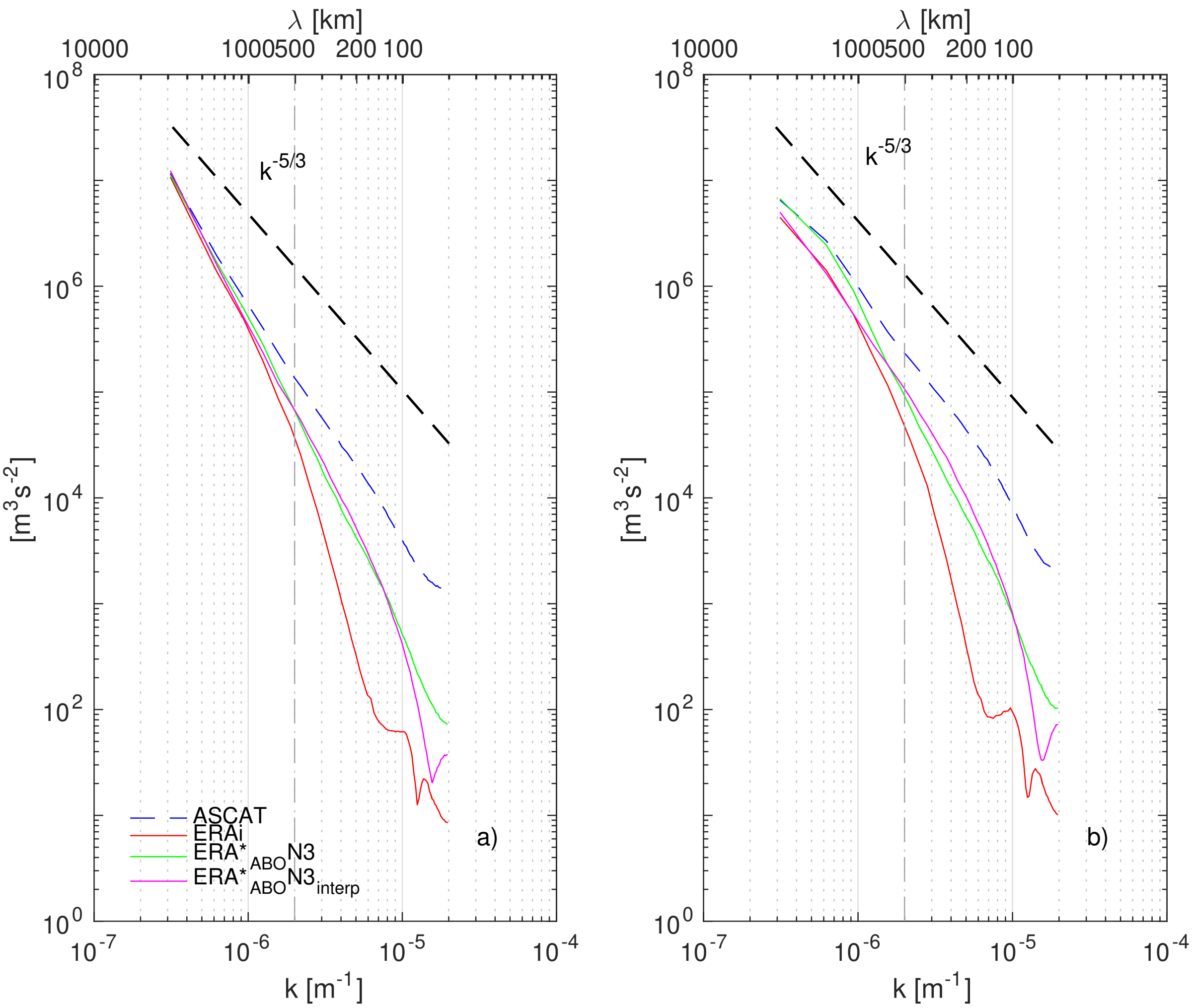

Figure 5.2: Power density spectra of ASCAT-B (dashed blue) and collocated ERAi (red) and ERA (see colour legend) products in the tropics, for the zonal U10S component (u) in (a) and the meridional component (v) in (b). The ERA* product is based on combined ASCAT-A, ASCAT-B and OSCAT-2 (ABO notation) SC for N3. Two different spectral curves are plotted for ERA*$_{ABO}$N3, in which ERA*$_{ABO}$N3 (green) is generated on a regular 25 km grid and ERA*$_{ABO}$N3$_{interp}$ (pink) is the latter interpolated to the NEMOS 1° circular grid.*

(Schulzweida, 2019) is used to perform this interpolation.

Note that the same U10S-to-stress conversion (see Eqs. 2.3 and 2.4) is applied to both ERAi and ERA* products. As such, a verification of the ERA* product in the U10S domain is indicative of the quality of the product in the wind stress domain (ERA$^*_\tau$). Indeed, as it can be seen from Fig. 5.3, the loss of spatial resolution in the derived wind stress map (ERA*$_\tau$) after the interpolation into the coarser grid (see ERA$^*_{\tau interp}$ in Fig. 5.3c) is noticeable when compared to the original 25-km resolution product (Fig. 5.3c). Although the same happens for the ERAi$_{\tau interp}$ field after the interpolation (not shown), this qualitative assessment suggests that some of the small scale variance is in fact lost with the interpolation. However, it is assumed that such loss in mesoscale variability would (hopefully) not be particularly relevant for this study, which is focused in climate variability modes and the large scale signal, yet this should be taken into consideration.

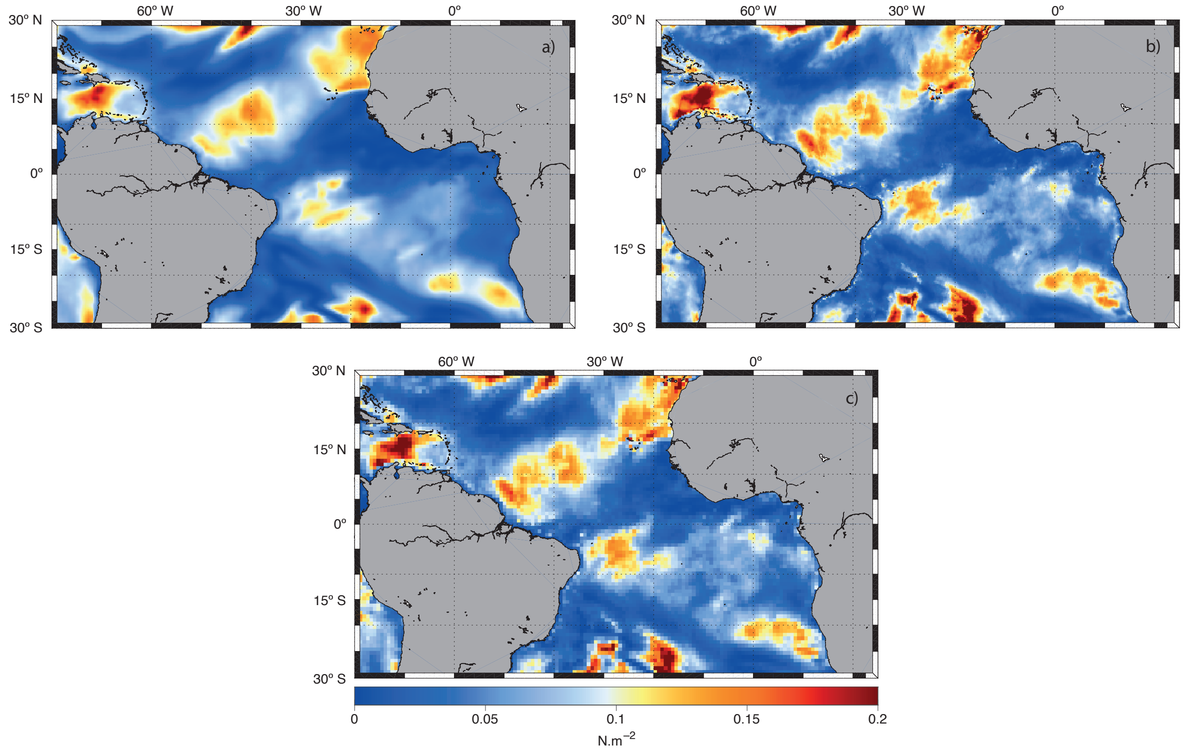

Figure 5.3: Wind stress magnitude in the Tropical Atlantic for a specific forecast time, e.g., on March 31st at 03 UTC, for ERAi$_{\tau}$ (a) and ERA$^{*}_{\tau}$ (b) wind stress fields, with the ERA$^{*}_{\tau}$ after the spatial interpolation (ERA$^{*}_{\tau interp}$) in (c).

A general summary of the set-up of the ocean model is provided next. The focus is on the details concerning the wind forcing prescribed, such that the performance of the realistic wind stress, in terms of reproducing the above mentioned wave mechanism, can be properly analysed.

5.1.2 Experimental set-up

The global coupled climate model EC-Earth-3.3 (Döscher et al., 2022) was used to perform sensitivity experiments using three ocean-forcing simulations. The oceanic and atmospheric components of the coupled model are respectively obtained from the NEMO-3.6 model (Madec and the NEMO Team, 2014), using the ORCA1 configuration, which corresponds to about 1° horizontal grid and has 75 vertical levels (Wyser et al., 2020), and the Integrated Forecasting System (IFS) with T255 spectral sampling, which corresponds to a horizontal grid size of about 80 km, and has 91 vertical levels (up to 0.1 hPa).

The set up for the three sensitivity experiments is specified as follows. All the experiments initialise on February 1st 2017, by ORA-S4 (Balmaseda et al., 2013) in the ocean and by ERAi in the atmosphere, and run for 11 months with 10 ensemble members (ending on December 31st). These three experiments are inter-annual climate predictions: the first is a free-running reference prediction i.e., using inter-annual EC-EARTH wind stress (hereinafter, MOD), whilst the others use original and corrected ERAi wind stress reanalysis (hereinafter INTER-ERAi and INTER-ERA*, respectively), to force the tropical Atlantic region [35°N-35°S, 70°W-20°E], with a 4° buffering zone to smooth the transition.

The focus of the study is on the inter-annual variability of the tropical Atlantic. In this region, different wind stress products are imposed in each time step. Although there is coupling between the IFS and the ocean, in what concerns the turbulent fluxes, the momentum fluxes that promote the dynamical wind-driven mechanisms (waves) only respond to the prescribed wind forcing, which is the changing element in the simulations. So, to first order, the excitation of the Rossby Wave (RW) reflected mechanism is attributed only to the ERAi/ERA* wind stress forcing. Note though, in what concerns the turbulent fluxes that contribute to create the SST pattern (depending on the wind forcing), some interference may arise from the dynamical contribution via momentum fluxes (forced winds) in the SST pattern that is afterwards translated to the thermodynamic turbulent fluxes (from the IFS).

Notice that the INTER-EC-Earth (from 2017) is contained within the historical climatology run (1980-2013), while in the wind-prescribed experiments (INTER-ERAi and INTER-ERA*), the model is forced every 3-hours throughout the 11-month period. Moreover, the wind stress computation differs for the ERAi and the ERA* forcing used in INTER-ERAi and INTER-ERA*, respectively. In particular, the bulk formulation in Eq.2.3 is used to compute the wind stress magnitude for the ERA* which, as mentioned, takes the average air density ($< \rho_{air} > = 1.225\ [kg/m^3]$), based on the linear relation for 1 year between the drag coefficient (CD) and U10S (Eq. 2.4). In contrast, for ERAi, the wind stress is computed by the atmospheric model (IFS CY36R1) through its own bulk formula (http://www.ecmwf.int/en/publications/ifs-documentation).

In subsection 5.1.3, the dynamical ocean model response to different wind forcings is assessed, with special focus on the interaction between NTA and equatorial variability described in previous studies (Foltz and McPhaden, 2010; Martín-Rey and Lazar, 2019). For such purpose, the ocean wave mechanism responsible for this connection is investigated using observational data sets. Then, the outcome of the sensitivity experiments is evaluated and compared with the observations.

5.1.3 Ocean model response

The warm event that took place in the north Tropical Atlantic in 2017 and its linkage to equatorial variability is investigated by the set-up of the three model simulations, i.e., using different wind stress forcing conditions, as described in the previous section.

The SST observations are displayed in Fig. 5.4 and the wind stress curl over the SSH in Fig. 5.5. The event is clearly marked by a positive Atlantic Meridional Mode (AMM) in the boreal spring of 2017 (5.4b), leading to equatorial warming conditions during the summer months (5.4c). The Hömoller diagrams between [-10 50]°W for the wind stress curl over SSH along the [2-4]°N in 5.5(a) and the zonal wind stress over the SSH for the equator in 5.5(b). A downwelling Rossby wave (dRW) that propagates westwards and reflects back as a downwelling Kelvin wave (dKW) is evident here.

The first simulation, i.e., the free running reference prediction (MOD), in which the EC-EARTH model IFS is used only with initialized conditions and SSH from AVISO (https://www.aviso.altimetry.fr/en/home.html) is shown in Fig. 5.6. Monthly and seasonal anomalies

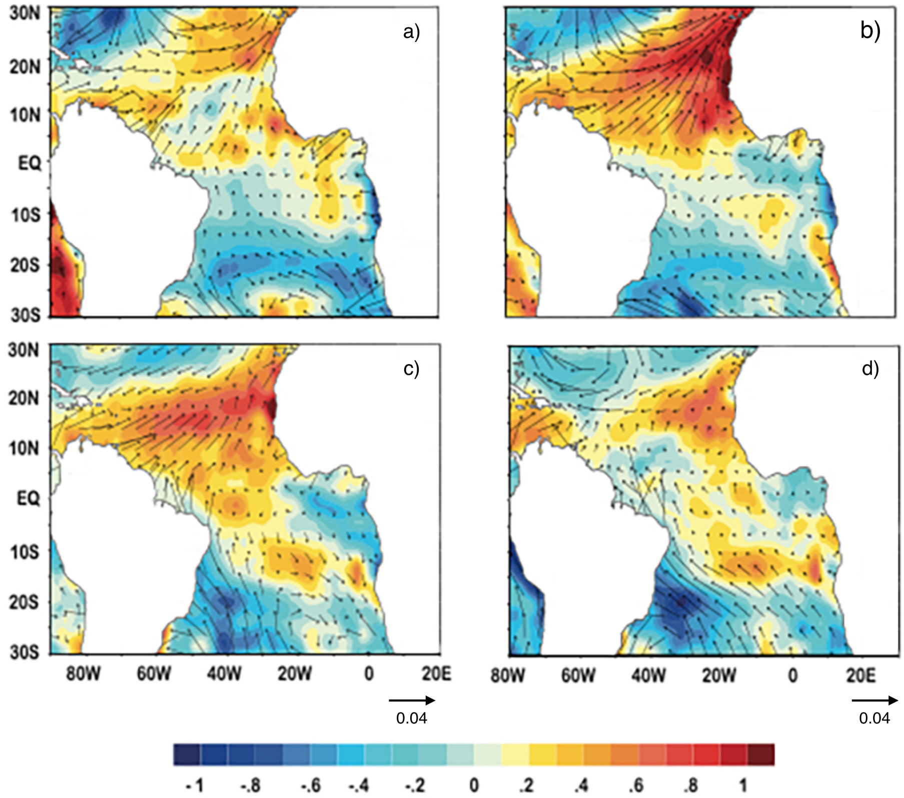

Figure 5.4: SST (shaded, in °C) and wind stress anomalies (vectors, in $N.m^{-2}$)) from boreal spring (March-May) to late summer (July-September). Each panel corresponds to 3-month periods, specifically FMA in (a), AMJ in (b), in JJA (c) and ASO in (d). Notice that observations here are referred to SST and wind stress anomalies from ERAi reanalysis.

for observations are computed by subtracting the ERAi (for SST and wind stress) climatologies for the period 1980-2013 and 1993-2013, respectively. Fig 5.6 shows these anomalies for the MOD simulation (5.6(a)(b)(c)) alongside the observed event (5.6(d)(e)(f)), for easy comparison, seasonally from March to September, i.e., MAM, MJJ, JAS. Notice the 3-month periods from (5.6(d)(e)(f)) do not correspond to those shown in 5.4, but are illustrative of the observed conditions in the latter. The MOD experiment is not able to properly capture the observed 2017 event in Fig. 5.4 with these conditions. A too strong meridional mode is detected in boreal spring and persists until fall.

For the realistic wind stress forcing simulations (INTER-ERAi and INTER-ERA*), the ocean model response is evaluated by plotting the outputs from these two model runs w.r.t MOD baseline, for same three month periods as in Fig. 5.6, and applying the added value (AV) estimator from (Di Luca et al., 2013; Gómara et al., 2018). This technique is based on the square error and applied for each pair of simulations in the following way:

$$AV_{ERAi-MOD} = (X_{MOD} - X_{OBS})^2 - (X_{ERAi} - X_{OBS})^2 \tag{5.1}$$

$$AV_{ERA^*-MOD} = (X_{MOD} - X_{OBS})^2 - (X_{ERA^*} - X_{OBS})^2 \tag{5.2}$$

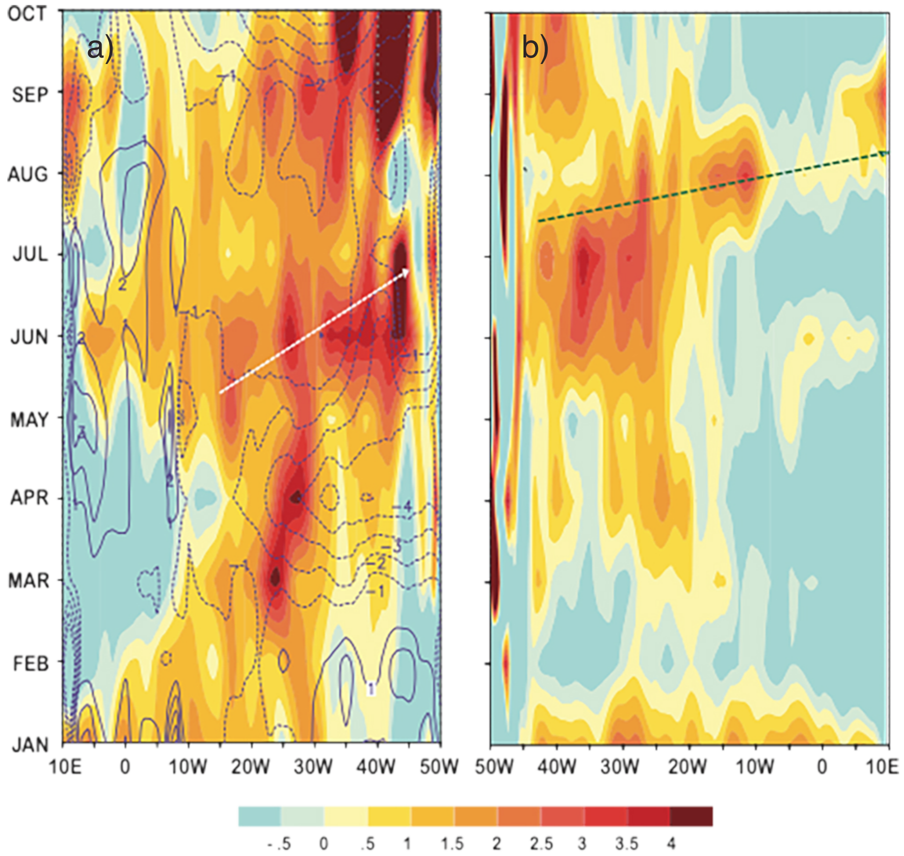

Figure 5.5: Time-longitude hövmoller diagram of observed (7-yr Butterworth) anomalies of wind stress curl and SSH along the equator (a) and [2-4]° N (b), for boreal spring.

$$AV_{ERA^*-ERAi} = (X_{ERAi} - X_{OBS})^2 - (X_{ERA^*} - X_{OBS})^2 \tag{5.3}$$

Where X_{MOD}, X_{ERAi}, X_{ERA^*} and X_{OBS} are the SST fields corresponding to, respectively, MOD, ERAi, ERA*, and observations. Positive (negative) AV values represent positive (negative) impact of the first forcing term w.r.t. that of the second, e.g., positive $AV_{ERAi-MOD}$ values in Eq. 5.1 represent positive impact of ERAi forcing w.r.t. MOD forcing, meaning that ERAi forcing is able to improve the ORA-S4 model SST output quality w.r.t. MOD forcing. Hence, in Fig. 5.7, the AV for SST and the wind stress difference between INTER-ERAi and MOD (Fig. 5.7(a)(d)(g)(j) and Eq. 5.1), between INTER-ERA* and MOD (Fig. 5.7(b)(e)(h)(k) and Eq. 5.2), and between INTER-ERA* and INTER-ERAi (Fig. 5.7(c)(f)(i)(l) and Eq. 5.3) for the 2017 spring, summer, and autumn periods, are shown. The use of realistic winds, both ERAi and ERA* effectively improves the Senegal-Mauritania during boreal spring/summer and in summer/fall. In particular, the ERA* forcing improves the model response to the SST signal in the NE tropical Atlantic, which implies a better representation of the AMM in spring time, also seen in the Western/Central equatorial region during the summer/spring, (see the red-marked AV region in Fig. 5.7(e))). Whereas the ERAi better resembles the observed conditions near the

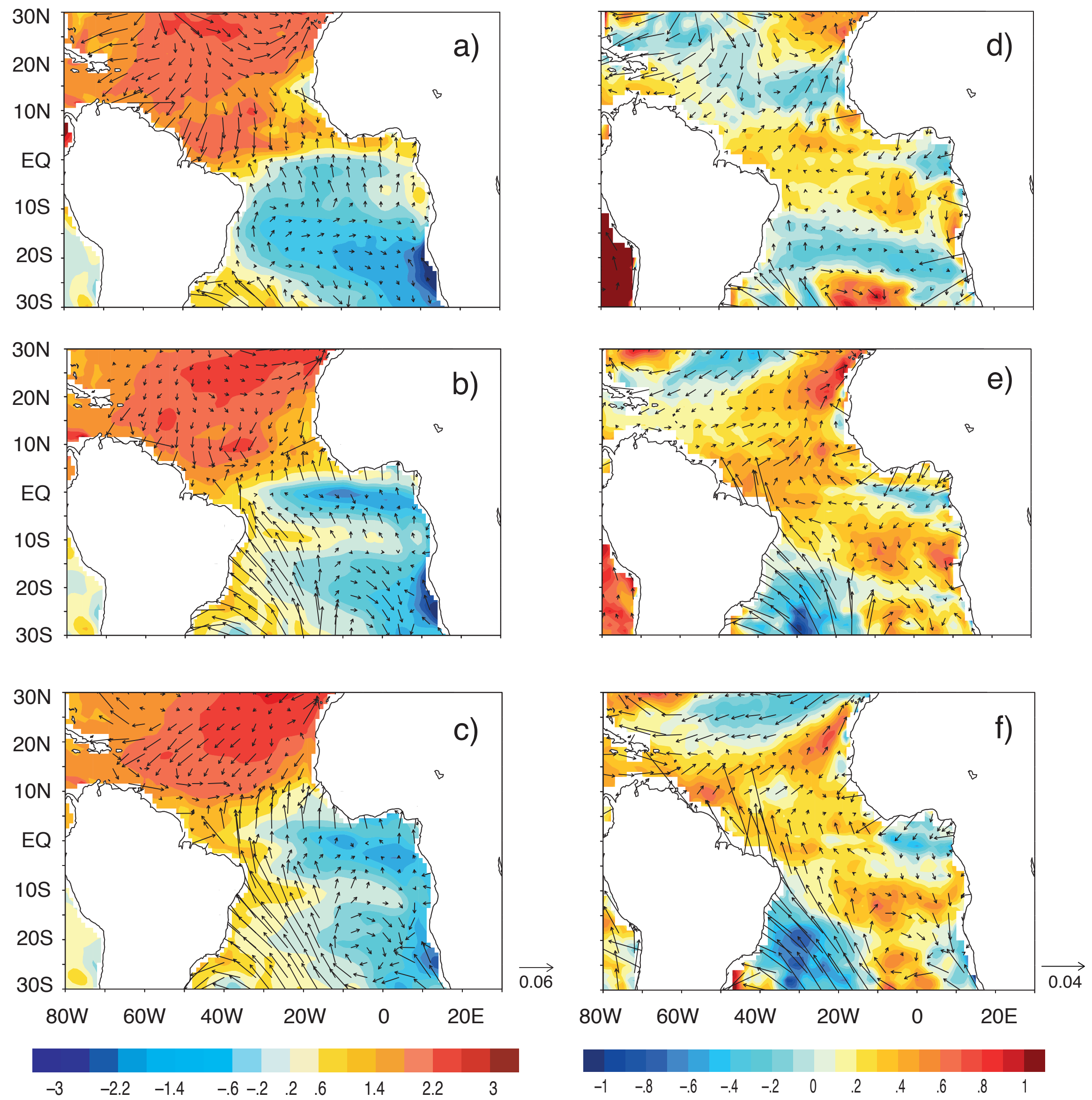

Figure 5.6: SST (shaded, in °C) and wind stress anomalies (vectors, in $N.m^{-2}$)) for MOD (a)(b)(c) and for observations (d)(e)(f), from the boreal spring (March-May) to late summer (July-September) in the tropical Atlantic region, during 2017. Notice that observations here are referred to SST and wind stress anomalies from ERAi reanalysis.

coast (see Fig. 5.7d). Surprisingly, despite the previously mentioned problem of ERA* winds close to the coast, Fig. 5.7(c) reveals that there is a clear improvement of the coastal SST signal, which responds to the correct simulation of the northward along-shore winds that reduce the upwelling.

Remarkably, the ocean wave activity proves highly sensitive to realistic wind stress during the entire NTA evolution. In Fig. 5.8, the wave propagation is seen both using the ERAi (see Fig. 5.8(a)(b)) and the ERA* (see Fig. 5.8(c)(d)) wind stress forcing. The downwelling RW triggered by ERAi and ERA*, with respect to MOD, agrees with a second-like RW baroclinic mode (0.49 $m.s^{-1}$) that displaces westward along 2°N-4°N band from mid-April to July (Figs.

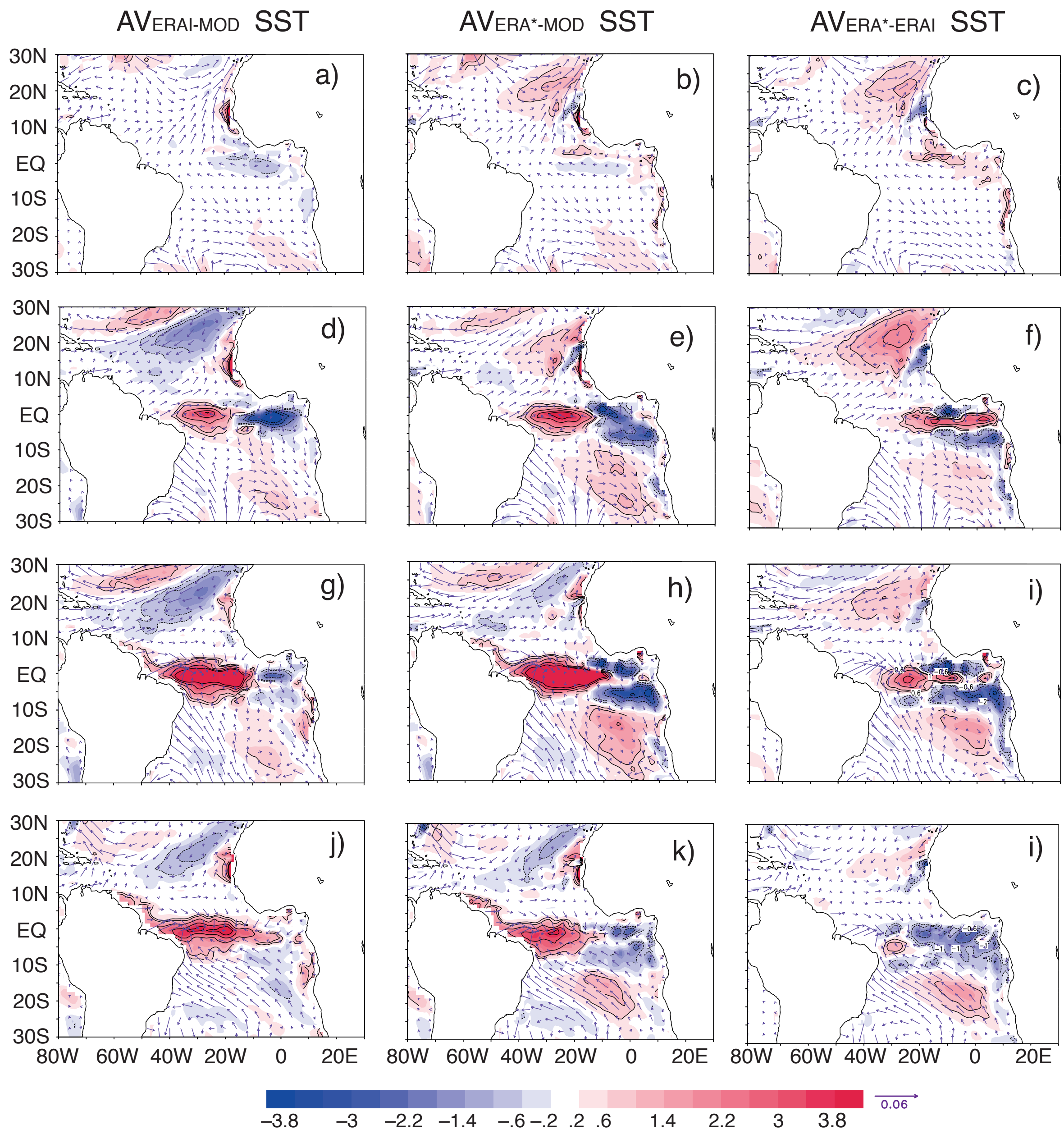

Figure 5.7: Added Value (AV) of simulated SST (in squared ºC) for INTER-ERAi vs. MOD, INTER-ERA vs. MOD, alongside INTER-ERA*-INTER-ERAi experiments, from boreal spring (March-May) to fall (September-November) 2017. Differences between associated wind stress forcings are overlaid in purple vectors. Significant values exceeding 95% confidence level according to a t-test applied over all members are presented in black contours.*

5.8(a)(c)).Then, it is boundary reflected, becoming a downwelling equatorial Kelvin wave that crosses the equatorial Atlantic in June-July, resembling the first baroclinic mode (2.97 $m.s^{-1}$, see Figs. 5.8(b)(d)).

The comparison between the simulations with ERA* and ERAi shows that, despite the former contains a stronger wind curl north of the equator (not shown), there are no significant changes in the generated downwelling RW (Fig. 5.8a). In contrast, an enhancement of the equatorial Kelvin wave propagation during boreal summer is found in ERA* with respect to ERAi (see

Fig. 5.8(f)). The large RW signature seen in wind-forced simulations (Figs. 5.8(a)(c)) can be understood by the spatial pattern of the local realistic winds.

The wind forcing clearly plays a dominant role in establishing the conditions that propel these waves and link the NTA to the equator SST variability. The importance of using proper wind forcing conditions is striking from the results above. This is evident from the outcome of the realistic wind forcing simulations, which properly capture the Rossby wave reflected mechanism linkage between the NTA and the equatorial regions. Moreover, the ERA*-based simulation is able to better resolve the dKW propagation over the equatorial Atlantic than the ERAi-based simulation.

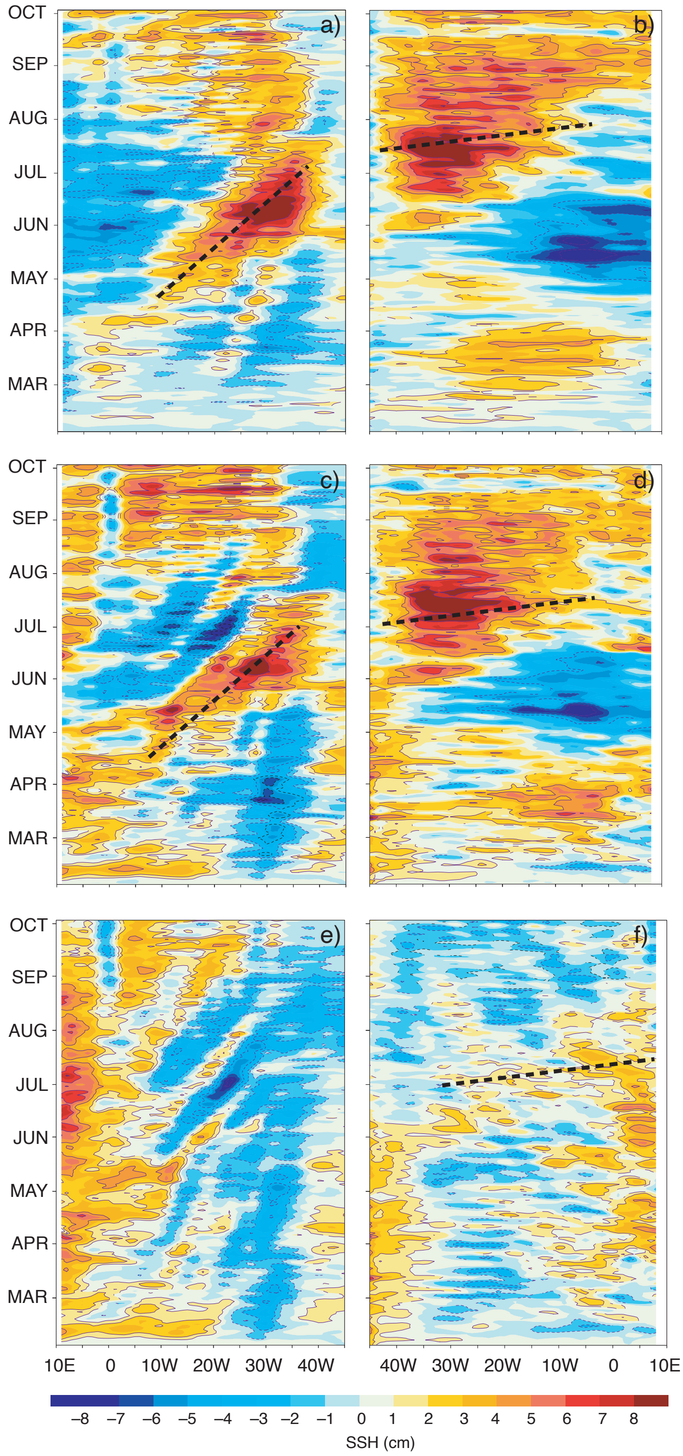

Figure 5.8: Changes in ocean wave propagation. Time-longitude hövmoller diagrams of the difference between daily SSH anomalies in INTER-ERAi w.r.t. MOD (a)(b), INTER-ERA w.r.t. MOD (c)(d) and ERA* w.r.t. ERAi (e)(f), along the [2-4]° N (left panels) and the equatorial (right panels) bands. Notice that the x-axis has been reversed along the 2°N-4°N band to better visualize the RW-reflected mechanism. Black-dash lines indicate the propagation of second Rossby (left) and first Kelvin wave (right) baroclinic modes. Significance has been evaluated according to a t-test applied over the 10 members of each experiment and those values exceeding 95 % confidence level are shown in black contours.*

5.2 Coastal case-study: Adriatic Storm Surges

Severe storm surges in the Adriatic basin leave the northernmost cities located along the coast extremely vulnerable to flooding. These are commonly referred to as '*Acqua Alta*' for floods within the Venice lagoon. These surges are periodic weather events with aggravating consequences to the economy, and a real threat to human lives. Atmospheric conditions favouring storm-surge development are more frequent during the cold season. They occur when a Mediterranean (atmospheric) low-pressure system moves towards the Adriatic inducing an air-pressure gradient over the basin resulting in strong south-easterly Sirocco wind blowing along the basin major axis (Trigo and Davies, 2002). The atmospheric low combined with the persistent Sirocco wind channels the water towards the northernmost and the shallowest part of the sea usually with a wind speed between 10 and 15 $m.s^{-1}$ (Lionello et al., 2012; Međugorac et al., 2018).

Furthermore, the Northern Adriatic sea, is highly affected by well-defined seiche periods and resonant amplification of tides (Tsimplis et al., 1995; Medvedev et al., 2020). Thus, coastal flooding occurs due to the mutual reinforcement between storm surge, tides, and seiches, and the alignment on the temporal phase difference between peak storm surge, peak tide, and peak seiche Cavaleri et al. (2010).

Although weather forecast has greatly advanced in recent years, and ECMWF winds are probably the best boundary conditions for storm surge simulations, local atmospheric models with high resolution and data assimilation give better forecasts than those from the ECMWF global model, which are too coarse to resolve small-scale local variability both in time and space, e.g., the 2019 Venice flood, in which the presence of a very localized low-pressure system went overlooked by all models (Cavaleri et al., 2020) by all models. Moreover, in comparison to scatterometers, the ECMWF outputs in the Adriatic generally underestimate the winds due to low resolution and consequent underestimation of air flow channeling over the Adriatic basin, (Zecchetto et al., 2015). As such, improving meteorological forecasts is one of the potential factors that may improve storm surge prediction.

To this end, considering the enhanced small scale variance (introduced with the SC) present in the ERA* (demonstrated throughout the manuscript), its performance against ERA5 U10S as NEMO-prescribed surface wind forcing is checked in the Adriatic Basin during storm surge conditions. For such purpose, a storm surge that took place during the mid-winter season in 2013, and caused a sea level rise of 143 cm at Venice–Punta della Salute on February 11^{th} at 23:05 UTC, is simulated. Furthermore, the rise in sea level during this event is categorized by Lionello et al. (2021), and percentage wise, 27% is attributed to the astronomical tide, another 27% to the storm surge and a 10% contribution from a seiche. Although a total of three events were actually analysed, two in 2013 (the latter in February and a small one in March) and a historical event that happened in November 2019, but for the sake of brevity, only the February storm surge is analyzed, since the conclusions are similar.

5.2.1 ERA* in the Mediterranean

As seen in subsection 4.2.2 the performance of the ERA* is less optimal in the Mediterranean basin as compared to that in the open ocean. Specifically over the Adriatic sea, the proximity to the coast, the orography, diurnal cycle and large-scale wind evolution over 3 days are expected to further affect the quality of the product.

The ERA5-corrected ERA* U10S products for this study-case are generated globally, using the 3σ filter, and on a regular 12.5 km spatial grid for three different periods. Following the selected storm surge cases, two different ERA configurations with a 3-day TW (N3) are used: one based on the sampling of three sun-synchronous scatterometers (ASCAT-A/B and OSCAT-1) for 2013 (ERA*$_{ABO}$N3), and another one based on four scatterometers (ASCAT-A/B/C and OSCAT-2) for 2019 (ERA*$_{ABCO}$N3). The U10S data products are then cropped for the domain [11 22]°E [38 47]°N and delivered. Note that the data sets are spatially interpolated on to the NEMO curvi-linear grid, which is of higher resolution than that of the ERA* products, and as such the resulting interpolated products preserve the additional small variance present in ERA*.

Although the focus is on the February event, the other two ERA* data sets are also tested. These correspond to a weaker 2013 event (in March), and to a recent stronger historical storm surge in November 2019. The latter is actually a very interesting study case, due to the (previously mentioned) specific weather conditions during the storm surge, which aggravated the surge, and made its accurate prediction more challenging (Cavaleri et al., 2020). Unfortunately, over this region the ERA5 and the ERA5-corrected U10S are quite alike in all three events. The February event is shown because there are more discrepancies between ERA5 and ERA* U10S fields in the 24 hours prior to the peak surge, than for the other two events. However, even for the selected case, one can see from the qualitative assessment of Fig. 5.9, where the wind vectors for both ERA5 (red) and ERA* (black) are plotted, that they actually are very similar during the Sirocco event.

Fig. 5.9 shows the wind vectors for a few hours in the afternoon on the day of the surge, i.e., February 11^{th}. For the most part the U10S direction from both ERA5 and ERA* forcings are quite alike, except in the northernmost part of the basin and along the coast (see Figs. 5.9b to 5.9d). Compared to the second event in 2013 (not shown), the magnitude of the winds is slightly higher here, whilst very similar to the one observed for 2019 (not shown). On the day of the peak surge, typical Sirocco wind (10-15 $m.s^{-1}$) dominates the channel, intensifying throughout the afternoon.

Apart from the qualitative characterization of the two wind fields during the hours before the recorded sea level maximum which, according to the Koper Mareographic Station ($45°33'N, 13°44'E$), happened at 21:20 pm (UTC), an independent scatterometer was used for a more quantitative validation, namely the HSCAT-A.

Table 5.1 shows the values of the metrics used for this evaluation, namely U10S component biases (b_u, b_v), and standard deviations (σ_u, σ_v), and the VRMSD, for both ERA5 and ERA*, w.r.t. HSCAT-A. The scores listed in the table are computed for both regions in Fig. 2.7, and for several periods. Specifically, for a 3-month period (i.e., February-April) for the entire Mediterranean basin, as well as for the Adriatic Sea, and the storm surge and surge periods.

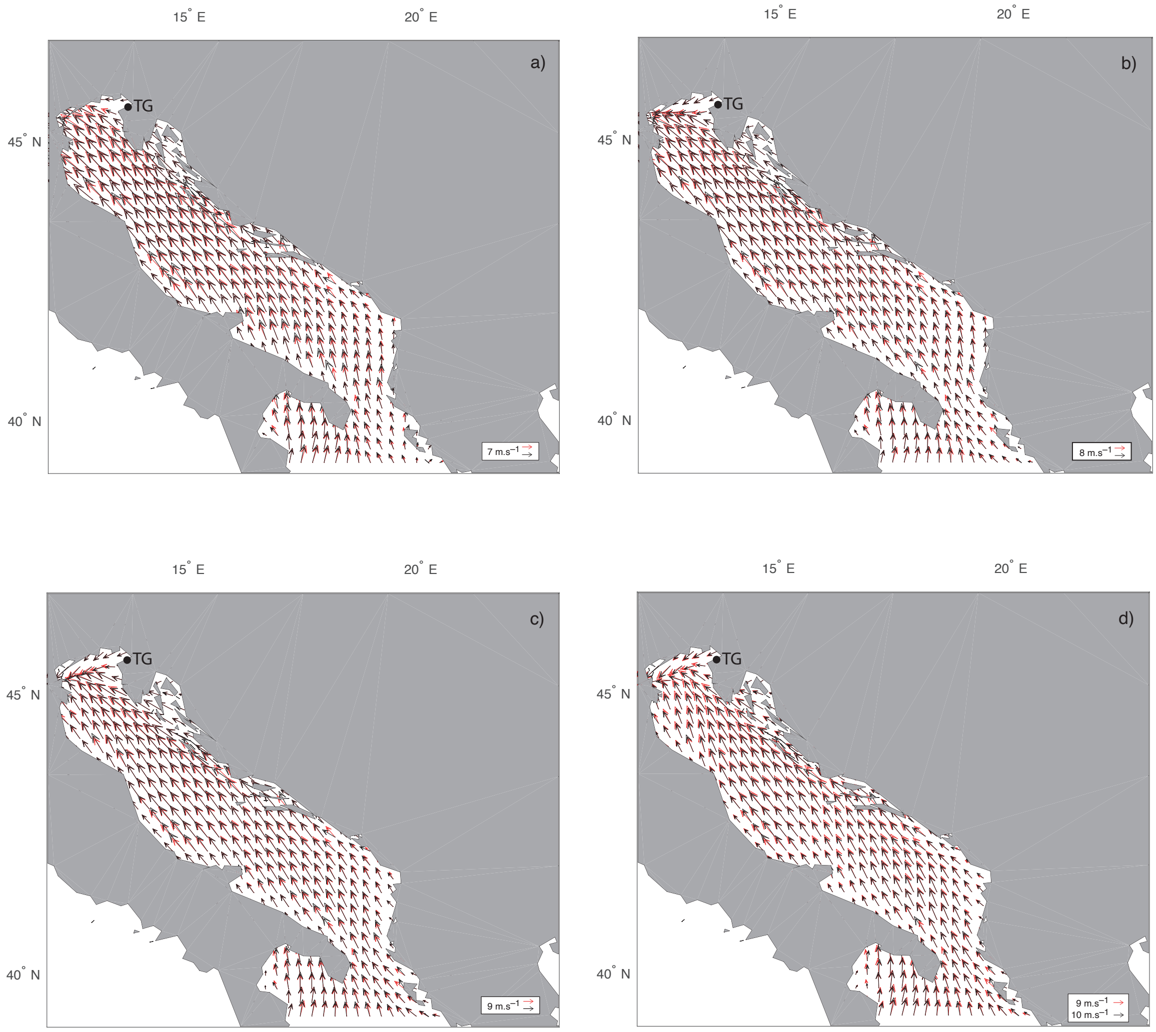

Figure 5.9: U10S derived wind vector maps for ERA5 (red arrows) and ERA (black arrows) in the Adriatic basin (cropped limits), on March 11^{th} for the 15:00 UTC (a), 17:00 UTC (b), 19:00 UTC (c) and 21:00 UTC (d) forecasts. A reference arrow corresponding to the median value in $m.s^{-1}$ is given for each UTC time, applicable to both U10S products. The Koper Tide Gauge location is shown in black.*

Table 5.1: Mean (b) and standard deviation (σ) of the differences between different ERA5/ERA products and HSCAT-A, in the Mediterranean and the Adriatic basins, for both the zonal (meridional) U10S component, over several time periods. VRMSD scores are also included. The numbers of valid winds over which the statistics are computed are shown in parenthesis in the first column.*

	ERA* ($m.s^{-1}$)			ERA5 ($m.s^{-1}$)		
Validation	$b_u(b_v)$	$\sigma_u(\sigma_v)$	VRMSD	$b_u(b_v)$	$\sigma_u(\sigma_v)$	VRMSD
Mediterranean 3M (300813)	0.0215(0.0268)	1.46(1.41)	2.0291	0.124(0.0906)	1.49(1.41)	2.0517
Adriatic 3M (35162)	0.0256(-0.0967)	1.55(1.53)	2.1851	0.1580(-0.1310)	1.56(1.53)	2.1964
7^{th}-14^{th} of February (3364)	0.316(-0.0357)	1.67(1.63)	2.3497	0.544(-0.2050)	1.74(1.64)	2.4574
11^{th}-12^{th} of February (1021)	0.174(-0.492)	1.29(1.19)	1.8311	0.7470(-0.8010)	1.22(1.15)	2.0055

These periods are defined here as follows: the storm surge period starts a few days before and ends a few days after the surge (lasting 7 days), i.e., from 7^{th} to 14^{th} of February, and also marks the beginning of the ocean model simulations; the surge period instead is taken as 24h before and after the surge, i.e., from the 11^{th} to the 12^{th} of February.

The metrics for the 3-month period helps evaluate the performance on a larger scale with average weather conditions in the basin, which also includes the smaller storm surge event on March 30 2013. As expected, a better quality product is obtained for the Mediterranean basin as compared to the Adriatic over the 3-month period, with respect to HSCAT-A, for both ERA5 and ERA* data sets. This was previously anticipated due to the close proximity of the coastline along the Adriatic channel that further aggravates coastal effects, and in turn affects the quality of the product. Moreover, periods of higher wind variability increase collocation errors. In particular, for the Mediterranean, the error variance reduction (see Eq. 2.10) is 2.1%, whilst for the Adriatic only 1%. However, during the surge period, both ERA5 and ERA* show the lowest errors w.r.t HSCAT-A. The rather uniform Sirocco wind that blows over the region is responsible for such low VRMSD scores, with a noticeable error variance reduction of ERA* with respect to ERA5 of a about 16.6%. Also note that ERA* outperforms ERA5 for all the analysed periods and regions. This was not found for the other two events, in which ERA5 and ERA* performances are overall very similar (not shown).

Additionally, the 2d-histogram in Fig. 5.10 shows the similarity between ERA5 and ERA* U10S from the 11^{th} to 12^{th} of February, for the grid locations previously used to obtain the metrics in Table 5.1. Note that the same analysis was performed for the other two events, and it is concluded that the largest ERA/ERA* differences are obtained during the February 2013 storm surge event. According to the bias and standard deviation values shown in Fig. 5.10a(b), the VRMSD between ERA* and ERA5 for the surge period is 0.9754 $m.s^{-1}$, substantially smaller than the VRMSD of either of the products w.r.t to HSCAT-A (see Table 5.1), but still not a negligible difference. Fig. 5.10(c) shows these metrics respectively for the U10S speed and direction components (the latter excluding U10S speeds below 4 $m.s^{-1}$). No relevant wind direction discrepancies between ERA5 and ERA* are found for this period. Note though that the ERA* speeds are on average 0.5 $m.s^{-1}$ lower than those of ERA5.

Although the information provided with spectral analysis would help understand the true scales resolved by these forcings, such analysis is not possible due to the size of the Adriatic basin (see subsection 4.2.2).

5.2.2 Experimental set-up

The impact of different meteorological forecasts for an accurate prediction of the three storm surge events already described, which resulted in flooding over the Northernmost coast of the Adriatic basin, is verified by the set-up of two model simulations using the ERA* and the ERA5 U10S data (see previous section) as the NEMO model prescribed ocean wind forcing.

The NEMO v3.6 model (Madec, 2008), configured on a 999x777 regular longitude-latitude grid with a resolution of 1°/111 over the Adriatic basin ([12-21]°E [39-46]°N), is used for the simulations. This set-up employs 33 vertical z-coordinate levels with partial steps. The Baroclinic timestep is set to 120 seconds, while the barotropic timestep is set automatically to satisfy the Courant-Friedrichs-Lewy (CFL) stability condition. The model is initialized from an operational Mediterranean Forecasting System (MFS), made available through the Copernicus Marine Environment Monitoring Service (CMEMS) product $MEDSEA\_ANALYSISFORECAST\_PHY\_006\_013$

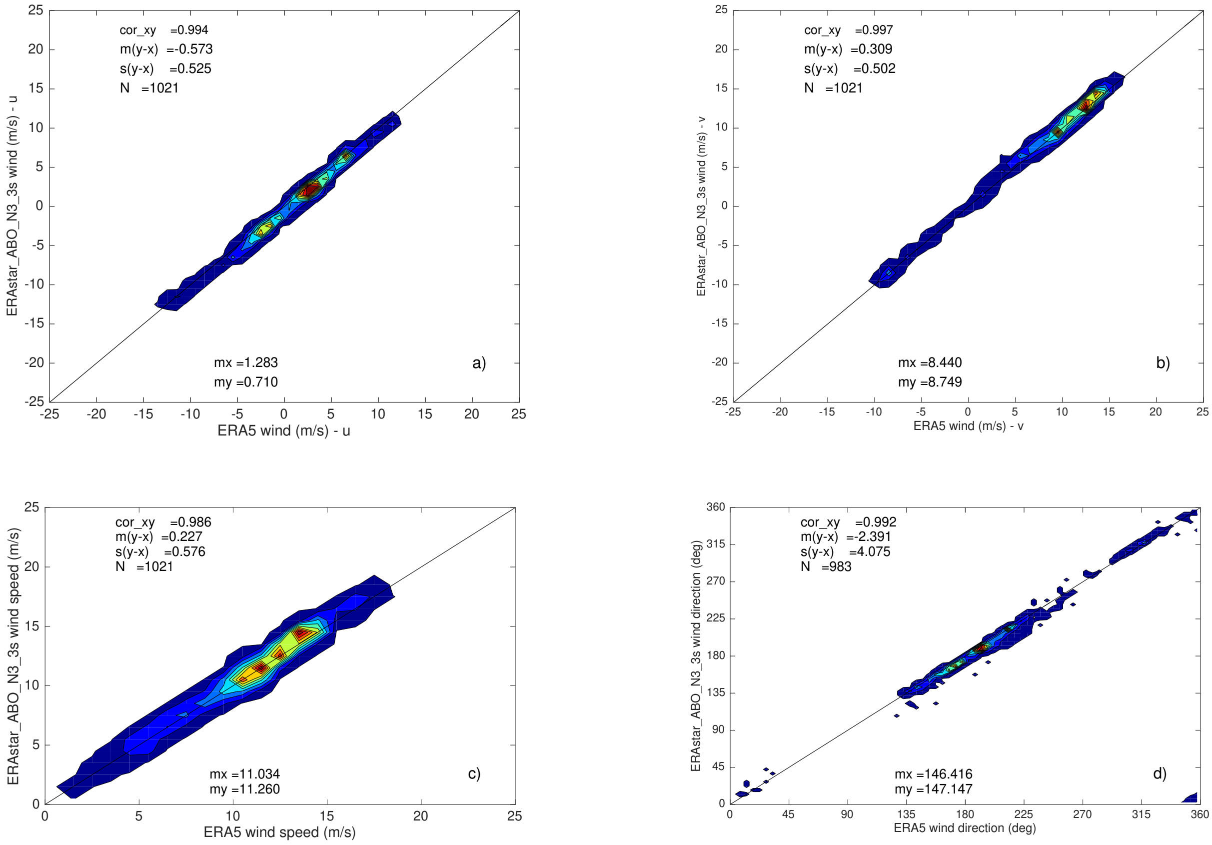

Figure 5.10: Two-dimensional histogram of ERA versus ERA5 U10S, collocated to HSCAT-A, from the 11^{th} to the 12^{th} of February, in the Adriatic Sea (see yellow polygon in Fig. 2.7), for the zonal (a), the meridional (b), the speed (c) and the direction (only for speeds over 4 $m.s^{-1}$, (d) U10S components. The legend shows the correlation coefficient (cor_{xy}), the mean (m(y-x)) and the standard deviation (s(y-x)) of the differences, as well as the number of points (N) used.*

(see Clementi et al. (2021)). The model domain is nested into the Mediterranean basin in the Ionian sea, south of the Otranto strait. Lateral boundary conditions for temperature, salinity and elevation at the open boundary are taken from CMEMS MFS.Flather boundary condition is enforced for elevation, and flow relaxation scheme is enforced for the baroclinic variables and tracers. For surface boundary conditions, this GCM employs the CORE formulation for bulk fluxes, requiring 10-m winds, shortwave and longwave fluxes, 2-m air temperature, humidity, precipitation and snowfall (Large and Yeager, 2004).

As pointed out, U10S from ERA5 and ERA5-corrected (ERA*) are used as the atmospheric fields for these simulations. Note all other atmospheric fields come from the ERA5. Adriatic rivers are included as described in (Ličer et al., 2016). Lateral diffusion is computed using Laplacian operators over geopotential surfaces and the $k - \epsilon$ scheme is used for vertical diffusion of momentum.

5.2.3 Impact on surge forecast

According to SSH measurements from the Koper Tide Gauge located in the Istria Peninsula, the first peak of the surge was registered on February 11^{th} at 21:20 UTC (22:20 CET). Fig. 5.11 shows the SSH time series (m) and the tidal forecast (cm) throughout February 2013, at the Koper TG location. To highlight the data within the storm surge and the surge periods these are shown shaded in gray and yellow, respectively (recall that the storm surge period is from the 7^{th} to the 14^{th} February, while the surge is between 11^{th}-12^{th} February).

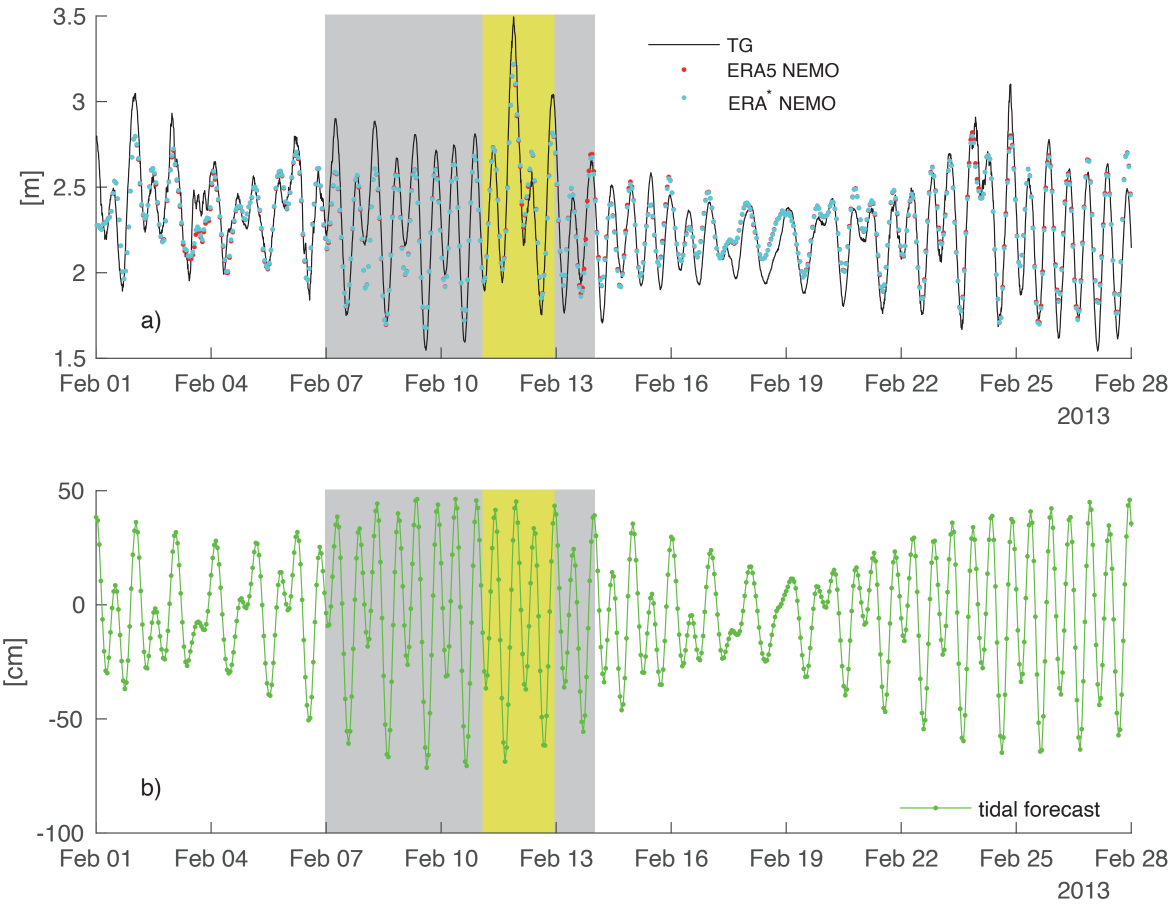

Figure 5.11: SSH (m) time series measured by the Koper Tide Gauge (TG, black line) (Pérez Gómez et al., 2022), and obtained from the NEMO output at the TG location for the ERA (cyan dots) and the ERA5 (red dots) based simulations in 5.11(a). Note that the mean sea level observed by the TG is added to the model outputs to adjust for the geoid. The shaded grey area corresponds to the storm surge period, while the shaded yellow area corresponds to the surge period. The tidal forecast (cm) for the same location is shown in green in 5.11(b).*

Consider that coastal floods in the Adriatic typically occur due to constructive superposition of tides and meteorologically-induced storm surges. According to the SSH observed (black line in Fig. 5.11a) and the tidal prediction (green line in Fig. 5.11b), the recorded peak surge occurs, as previously noted, at 21:20 UTC, and can be identified by the maximum SSH value in phase with the high tide. The tides in the Adriatic Sea have a mixed semi-diurnal cycle with two high and two low tide levels of different height every day. Moreover, the diurnal cycle is also important for the total tidal signal in the basin.

The ocean model response to the atmospheric forcing prescribed for these two simulations (i.e., with ERA5 and with ERA*) is also shown in Fig. 5.11(a). The NEMO SSH output at the tide gauge location almost always overlaps for the ERA5 (red dots) and the ERA* (cyan dots) forced simulations. Note that the TG continuously records the sea level every 10 min, whilst the NEMO output for the SSH is stored on a hourly time step, at 30 min past the hour, i.e., 00:30, 01:30, 02:30 and so on until 23:30. As such, the maximum SSH is depicted at 21:30 (UTC) and the amplitude of the total sea level signal is equally underestimated by both simulations (∼3.22 m) w.r.t. to the TG record (∼3.495 m). These results indicate that unfortunately the ERA* forcing does not improve the storm surge simulation w.r.t. that of ERA5, despite the fact that model sea level predictions are highly sensitive to the correct meteorological forecast.

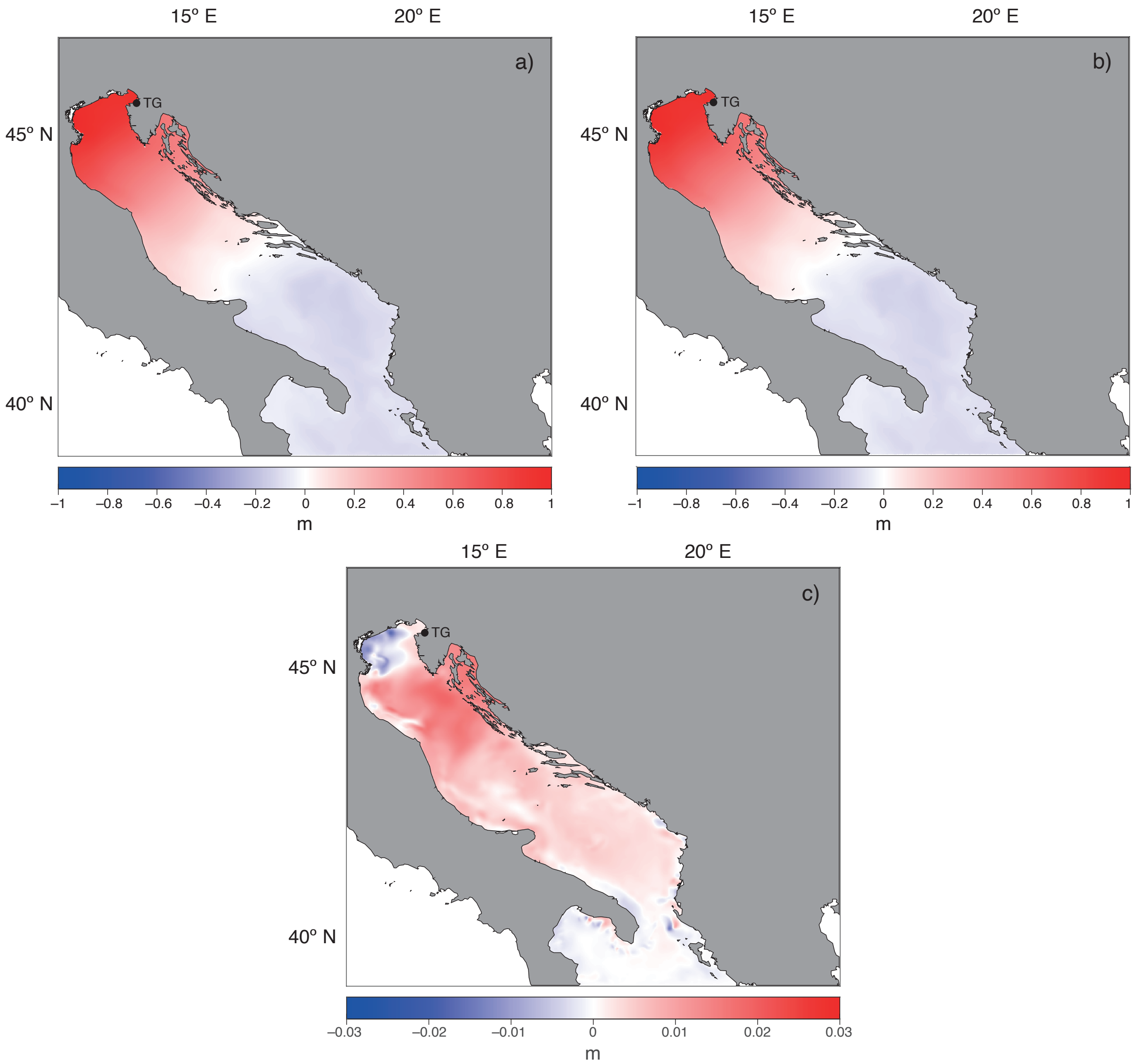

Figure 5.12: NEMO SSH output (m) over the Adriatic basin on February 11^{th} 2013 at 21:30 UTC (closest time to the TG registered surge peak), based on ERA5 ((a)) and ERA (b) forcing. The difference between both model outputs are also shown ((c)). The black dot marks the Tide Gauge location.*

Despite the fact that the simulations fail at predicting the observed surge at the TG location in the Slovenian coast, presenting almost always the same predicted SSH for both simulations, a wider look at the model response over the elongated channel is shown in Fig. 5.12. The NEMO SSH response looks very similar regardless of the wind forcing used, i.e., ERA5 (5.12a) or ERA* (5.12b). Note also that tide gauge observations in Koper measure the total local water depth at the tide gauge location, while the NEMO model only outputs sea level anomaly from the geoid, determined in geodesy as a 18.6-year average over the tide gauge water depth time series. To make quantitative comparisons, we therefore need to shift model SSH so that it matches the mean value of the observed SSH time series within the comparison time window. Figs 5.12a and 5.12a depict basin scale sea level surface, closest to the time of the observed peak surge. Note that the water is pushed along the channel, accumulating all over the Northernmost Adriatic, with a maximum SSH of about 1 m. This qualitative analysis confirms an equal response to the forcing over the entire basin, with model predictions differing about 0.03 m at most. The predicted SSH difference from each simulation (ERA* forced - ERA5 forced) is represented in Fig. 5.12c). In fact, over the TG location, the ERA* predicts higher SSH, as compared to ERA5, however the two simulations present an SSH difference under 0.01 m, thus not significant.

Considering the predicted model SSH for each forcing, i.e., the surge prediction, it is concluded that over the Adriatic, the use of the ERA* product, is as (un)suitable as the ERA5, to improve the Adriatic surge predictions.

5.3 Discussion

Two different application scenarios are considered, where the ERA* is used as the ocean surface forcing prescribed for the GCM NEMO and compared to other atmospheric forcings.

In the open ocean case study presented in section 5.1, the impact of the 2017 NTA warm event on the equatorial Atlantic variability is investigated through a suite of initialized predictions with the EC-Earth3.3 model. Amongst them, the model free-run (MOD) and two realistic wind stress forcing data sets, namely ERAi and ERAi-corrected (ERA*), are prescribed for the tropical Atlantic region.

By using realistic wind stress (both ERA* and ERAi) as NEMO atmospheric forcing, the model is able to reproduce the SST variability triggered by these winds and promoted by the equatorial Rossby wave reflected mechanism, thereby confirming the existence of NTA-equatorial linkage in the 2017 event via wind-induced remote ocean waves, seen in observations and in agreement with previous findings from Martín-Rey and Lazar (2019). On the contrary, because large differences in wind stress can cause distinct SST anomalies, the MOD simulation is unable to correctly capture the observed NTA 2017 warm pattern just with initialized conditions. Note that the reduced north-easterly winds in the ERAi and ERA* reanalysis products (with respect to the modelled wind stress) can activate the latent heat fluxes and damp the coastal upwelling, giving rise to a more realistic SST pattern in ERA* and ERAi based forecasts as compared to those in MOD.

Further addressing the AV of the realistic predictions in the reproducibility of the event, specifically addressing the ERA* forced with respect to ERAi forced simulations, the following findings are listed: the representation of the off-shore NTA and equatorial Atlantic SST during boreal spring is considerably ameliorated in the ERA* forced simulation; also in ERA*, the SW winds and equatorward position of ITCZ contributes to improve the SSTs; and finally, ERA* enhances the propagation of the equatorial downwelling Kelvin wave during the boreal summer.

Overall, the weaker equatorial trades from May to September in both realistic wind stress forecasts with respect to MOD, favor an efficient propagation of the equatorial waves in the Atlantic.

Note though, currently the results do not account for the model SST drift. It is worth mentioning that all climate predictions or forecasts initialized, own a drift that is strongly dependent on the mean state. This drift is large during the first 2-3 months of the forecast and then experiences a smooth transition to reach the equilibrium Exarchou et al. (2018); Voldoire et al. (2019). To remove the drift in the sensitivity experiments, two additional 20-year hindcasts are performed with forcing: a normal prediction from EC-EARTH and another one forced by ERAi wind stress covering the period 1997 to 2017, i.e., a control-hindcast and an ERAi-hindcast. Because it is not possible (yet) to generate a 20-year hindcast for ERA* (since there is insufficient scatterometer sampling to produce a viable scatterometer correction before 2010), and considering the findings presented here using INTER-ERAi and MOD, the ERAi-hindcast is used to correct for the ERA* drift. The results after the drift correction are disclosed on the paper in preparation.

In summary, despite the fact that some of the mesoscale variability in the original ERA* (before being interpolated into the coarser grid) is lost w.r.t. the product used in the INTER-ERA* simulation, for this study, which is focused on climate variability modes and the large scale signal, the performance of ERA* is notable, suggesting that the product may be of an AV for this type of studies.

For the coastal case study presented in section 5.2, which attained at improving the storm surge predictions in the Adriatic Sea, several factors contributed to the fact that the storm-surge prediction capabilities are not improved by none of the forcings, i.e., ERA5 or ERA5-corrected (ERA*).

Note that for this section, three storm surge events are analyzed, and although results are only presented for the February 2013 event, similar outcomes were obtained for the events from March 2013 and November 2019. As such, the same conclusions (as discussed below) can be drawn for all three cases.

Departing from small discrepancies between the ERA5 U10S and the generated ERA* U10S field during the storm surge period (subsection 5.2.1), all the NEMO simulations yielded very similar SSH predictions. The storm surge event is inaccurately reproduced by the NEMO simulations, this may be because neither ERA5 nor ERA* are accurately resolving the sea-surface wind (U10S) prior or during the event. The peak storm surge in the SSH predictions misses the true amplitude of the surge as well as its timing, with a delay of about 10 min (although the latter is mainly due to the hourly binning of the model forecasts). Note that floods occur when the Sirocco wind is in phase with the tide. Hence, the actual peak in the total sea level recorded at the Koper tide gauge (over the Slovenian coast), in phase with the high tide from the tidal forecast for this location, gives a total sea level about 20 cm higher than the NEMO predictions.

It is argued that both the mean magnitude and direction of typical Sirocco wind is well represented in the prescribed atmospheric forcing during the storm surge period, and as such a storm surge is reproduced by NEMO. However, the presence of fast evolving weather conditions during the surge, not well captured by ERA5, cannot be resolved by ERA* (by definition). Indeed, a 3-day based correction in ERA* will filter out transient weather, while only correcting for persistent local ERA5 biases. As explained by Cavaleri et al. (2020), for the 2019 floods over the Venice bay, the presence of a very localized cyclonic activity unresolved in most NWP models was behind the inaccurately predicted floods.

A reason for the resemblance between the ERA* and ERA5 U10S fields in the Adriatic Sea, is the fact that near the coast the 3σ filter should be more active than in open ocean regions, since more wind variability is expected near the coast. This will in turn lead to rather smooth scatterometer-based corrections. A shorter temporal window of 1-day has been tested in the Adriatic with rather inconclusive results. Indeed, the proposed methodology does not aim at resolving transient weather. While a 1-day TW may be able to depict some more transient features (on a daily scale) over the storm surge period, the relatively poor sampling within such short TW hampers the ability of ERA* to properly correct for transient local ERA5 biases. Moreover, since the true transient weather is under-sampled, potential artifacts in the resulting ERA* U10S fields will arise. Future work should focus on looking for other storm surge events for which ERA* (N3 configurations) and ERA5 U10S fields are more discrepant, in order to check for potential benefits of this methodology under specific storm surge preconditions.

Chapter 6

Conclusions and Outlook

Throughout this manuscript, all the stages involved in the development of the L4 high resolution ocean wind forcing product *ERA** are carefully disclosed. Considering the high demand for an accurate ocean surface wind forcing product, particularly in what concerns ocean modelling activities and atmosphere-ocean coupling, as well as the limitations of the most commonly used atmospheric forcing solutions, this closing chapter begins by addressing the research question proposed in the thesis.

1. Is it possible to improve the currently available surface wind forcing products by developing a more accurate, high resolution forcing with the information contained in the scatterometer data?

The requirements for ocean forcing products are evolving as coupled atmosphere-ocean models become more sophisticated. Where earlier products were monthly, today's modelling systems may produce hourly outputs. As opposed to ocean vector wind or stress observations that although ever more abundant, are not globally available every hour. Many publications in the past decade show however the lack of mesoscale detail in atmospheric model winds as compared to collocated scatterometer winds. Moreover, many of these differences appear locally bound and persistent in time. This leads to the idea that model winds may be amended by scatterometer corrections (SC) at every time step, but where the SC is estimated over a long time period. This idea is verified in this thesis.

Moreover, it is worth noting that the limitations of currently available surface wind forcing products are still generally associated either with their insufficient spatio-temporal coverage (as in the case of observations, e.g., high quality U10S from scatterometers) or with their coarser effective resolution and lower accuracies, as is the case of atmospheric models (NWP or reanalysis) (Saha et al., 2014; Dee et al., 2011; Hersbach et al., 2020) or hybrid products (Desbiolles et al., 2017; Mears et al., 2019). As for the particular question above, throughout the thesis it has been verified that the proposed product (ERA*) is indeed of higher resolution and accuracy than the (uncorrected) ERA product, particularly so in open ocean regions, due to the introduction of the oceanic mesoscales captured by the scatterometers into the ERAi/ERA5 NWP reanalysis.

Unlike these other forcing solutions that integrate observations, ERA* is based on a slowly evolving mean scatterometer correction for local biases in the NWP reanalysis, for which a sufficient amount of scatterometer winds is available at each location. This largely guarantees that mixed spatio-temporal interpolation functions are avoided in the proposed product. In periods of long-term (greater than 2 days) instrument failure or other problems resulting in missing data or under-sampling, longer time windows (TW) for the SC may be allowed at the expense of a small degradation in quality.

The additional variance is evident in visual assessments of the U10S-derived maps for all configurations presented, and corresponds to physical processes absent or misrepresented by the NWP model, e.g., strong current effects (such as WBCS, highly stationary), wind effects associated with the ocean mesoscales (SST), coastal effects (land sea breezes, katabatic winds), parameterization errors, and large-scale circulation effects. As expected, additional variance in the ERA* is localized where model biases have been accentuated in the SC maps.

Using U10S scatterometer data as an independent validation source (HSCAT) it was verified that this variance is dominated by true local wind signals rather than by random noise. From the overall configurations addressed in the manuscript, the optimal ERA* is obtained with the best compromise between sufficient scatterometer sampling and capturing the spatial and temporal mesoscales. Thus, using multiple scatterometers and a TW of about 3 days shows the best potential. Note though, this conclusion is sustained for the scatterometer constellations available from 2010-2020, while it should apply to future operational scatterometer constellations that are complementary, as the ASCATs and the OSCATs were.

Incidentally, the SC is used to correct model biases in the nowadays obsolete ERAi and in today's ERA5 reanalysis, and the above conclusions apply to both. Although the two contain similar error structures, as found here and previously by Belmonte Rivas and Stoffelen (2019), the biases in the ECMWF model have evolved in recent years (mainly with respect to amplitude) and are smaller for ERA5 than for ERAi. As a result, for the same ERA^*_{ABO}N3 configuration, the ERAi-corrected product achieves a an error variance reduction of 10% w.r.t HSCAT, while the ERA5-corrected product shows a smaller reduction of 6% (globally) in HSCAT differences.

Spatial spectral analysis using HSCAT as an independent validation source shows that, over the open ocean, ERA* effectively adds variance at both longer and smaller (about 50 km) spatial scales, significantly smaller than those resolved by ERAi (about 150 km), and even smaller than the structures resolved by ERA5 (Jourdier, 2020; Vogelzang and Stoffelen, 2021). Yet the new U10S fields are still smoother than those of the scatterometer. Furthermore, at smaller scales, the spectra are less affected by the spatial sampling (number of scatterometers used) than by the size of the temporal window, although a slight smoothing effect is shown when more scatterometers are used in the SC. As a rule, this method shows improvements for increased number of scatterometers accumulated over reduced TWs, as consistently seen for different years and scatterometer combinations. Yet, daily TWs are generally of worst quality even if enough scatterometers are used.

It should be noted that although both the ERAi-corrected and ERA5-corrected ERA* result in a sea surface wind forcing product containing smaller scales than the original reanalysis (showing the same performance trends), the latest ERA* is a higher quality product than its predecessor. To summarise, the ERA5 U10S is better than ERAi U10S, while ERA5-corrected is better than ERAi-corrected, and overall, the ERA5-corrected ERA^* is the best.

In either case, for the optimal ERA* configuration, local model biases due to wind effects associated with ocean mesoscale processes, parameterizations and dynamics are reduced by the SC, particularly over open ocean regions. Yet, as explained next, there is room for further improvements, notably so in coastal regions.

2. How does regional scatterometer sampling and weather affect the performance of static corrections, particularly in regions dominated by fast evolving atmospheric phenomena or increased wind variability?

Indeed, the effectiveness of the ERA* method is intrinsically modulated by the regional scatterometer sampling, wind variability and local bias persistence, as seen in Chapters 3 and 4. Before addressing the question itself, note that, the static mean correction is not meant to depict random atmospheric 3D turbulence, which has a life cycle of a few hours and therefore it's averaged out by the SC (longer time windows). Still, transient weather affects the quality of the ERA*, particularly in case of insufficient sampling, in case of high local variability, and/or in case the local variability changes the mean state, e.g., persistent moist convection or coastal effects. Therefore, regional product quality improvement by ERA* is more limited in the middle latitudes or in coastal regions and larger in the tropics and high latitudes.

The middle latitude regions are dominated by increased variability, in particular due to transient weather processes near the storm tracks. Wright et al. (2021) describes the variable conditions as a function of latitude, but also longitude, showing different triple collocation statistics of buoys, ERA5 and ASCAT, indicating variable biases and errors across the ocean due to the transient weather and its interaction with the land masses. On the one hand, it will be interesting to investigate the quality of ERA* further as a function of season and hemisphere. Nevertheless, it is likely that biases due to transient weather effects are also reduced in the averaging over the TW. On the other hand, errors associated to the distribution of land masses and the implied local flow regimes, both in the ocean and atmosphere, will persist and are corrected in the SC. Both the effects of the transient errors and the persistent errors, as further analyzed in (Belmonte Rivas and Stoffelen, 2019), appear in the SC for the middle latitudes. Hence, despite increased sampling in the middle latitudes, the tropics outperforms the former in reducing systematic error variance. It is clear that for shorter TWs transient weather errors may be captured as noise, degrading the product (recall N1 results from subsection 4.2.2).

Note that wind variability is also present in the tropics, particularly through moist convection near the ITCZ, while systematic errors are well corrected in most areas at these latitudes. Note, however, that this region is more prone to under-sampling than others due to the sun-synchronous orbit of the scatterometers, especially for configurations with few complementary scatterometers. As first discussed in Chapter 3, under-sampling in the SC corresponds to less than 4 scatterometer samples per grid location, in which case ERA* is either of equal or worse quality than the original ERA. Still, the latter can be avoided by using longer temporal windows of accumulation, at the cost of somewhat smoothing U10S as compared to the shorter TWs. For the trades, which is considered a region characterized for the most part by persistent local conditions, when optimal sampling is achieved the static mean correction improves the product.

High latitudes are at the same time the region with more transient dynamic weather errors as well as with the largest scatterometer sampling (provided by the wider range of overpass times, due to the wider longitudinal coverage of the swaths closer to the poles), hence generally resulting in good performance to compute the static part of the SC. However conclusions for this region should be taken with caution as using a verification source with closer over passing times to the SC may positively bias the validation. Alternatively, this potential effect may be tested by carefully choosing scatterometer verification passes further apart from those of the scatterometers used in the SC.

Increased wind variability conditions, including the diurnal cycle and relatively steep wind gradients, such as katabatic winds, are expected near the coast culminating in a reduced performance of the ERA models. On the other hand, reduced and irregular scatterometer sampling is also characteristic of these regions. Consequently, the performance of the static correction drops in coastal regions. Coastal effects hence degrade the quality of both the ERA and ERA* products near the coast, due to reduced model performance, insufficient/non-uniform scatterometer sampling (which leads to mixed spatio-temporal characteristics affecting the accuracy of the U10S), and reduced local bias persistence. In fact, the method implicitly assumes that the diurnal cycle near the coast is perfectly represented by ERA, since only long-term biases are corrected, which are measured at the satellite overpass times only.

Overall, the performance of the method is degraded by the presence of transient weather, and this is further aggravated in under-sampled regions. Moreover, both transient and persistent model errors are spatially correlated as, e.g., in resp. Vogelzang and Stoffelen (2018) and Belmonte Rivas and Stoffelen (2019), and transient weather effects cannot be fully resolved using a static mean correction of 1-day, i.e., the smallest TW shown in the analyses is too long to properly capture the synoptic variability. Yet, a small part of the fast and random $k^{-5/3}$ 3D turbulence and convection is present as sampling noise. Essentially, the biases in rapidly evolving atmospheric weather are not intended to be accurately depicted by the method used, only its mean contribution to ERA biases. To reduce random red noise from the SC corrections, outliers are filtered out (using a 3σ filter).

As a summary, the static correction is relatively straightforward to estimate over regions with the more persistent local weather, e.g., in the trade winds region (excluding the ITCZ), and is more noisy in areas characterized by transient weather (middle latitudes and coastal regions). More so, it is demonstrated that to effectively correct for persistent biases, the optimal trade-off between sampling and local bias persistence is achieved by combining complementary scatterometers (in terms of sampling) over a relatively short TW. In this manner, the effects of transient phenomena and sampling artifacts are minimized without smoothing the signature of oceanic mesoscale features and other contributions to the SC.

3. Does ERA* wind forcing make for more realistic representations of oceanic circulation in numerical simulations than NWP forcing?

Compared to other forcing solutions (including NWP), there is value in using wind stress fields from ERA* as atmospheric forcing for large-scale ocean simulations, as presented in a case-study on tropical Atlantic variability discussed in Chapter 5). The following conclusions are based on the comparison between the ERAi reanalysis (NWP forcing example) and the ERAi-corrected ERA*. Note that it has been verified that between ERAi and ERA*, the latter is a higher quality surface wind product (results in subsection 5.1.1).

Using GCM NEMO as the ocean model in the EC-EARTH climate model, a set of three prescribed atmospheric forcings, i.e., an EC-EARTH model run and two higher resolution realistic forcings (ERAi and ERA*), are analysed for their ability to drive the oceans dynamical response to the wind (i.e., oceanic waves) and reproduce the 2017 warm event over the tropical Atlantic that led to one of the most devastating hurricane season over the past decade (Nobre and Srukla, 1996; Xie and Carton, 2014; Klotzbach et al., 2018). Of the three, only the simulations forced by realistic winds, produced the ocean wave mechanisms linking NTA and equatorial-Atlantic SST variability.

For these simulations, the ERA* wind stress fields (produced for a 25 km regular grid) are interpolated into a coarser grid (NEMO grid) losing some of the mesoscale variability introduced in the ERAi-corrected fields. However, through the ERA* method, intermediate and large scale model biases are also corrected, which, for the purpose of this study that is focused in climate variability modes and the large scale signal, are considered more relevant.

Indeed, added value is generally found from using the corrected (ERA*) wind stress fields with respect to those of ERAi, e.g., improved model response to the SST signal in the NE tropical Atlantic, better representation of the Atlantic Meridional Mode (AMM) in spring time, also seen in the Western/Central equatorial during the summer/spring. Most importantly, the stronger wind stress curl resolved by ERA* (w.r.t. ERAi) leads to an enhancement of the equatorial Kelvin wave propagation during boreal summer.

4. Can the ocean models response to high wind variability conditions, e.g., storm surges, be improved by static corrections of the NWP forecast winds?

As already mentioned, most biases due to transient weather phenomena, e.g., extra-tropical storms, moist convection induced wind variability or storm surges, are too fast to be properly captured using long TW in a static SC, as theoretically demonstrated by simulated phase shift in section 3.2. However, even in regions where high wind variability usually prevails over more steady weather, systematic errors are also present, though these are harder to mitigate under such conditions using the static correction. Therefore, although improvements in performance can still be obtained by excluding the more transient biases, as can be seen throughout Chapter 4 for the middle latitudes and coastal regions, the signal from transient weather may be partially captured by the method as noise (shorter TWs).

Nevertheless, for high resolution numerical simulation purposes, small-scale variability associated with relatively rapidly evolving atmospheric phenomena affects ocean-atmosphere exchanges and is of fundamental importance for forcing ocean models. Therefore, removing/smoothing this variability from the product may work for large-scale simulations, but does not improve the ocean model's response to very localized transient events.

The latter has been verified in section 5.2 by trying to improve the storm surge prediction capabilities of the GCM NEMO over the Adriatic using the ERA5 and ERA5-corrected ERA* U10S product. A three-day TW is used for forcing the ocean model. Note though that for the Adriatic basin the diurnal cycle is very important and neither ERA5, nor subsequently ERA*, are able to depict it. Accurate storm surge prediction in the Adriatic bay is at the same time very challenging and very pressing (Giesen et al., 2021). The combination of a very steady Sirocco wind with the meteorological displacement of a low pressure system towards the Northern Adriatic requires a wind forcing able to capture the evolution of the storm locally, while the 3-day ERA* depicts the same (inaccurate) ERA5 transient weather during the storm, as the SC is static. The three Adriatic storm surge events analyzed in this study give the same model response to both the ERA5 and the ERA5-corrected ERA* U10S forcing, none of which accurately capturing the storm surge. Moreover, although U10S discrepancies between ERA5 and ERA* U10S are seen before and after the storm surge event, these are small in the day prior to the surge, indicating that very similar Sirocco wind conditions are captured by both forcing products when the relatively strong wind is in phase with the tidal wave (precondition for surge). As such, the same (and inaccurate) modeled SSH is obtained from both forcings.

To conclude, a static mean correction will not improve the reanalysis U10S in what concerns capturing high frequency atmospheric variability, therefore more physically-based corrections, e.g., improved drag formulations or improved NWP model initialization, are much more likely to improve the ocean model response in high wind variability conditions.

All combined, the findings emphasized while answering these research questions briefly summarize some of the main conclusions regarding the development and validation of the ERA*. The potential of this methodology in the development of high resolution ocean wind forcing products is seen in the extensive product validation that indicates that indeed smaller scales are introduced by the scatterometers in the new product because the signature of oceanic mesoscale features is imprinted in the atmosphere. A further potential is seen in the application section for large-scale ocean circulation studies, where the larger scale corrections are most relevant (by better capturing the wind curl w.r.t. other tested forcings). In summary, this work shows the added value in using a static mean scatterometer-based correction for correcting NWP model output local biases, and also its drawbacks, for two ECMWF reanalyses.

Essentially, the methodology developed during this PhD thesis proves regionally dependent both on scatterometer sampling and wind bias persistence (local weather regimes). Consequently, in regions of persistent local conditions, e.g., the trade winds regions, the method is very effective. As expected though, in areas more often affected by transient weather phenomena the SC is more noisy, and this is reflected in the quality of the ERA*. On the other hand, corrections in these more dynamic regions are larger and associated with the transition of large-scale dynamical modes that models often poorly predict. Hence, an improved description of the mean forcing in these variable conditions may be relevant.

In particular, coastal effects are poorly described in ERA, but have high societal and economic relevance. Furthermore, ERA* implies a perfect diurnal cycle in ERA, as its corrections are accumulated over several days and different times of the day. In addition, the higher wind variability conditions, including diurnal effects, combined with the irregular scatterometer sampling very close to the coast (25 km) make it difficult to develop and test the SC here. More future work will be needed, following current developments to improve scatterometer wind processing in coastal areas.

Future work is focused on further improving the quality of L4 ocean surface gridded winds. In particular, besides providing biases in the SC, also differences in scatterometer and model wind variances over the TW could be provided to capture model deficiencies in dynamical and physical processes.

Considering the results with scatterometer sea surface wind data for correcting NWP model output local biases, there are planned activities for future improvements of the present ERA* approach (in particular for better correcting in high wind variability conditions). These would include the use of Ku-band rotating pencil beam scatterometer-derived U10S fields less affected by across-track biases, further reducing the transient weather effects and characterizing low sampling effects in the computation of the SC (e.g., in coastal areas). But mostly, knowing that the NWP wind vector biases are linked to atmospheric stability effects, moist convection, ocean currents, SSTs, etc., it is considered that more flexible SCs ought to be applied in order to improve the quality of NWP winds.

NWP stability-dependent errors in the boundary layer formulation are quite important. According to Brown et al. (2005a, 2006) in the ECMWF model formulation, momentum mixing seems too strong in the stable and neutral boundary layer and too weak under unstable conditions, this leads to too strong ECMWF winds under stable conditions and too weak under unstable conditions, and this shows up as a residual wind speed bias when compared to scatterometer winds. Moreover, a lack of NWP cross-isobaric flow has been reported Hersbach (2010a); Sandu et al. (2013b).

Such biases are problematic in data assimilation, as current data assimilation methods imply unbiased model and observation fields (Stoffelen and Vogelzang, 2020). Hence, SC would be helpful to achieve this and provide a better dynamical initialization of NWP models. In operational NWP, however, the SC can only be based on past scatterometer data and not use centered TW as performed in this thesis. Such lagged operational L4 product has been developed, tested and implemented in the European Union Copernicus Marine Service (CMEMS) recently.

ECMWF-based corrections applied to ASCAT U10S are expected to make these observations unbiased with respect to the ECMWF model, thus guaranteeing locally unbiased data sets. Applying ECMWF-based corrections to ASCAT (generating a so-called ASCAT*) would make the scatterometer winds less accurate yet consistent (unbiased) with respect to the NWP model. Consequently, the outcome from data assimilation should provide better dynamical initialization of weather disturbances. Note that this correction would be a reversed-ERA* applied operationally, i.e., locally correcting for ASCAT wind component biases with respect to the NWP, using a SC based on past ASCAT data.

As is, the ERA* method aims at removing NWP local biases but it is not always effective in doing so. The method is intrinsically dependent on scatterometer sampling at each particular grid point, while stability-dependent biases are not, and SST gradient wind effects are dependent on the local flow (weather). Consequently, it is believed that a more functional relationship between stability, SST, current and scatterometer versus NWP differences can lead to more effective SC and therefore improved NWP bias mitigation. In addition, such model-dependent SC can be applied in forecasts too, e.g., to test the coupling of atmospheric and ocean models.

Deep learning methods (Sonnewald et al., 2021) are currently being used to generate sea level forecasts, driven partly with direct sea level observations (Žust et al., 2021) or to provide better estimates of relevant variable fields (Barth et al., 2020, 2022) which can be used to force numerical models. These methods are fast and numerically cheaper than data assimilation and have already been demonstrated to allow reliable reconstructions of sparse satellite measurements of SST and SSH anomalies (Barth et al., 2020, 2022).

Taking the previous examples, employing machine learning methods built upon NWP forecast fields of ocean vector winds and associated ocean surface and atmospheric parameters to predict SC, should improve NWP surface wind and stress fields for both atmospheric and oceanic applications. This is considered for the near future. These new SC may be used for data assimilation, seasonal forecasting and of course in NWP and ocean model parameterization studies.

Bibliography

Atlas, R., Hoffman, R. N., Ardizzone, J., Leidner, S. M., Jusem, J. C., Smith, D. K., and Gombos, D. (2011). A Cross-calibrated, Multiplatform Ocean Surface Wind Velocity Product for Meteorological and Oceanographic Applications. *Bulletin of the American Meteorological Society*, 92(2). 3, 15

Bajo, M., De Biasio, F., Umgiesser, G., Vignudelli, S., and Zecchetto, S. (2017). Impact of using scatterometer and altimeter data on storm surge forecasting. *Ocean Modelling*, 113:85–94. 18

Balmaseda, M. A., Trenberth, K. E., and Källén, E. (2013). Distinctive climate signals in reanalysis of global ocean heat content. *Geophysical Research Letters*, 40(9):1754–1759. 107

Barth, A., Alvera-Azcárate, A., Licer, M., and Beckers, J.-M. (2020). DINCAE 1.0: a convolutional neural network with error estimates to reconstruct sea surface temperature satellite observations. *Geoscientific Model Development*, 13(3):1609–1622. 130

Barth, A., Alvera-Azcárate, A., Troupin, C., and Beckers, J.-M. (2022). DINCAE 2.0: multivariate convolutional neural network with error estimates to reconstruct sea surface temperature satellite and altimetry observations. *Geoscientific Model Development*, 15(5):2183–2196. 130

Belmonte Rivas, M. and Stoffelen, A. (2019). Characterizing era-interim and era5 surface wind biases using ascat. *Ocean Science Discussions*, 2019:1–31. 6, 8, 13, 17, 34, 49, 52, 53, 58, 65, 68, 74, 93, 99, 126, 127

Bentamy, A. and Fillon, D. C. (2012). Gridded surface wind fields from Metop/ASCAT measurements. *International Journal of Remote Sensing*, 33(6):1729–1754. 11

Bentamy, A., Katsaros, K. B., Drennan, W. M., and Forde, E. B. (2001). Daily surface wind fields produced by merged satellite data. In *Geophysical Monograph Series*, volume 127, pages 343–349. Blackwell Publishing Ltd. 15

Bentamy, A., Katsaros, K. B., Mestas-Nuñez, A. M., Drennan, W. M., Forde, E. B., and Roquet, H. (2003). Satellite Estimates of Wind Speed and Latent Heat Flux over the Global Oceans. *Journal of Climate*, 16(4):637–656. 15

Bentamy, A., Quilfen, Y., Gohin, F., Grima, N., Lenaour, M., and Servain, J. (1996). Determination and validation of average wind fields from ERS-1 scatterometer measurements. *Global Atmosphere and Ocean System*, 4(1). 15

Biasio, F. D., Bajo, M., Vignudelli, S., Umgiesser, G., and Zecchetto, S. (2017). Improvements of storm surge forecasting in the gulf of venice exploiting the potential of satellite data: the esa due esurge-venice project. *European Journal of Remote Sensing*, 50(1):428–441. 18

Blanke, B., Speich, S., Bentamy, A., Roy, C., and Sow, B. (2005). Modeling the structure and variability of the southern Benguela upwelling using QuikSCAT wind forcing. *Journal of Geophysical Research C: Oceans*, 110(7):1–18. 6

Bourassa, M. A., Meissner, T., Cerovecki, I., Chang, P. S., Dong, X., De Chiara, G., Donlon, C., Dukhovskoy, D. S., Elya, J., Fore, A., Fewings, M. R., Foster, R. C., Gille, S. T., Haus, B. K., Hristova-Veleva, S., Holbach, H. M., Jelenak, Z., Knaff, J. A., Kranz, S. A., Manaster, A., Mazloff, M., Mears, C., Mouche, A., Portabella, M., Reul, N., Ricciardulli, L., Rodriguez, E., Sampson, C., Solis, D., Stoffelen, A., Stukel, M. R., Stiles, B., Weissman, D., and Wentz, F. (2019). Remotely

Sensed Winds and Wind Stresses for Marine Forecasting and Ocean Modeling. *Frontiers in Marine Science*, 6. xiii, 8, 11, 17

Brown, A. R., Beljaars, A. C., Hersbach, H., Hollingsworth, A., Miller, M., and Vasiljevic, D. (2005a). Wind turning across the marine atmospheric boundary layer. *Quarterly Journal of the Royal Meteorological Society*, 131(607):1233–1250. 130

Brown, A. R., Beljaars, A. C. M., and Hersbach, H. (2006). Errors in parametrizations of convective boundary-layer turbulent momentum mixing. *Quarterly Journal of the Royal Meteorological Society*, 132(619):1859–1876. 130

Brown, A. R., Beljaars, A. C. M., Hersbach, H., A., H., Miller, M., and Vasiljevic, D. (2005b). Wind turning across the marine atmospheric boundary layer. *Q.J.R. Meteorol. Soc.*, 131(607):1233–1250. 17

Bryan, F. O., Tomas, R., Dennis, J. M., Chelton, D. B., Loeb, N. G., and McClean, J. L. (2010). Frontal Scale Air–Sea Interaction in High-Resolution Coupled Climate Models. *Journal of Climate*, 23(23). 5

Bryan, K. and Cox, M. D. (1967). A numerical investigation of the oceanic general circulation. *Tellus*, 19(1). 5

Carton, J. A. and Giese, B. S. (2008). A Reanalysis of Ocean Climate Using Simple Ocean Data Assimilation (SODA). *Monthly Weather Review*, 136(8):2999–3017. 16

Cavaleri, L., Bajo, M., Barbariol, F., Bastianini, M., Benetazzo, A., Bertotti, L., Chiggiato, J., Ferrarin, C., Trincardi, F., and Umgiesser, G. (2020). The 2019 Flooding of Venice and Its Implications for Future Predictions. *Oceanography*, 33(1):42–49. 115, 116, 123

Cavaleri, L., Bertotti, L., Buizza, R., Buzzi, A., Masato, V., Umgiesser, G., and Zampieri, M. (2010). Predictability of extreme meteo-oceanographic events in the Adriatic Sea. *Quarterly Journal of the Royal Meteorological Society*, 136(647):400–413. 115

Chassignet, E. P., Le Sommer, J., and Wallcraft, A. J. (2019). General Circulation Models. In *Encyclopedia of Ocean Sciences*. Elsevier. 5, 6

Chassignet, E. P. and Verron, J. (2006). *Ocean Weather Forecasting: An Integrated View of Oceanography*. Springer. 5, 6

Chelton, D. and Freilich, M. H. (2005). Scatterometer-based assessment of 10-m wind analyses from the operational ecmwf and ncep numerical weather prediction models. *Monthly Weather Review*, 133(•):409–429. 9, 14

Chelton, D., Schlax, M., Freilich, M., and Milliff, R. (2004). Satellite measurements reveal persistent small-scale features in ocean winds. *Science*, 303:978–983. 6

Chelton, D. and Xie, S.-P. (2010). Coupled ocean-atmosphere interaction at oceanic mesoscales. *Oceanography*, 23(4):52–69. doi:10.5670/oceanog.2010.05. 8

Chelton, D. B. (1982). Large-scale response of the California current to forcing by the wind stress curl. *CalCOFI Reports*, 23. 4

Chelton, D. B., Freilich, M. H., Sienkiewicz, J. M., and Von Ahn, J. M. (2006). On the use of quikscat scatterometer measurements of surface winds for marine weather prediction. *Monthly Weather Review*, 134(8):2055–2071. 65

Chelton, Jr., D. B. (2016). The Prospects for Future Satellite Mapping of Mesoscale and Submesoscale Vorticity. *AGU Fall Meeting Abstracts*. 17

Clarke, A., Church, J., and Gould, J. (2001). Chapter 1.2 Ocean processes and climate phenomena. *International Geophysics*, 77(C). 3

Clementi, E., Aydogdu, A., Goglio, A. C., Pistoia, J., Escudier, R., Drudi, M., Grandi, A., Mariani, A., Lyubartsev, V., Lecci, R., Cretí, S., Coppini, G., Masina, S., and Pinardi, N. (2021). Mediterranean Sea Analysis and Forecast (CMEMS MED-Currents, EAS6 system)(Version 1). Technical report, Copernicus Monitoring Environment Marine Service (CMEMS),. 119

Crapolicchio, R., De Chiara, G., Paciucci, A., and Lecomte, P. (2007). The ERS-2 scatterometer: Instrument and data performances assessment since the beginning of the mission. In *European Space Agency, (Special Publication) ESA SP*, number SP-636. 12

Cronin, M. F., Gentemann, C. L., Edson, J., Ueki, I., Bourassa, M., Brown, S., Clayson, C. A., Fairall, C. W., Farrar, J. T., Gille, S. T., Gulev, S., Josey, S. A., Kato, S., Katsumata, M., Kent, E., Krug, M., Minnett, P. J., Parfitt, R., Pinker, R. T., Stackhouse, P. W., Swart, S., Tomita, H., Vandemark, D., Weller, A. R., Yoneyama, K., Yu, L., and Zhang, D. (2019). Air-Sea Fluxes With a Focus on Heat and Momentum. *Frontiers in Marine Science*, 6. 3

De Biasio, F., Bajo, M., Vignudelli, S., Umgiesser, G., and Zecchetto, S. (2017). Improvements of storm surge forecasting in the Gulf of Venice exploiting the potential of satellite data: the ESA DUE eSurge-Venice project. *European Journal of Remote Sensing*, 50(1):428–441. 4

De Chiara, G. (2014). ECMWF Seminar on the Use of Satellite Observations in NWP. Technical report, ECMWF. 6, 9

De Kloe, J., Stoffelen, A., and Verhoef, A. (2017a). Improved use of scatterometer measurements by using stress-equivalent reference winds. *IEEE Journal of Selected Topics in Applied Earth Obs and Remote Sensing*, 10(5):2340–2347. 7, 10, 14

De Kloe, J., Stoffelen, A., and Verhoef, A. (2017b). Improved Use of Scatterometer Measurements by Using Stress-Equivalent Reference Winds. *IEEE Journal of Selected Topics in Applied Earth Observations and Remote Sensing*, 10(5):2340–2347. 30

Dee, D. P., Uppala, S. M., Simmons, A. J., Berrisford, P., Poli, P., Kobayashi, S., Andrae, U., Balmaseda, M. A., Balsamo, G., Bauer, P., Bechtold, P., Beljaars, A. C., van de Berg, L., Bidlot, J., Bormann, N., Delsol, C., Dragani, R., Fuentes, M., Geer, A. J., Haimberger, L., Healy, S. B., Hersbach, H., Hólm, E. V., Isaksen, L., Kållberg, P., Köhler, M., Matricardi, M., Mcnally, A. P., Monge-Sanz, B. M., Morcrette, J. J., Park, B. K., Peubey, C., de Rosnay, P., Tavolato, C., Thépaut, J. N., and Vitart, F. (2011). The ERA-Interim reanalysis: Configuration and performance of the data assimilation system. *Quarterly Journal of the Royal Meteorological Society*, 137(656):553–597. 16, 125

Desbiolles, F., Bentamy, A., Blanke, B., Roy, C., Mestas-Nuñez, A. M., Grodsky, S. A., Herbette, S., Cambon, G., and Maes, C. (2017). Two decades [1992–2012] of surface wind analyses based on satellite scatterometer observations. *Journal of Marine Systems*, 168. 15, 125

Desbiolles, F., Blanke, B., and Bentamy, A. (2014a). Short-term upwelling events at the western African coast related to synoptic atmospheric structures as derived from satellite observations. *Journal of Geophysical Research: Oceans*, 119(1). 4

Desbiolles, F., Blanke, B., Bentamy, A., and Grima, N. (2014b). Origin of fine-scale wind stress curl structures in the Benguela and Canary upwelling systems. *Journal of Geophysical Research: Oceans*, 119(11). 4, 8

Di Luca, A., de Elía, R., and Laprise, R. (2013). Potential for small scale added value of RCM's downscaled climate change signal. *Climate Dynamics*, 40(3-4):601–618. 109

Dombrowsky, E., Bertino, L., Brassington, G. B., Chassignet, E. P., Davidson, F., Hurlburt, H. E., Kamachi, M., Lee, T., Martin, M. J., Mei, S., and Tonani, M. (2009). GODAE systems in operation. *Oceanography*, 22(SPL.ISS. 3). 5

Döscher, R., Acosta, M., Alessandri, A., Anthoni, P., Arsouze, T., Bergman, T., Bernardello, R., Boussetta, S., Caron, L.-P., Carver, G., Castrillo, M., Catalano, F., Cvijanovic, I., Davini, P., Dekker, E., Doblas-Reyes, F. J., Docquier, D., Echevarria, P., Fladrich, U., Fuentes-Franco, R., Gröger, M., v. Hardenberg, J., Hieronymus, J., Karami, M. P., Keskinen, J.-P., Koenigk, T., Makkonen, R., Massonnet, F., Ménégoz, M., Miller, P. A., Moreno-Chamarro, E., Nieradzik, L., van Noije, T., Nolan, P., O'Donnell, D., Ollinaho, P., van den Oord, G., Ortega, P., Prims, O. T., Ramos, A., Reerink, T., Rousset, C., Ruprich-Robert, Y., Le Sager, P., Schmith, T., Schrödner, R., Serva, F., Sicardi, V., Sloth Madsen, M., Smith, B., Tian, T., Tourigny, E., Uotila, P., Vancoppenolle, M., Wang, S., Wårlind, D., Willén, U., Wyser, K., Yang, S., Yepes-Arbós, X., and Zhang, Q. (2022). The EC-Earth3 Earth system model for the Coupled Model Intercomparison Project 6. *Geoscientific Model Development*, 15(7):2973–3020. 107

Driesenaar, T., Bentamy, A., de Kloe, J., Belmonte Rivas, M., and Giesen, R. (2022). QUALITY INFORMATION DOCUMENT For the Global Ocean Wind Products WIND_GLO_WIND_L3_NRT_OBSERVATIONS_012_002 WIND_GLO_WIND_L3_REP_OBSERVATIONS_012_005 WIND_GLO_PHY_CLIMATE_L4_REP_012_003 Issue: 1.16. Technical report, CMEMS. 36

Dunbar, S., Weiss, B., Stiles, B., Huddleston, J., Callahan, P., Shirtliffe, G., Perry, K. L., Mears, C. H. C., Wentz, F., and Smith, D. (2006). QuikSCAT Science Data Product User's Manual Overview & Geophysical Data Products. Technical report, JPL. 12

Edson, J. B., Jampana, V., Weller, R. A., Bigorre, S. P., Plueddemann, A. J., Fairall, C. W., Miller, S. D., Mahrt, L., Vickers, D., and Hersbach, H. (2013). On the Exchange of Momentum over the Open Ocean. *Journal of Physical Oceanography*, 43(8):1589–1610. 30

Exarchou, E., Prodhomme, C., Brodeau, L., Guemas, V., and Doblas-Reyes, F. (2018). Origin of the warm eastern tropical Atlantic SST bias in a climate model. *Climate Dynamics*, 51(5-6):1819–1840. 122

Figa, J. and Stoffelen, A. (2000). On the assimilation of Ku-band scatterometer winds for weather analysis and forecasting. *IEEE Transactions on Geoscience and Remote Sensing*, 38(4 II). 10

Figa-Saldaña, J., Wilson, J., Attema, E., Gelsthorpe, R., Drinkwater, M., and Stoffelen, A. (2002). The advanced scatterometer (ascat) on the meteorological operational (metop) platform: A follow on for european wind scatterometers. *Canadian Journal of Remote Sensing*, 28(3):404–412. xiii, 9, 10

Fois, F., Hoogeboom, P., Le Chevalier, F., and Stoffelen, A. (2015). An analytical model for the description of the full-polarimetric sea surface doppler signature. *Journal of Geophysical Research: Oceans*, 120(2):988–1015. _eprint: https://agupubs.onlinelibrary.wiley.com/doi/pdf/10.1002/2014JC010589. 10

Foltz, G. R. and McPhaden, M. J. (2010). Interaction between the Atlantic meridional and Niño modes. *Geophysical Research Letters*, 37(18):n/a–n/a. 103, 108

Freeman, E., Woodruff, S. D., Worley, S. J., Lubker, S. J., Kent, E. C., Angel, W. E., Berry, D. I., Brohan, P., Eastman, R., Gates, L., Gloeden, W., Ji, Z., Lawrimore, J., Rayner, N. A., Rosenhagen, G., and Smith, S. R. (2017). ICOADS Release 3.0: a major update to the historical marine climate record. *International Journal of Climatology*, 37(5). 7

Freilich, M. H. and Vanhoff, B. A. (2006). The accuracy of preliminary WindSat vector wind measurements: Comparisons with NDBC buoys and QuikSCAT. *IEEE Transactions on Geoscience and Remote Sensing*, 44(3). 8

Fu, L.-L. and Chao, Y. (1997). The sensitivity of a global ocean model to wind forcing: A test using sea level and wind observations from satellites and operational wind analysis. *Geophysical Research Letters*, 24(14):1783–1786. 16

Gade, M. and Stoffelen, A. (2019). An Introduction to Microwave Remote Sensing of the Asian Seas. In Barale, V. and Gade, M., editors, *Remote Sensing of the Asian Seas*, pages 81–101. Springer International Publishing, Cham. 8

Gaiser, P., St Germain, K., Twarog, E., Poe, G., Purdy, W., Richardson, D., Grossman, W., Jones, W., Spencer, D., Golba, G., Cleveland, J., Choy, L., Bevilacqua, R., and Chang, P. (2004). The WindSat spaceborne polarimetric microwave radiometer: sensor description and early orbit performance. *IEEE Transactions on Geoscience and Remote Sensing*, 42(11):2347–2361. 8

García-Reyes, M. and Largier, J. (2010). Observations of increased wind-driven coastal upwelling off central California. *Journal of Geophysical Research*, 115(C4). 7

Gaube, P., Chelton, D., Samelson, R., Schlax, M., and neill, L. (2015). Satellite observations of mesoscale eddy-induced ekman pumping. *Journal of Physical Oceanography*, 45:104–132. 4

Gelaro, R., McCarty, W., Suárez, M. J., Todling, R., Molod, A., Takacs, L., Randles, C. A., Darmenov, A., Bosilovich, M. G., Reichle, R., Wargan, K., Coy, L., Cullather, R., Draper, C., Akella, S., Buchard, V., Conaty, A., da Silva, A. M., Gu, W., Kim, G.-K., Koster, R., Lucchesi, R., Merkova, D., Nielsen, J. E., Partyka, G., Pawson, S., Putman, W., Rienecker, M., Schubert, S. D., Sienkiewicz, M., and Zhao, B. (2017). The Modern-Era Retrospective Analysis for Research and Applications, Version 2 (MERRA-2). *Journal of Climate*, 30(14):5419–5454. 16

Giesen, R., Clementi, E., Bajo, M., Federico, I., Stoffelen, A., and Santoleri, R. (2021). The november 2019 record high water levels in venice, italy. *Journal of Operational Oceanography*, 14(5):156–162. Copernicus Marine Service Ocean State Report, Issue 5. 4, 12, 129

Gille, S. T., Llewellyn Smith, S. G., and Statom, N. M. (2005). Global observations of the land breeze. *Geophysical Research Letters*, 32(5):L05605. 17

Gómara, I., Mohino, E., Losada, T., Domínguez, M., Suárez-Moreno, R., and Rodríguez-Fonseca, B. (2018). Impact of dynamical regionalization on precipitation biases and teleconnections over West Africa. *Climate Dynamics*, 50(11-12):4481–4506. 109

Griffies, S. (2008). Science of Ocean Climate Models. In *Encyclopedia of Ocean Sciences*. Elsevier. 5

Gruber, N., Lachkar, Z., Frenzel, H., Marchesiello, P., Münnich, M., Mcwilliams, J., Nagai, T., and Plattner, G.-K. (2011). Eddy-induced reduction of biological production in eastern boundary upwelling systems. *Nat. Geosci.*, 4:787–792. 4

Hersbach, H. (2010a). Comparison of C-Band scatterometer CMOD5.N equivalent neutral winds with ECMWF. *Journal of Atmospheric and Oceanic Technology*, 27(4):721–736. 130

Hersbach, H. (2010b). Comparison of c-band scatterometer cmod5.n equivalent neutral winds with ecmwf. *J. Atmos. Oceanic Technol.*, 27(•):721–736. 17

Hersbach, H., Bell, B., Berrisford, P., Hirahara, S., Horányi, A., Muñoz-Sabater, J., Nicolas, J., Peubey, C., Radu, R., Schepers, D., Simmons, A., Soci, C., Abdalla, S., Abellan, X., Balsamo, G., Bechtold, P., Biavati, G., Bidlot, J., Bonavita, M., De Chiara, G., Dahlgren, P., Dee, D., Diamantakis, M., Dragani, R., Flemming, J., Forbes, R., Fuentes, M., Geer, A., Haimberger, L., Healy, S., Hogan, R. J., Hólm, E., Janisková, M., Keeley, S., Laloyaux, P., Lopez, P., Lupu, C., Radnoti, G., de Rosnay, P., Rozum, I., Vamborg, F., Villaume, S., and Thépaut, J. N. (2020). The ERA5 global reanalysis. *Quarterly Journal of the Royal Meteorological Society*, 146(730). 16, 125

Hoareau, N., Turiel, A., Portabella, M., Ballabrera-Poy, J., and Vogelzang, J. (2018). Singularity power spectra: A method to assess geophysical consistency of gridded products—application to sea-surface salinity remote sensing maps. *IEEE Transactions on Geoscience and Remote Sensing*, 56(9):5525–5536. 65

Hong, X., Peng, M., Wang, S., and Wang, Q. (2018). Simulating and understanding the gap outflow and oceanic response over the Gulf of Tehuantepec during GOTEX. *Dynamics of Atmospheres and Oceans*, 82:1–19. 4

Hurrell, J. W. (2008). Decadel climate prediction: Challenges and opportunities. *Journal of Physics: Conference Series*, 125. 3

Jacobson, M. (2005). Introduction. In *Fundamentals of Atmospheric Modeling*, pages 1–11. Cambridge University Press. 16

Jourdier, B. (2020). Evaluation of ERA5, MERRA-2, COSMO-REA6, NEWA and AROME to simulate wind power production over France. *Advances in Science and Research*, 17:63–77. 126

Kantha, L. H. and Clayson, C. A., editors (2000). *Numerical Models of Oceans and Oceanic Processes*, volume 66, chapter 2, pages 127–245. Elsevier. 5

Kelly, K., Dickinson, S., McPhaden, M. J., and Johnson, G. C. (2001). Ocean currents evident in satellite wind data. *Geophys. Res. Lett.*, 28:2469–2472. 14

Kilpatrick, T. J. and Xie, S. P. (2016). Circumventing rain-related errors in scatterometer wind observations. *Journal of Geophysical Research*, 121(16). 8

King, G. P., Portabella, M., Lin, W., and Stoffelen, A. (2017). Ocean and Sea Ice SAF Correlating extremes in wind and stress divergence with extremes in rain over the Tropical Atlantic. Technical report, EUMETSAT OSI-SAF KNMI CSIC. 11, 13

King, G. P., Portabella, M., Lin, W., and Stoffelen, A. (2022). Correlating Extremes in Wind Divergence with Extremes in Rain over the Tropical Atlantic. *Remote Sensing*, 14(5):1147. 8, 43, 60, 85, 97

Kirti Padia (2010). Oceansat-2 Scatterometer algorithms for sigma-0, processing and products format (April-2010) (Version 1.1) by SCAT-DP TEAM (compiled by Kirti Padia) Originating Unit Advanced Image Processing Group Signal and Image Processing Area Space Applications Centre Ahmedabad-380015 Gujarat, India 2 CONTENT. Technical report, Space Applications Centre. xiii, 10

Klotzbach, P. J., Schreck, C. J., Collins, J. M., Bell, M. M., Blake, E. S., and Roache, D. (2018). The extremely active 2017 North Atlantic hurricane season. *Monthly Weather Review*, 146(10). 103, 128

Large, W. G. and Yeager, S. G. (2004). Diurnal to decadal global forcing for oceans and sea-ice models : the data ses and flux climatologies. Technical report, National Center for Atmospheric Research, Boulder. 119

Lee, T., Wang, O., Tang, W., and Liu, W. T. (2008). Wind stress measurements from the QuikSCAT-SeaWinds scatterometer tandem mission and the impact on an ocean model. *Journal of Geophysical Research: Oceans*, 113(12). 17

Lenti, F., Nunziata, F., Migliaccio, M., and Pedersen, L. T. (2015). Wind speed estimation using spatial resolution enhanced AMSR-E microwave radiometer data. In *International Geoscience and Remote Sensing Symposium (IGARSS)*, volume 2015-November. 8

Lewis, H. W., Siddorn, J., Manuel Castillo Sanchez, J., Petch, J., Edwards, J. M., and Smyth, T. (2019). Evaluating the impact of atmospheric forcing and air-sea coupling on near-coastal regional ocean prediction. *Ocean Science*, 15(3). 103

Ličer, M., Smerkol, P., Fettich, A., Ravdas, M., Papapostolou, A., Mantziafou, A., Strajnar, B., Cedilnik, J., Jeromel, M., Jerman, J., Petan, S., Malačič, V., and Sofianos, S. (2016). Modeling the ocean and atmosphere during an extreme bora event in northern Adriatic using one-way and two-way atmosphere–ocean coupling. *Ocean Science*, 12(1):71–86. 119

Lin, H., Xu, Q., and Zheng, Q. (2008). An overview on SAR measurements of sea surface wind. *Progress in Natural Science*, 18(8):913–919. 8

Lin, W. and Portabella, M. (2017). Toward an improved wind quality control for rapidscat. *IEEE Transactions on Geoscience and Remote Sensing*, 55(7):3922–3930. 33, 38

Lin, W., Portabella, M., Stoffelen, A., Verhoef, A., Lang, S., Zhang, Y., and Lin, M. (2016). On the improvement of the hy-2a scatterometer wind quality control. In *2016 IEEE International Geoscience and Remote Sensing Symposium (IGARSS)*, pages 407–410. 10

Lin, W., Portabella, M., Stoffelen, A., Verhoef, A., and Turiel, A. (2015a). Ascat wind quality control near rain. *IEEE Trans. Geosci. Remote Sens.*, 53(8):4165–4177. 7, 8, 10, 13, 38, 51, 60, 86

Lin, W., Portabella, M., Stoffelen, A., Vogelzang, J., and Verhoef, A. (2015b). ASCAT wind quality under high subcell wind variability conditions. *Journal of Geophysical Research: Oceans*, 120(8):5804–5819. 10, 12, 26, 33, 60

Lionello, P., Barriopedro, D., Ferrarin, C., Nicholls, R. J., Orlić, M., Raicich, F., Reale, M., Umgiesser, G., Vousdoukas, M., and Zanchettin, D. (2021). Extreme floods of Venice: characteristics, dynamics, past and future evolution (review article). *Natural Hazards and Earth System Sciences*, 21(8):2705–2731. 115

Lionello, P., Cavaleri, L., Nissen, K., Pino, C., Raicich, F., and Ulbrich, U. (2012). Severe marine storms in the Northern Adriatic: Characteristics and trends. *Physics and Chemistry of the Earth, Parts A/B/C*, 40-41:93–105. 115

Madec, G. (2008). NEMO ocean engine Gurvan Madec, and the NEMO team. Technical report, Institut Pierre-Simon Laplace (IPSL). 118

Madec, G. and the NEMO Team (2014). NEMO ocean engine - version 3.6. *Note du Pôle de modélisation, Institut Pierre-Simon Laplace*, 27. 5, 107

Martín-Rey, M. and Lazar, A. (2019). Is the boreal spring tropical Atlantic variability a precursor of the Equatorial Mode? *Climate Dynamics*, 53(3-4):2339–2353. 103, 108, 122

Mastenbroek, C. (1996). *Wind-wave interaction*. PhD thesis, TU Delft, the Netherlands. 10

Mears, C. A., Scott, J., Wentz, F. J., Ricciardulli, L., Leidner, S. M., Hoffman, R., and Atlas, R. (2019). A Near-Real-Time Version of the Cross-Calibrated Multiplatform (CCMP) Ocean Surface Wind Velocity Data Set. *Journal of Geophysical Research: Oceans*, 124(10):6997–7010. 15, 17, 125

Medvedev, I. P., Vilibić, I., and Rabinovich, A. B. (2020). Tidal Resonance in the Adriatic Sea: Observational Evidence. *Journal of Geophysical Research: Oceans*, 125(8). 115

Meissner, T. and Wentz, F. J. (2009). Wind-vector retrievals under rain with passive satellite microwave radiometers. *IEEE Transactions on Geoscience and Remote Sensing*, 47(9). 8

Meissner, T., Wentz, F. J., and Ricciardulli, L. (2014). The emission and scattering of L-band microwave radiation from rough ocean surfaces and wind speed measurements from the Aquarius sensor. *Journal of Geophysical Research: Oceans*, 119(9):6499–6522. 8

Međugorac, I., Orlić, M., Janeković, I., Pasarić, Z., and Pasarić, M. (2018). Adriatic storm surges and related cross-basin sea-level slope. *Journal of Marine Systems*, 181:79–90. 115

Milliff, R. F., Morzel, J., Chelton, D. B., and Freilich, M. H. (2004). Wind stress curl and divergence biases from rain effects on quikscat surface wind retrievals. *J. Atmos. Oceanic Technol.*, 21(•):1216–1231. 10

Monaldo, F. M. (2006). Evaluation of WindSat wind vector performance with respect to QuikSCAT estimates. *IEEE Transactions on Geoscience and Remote Sensing*, 44(3). 8

Naderi, F. M., Freilich, M. H., and Long, D. G. (1991). Spaceborne Radar Measurement of Wind Velocity Over the Ocean—An Overview of the NSCAT Scatterometer System. *Proceedings of the IEEE*, 79(6). 9

Nastrom, G. and Gage, K. S. (1985). A climatology of atmospheric wave number spectra of wind and temperature observed by commercial aircraft. *J. Atmos. Sci*, 42:950–960. 65

Nobre, P. and Srukla, J. (1996). Variations of Sea Surface Temperature, Wind Stress, and Rainfall over the Tropical Atlantic and South America. *Journal of Climate*, 9(10):2464–2479. 103, 128

O'Neill, L. W., Haack, T., and Durland, T. (2015). Estimation of Time-Averaged Surface Divergence and Vorticity from Satellite Ocean Vector Winds. *Journal of Climate*, 28(19). 8

Patoux, J. and Brown, R. A. (2001). Spectral analysis of quikscat surface winds and two-dimensional turbulence. *J. Geophys. Res.*, 106(D20):23995–24005. 12, 65

Pérez Gómez, B., Vilibić, I., Šepić, J., Međugorac, I., Ličer, M., Testut, L., Fraboul, C., Marcos, M., Abdellaoui, H., Álvarez Fanjul, E., Barbalić, D., Casas, B., Castaño-Tierno, A., Čupić, S., Drago, A., Fraile, M. A., Galliano, D. A., Gauci, A., Gloginja, B., Martín Guijarro, V., Jeromel, M., Larrad Revuelto, M., Lazar, A., Keskin, I. H., Medvedev, I., Menassri, A., Meslem, M. A., Mihanović, H., Morucci, S., Niculescu, D., Quijano de Benito, J. M., Pascual, J., Palazov, A., Picone, M., Raicich, F., Said, M., Salat, J., Sezen, E., Simav, M., Sylaios, G., Tel, E., Tintoré, J., Zaimi, K., and Zodiatis, G. (2022). Coastal sea level monitoring in the Mediterranean and Black seas. *Ocean Science*, 18(4):997–1053. xix, 120

Polito, P. S., Ryan, J. P., Liu, W. T., and Chavez, F. P. (2001). Oceanic and atmospheric anomalies of tropical instability waves. *Geophysical Research Letters*, 28(11). 10

Portabella, M. (2002). Toward an optimal inversion method for synthetic aperture radar wind retrieval. *Journal of Geophysical Research*, 107(C8):3086. 8

Portabella, M. and Stoffelen, A. (2001a). Rain detection and quality control of sea winds. *Journal of Atmospheric and Oceanic Technology*, 18(7). 10

Portabella, M. and Stoffelen, A. (2001b). Rain detection and quality control of seawinds. *Journal of Atmospheric and Oceanic Technology*, 18(7):1171–1183. 33

Portabella, M. and Stoffelen, A. (2004). A probabilistic approach for seawinds data assimilation. *Quarterly Journal of the Royal Meteorological Society*, 130:127 – 152. 14, 83

Portabella, M. and Stoffelen, A. (2009). On scatterometer ocean stress. *Journal of Atmospheric and Ocean Technology*, 26(2):368–382. doi: 10.1175/2008JTECHO578.1. 7, 62

Portabella, M., Stoffelen, A., Lin, W., Turiel, A., Verhoef, A., Verspeek, J., and Ballabrera-Poy, J. (2012). Rain effects on ASCAT-retrieved winds: Toward an improved quality control. *IEEE Transactions on Geoscience and Remote Sensing*, 50(7 PART1):2495–2506. 10

Portabella, M., Trindade, A., Grieco, G., and Makarova, E. (2022). WORLD OCEAN CIRCULATION ALGORITHM THEORETICAL BASIS DOCUMENT FOR ERA STAR (THEME 1). Technical report, CMEMS. xvi, 38, 81

Reynolds, R. W. and Chelton, D. B. (2010). Comparisons of daily sea surface temperature analyses for 2007-08. *Journal of Climate*, 23(13):3545–3562. 65

Ricciardulli, L. and Manaster, A. (2021). Intercalibration of ASCAT Scatterometer Winds from MetOp-A, -B, and -C, for a Stable Climate Data Record. *Remote Sensing*, 13(18):3678. 6, 12

Saha, S., Moorthi, S., Wu, X., Wang, J., Nadiga, S., Tripp, P., Behringer, D., Hou, Y.-T., Chuang, H.-y., Iredell, M., Ek, M., Meng, J., Yang, R., Mendez, M. P., van den Dool, H., Zhang, Q., Wang, W., Chen, M., and Becker, E. (2014). The NCEP Climate Forecast System Version 2. *Journal of Climate*, 27(6):2185–2208. 16, 125

Sandu, I., Beljaars, A., Bechtold, P., Mauritsen, T., and Balsamo, G. (2013a). Why is it so difficult to represent stably stratified conditions in numerical weather prediction (nwp) models? *Journal of Advances in Modeling Earth Systems*, 5(2):117–133. 17

Sandu, I., Beljaars, A., Bechtold, P., Mauritsen, T., and Balsamo, G. (2013b). Why is it so difficult to represent stably stratified conditions in numerical weather prediction (NWP) models? *Journal of Advances in Modeling Earth Systems*, 5(2):117–133. 130

Schulzweida, U. (2019). CDO User Guide. 106

Seo, H. (2017). Distinct Influence of Air–Sea Interactions Mediated by Mesoscale Sea Surface Temperature and Surface Current in the Arabian Sea. *Journal of Climate*, 30(20). 4, 5

Shchepetkin, A. F. and McWilliams, J. C. (2005). The regional oceanic modeling system (ROMS): A split-explicit, free-surface, topography-following-coordinate oceanic model. *Ocean Modelling*, 9(4):347–404. 5

Small, R. J., Bacmeister, J., Bailey, D., Baker, A., Bishop, S., Bryan, F., Caron, J., Dennis, J., Gent, P., Hsu, H., Jochum, M., Lawrence, D., Muñoz, E., diNezio, P., Scheitlin, T., Tomas, R., Tribbia, J., Tseng, Y., and Vertenstein, M. (2014). A new synoptic scale resolving global climate simulation using the Community Earth System Model. *Journal of Advances in Modeling Earth Systems*, 6(4). 5

Soisuvarn, S., Jelenak, Z., and Chang, P. S. (2007). A geophysical model function for WindSat polarimetric radiometer wind retrievals using linear polarizations. In *International Geoscience and Remote Sensing Symposium (IGARSS)*. 8

Sonnewald, M., Lguensat, R., Jones, D. C., Dueben, P. D., Brajard, J., and Balaji, V. (2021). Bridging observations, theory and numerical simulation of the ocean using machine learning. *Environmental Research Letters*, 16(7):073008. 130

Stiles, B. W. and Dunbar, R. S. (2010). A neural network technique for improving the accuracy of scatterometer winds in rainy conditions. *IEEE Transactions on Geoscience and Remote Sensing*, 48(8):3114–3122. 33

Stoffelen, A. (1998). Toward the true near-surface wind speed: Error modeling and calibration using triple collocation. *Journal of Geophysical Research: Oceans*, 103(C4). 7

Stoffelen, A., Kumar, R., Zou, J., Karaev, V., Chang, P. S., and Rodriguez, E. (2019). Ocean Surface Vector Wind Observations. In *Remote Sensing of the Asian Seas*. Springer International Publishing, Cham. 6, 10

Stoffelen, A., Verspeek, J. A., Vogelzang, J., and Verhoef, A. (2017). The CMOD7 Geophysical Model Function for ASCAT and ERS Wind Retrievals. *IEEE Journal of Selected Topics in Applied Earth Observations and Remote Sensing*, 10(5):2123–2134. 10

Stoffelen, A. and Vogelzang, J. (2020). Wind Bias Correction Guide. Technical report, EUMETSAT OSISAF KNMI. 13, 130

Stopa, J. E., Mouche, A. A., Chapron, B., and Collard, F. (2017). Sea State Impacts on Wind Speed Retrievals from C-Band Radars. *IEEE Journal of Selected Topics in Applied Earth Observations and Remote Sensing*, 10(5):2147–2155. 10

Subrahamanyam, D. B., Rani, S. I., Ramachandran, R., Kunhikrishnan, P., and Kumar, B. P. (2009). Impact of wind speed and atmospheric stability on air–sea interface fluxes over the East Asian Marginal Seas. *Atmospheric Research*, 94(1). 4

Tang, W., Liu, W. T., Stiles, B., and Fore, A. (2014). Detection of diurnal cycle of ocean surface wind from space-based observations. *International Journal of Remote Sensing*, 35(14):5328–5341. 27, 99

Tokmakian, R. (2005). An ocean model's response to scatterometer winds. *Ocean Modelling*, 9(1). 6

Trigo, I. F. and Davies, T. D. (2002). Meteorological conditions associated with sea surges in Venice: a 40 year climatology. *International Journal of Climatology*, 22(7):787–803. 115

Trindade, A., Portabella, M., Stoffelen, A., Lin, W., and Verhoef, A. (2020). ERAstar: A High-Resolution Ocean Forcing Product. *IEEE Transactions on Geoscience and Remote Sensing*, 58(2). xii, xiv, xv, 15, 27, 28, 36, 38, 59, 60, 61, 63, 66, 68, 70, 71, 74

Tsimplis, M. N., Proctor, R., and Flather, R. A. (1995). A two-dimensional tidal model for the Mediterranean Sea. *Journal of Geophysical Research*, 100(C8):16223. 115

van Cranenburgh, L. (2022). *A critical evaluation of (scatterometer-based) ocean surface wind products over sea.* PhD thesis, Delft University of Technology, the Netherlands. 15

Verhoef, A., Vogelzang, J., Verspeek, J., and Stoffelen, A. (2017). Long-Term Scatterometer Wind Climate Data Records. *IEEE Journal of Selected Topics in Applied Earth Observations and Remote Sensing*, 10(5):2186–2194. 7, 12

Verhoef, A., Vogelzang, J., Verspeek, J., and Stoffelen, A. (2018). PenWP User Manual and Reference Guide. Technical report, EUMETSAT OSI SAF, NWPSAF-KN-UD-009, v2.2. 25

Verhoef, A., Vogelzang, J., Verspeek, J., and Stoffelen, A. (2020). AWDP User Manual and Reference Guide. Technical report, EUMETSAT OSI SAF, NWPSAF-KN-UD-005, v3.3. 31

Vogelzang, J., King, G. P., and Stoffelen, A. (2015a). Spatial variances of wind fields and their relation to second-order structure functions and spectra. *Journal of Geophysical Research: Oceans*, 120(2):1048–1064. 8

Vogelzang, J., King, G. P., and Stoffelen, A. (2015b). Spatial variances of wind fields and their relation to second-order structure functions and spectra. *Journal of Geophysical Research: Oceans*, 120(2):1048–1064. 38

Vogelzang, J. and Stoffelen, A. (2017). ASCAT Ultrahigh-Resolution Wind Products on Optimized Grids. *IEEE Journal of Selected Topics in Applied Earth Observations and Remote Sensing*, 10(5). 8

Vogelzang, J. and Stoffelen, A. (2018). Improvements in K _u -band scatterometer wind ambiguity removal using ASCAT-based empirical background error correlations. *Quarterly Journal of the Royal Meteorological Society*, 144(716):2245–2259. 25, 34, 83, 127

Vogelzang, J. and Stoffelen, A. (2021). Quadruple Collocation Analysis of In-Situ, Scatterometer, and NWP Winds. *Journal of Geophysical Research: Oceans*, 126(5). 6, 7, 12, 25, 28, 83, 126

Vogelzang, J., Stoffelen, A., Verhoef, A., and Figa-Saldaña, J. (2011a). On the quality of high-resolution scatterometer winds. *Journal of Geophysical Research: Oceans*, 116(C10033). C10033. 8, 12, 33, 64, 65, 67

Vogelzang, J., Stoffelen, A., Verhoef, A., and Figa-Saldaña, J. (2011b). On the quality of high-resolution scatterometer winds. *Journal of Geophysical Research: Oceans*, 116(10). 7, 37, 83

Voldoire, A., Exarchou, E., Sanchez-Gomez, E., Demissie, T., Deppenmeier, A.-L., Frauen, C., Goubanova, K., Hazeleger, W., Keenlyside, N., Koseki, S., Prodhomme, C., Shonk, J., Toniazzo, T., and Traoré, A.-K. (2019). Role of wind stress in driving SST biases in the Tropical Atlantic. *Climate Dynamics*, 53(5-6):3481–3504. 122

Volgenzang, J. (2013). How to calculate wind spectra. NWPSAF-KN-TR-008, EUMETSAT-NWP SAF report v1.1. 65

Wang, Z., Stoffelen, A., Fois, F., Verhoef, A., Zhao, C., Lin, M., and Chen, G. (2017). Sst dependence of ku- and c-band backscatter measurements. *IEEE Journal of Selected Topics in Applied Earth Observations and Remote Sensing*, 10(5):2135–2146. 10, 11, 33, 57

Wang, Z., Stoffelen, A., Zhang, B., He, Y., Lin, W., and Li, X. (2019). Inconsistencies in scatterometer wind products based on ASCAT and OSCAT-2 collocations. *Remote Sensing of Environment*, 225:207–216. 10, 25

Wang, Z., Stoffelen, A., Zhao, C., Vogelzang, J., Verhoef, A., Verspeek, J., Lin, M., and Chen, G. (2017). An sst-dependent ku-band geophysical model function for rapidscat. *Journal of Geophysical Research: Oceans*, 122(4):3461–3480. 10, 57

Wang, Z., Zou, J., Stoffelen, A., Lin, W., Verhoef, A., Li, X., He, Y., Zhang, Y., and Lin, M. (2021). Scatterometer sea surface wind product validation for hy-2c. *IEEE Journal of Selected Topics in Applied Earth Observations and Remote Sensing*, 14:6156–6164. 12, 82

Warner, J. C., Perlin, N., and Skyllingstad, E. D. (2008). Using the Model Coupling Toolkit to couple earth system models. *Environmental Modelling & Software*, 23(10-11). 5

Wentz, F. J. (1997). A well-calibrated ocean algorithm for special sensor microwave / imager. *Journal of Geophysical Research: Oceans*, 102(C4). 8

Wentz, F. J., Ricciardulli, L., Rodriguez, E., Stiles, B. W., Bourassa, M. A., Long, D. G., Hoffman, R. N., Stoffelen, A., Verhoef, A., O'Neill, L. W., Farrar, J. T., Vandemark, D., Fore, A. G., Hristova-Veleva, S. M., Turk, F. J., Gaston, R., and Tyler, D. (2017). Evaluating and Extending the Ocean Wind Climate Data Record. *IEEE Journal of Selected Topics in Applied Earth Observations and Remote Sensing*, 10(5):2165–2185. 6, 7, 12

Wentz, F. J. and Smith, D. K. (1999). A model function for the ocean-normalized radar cross section at 14 GHz derived from NSCAT observations. *Journal of Geophysical Research: Oceans*, 104(C5):11499–11514. 10

Wright, E. E., Bourassa, M. A., Stoffelen, A., and Bidlot, J. R. (2021). Characterizing buoy wind speed error in high winds and varying sea state with ascat and era5. *Remote Sensing*, 13(22). 7, 126

Wyser, K., van Noije, T., Yang, S., von Hardenberg, J., O'Donnell, D., and Döscher, R. (2020). On the increased climate sensitivity in the EC-Earth model from CMIP5 to CMIP6. *Geoscientific Model Development*, 13(8):3465–3474. 107

Xie, S.-P. and Carton, J. A. (2014). Tropical Atlantic Variability: Patterns, Mechanisms, and Impacts. In *Earth's Climate: The Ocean-Atmosphere Interaction*, volume 147, pages 121–142. 103, 128

Xu, X. and Stoffelen, A. (2020a). Improved rain screening for ku-band wind scatterometry. *IEEE Transactions on Geoscience and Remote Sensing*, 58(4):2494–2503. 10, 11

Xu, X. and Stoffelen, A. (2020b). Improved Rain Screening for Ku-Band Wind Scatterometry. *IEEE Transactions on Geoscience and Remote Sensing*, 58(4). 25, 33, 85

Xu, X. and Stoffelen, A. (2020c). Improved rain screening for ku-band wind scatterometry. 58(4):2494–2503. 97

Yu, L. and Jin, X. (2014). Insights on the OAFlux ocean surface vector wind analysis merged from scatterometers and passive microwave radiometers (1987 onward). *Journal of Geophysical Research: Oceans*, 119(8):5244–5269. 15

Zecchetto, S., della Valle, A., and De Biasio, F. (2015). Mitigation of ECMWF–scatterometer wind biases in view of storm surge applications in the Adriatic Sea. *Advances in Space Research*, 55(5):1291–1299. 115

Zhang, H. M., Reynolds, R. W., and Bates, J. J. (2006). Blended and gridded high resolution global sea surface wind speed and climatology from multiple satellites: 1987 - Present. In *86th AMS Annual Meeting*. 15

Žust, L., Fettich, A., Kristan, M., and Ličer, M. (2021). HIDRA 1.0: deep-learning-based ensemble sea level forecasting in the northern Adriatic. *Geoscientific Model Development*, 14(4):2057–2074. 130

Acknowledgements

For your support, your care and your unconditional belief in me, a sincere thank you to everyone that accompanied me in this journey.

I begin by thanking my director Marcos Portabella, Marcos thank you for the infinite patience and availability over the years, you manage to make complicated concepts easier for me to grasp (that is saying a lot) and put in the time to listen whenever I got stuck. On a day-to day basis, from you I learned not only about scatterometry, but also about how research gets done, from writing engaging scientific texts, to the endless (but necessary) consistency checks. It was a long run, but I am happy and proud to be your first PhD student. Then, I would like to thank my co-director Ad Stoffelen. Ad, you tried to stimulate my critical thinking by asking the right questing and piqued my curiosity. I am immensely grateful for all your comments and the way you helped shape this research. I would also like to extend my gratitude to Marta Martim-Rey from UCM, and Matjaz Licer from NIB, for you enthusiasm and for accepting to try the new product in your ocean simulations. To my colleges and ex-colleges from the Winds Group at ICM: Federico Cossu, Albert Rabanada, Eugenia Makarova and Greg King: it has been a pleasure working alongside you. To Giuseppe Grieco and Wenming Lin, thank you for your precious help in scripting and debugging my algorithms. A very special thank you to Federica Polverari, colleague and friend, for all the discussions inside and outside the office, it wouldn't have been the same without you. I would like to continue by expressing my gratitude to everyone from the winds group at KNMI, namely a big thank you to Jos de Kloe and Anton Verhoef, for the many explanations on how to create scatterometer data sets with the wind software(s), for your help with coding and also for making me feel very welcome at KNMI. On that note, thank you also to my old PhD buddies from KNMI, Antonello and Martijn, you made life in the Netherlands a blast, and to Jieying and Marie, thank you for the warmth of your friendship. Then, I would like to say thank you to my dear ICM/IBE friends, although it is impossible to name all of you. Thank you to Marta and Arianna, by far you have put up with me more than anyone else, I deeply appreciate your guidance and friendship. To Alfonso and Roman, for the laughs and the good times! To Guillem and Cristina, always pushing me towards my goals. To the family I didn't choose, Alicia, Ignasi, Κωνσταντίνα, Θάλεια, Ιφιγένεια, Joan, Alfred, Pau and Miguel, you have made me feel at home in a foreign country, gracias. To Abu, for the last stretch.

Finalmente, aos meus pais, Luis e Virginia, e a minha irmã Patricia, a quem estarei eternamente agradecida por todo o apoio que me dão nos momentos mais importantes de minha vida, sem eles nada disto seria possível. Obrigada.

Publications and Conferences

PUBLICATIONS

1. **ERAstar: a high resolution ocean forcing product.**
Trindade, A., Portabella, M., Stoffelen, A., Lin, W., and Verhoef, A.
IEEE Trans. Geosci. Rem. Sens., 58 (2), pp. 1337-1347, https://doi.org/10.1109/TGRS.2019.2946019*, 2020.*

2. **Copernicus Marine Service Ocean State Report.**
von Schuckmann, K., Le Traon, P., Smith, N., Pascual, A., Brasseur, P., Fennel, K., Djavidnia, S., Aaboe, S., Fanjul, E., Autret, E., Axell, L., Aznar, R., Benincasa, M., Bentamy, A., Boberg, F., Bourdallé-Badie, R., Nardelli, B., Brando, V., Bricaud, C., Breivik, L., Brewin, R., Capet, A., Ceschin, A., Ciliberti, S., Cossarini, G., de Alfonso, M., de Pascual Collar, A., de Kloe, J., Deshayes, J., Desportes, C., Drévillon, M., Drillet, Y., Droghei, R., Dubois, C., Embury, O., Etienne, H., Fratianni, C., Lafuente, J., Sotillo, M., Garric, G., Gasparin, F., Gerin, R., Good, S., Gourrion, J., Grégoire, M., Greiner, E., Guinehut, S., Gutknecht, E., Hernandez, F., Hernandez, O., Høyer, J., Jackson, L., Jandt, S., Josey, S., Juza, M., Kennedy, J., Kokkini, Z., Korres, G., Kõuts, M., Lagemaa, P., Lavergne, T., le Cann, B., Legeais, J., Lemieux-Dudon, B., Levier, B., Lien, V., Maljutenko, I., Manzano, F., Marcos, M., Marinova, V., Masina, S., Mauri, E., Mayer, M., Melet, A., Mélin, F., Meyssignac, B., Monier, M., Müller, M., Mulet, S., Naranjo, C., Notarstefano, G., Paulmier, A., Gomez, B., Pérez Gonzalez, I., Peneva, E., Perruche, C., Peterson, K., Pinardi, N., Pisano, A., Pardo, S., Poulain, P., Raj, R., Raudsepp, U., Ravdas, M., Reid, R., Rio, M., Salon, S., Samuelsen, A., Sammartino, M., Sammartino, S., Sandø, A., Santoleri, R., Sathyendranath, S., She, J., Simoncelli, S., Solidoro, C., Stoffelen, A., Storto, A., Szerkely, T., Tamm, S., Tietsche, S., Tinker, J., Tintore, J., Trindade, A., van Zanten, D., Vandenbulcke, L., Verhoef, A., Verbrugge, N., Viktorsson, L., von Schuckmann, K., Wakelin, S., Zacharioudaki, A. and Zuo, H.
Journal of Operational Oceanography, 11 (sup1), pp. S1-S142, 10.1080/1755876X.2018.1489208*, 2018.*

3. **On the spatial resolution and quality enhancement of the ERA* ocean forcing.**
Trindade, A., Grieco, G., Makarova, E., Portabella, M., Giesen, R., Verhoef, A, Stoffelen, A.
(2022) in prep. for IEEE TGRSS

4. **Dominant role of North tropical Atlantic 2017 warm event on equatorial variability**
Martín-Rey, M., Trindade, A., Exarchou, E., Ortega, P., Portabella, M. and Gómara, I.
(2022) in prep.

5. **Development of a 11-year ERA* eddy-scale ocean forcing product**
Trindade, A., Grieco, G., Makarova, E., Portabella, M., Giesen, R., Verhoef, A, Stoffelen, A.
(2022) in prep. for Earth System Science Data

PROCEEDINGS

A NEW HIGH-RESOLUTION OCEAN FORCING BASED ON ERA5 AND SCATTEROMETER DATA.
Portabella, M., Trindade, A., Grieco, G. and Makarova, E.
2022 IEEE International Geoscience and Remote Sensing Symposium (IGARSS), Kuala Lumpur, Malaysia.

On the development of a scatterometer-based correction for NWP wind forcing systematic errors: Impact of satellite sampling.
Trindade, A., Portabella, M., Lin, W., and Stoffelen, A.
2017 IEEE International Geoscience and Remote Sensing Symposium (IGARSS), Fort Worth, TX, 2017, pp. 2160-2163, doi:10.1109/IGARSS.2017.8127414.

REPORTS

1. **World Ocean Circulation Algorithm Technical Baseline Document for ERAstar v2.0.**
Portabella, M., Trindade, A., Grieco, G., and Makarova, E.
ESA report $WOC-ESA-ODL-NR-009\_T1\_ERAstar\_V2.0$ *(Contract No. 4000130730/20/I-NB), available at* https://oce.icm.csic.es/es/otras*, June 2022.*

2. **World Ocean Circulation Algorithm Technical Baseline Document for ERAstar v2.0.**
Portabella, M., Polverari, F., Lin, W., Stoffelen, A., Rabaneda, A.S., Sapp, J., Chang, P., Jelenak, Z., Grieco, G., Trindade, A., Makarova, A. and Cossu, F.
Too extreme, or not too extreme, that is the question, in Pelegrí J.L., Gili J.M., Martínez de Albéniz M.V. (eds.), The ocean we want: inclusive and transformative ocean science, Institut de Ciències del Mar, CSIC, Barcelona. pp. 180-182, ISBN: 978-84-00-10967-7, available at https://doi.org/10.20350/digitalCSIC/14106*, 2022.*

3. **World Ocean Circulation Algorithm Technical Baseline Document for ERAstar v1.0**
Portabella, M., Trindade, A., Grieco, G. and Makarova, E.,
ESA report $WOC-ESA-ODL-NR-009\_T1\_ERAstar\_V1.0$ *(Contract No. 4000130730/20/I-NB), available at* https://oce.icm.csic.es/es/otras*, June 2021.*

4. **World Ocean Circulation Product User Manual for ERAstar v1.0.**
Portabella, M., Trindade, A., Grieco, G. and Makarova, E.
ESA report $WOC-ESA-ODL-NR-010\_T1\_ERAstar\_V1.0$ *(Contract No. 4000130730/20/I-NB), available at* https://oce.icm.csic.es/es/otras*, June 2021.*

5. **International research and development collaboration results for the global application of the Chinese HY-2B scatterometer.**
Stoffelen, A., Verhoef, A., Verpeek, J., Vogelzang, J., Portabella, M., Trindade, A., Wang, Z., De Chiara, G., Payan, C., Dhomps, A.-L., Cress, A., Cotton, J., Brocca, L., Long, D., Monteiro, I., and Bentamy, A.
Final report of the HY-2B Cal/Val Announcement of Opportunity, available at https://oce.icm.csic.es/es/otras*, December 2019.*

ORAL PRESENTATIONS

- Trindade, A., Grieco, G, Portabella, M., Giesen, R., Stoffelen, A. and A. Verhoef, "Development of a 11-year ERA* high resolution ocean forcing dataset", EUMETSAT 2022 - Meteorological Satellite Conference, Brussels, Belgium, 19-23 September, 2022.

- Makarova, E., Trindade, A., Grieco, G, Portabella, M., Giesen, R., Stoffelen, A. and A. Verhoef,"Development of a 11-year ERA* high resolution ocean forcing dataset", 2022 International Ocean Vector Winds Science Team Workshop, online, 12-19 April, 2022.

- Giesen, R., Stoffelen, A., Trindade, A., van Cranenburgh, L. and M. Portabella,"A new high-resolution ocean wind forcing product for the Copernicus Marine Service",2022 EGU General Assembly, Vienna, Austria, 23-27 May, 2022.

- Portabella, M., Trindade, A., Makarova, E., Grieco, G., Giesen, R., Verhoef, A., Stoffelen, A., Martín-Rey, M., Exarchou, E., Ortega, P. and I. Gómara, "ERA* high resolution ocean forcing product development and application", 2022 ESA Living Planet Symposium, Bonn, Germany, 23-27 May, 2022.

- Makarova, E., Trindade, A., Grieco, G. and M. Portabella, "Development of a 11-year ERA* high resolution ocean forcing dataset", 2022 VII Expanding Ocean Frontiers (EOF), Las Palmas, Espanya & online, 6-8 July, 2022.

- Cossu, F., Makarova E., Trindade, A., Grieco, G. and M. Portabella, "A new high-resolution ocean forcing based on ERA5 and scatterometer data", 2022 International Geoscience and Remote Sensing Symposium (IGARSS), Kuala Lumpur, Malasia & online, 17-22 July, 2022.

- Stoffelen, A., A. Verhoef, J. Verspeek, J. Vogelzang, M. Portabella, A. Trindade, Z. Wang, G. De Chiara, C. Payan, A.-L. Dhomps, A. Cress, J. Cotton, L. Brocca, D. Long, and I. Monteiro, "NWP, Ocean and Other Application Benefits of the Virtual Scatterometer Constellation," 2021 EUMETSAT Meteorological Satellite Conference, Bucharest, Romania (online), 20-24 September, 2021.

- Giesen, R., L. van Cranenburgh, A. Stoffelen, A., Trindade, A., Bentamy, A. and M. Portabella, "Comparison of Level-4 ocean surface wind products based on scatterometer observations and model wind fields," 2021 EUMETSAT Meteorological Satellite Conference, Bucharest, Romania (online), 20-24 September, 2021.

- Trindade, A., E. Makarova, M. Portabella, G. Grieco, A. Verhoef, A. Stoffelen, M. Martín-Rey, E. Exarchou, P. Ortega, and I. Gómara, "Development of the ERA* high resolution forcing from ERA5 reanalysis and scatterometer stress-equivalent winds," 2021 EUMETSAT Meteorological Satellite Conference, Bucharest, Romania (online), 20-24 September, 2021.

- Portabella, M., A. Trindade, G. Grieco, E. Makarova, A. Stoffelen, M. Martín-Rey, E. Exarchou, P. Ortega, I. Gómara, W. Lin, F. Polverari, F. Cossu, A.S. Rabaneda, and G.P. King, "The role of scatterometry in ocean model forcing," VI Expanding Ocean Frontiers Conference, Barcelona, Spain (online), 5-7 July, 2021. (Invited)

- Trindade, A., M. Martín-Rey, M. Portabella, E. Exarchou, P. Ortega, and I. Gómara, "Dominant role of North tropical Atlantic 2017 warm event on equatorial variability," EGU General Assembly, Vienna, Austria (online), 19-30 April, 2021.

- Stoffelen, A., M. Belmonte, A. Trindade, M. Portabella, and G. De Chiara, "BLUE for the scatterometer constellation," 15th International Winds Workshop, online, 12-16 April, 2021.

- Makarova, E., M. Portabella, and A. Trindade, "Evaluation of the ERA* Ocean Forcing Product Under Storm Surge Conditions in the Adriatic Sea," International Ocean Vector Winds Science Team Workshop, online, 24 February - 10 March, 2021.

- Portabella, M., Trindade, A., Cossu, F., Grieco, G., Rabaneda, A., Makarova, E., Martín-Rey, M., Exarchou, E., Lin, W., Polverari, F., and King, G., "Scatterometer-derived stress-equivalent wind fields: retrievals and applications," International workshop on metrology for the sea (Metrosea), online, October 5-7, 2020. (Invited)

- Makarova, E., Portabella, M., and Trindade, A., "Evaluation of the ERA* ocean forcing product under storm surge conditions in the Adriatic Sea," International Symposium on Marine Sciences (ISMS), online, July 1-3, 2020.

- Giesen, R., Trindade, A., Portabella, M., and Stoffelen, A., “Improved ocean wind forcing products,” EGU General Assembly, online, 4-8 May, 2020.

- Trindade, A., Portabella, M., Stoffelen, A., Lin, W., and Verhoef, A., “Improvement of the ERA* ocean forcing product: Benefits from the scatterometer constellation,” International Ocean Vector Winds Science Team Workshop, Portland, USA, 28-31 May, 2019.

- Trindade, A., Portabella, M., Stoffelen, A., and Verhoef, A., “Improvement of the ERA* high-resolution forcing product: benefits from the scatterometer constellation,” ESA Living Planet Symposium, Milan, Italy, 13-17 May, 2019.

- Trindade, A., Portabella, M., Stoffelen, A., and Verhoef, A., “ERA*: Towards an eddy resolving ocean forcing,” EGU General Assembly, Vienna, Austria, 7-12 April, 2019.

- Portabella, M., Lin, W., Polverari, F., Trindade, A., and King, G., “Are satellite-derived mesoscale sea surface winds useful in the Mediterranean?,” 7th International Conference on Meteorology and Climatology of the Mediterranean (MetMed), Palma de Mallorca, Spain, 4-6 March, 2019.

POSTERS

- Giesen, R., Trindade, A., Portabella, M., and Stoffelen, A., “Improved ocean wind forcing products,” Remote Sensing for Ocean-Atmosphere Interactions Studies and Applications Workshop, online, 1-3 December 2021.

- Trindade, A., Portabella, M., Lin, W., and Stoffelen, A., “On the development of a scatterometer-based correction for NWP wind forcing systematic errors: impact of satellite sampling,” Proc. of the International Geoscience and Remote Sensing Symposium (IGARSS), Fort Worth, USA, 23-28 July, 2017

- Stoffelen, A., Trindade, A., De Kloe, J., and Portabella, M., “Ocean state diagnostics from scatterometers,” International Ocean Vector Winds Science Team Workshop, San Diego, USA, 2-4 May, 2017.

- Portabella, M., Trindade, A., Stoffelen, A., Lin, W., and Belmonte-Rivas, M., “ERA*: An eddy-scale ocean forcing product,” EGU General Assembly, Vienna, Austria, 24-28 April, 2017.